EFFECT OF TEMPERATURE ON THE FLEXURAL BEHAVIOR OF NSM CFRPSTRENGTHENED RC BEAMS UNDER TIME-DEPENDENT LOADING AND FATIGUE

Younes Jahani

Universitat de Girona

Effect of temperature on the flexural behavior of NSM CFRP-strengthened RC beams under time-dependent loading and fatigue

YOUNES JAHANI

2022

Escola Politècnica Superior

Doctoral Thesis

Effect of temperature on the flexural behavior of NSM CFRP-strengthened RC beams under time-dependent loading and fatigue

Younes Jahani

2022

Doctoral Program in Technology

Supervisor:

Dr. Marta Baena Muñoz

Universitat de Girona

Thesis submitted to the University of Girona for the degree of Doctor

Younes Jahani

Effect of temperature on the flexural behavior of NSM CFRP-strengthened RC beams under time-dependent loading and fatigue

Doctoral Thesis, 2022

Doctoral Program in Technology

Supervisors: Dr. Marta Baena Muñoz

University of Girona

AMADE Research Group

Escola Politècnica Superior

Department of Mechanical Engineering and Industrial Construction

Carrer Universitat de Girona, 4

17003, Girona

To my family.

"Anyone who has never made a mistake has never tried anything new"

Albert Einstein

Acknowledgements

First, I would like to acknowledge and give my warmest regard to my supervisor Dr. Marta Baena who made this thesis possible. Your comprehensive guidance helped me to carry out this thesis from the first day till the last moment. I will never forget how hard you tried to bring me here, with all the difficulties that you faced. You were not only my supervisor, but also my friend. Words cannot express my gratitude, thank you so much for everything that you have done.

This work could not be undertaken without the help of Dr. Lluís Torres and Dr. Cristina Barris who generously provided knowledge and expertise during this thesis. Definitely, your experiences were very important and helped me to achieve the objectives in this thesis. I would also like to thank Pau who taught me how to work in a structures' laboratory. Everything that I know today from experimental work is because of you. Thank you for being a good friend and an amazing teacher.

Besides, I also appreciate Dr. José Sena-Cruz who hosted my research stay in the ISISE Institute at Minho University. I am really grateful for all your technical support. I must say that I was so lucky to have a chance to get a hard copy of your amazing PhD thesis signed by you.

I would also like to thank all AMADE members, friends and colleagues; Javi, Aravind, Santi Jordi, Sergio, Anni, José Manuel, Adrià, Oriol, Ivan, Juan José, Jonathon, Said, Alba, Edwin, Anbu, Alex, Joan and Mehdi. We had a great time together that I will never forget. Furthermore, I thank the people from the structures' laboratory, Pere, Sergi and Jordi, and people from AMADE laboratory, Dani, Ivan, Albert, Carlos, who have always helped me during this thesis.

I would like to say that this honor doesn't just belong to me. I have been encouraged, sustained and inspired not only by my supervisor but also by my family and friends. I would not be up here if it weren't for some very important people in my life. Beginning with my mother, father, sisters and brothers. Mother and father, you have kept my spirits and motivation high during this thesis, thank you for all your support throughout my life, I am proud of you and I love you so much. Lastly, I deeply express my gratitude to my dear Núria, this work would not have been completed without your support. Thank you for being a part of this journey.

Thank you all.

Preface

The work performed in this thesis was conducted in the AMADE research group (Department of Mechanical Engineering and Industrial Construction, University of Girona, Spain).

List of publications

The present thesis is prepared as a compendium of journal papers, according to the requirements of the Universitat de Girona. The following papers have been generated from this thesis:

- **Jahani Y.**, Baena M., Gómez J., Barris C., Torres L. Experimental Study of the Effect of High Service Temperature on the Flexural Performance of Near-Surface Mounted (NSM) Carbon Fiber-Reinforced Polymer (CFRP)-Strengthened Concrete Beams. ***Polymers***, 13 (6) (2021), 920. doi: 10.3390/polym13060920.
- EISSN: 2073-4360, Impact factor: 4.967 and ranked 16/90 in the category of *Polymer Science* (1st quartile)[1].

- **Jahani Y.**, Baena M., Barris C., Ricardo P., Torres L. Influence of curing, post-curing and testing temperatures on mechanical properties of a structural adhesive. ***Construction and Building Materials***, 324 (2022) 126698. doi: 10.1016/j.conbuildmat.2022.126698
- ISSN: 0950-0618, Impact factor: 7.693 and ranked 5/138 in the category of *Civil Engineering* (1st quartile)[1].

- **Jahani Y.**, Baena M., Codina A., Barris C., Torres L. Time-dependent behavior of NSM CFRP-strengthened RC beams under different service temperatures. ***Composite Structures***, 300 (2022) 116106. Doi: 10.1016/j.compstruct.2022.116106
- ISSN: 0263-8223, Impact factor: 6.603 and ranked 7/28 in the category of *Composites* (1st quartile)[1].

- **Jahani Y.**, Baena M., Barris C., Torres L., Sena-Cruz J. Effect of fatigue loading on flexural performance of NSM CFRP-strengthened RC beams under different service temperatures. Submitted to ***Engineering Structures*** on 1st July 2022.
- ISSN: 0141-0296, Impact factor: 6.582 and ranked 20/138 in the category of *Civil Engineering* (1st quartile)[1].

[1]According to the 2021 Journal Citation Reports

Conferences

- **Jahani Y.**, Baena M., Gómez J., Barris C., Torres L. Flexural Performance of NSM CFRP-Strengthened Concrete Beams Under Temperature. 10th International Conference on FRP Composites in Civil Engineering (CICE2020). Istanbul (Turkey), 8-10th December 2021.

- **Jahani Y.**, Baena M., Gómez J., Barris C., Torres L. Temperature effects on the flexural response of NSM CFRP-strengthened RC beams under sustained load. 24th International Conference on Composite Structures (ICCS). Porto (Portugal), 14-18th June 2021.

- **Jahani Y.,** Baena M., Sena-Cruz J., Aghabagloo M., Barris C., Torres L. Experimental fatigue behavior of NSM CFRP-strengthened RC beams under high service temperature. 6th International Conference on Smart Monitoring, Assessment and Rehabilitation of Civil Structures (SMAR). Shanghai (China), 6-8th September 2022.

To whom it might concern,

Dr. Marta Baena Muñoz, associate professor at the Universitat de Girona of the Department of Enginyeria Mecànica i de la Construcció Industrial,

CERTIFIES that,

The study entitled *Effect of temperature on the flexural behavior of NSM CFRP-strengthened RC beams under time-dependent loading and fatigue* has been carried out under her supervision by Younes Jahani and that it fulfils the requirements to aim for the International Mention.

Girona, July 2022,

Dr. Marta Baena Muñoz
Universitat de Girona, Spain

Table of Contents

List of Figures

xvii

List of Tables

Nomenclature

ΔM	restraining moment against shrinkage
ΔM_{cr} and ΔM_{ucr}	restraining moments against shrinkage for cracked and uncracked section, respectively
ΔM_{sh}	additional moment due to shrinkage
ΔN	restraining axial force against shrinkage
ΔN_{cr} and ΔN_{ucr}	restraining forces against shrinkage for cracked and uncracked section, respectively
μ	viscosity
A	area of transformed section
A_{cr} and A_{ucr}	area of cracked and uncracked transformed section, respectively
A_c	area of concrete (ignoring steel reinforcement)
$A_{c,cr}$ and $A_{c,ucr}$	area of cracked and uncracked concrete, respectively (ignoring steel reinforcement)
$A_e(t,t_0)$	area of transformed section with time
A_{FRP}	area of FRP
A_{s1}	area of compression steel reinforcement
A_{s2}	area of tension steel reinforcement
b	width of section
B	first moment of inertia of the area of transformed section
B_{cr} and B_{ucr}	first moments of inertia of the area of cracked and uncracked transformed section, respectively
B_c	first moment of inertia of the area of concrete (ignoring steel reinforcement)
$B_{c,cr}$ and $B_{c,ucr}$	first moments of inertia of the area of cracked and uncracked concrete, respectively (ignoring steel reinforcement)
$B_e(t,t_0)$	first moments of inertia of the area of the transformed section with time
d_{FRP}	effective depth of FRP
d_n	neutral axis depth of section
$d_{n,cr}$ and $d_{n,ucr}$	neutral axis depth of cracked and uncracked section, respectively
d_{ser}	deflection at service load

d_{s1}	effective depth of compression steel reinforcement
d_{s2}	effective depth of tension steel reinforcement
E'	storage modulus
E''	loss modulus
$E_{acc,diss}$	accumulated dissipated energy
E_c	modulus of elasticity of concrete
$E_c(T)$	modulus of elasticity of concrete at temperature T (in °c)
E_{diss}	dissipated energy
$E_e(t,t_0)$	effective modulus of elasticity of concrete with time
E_{epoxy}	tensile elastic modulus of epoxy
E_{FRP}	modulus of elasticity of FRP
$E_{FRP}(t_0)$	modulus of elasticity of FRP at loading time
$E_{FRP,e}(t,t_0)$	modulus of elasticity of FRP with time
E_s	modulus of elasticity of steel reinforcement
$E_{tot,acc,diss}$	total accumulated dissipated energy at the end of fatigue test
$F_{c,epoxy}$	compressive load of epoxy
f_c	compressive strength of concrete
$f_c(T)$	compressive strength of concrete at temperature T (in °c)
$F_{cu,epoxy}$	ultimate compressive load of epoxy
f_t	concrete tensile strength
$f_t(T)$	concrete tensile strength at temperature T (in °c)
$f_{t,sp}$	concrete splitting tensile strength
f_u	ultimate strength of steel reinforcement
$f_{u,epoxy}$	tensile strength of epoxy
$f_{u,FRP}$	ultimate tensile strength of FRP
f_y	yielding strength of steel reinforcement
h	height of section
I	second moment of inertia of the area of the transformed section
I_{cr} and I_{ucr}	second moments of inertia of the area of cracked and uncracked transformed section, respectively
I_c	second moment of inertia of the area of the concrete (ignoring steel reinforcement)

$I_{c,cr}$ and $I_{c,ucr}$	second moments of inertia of the area of cracked and uncracked concrete, respectively (ignoring steel reinforcement)
$I_e(t,t_0)$	second moment of inertia of the area of transformed section with time
K	stiffness
K_c	ratio of the second stress invariant on the tensile meridian to that on the compressive meridian
m	slope of the best-fit line relating log $\varepsilon_{FRP}(t,t_0)$ and $\log(t/t_0)$
M	external moment
M_{cr}	cracking moment
$M_{cr,sh}$	reduced cracking moment due to shrinkage
M_{LT}	moment applied at the beginning of long-term loading
$M_{n,cr}$ and $M_{n,ucr}$	moment capacity of cracked and uncracked section, respectively
N_c	resultant force from the compression concrete stress block
n_{FRP}	modular ratios of FRP
N_{FRP}	resultant force from FRP
$n_{FRP}(t,t_0)$	modular ratios of FRP with time
N_{LT}	axial force applied at the beginning of long-term loading
n_s	modular ratios of steel reinforcement
$n_s(t,t_0)$	modular ratios of steel reinforcement with time
N_{s1}	resultant force from compression steel reinforcement
N_{s2}	resultant force from tension steel reinforcement
P_{amp}	fatigue amplitude
P_{ave}	average fatigue load
P_{cr}	cracking load
P_{LT}	level of long-term load
P_{max}	maximum fatigue load
P_{min}	minimum fatigue load
P_{ser}	service load level
P_u	ultimate load
P_y	yielding load
R	ratio between minimum load and maximum load of fatigue cycle
t	age of specimen at the moment considered

t_0	age at the start of loading
$tan\delta$	loss factor
T_e	extrapolated end temperature
T_f	extrapolated onset temperature
T_g	glass transition temperature
$T_{g\infty}$	upper bound value corresponds to the glass transition temperature of fully cured network
T_m	mid-point temperature
α	parameter to determine the resultant force from the concrete compression stress block
α_1 and α_2	coefficients that define the tensile post-cracking stress-strain relationship of concrete
α_{sp}	coefficient to transform the splitting tensile strength to tensile strength
δ_{ave}	average fatigue deflection
$\delta_{ave,n}$	average normalized fatigue deflection
δ_{cr}	cracking deflection
δ_{ins}	instantaneous deflection after the application of long-term load
$\Delta M\,(t,t_0)$	restraining moment to prevent free development of creep and shrinkage in concrete with time
$\delta_{max,i}$	deflections corresponding to $p_{max,i}$ at the ith cycle of fatigue loading
$\delta_{min,i}$	deflections corresponding to $p_{min,i}$ at the ith cycle of fatigue loading
$\Delta N\,(t,t_0)$	restraining force to prevent free development of creep and shrinkage in concrete with time
δ_p	plastic deflection after fatigue loading
$\delta_{p,0}$	permanent deflection after a one-day relaxation following the pre-loading
$\delta_{p,u}$	ultimate permanent deflection after long-term loading
δ_{td}	time-dependent deflection due to long-term load
δ_{tot}	total deflection in long-term loading
δ_u	ultimate deflection in short-term loading
$\delta_{u,ave,n}$	ultimate average normalized fatigue deflection
δ_y	yielding deflection in short-term loading
$\Delta\varepsilon_0\,(t,t_0)$	variation maximum concrete compressive strain with time

$\Delta\kappa\,(t,t_0)$	variation of the section curvature with time
ε_{0i}	instantaneous maximum concrete compressive strain
ε_{ave}	average concrete strain in fatigue loading
$\varepsilon_{ave,n}$	average normalized concrete strain in fatigue loading
ε_c	strain in compression concrete
$\varepsilon_c\,(t,t_0)$	strain in compression concrete with time
$\varepsilon_{c,max}$	maximum concrete compression strain registered in experimental work
$\varepsilon_{ci}\,(t_0)$	instantaneous concrete strain after the application of long-term load
$\varepsilon_{cs}\,(t,t_0)$	concrete shrinkage strain with time
$\varepsilon_{epoxy}\,(t,t_0)$	epoxy adhesive strain with time
$\varepsilon_{epoxy}\,(t_0)$	epoxy adhesive strain at the loading moment
ε_{FRP}	strain in FRP
$\varepsilon_{FRP}\,(t,t_0)$	strain in FRP with time
$\varepsilon_{FRP}\,(t_0)$	instantaneous strain in FRP at loading time
ε_{s1}	strain in compression steel reinforcement
ε_{s2}	strain in tension steel reinforcement
ε_{sh}	free shrinkage strain in concrete
$\varepsilon_{sh}\,(t,t_0)$	free shrinkage strain in concrete with time
ε_t	strain in tension concrete
$\varepsilon_{u,ave,n}$	ultimate average normalized concrete strain in fatigue loading
$\varepsilon_{u,epoxy}$	epoxy ultimate strain
$\varepsilon_{u,FRP}$	ultimate tensile strain in FRP
κ_i	initial section curvature
κ_{ucr}	curvature of the uncracked section
λ	parameter to modify the neutral axis depth in concrete compression stress block
ρ_s	steel reinforcement ratio
ρ_{FRP}	FRP strengthening ratio
σ_{b0}	biaxial compressive stress
σ_c	stress in compressed concrete
σ_{c0}	uniaxial compressive stress
$\sigma_{cu,epoxy}$	ultimate compressive strength of epoxy

σ_{FRP}	stress in FRP
σ_s	stress in steel reinforcement
σ_{s1}	stress in compression steel reinforcement
σ_{s2}	stress in tension steel reinforcement
φ_c	concrete creep coefficient
$\varphi_c\,(t,t_0)$	concrete creep coefficient with time
φ_{cr} and φ_{ucr}	cracked and uncracked additional curvatures due to shrinkage, respectively
φ_{epoxy}	creep coefficient of epoxy adhesive
$\varphi_{FRP}\,(t,t_0)$	creep coefficient of FRP with time
$\chi\,(t,t_0)$	reduction factor for concrete creep coefficient with time
ψ	dilation angle
ϵ	flow potential eccentricity

Abstract

There is a general trend towards rehabilitation and strengthening of existing reinforced concrete (RC) structures due to the costs associated with the replacement of the structural members and the environmental impact associated with the consumption of raw materials for new constructions. In this regard, fiber reinforced polymers (FRP) are presented to be an excellent solution for strengthening purposes, being the near-surface mounted (NSM) one of the main used techniques, because of the several advantages that it provides over the traditional plate bonding (i.e. externally bonded reinforcement (EBR)) technique. However, in spite of the advantages of NSM technique, premature debonding failure is still of concern.

The effectiveness of a strengthening system relies on the capacity of the joint to allow the stress transfer during the loading process, which has been acknowledged to be partially governed by the mechanical properties of the bonding agent. In this sense, epoxy adhesives are usually chosen to be the bonding agent in NSM technique. However, due to their nature, performance of epoxy adhesives can be affected by temperature, as near or beyond their glass transition temperature (T_g) their mechanical properties may change, thus affecting the behavior of the NSM strengthened member.

Besides, although NSM FRP strengthening has attracted an increasing amount of research, studies are still needed to fully understand their long-term performance, which partially depends on the material's long-term properties. In this sense, creep and shrinkage of concrete and creep of epoxy adhesive, which are dependent on environmental conditions, are of high importance. Similar to long-term loading, attention should also be given to fatigue loading, where the stiffness of the system degrades due to progressive cracking and stress/strain accumulation in the material.

This work aimed to experimentally and analytically study the flexural performance of NSM carbon FRP (CFRP)-strengthened RC beams subjected to short-term, long-term and fatigue loading under different high service temperatures. To this end, the first experimental program with 14 beams has been performed, where the effect of CFRP strengthening ratio, concrete strength and applied temperatures has been evaluated. The aim was to evaluate the effect of different parameters on the short-term behavior of the beams in order to easily design the long-

term and fatigue experimental programs. Analytical simulations have also been performed to predict the load-deflection responses of the tested beams, where shrinkage effects have been accounted for.

Based on the observations from the first experimental program, a comprehensive experimental program (more than 113 epoxy adhesive samples) has been designed, where the effect of curing, post-curing and testing temperature on the instantaneous mechanical (tensile and compressive) properties of the adhesive has been studied. The range of temperatures considered in this experimental program was in line with temperatures applied in the instantaneous flexural program (i.e. temperature varied from 20 °C to 85 °C).

Afterwards, a long-term loading experimental program has been performed, where the effect of steel reinforcement ratio, CFRP strengthening ratio and temperature has been considered, thus giving a total of 23 beams. The distribution of the beams was as follows: i) 10 beams have been tested under short-term loading; ii) 10 beams have been initially tested under long-term loading to be thereafter tested until failure (post long-term); and finally, iii) 3 beams have been rested at laboratory conditions in order to examine the aging effect on their instantaneous response. Besides, the long-term behavior of the involved materials (concrete and epoxy adhesive) has been also evaluated. Furthermore, an analytical procedure based on the age-adjusted modulus method (AEMM) has been presented to correctly predict the experimental time-dependent deflection of the tested beams.

Finally, in the last experimental program, the effect of fatigue loading on the flexural response of the NSM CFRP-strengthened RC beams under different temperatures has been evaluated. The experimental program included 11 beams, 3 of them for short-term loading, in order to define the fatigue load levels, and 8 of them for fatigue loading, to evaluate the effect of CFRP strengthening ratio, fatigue load level and temperature. The fatigue load has been applied for 2 million cycles or failure of the beam (whichever occurs first) with a frequency of 2 Hz.

Resum

Hi ha una tendència cada vegada més generalitzada cap a la rehabilitació i el reforç de les estructures existents de formigó armat (FA) degut als costos associats a la seva substitució i a l'impacte ambiental derivat del consum de matèries primeres associat a la nova construcció. En aquest context, els polímers reforçats amb fibres (FRP, de l'anglès fiber reinforced polymer) es presenten com una solució excel·lent per al reforç estructural, sent la tècnica del reforç inserit en el recobriment del formigó (NSM, de l'anglès near surface mounted) una de les principals tècniques emprades degut als avantatges que aquesta ofereix enfront al reforç extern (EBR, de l'anglès externally bonded reinforcement). No obstant, malgrat els avantatges del reforç NSM, la fallada prematura per desenganxament continua sent una problemàtica.

L'eficàcia de qualsevol sistema de reforç estructural depèn de la capacitat de transmissió d'esforços de la unió, que depèn parcialment de les propietats mecàniques del material adherent. En aquest sentit, les resines epoxídiques son el material adherent més utilitzat en la tècnica de reforç NSM. Ara bé, degut a la naturalesa d'aquests adhesius, el seu comportament es pot veure afectat per temperatures properes o superiors a la seva temperatura de transició vítria (T_g) i poden experimentar canvis en les seves propietats mecàniques.

D'altra banda, encara que el reforç amb NSM FRP ha estat objecte d'un esforç creixent en recerca, es requereixen més estudis per entendre millor el seu comportament a llarg termini. En aquest sentit, la fluència i la retracció del formigó, així com la fluència de l'epoxy, prenen una gran importància, que és de gran rellevància si es té en compte que aquests fenòmens depenen de les condicions ambientals. D'altra banda, també és necessari estudiar el comportament d'aquests elements reforçats sota càrregues de fatiga.

L'objectiu d'aquest treball és l'estudi experimental i analític del comportament de bigues de FA reforçades amb FRP a base de fibres de carboni (CFRP, de l'anglès carbon fiber reinforced polimers) mitjançant la tècnica NSM, que es troben sotmeses a temperatures de servei elevades. Aquest estudi inclou el comportament instantani, el comportament a llarg termini sota càrregues mantingudes i el comportament sota càrregues de fatiga. Amb aquesta finalitat, s'ha portat a terme un primer programa experimental per investigar el comportament instantani (càrrega monotònica fins a ruptura) a flexió que incloïa un total de 14 bigues. Els paràmetres de l'estudi han estat la quantia de reforç de CFRP, el tipus de formigó i la temperatura. Per complementar aquest primer programa experimental, s'han realitzat

prediccions analítiques de la relació càrrega-fletxa de les bigues assajades, en les que s'ha tingut en compte l'efecte de la retracció del formigó.

A partir dels resultats de l'estudi del comportament instantani a flexió, s'ha dissenyat un extens programa experimental (amb més de 113 mostres d'adhesiu epoxy) per l'estudi de l'efecte de la temperatura (temperatura de curat, temperatura de post-curat i temperatura d'assaig) sobre les propietats mecàniques (tracció i compressió) de l'epoxy. El rang de valors de temperatura aplicada es corresponia amb les temperatures aplicades a l'estudi del comportament instantani a flexió (és a dir, des dels 20 °C fins als 85 °C).

Posteriorment, s'ha portat a terme un programa experimental per investigar el comportament a llarg termini sota càrregues mantingudes amb els següents paràmetres d'estudi: quantia d'armadura d'acer, quantia de reforç de CFRP i temperatura aplicada durant la càrrega mantinguda. Del total de 23 bigues assajades, es van assajar 10 bigues sota càrrega monotònica fins a ruptura, es van assajar 10 bigues sota càrrega mantinguda a llarg termini (que posteriorment es van assajar fins a ruptura) i es van deixar 3 bigues reposant al laboratori, per tal d'analitzar l'efecte de l'envelliment. Addicionalment, també s'ha estudiat el comportament sota càrrega mantinguda dels diferents materials involucrats (formigó i epoxy). Finalment, s'ha implementat una metodologia, basada en el mètode del mòdul efectiu ajustat (AEMM, de l'anglès aged adjusted modulus method), per la predicció analítica de la fletxa a llarg termini, que ha demostrat donar bons resultats.

La tesi conclou amb un últim programa experimental on s'ha investigat l'efecte de la temperatura sobre el comportament a fatiga de bigues de FA reforçades amb CFRP mitjançant la tècnica NSM. S'han assajat un total de 11 bigues, de les quals 3 van ser assajades monotònicament fins a ruptura i 8 van ser sotmeses a cicles de fatiga. Els paràmetres estudiats han estat la quantia de reforç de CFRP, el nivell de càrrega de fatiga aplicat i la temperatura aplicada durant l'assaig de fatiga. L'assaig a fatiga va ser dissenyat per durar 2 milions de cicles (o fins a ruptura de la biga) a una freqüència de 2 Hz.

Resumen

Cada vez es más generalizada la tendencia hacia la rehabilitación y refuerzo de las estructuras existentes de hormigón armado (HA) debido a los costes asociados a su sustitución y al impacto ambiental derivado del consumo de materias primas asociado a la nueva construcción. En este contexto, los polímeros reforzados con fibras (FRP, del inglés fiber reinforced polymer) se presentan como una solución excelente para el refuerzo estructural, siendo la técnica del refuerzo inserido en el recubrimiento del hormigón (NSM, del inglés near surface mounted) una de las principales técnicas utilizadas debido a las ventajas que ésta ofrece en comparación con el refuerzo externo (EBR, del inglés externally bonded reinforcement). Sin embargo, a pesar de las ventajas del refuerzo NSM, el fallo prematuro por adherencia continúa siendo una problemática.

La eficacia de cualquier sistema de refuerzo estructural depende de la capacidad de transmisión de esfuerzos de la unión, que a su vez depende parcialmente de las propiedades mecánicas del material adherente. En este sentido, las resinas epoxídicas son el material adherente más utilizado en la técnica de refuerzo NSM. Sin embargo, debido a la naturaleza de estos adhesivos, su comportamiento puede verse afectado por temperaturas cercanas o superiores a su temperatura de transición vítrea (T_g) y pueden experimentar cambios en las propiedades mecánicas.

Por otra parte, aunque el refuerzo con NSM FRP ha sido objeto de un esfuerzo creciente en investigación, se necesitan más estudios para entender mejor su comportamiento a largo plazo. En este sentido, las deformaciones a largo plazo del hormigón (fluencia y retracción) y del epoxy (fluencia) son especialmente relevantes si se tiene en cuenta que estos fenómenos dependen de las condiciones ambientales. Asimismo, también se requiere de más atención en el estudio del comportamiento de estos elementos reforzados bajo cargas de fatiga.

El objetivo de este trabajo es el estudio experimental y analítico del comportamiento de vigas de HA reforzadas con FRP a base de fibras de carbono (CFRP, del inglés carbón fiber reinforced polymers) mediante la técnica NSM, que se encuentren sometidas a elevadas temperaturas de servicio. Este estudio incluye el comportamiento instantáneo, el comportamiento a largo plazo bajo cargas mantenidas y el comportamiento bajo cargas de fatiga. Para ello, se ha llevado a cabo un primer programa experimental para investigar el comportamiento instantáneo (carga monotònica hasta rotura) a flexión, que incluye un total de 14 vigas. Los parámetros de estudio

han sido la cuantía de refuerzo de CFRP, el tipo de hormigón y la temperatura. El trabajo experimental de este primer programa se complementa con predicciones analíticas de la relación carga-flecha de las vigas ensayadas, en las que se ha incorporado el efecto de la retracción del hormigón.

A partir de los resultados del estudio del comportamiento instantáneo a flexión, se ha diseñado un amplio programa experimental (con más de 113 muestras de adhesivo epoxy) en el que estudiar el efecto de la temperatura (temperatura de curado, temperatura de post-curado y temperatura de ensayo) sobre las propiedades mecánicas (tracción y compresión) del epoxy. El rango de valores de temperatura aplicada se corresponde con las temperaturas aplicadas en el estudio del comportamiento instantáneo a flexión (es decir, desde los 20 °C hasta los 85 °C).

Posteriormente, se ha llevado a cabo un programa experimental para investigar el comportamiento a largo plazo bajo cargas mantenidas, en el que se han considerado los siguientes parámetros de estudio: cuantía de armadura de acero, cuantía de refuerzo de CFRP y temperatura aplicada durante la carga mantenida. Del total de 23 vigas ensayadas, 10 fueron ensayadas bajo carga monotónica hasta rotura, otras 10 fueron ensayadas a largo plazo bajo carga mantenida (y posteriormente fueron ensayadas hasta rotura), y se dejaron reposar en el laboratorio las 3 vigas restantes, para poder así analizar el efecto del envejecimiento. Además, también se ha estudiado el comportamiento bajo carga mantenida de los diferentes materiales involucrados (hormigón y epoxy). Para finalizar, se ha implementado una metodología, basada en el método de modulo efectivo ajustado (AEMM, del inglés aged adjusted modulus method), para la predicción analítica de la flecha a largo plazo, que ha demostrado obtener buenos resultados.

Para concluir con la tesis, se ha llevado a cabo un último programa experimental para investigar el efecto de la temperatura en el comportamiento bajo cargas de fatiga de vigas de HA reforzadas con CFRP mediante la técnica NSM. Se han ensayado un total de 11 vigas, 3 de las cuales han sido ensayadas bajo carga monotónica hasta rotura, y las 8 vigas restantes han sido sometidas a ciclos de fatiga. Los parámetros de estudio han sido la cuantía de refuerzo de CFRP, el nivel de carga de fatiga aplicado y la temperatura aplicada durante el ensayo de fatiga. El ensayo a fatiga fue diseñado para durar 2 millones de ciclos (o hasta rotura de la viga) a una frecuencia de 2 Hz.

PART I: Introduction

1 Introduction

1.1 Overview and motivation

Rehabilitation of existing damaged structures is vital to extend their service life and to increase their safety, at the same time that consumption of raw material is reduced and, consequently, the environmental impact associated with building new structures is also reduced. In the last decades, due to emerging new strengthening materials and techniques, a general tendency towards rehabilitation of structures has been created [1]. In this sense, the cost analysis of the projects and construction speed leads to strengthening the existing structures rather than making new ones.

Fiber reinforced polymer (FRP) materials have been widely used to strengthen damaged reinforced concrete (RC) structures due to their unique characteristics. They have several advantages when compared to the traditional material (i.e. steel reinforcement) such as, light weight, higher tensile strength and higher resistance to corrosion. However, lower fire resistance and higher manufacturing cost are the most important disadvantages of these materials [2-4].

Nowadays, different FRP-strengthening techniques are used to strengthen RC structures. Among them, externally bonded reinforcement (EBR) and near-surface mounted (NSM) techniques are the most common methods. The EBR method consists of bonding the FRP laminates or sheets onto the concrete surface using an adhesive. In this method, the surface of the concrete is treated prior to bonding in order to assure high bonding between concrete and FRP. The EBR system is easy to install, but it is more affected by environmental conditions and vandalism. On the other hand, in the NSM technique, which is the most recent method, grooves are cut in the concrete surface and then the FRP (strips or bars) are inserted into the grooves using a proper adhesive. This technique has several advantages when compared to the EBR system, such as: higher anchorage capacity, no need for surface treatment except groove cutting, less susceptible to environmental conditions, less prone to vandalism and good finished surface [5,6]. The epoxy adhesive is the most used bonding material in the FRP-strengthened structures. Due to the nature of this material, its mechanical properties can be affected when working temperature approaches its glass transition temperature (T_g) [7-9]. As a result, the

performance of the strengthening system can be also affected, especially when high service temperatures are combined with time-dependent loads (long-term or fatigue loading).

A significant amount of work has been done in order to study the performance of NSM FRP-strengthened RC beams under short-term loading, while a few of them deal with long-term loading and fatigue conditions. Furthermore, the available work in the literature is mainly focused on the flexural performance of this system under room temperature or fire conditions, but their behavior under high service temperature (near or beyond the T_g of the epoxy adhesive) is missing or needs further research. Therefore, this PhD thesis aims to contribute to the understanding of these issues. To this end, a comprehensive experimental work has been performed to evaluate the flexural performance of NSM carbon FRP (CFRP)-strengthened RC beams subjected to short-term, long-term and fatigue loading under high service temperatures. Furthermore, the effect of temperature on mechanical properties of epoxy adhesive has been also investigated.

1.2   Objectives of the PhD

The main objective of this PhD thesis is to experimentally and analytically investigate the flexural performance of NSM CFRP-strengthened RC beams subjected to short-term, long-term and fatigue loading under different high service temperatures.

This main goal is divided into six sub-objectives that will be addressed along with the thesis:

1. The study of the effect of different service temperatures on the flexural performance of NSM CFRP-strengthened RC beams under short-term loading.
2. The development of analytical predictions on the load-deflection response of NSM CFRP-strengthened RC beams subjected to short-term loading, where shrinkage effects are accounted for.
3. The study of the effect of curing, post-curing and testing temperatures on mechanical properties of the epoxy adhesive.
4. The study of the time-dependent behavior of NSM CFRP-strengthened RC beams under long-term loading and high service temperatures.
5. The analytical study on the time-dependent deflections of NSM CFRP-strengthened RC beams, where temperature effects are accounted for.

6. The study of the effect of fatigue loading on the flexural behavior of NSM CFRP-strengthened RC beams under high service temperatures.

1.3 Thesis layout

This thesis is written as a compendium of journal papers, each of them being presented in a chapter. Initially, the state-of-the-art is presented in Chapter 2 where a detailed review of the current state of the art is carried out.

In Chapter 3, the methodology followed in the experimental programs carried out in this PhD thesis is presented. In this section, the characterization of the materials, the instrumentation and the short-term, long-term and fatigue loading tests setups for the different experimental programs are described. Furthermore, analytical models to predict the instantaneous and the time-dependent responses are also presented in this chapter.

Chapter 4 presents the first article of the thesis, where the effect of different service temperatures on the instantaneous flexural response of NSM CFRP-strengthened RC beams is presented. The second paper of the thesis is presented in Chapter 5, where the effect of curing, post-curing and testing temperature on mechanical properties of the epoxy adhesive is presented. Furthermore, the effect of temperature on T_g of the epoxy adhesive is also addressed. Chapter 6 provides the third paper, where the time-dependent behavior of NSM CFRP-strengthened RC beams under high service temperature is reported. In addition, the time-dependent behavior of involved materials is also investigated. In Chapter 7 the fourth article of this PhD thesis is presented, where the effect of fatigue loading on the flexural performance of NSM CFRP-strengthened RC beams under high service temperature is studied.

The discussion and the concluding remarks of this thesis are presented in Chapters 8 and 9, respectively. Finally, Chapter 10 provides the possible future works derived from the research line followed in this PhD thesis.

PART II: Literature review and methodology

2   Literature review

2.1   Introduction

Concrete material is the most widely used in civil structures due to its numerous advantages, such as, high durability, lower cost and higher performance, resistance against corrosion and fire. Although civil structures are designed for different types of loads, their performance can be affected by long-term and repeated loads, environmental conditions, change in the service load and seismic activities [10,11]. Therefore, new materials and techniques are being developed and applied to rehabilitate and strengthen damaged RC structures [2,3].

2.2   Fiber-reinforced polymers (FRPs) in civil engineering

Due to their several advantages, FRP materials are widely used in different fields such as civil engineering, aerospace and aircraft, wind turbine and marine structures, among others [12]. One of the most important advantages of FRP materials is having a high ratio of tensile strength to self-weight. Besides, the reduced weight is resulting in an ease in handling and installation, and a reduction in the dead load of the structures. Moreover, FRP materials are providing a high corrosion resistance and low coefficient of thermal expansion and they can be found in different types and shapes [13]. On the other hand, their higher manufacturing cost can be one of the disadvantages of these materials [14].

In the field of civil engineering, three main applications are illustrated for FRP materials: (i) as main materials to build a complete structure (small bridge made from FRP, Figure 2.1a), (ii) as an alternative to steel for internal reinforcement of concrete elements (internal reinforcement with FRP bars, Figure 2.1b), and (iii) as strengthening system of existing damaged structures (strengthening with FRP sheets, Figure 2.1c).

Figure 2.1. Examples of the use of FRP materials as: (a) building complete structure, (b) reinforcing method and (c) strengthening method [4].

FRP materials are composed of two major components namely fibers and matrix, where the first component provides the strength and stiffness and the second component provides the transfer of stress and strain between fibers [15].

2.2.1 Fibers

The fibers provide the strength and stiffness to the FRP in order to resist the applied load. Therefore, they are the main component and their properties influence the overall behavior of the FRP system. Fibers are normally selected to have high strength and high elastic modulus [4]. Typically, four fiber types can be found in FRP system: Carbon FRP (CFRP), Glass FRP (GFRP), Aramid FRP (AFRP) and Basalt FRP (BFRP) [4].

Carbon

Carbon fibers are manufactured from heating fibers without the presence of oxygen. This process removes the non-carbon atoms and obtains a long interlocked chain of carbon atoms. Carbon fibers are widely used in composite materials due to their high stiffness and strength and high resistance against corrosion. In addition, carbon fiber has a high fatigue strength and very low or even negative coefficient of thermal expansion [12,15]. The main disadvantage of carbon fibers is being electrically conductive, which may cause galvanic corrosion in direct contact with steel [16].

Glass

Glass fibers are made of filaments of glass, obtained from melting and molding processes. Due to lower cost, high tensile strength and chemical resistance, glass fibers are the most

common and popular of all reinforcing fibers used in FRP materials. On the other hand, they present lower fatigue resistance and stiffness than carbon fibers [15].

Aramid

Aramid fibers are organic fibers formed by a long chain of synthetic polyamide and are created from a solution of PPTA (p-phenylene terephthalamides) polymer and sulfuric acid [17]. Similar to carbon fibers, aramid fibers present relatively high tensile strength, but their elastic modulus is low in comparison with carbon fibers. Moreover, they have better fracture toughness. Furthermore, compared with the other types of FRPs, aramid fibers exhibit lower compressive and shear strengths [15,18].

Basalt

Basalt fibers are obtained from volcanic basalt rock and they are produced by heating the rock until melting. Basalt fibers have better mechanical properties than glass fibers and a cheaper manufacturing process in comparison to carbon fibers [15]. The main disadvantages of the basalt fibers are the difficulty of the heating process and the quality control of the fibers [13].

2.2.2 Matrix

The matrix is used as a binder in order to hold all the fibers together. Furthermore, the matrix is involved in transferring the stress between individual fibers and protecting them from environmental conditions. Resin and polymers are the most used types of matrices. Polymers can be classified under two types, thermoplastics and thermosets, according to the effect of heat on their properties [4,15]. Usually, the matrix is made from thermoset polymers, which in comparison to thermoplastics, have better thermal stability and better chemical resistance. Among others, polyester, vinylester and epoxy are the most used thermoset polymers. Vinylester provides higher mechanical properties and higher resistance to environmental conditions in comparison to polyester. On the other hand, epoxy has excellent bond properties, lower shrinkage during curing time, good resistance to environmental degradation and good chemical properties, but it is the most expensive option. The main disadvantages of thermoset adhesives are that their properties are highly affected at temperatures near or above their T_g and that they are not recyclable [15,18].

2.2.3 Mechanical properties of FRP materials

The mechanical properties of FRPs depend on the mechanical properties of the constituent materials (i.e. fiber and matrix), the fibers orientation, the interface adhesion between fibers and matrix and the manufacturing process. Therefore, there is no unique value for their mechanical properties [4]. The typical comparison of stress-strain relationship for different types of FRP materials and steel, according to *fib* Bulletin 90 [1], is shown in Figure 2.2. In comparison to conventional steel, FRP materials usually present significantly higher tensile strengths and lower modulus of elasticity. However, their failure is brittle [19].
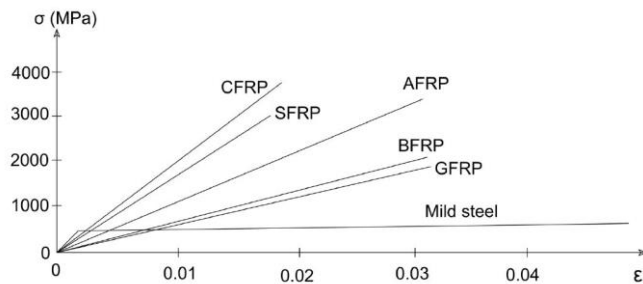
Figure 2.2. Uniaxial tensile stress-strain diagrams of FRP materials compared to steel [1].

2.2.4 FRP products

FRP materials can be found in different shapes such as laminates/strips, sheets and bars (see Figure 2.3). Among them, FRP laminates/strips and sheets are mainly used to strengthen existing RC damaged structures, whilst FRP bars can be used for strengthening or as internal reinforcement.
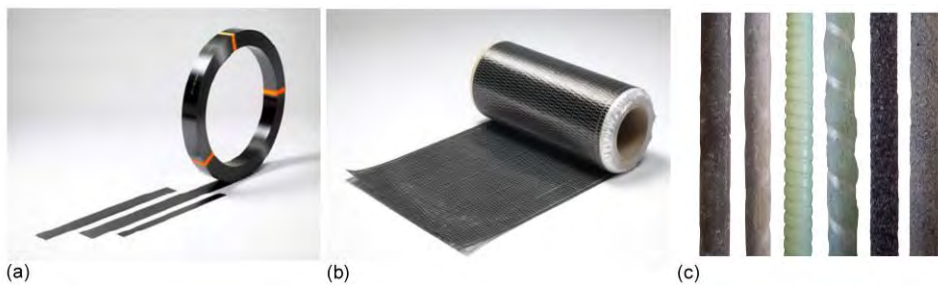
Figure 2.3. Different shapes of FRP materials: (a) FRP laminates, (b) FRP sheets and (c) FRP bars [20].

2.3 FRP-strengthening techniques

Strengthening is an optimal solution to rehabilitate and repair existing buildings and infrastructures in order to enlarge their service life and increase their carrying capacity. There are different techniques to strengthen RC structures, being the steel or concrete jacketing, the external post-tensioning, the externally-bonded (EB) steel plates and the replacement of degraded members or the addition of new extra members the more traditional repairing methods. However, although these methods can improve the strength, capacity and stiffness of deficient concrete structures, they may also increase the dead load of repaired structures and are time consuming. Therefore, there is a necessity to find alternative materials or methods.

In this scenario, FRP have been presented as an appropriate alternative due to their unique properties when compared to steel. In this section, two main techniques in strengthening with FRP materials, namely EBR and NSM technique, are presented. Figure 2.4 shows illustrative sketches of both techniques.
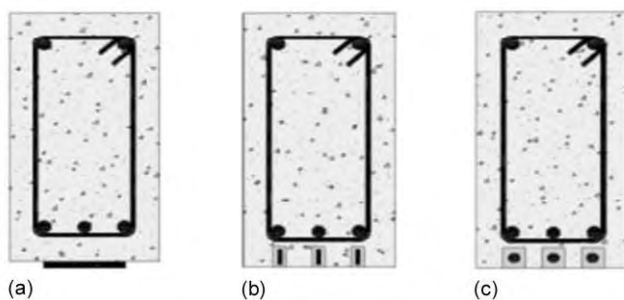
Figure 2.4. FRP-strengthening techniques: (a) EBR laminates, (b) NSM strips and (c) NSM bars [21].

2.3.1 Externally bonded reinforcement (EBR) technique

EBR technique is one of the most popular and old methods in FRP-strengthened structures. In this technique, FRP laminates or sheets are applied to the external part of the element using a proper bonding material (usually an epoxy adhesive). In this technique, prior to strengthening, the surface of the concrete should be treated and cleaned in order to increase the efficiency of the system and properly transfer the load from concrete to FRP. Two systems are used in EBR technique, namely wet lay-up and prefabricated. The wet lay-up system involves using a liquid

resin system to saturate a FRP material and then apply the saturated material to a prepared surface. This system, due to flexibility of FRP sheets, is suitable for the curve and convex surfaces. Focusing on prefabricated FRP laminates, after preparing the concrete surface, a layer of adhesive is applied and then the FRP laminate is installed onto the member. This method is suitable for flat surfaces.

The main advantage of EBR technique is the simplicity of installation in different types of surfaces. Some examples on the application of EBR technique are shown in Figure 2.5.
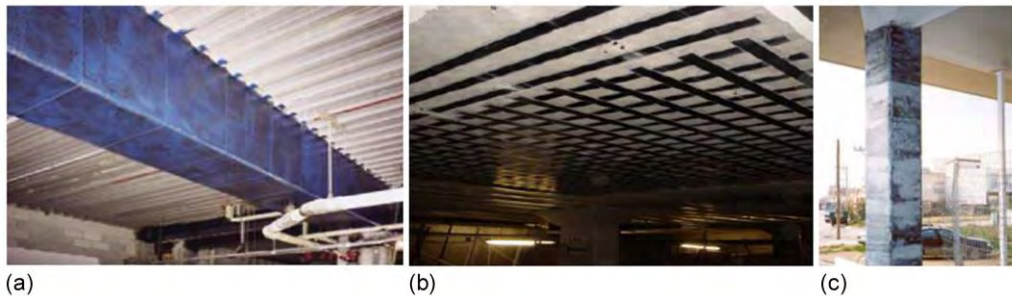
Figure 2.5. Examples of EBR installation in strengthening: (a) Beams, (b) Slabs and (c) Columns [22,23].

In spite of the above mentioned advantages, EBR technique has some disadvantages, such as need of surface treatment, premature debonding, brittle failure mode and being more susceptible to vandalism and to environmental conditions, among others [24,25].

2.3.2 Near-surface mounted (NSM) technique

In the early 1940s, the NSM strengthening technique started to be used for strengthening concrete structures with steel. However, in the last two decades this technique has been applied with FRP materials, as an alternative to the EBR system. In the NSM technique, grooves are cut in the concrete surface and, after cleaning the groove, NSM strips or bars are introduced onto the grooves with a proper bonding material (usually an epoxy adhesive), thus the FRP is completely embedded inside the epoxy adhesive. Figure 2.6 shows an example of the installation of FRP in concrete slab with NSM technique.

(a)   (b)
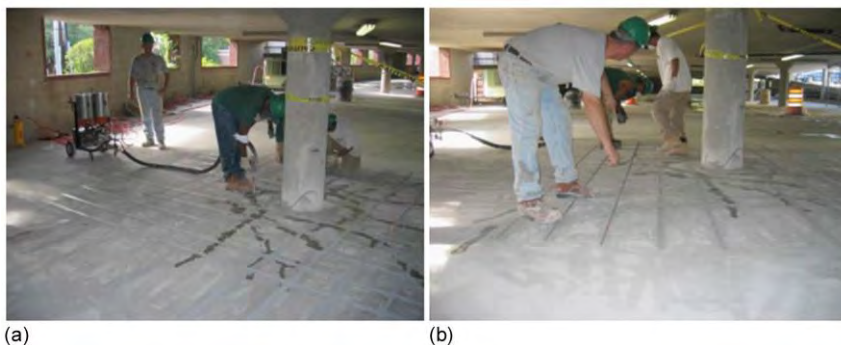
Figure 2.6. NSM installation: (a) Filling of the grooves with an epoxy adhesive and (b) Placement/insert of the CFRP bar [26].

In the NSM technique, in general, CFRP materials are used to strengthen RC structures and GFRP materials are mostly used for masonry and timber structures [5]. Besides, limited reports of the application of other types of FRP materials (such as AFRP and BFRP) can be found [13,27]. Furthermore, FRP materials used in the NSM strengthening can be in different shapes, such as round bars or rectangular/square strips, and with different surface treatments [28,29] A typical view of cross-section in the NSM strengthening technique with strips and bars is shown in Figure 2.7.
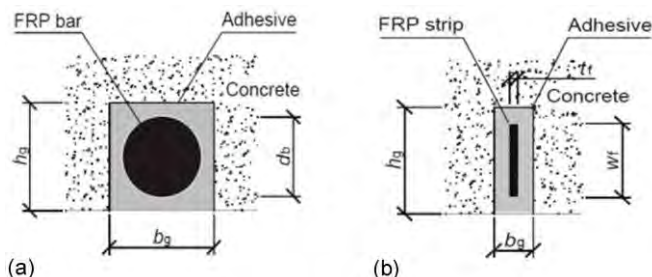
Figure 2.7. Cross-section of NSM systems: (a) Using a bar and (b) Using a strip [30].

The NSM technique presents some advantages when compared to the EBR system. One of the main advantages is the less prone to premature debonding because of the higher confinement of the FRP material, which improves the efficiency of NSM technique allowing, in some cases, the development of the maximum tensile strength of the FRP material [5,31,32]. Besides, the FRP is less affected by harsh environmental conditions, and less prone to vandalism. In addition, the NSM system needs no surface treatment, except cutting the grooves, and pre-

stressing the strips/bars can be done without anchorage. Finally, the aesthetic of the strengthened structure is almost unchanged [5,6,30-33].

2.3.3 Structural adhesives used in strengthening

Whatever strengthening system is used, the structural adhesive (bonding material) plays an important role as it is responsible for transferring the load between the FRP and the strengthened element [34]. Epoxy based and cement based adhesives are the most commonly used structural adhesives for strengthening RC structures with FRP [5]. Epoxy adhesives are based on polymeric materials and, therefore, their properties can change because of temperature. This means that the increase in the temperature to near or beyond the T_g, leads to a change from hard to glass (rubbery) state, which is a limiting parameter in the applications of epoxy adhesives [34]. Therefore, the performance of epoxy based adhesives may be affected by temperature [5,34]. In this sense, cement based adhesives can be a good alternative to resist higher temperatures. However, low bond strength in cement based adhesives can be a limitation for the application of these adhesives in structural strengthening [35].

2.4 Instantaneous flexural behavior of NSM FRP-strengthened RC beams

In this section, a review on the existing works on the instantaneous flexural behavior of NSM FRP-strengthened RC beams is presented. According to literature, epoxy adhesives usually used in NSM technique are sensitive to temperature, especially when temperature approaches the adhesive T_g. This can lead to changes in epoxy mechanical properties that may affect the performance of the strengthening system [7-9,36-38]. Based on this, the review includes existing works at room temperature and also works where higher temperatures have been applied, but never achieving fire conditions.

2.4.1 Instantaneous flexural behavior of NSM FRP-strengthened RC beams tested at room temperature

A significant amount of work has been done on the flexural performance of NSM FRP-strengthened RC beams under room temperature (laboratory conditions). In this sense, the effect of CFRP and GFRP bars [39,40], CFRP and GFRP strips [41-48], FRP bonded length

[39,42,46,49], different bonding materials (i.e. epoxy and cement based adhesives) [50], groove size [51,52], bar position [40,52] and use of mechanical anchorage [53-55] on the flexural behavior of NSM strengthening system has been evaluated.

According to the literature, the NSM strengthening system helps to significantly increase the flexural capacity of the strengthened element [39,41-45,48]. However, efficiency of this technique is dependent on the bonded length of FRP [39,42,46,49], as for short bonded lengths, the FRP-strengthening system did not involve in load carrying process [46], whilst for larger bonded lengths, the maximum capacity of the strengthening system can be exploited, as premature debonding of the FRP is avoided, and failure mode changes from debonding to FRP rupture [42]. Besides, the performance of the bonded joint is not only dependent on the bonded length but also on the bonding material, as it is responsible for transferring the stress between concrete and FRP. In this regard, NSM FRP-strengthened beams, where an epoxy adhesive was used have shown a ductile behavior with higher capacity in comparison to that of strengthened beams that used cement based grouts [50].

Furthermore, the groove dimension, bar position and location can also effect the flexural performance of NSM CFRP-strengthened beams [51,52]. In this sense, experimental works revealed that small groove size tolerance of 3 mm did not have a significant impact on the performance of the strengthened beams [51], while deeper groove resulted in high ultimate load capacity [52]. Moreover, for the GFRP bars installed side by side, lower interfacial stress was observed when compared to those installed separately [52]. In addition, the NSM bars installed in the bottom of the beam resulted in higher ultimate capacity when compared to the bars installed to the side of the beam.

With the aim at preventing the problem of premature debonding of the strengthening system, anchoring systems have also been proposed. In this sense, application of mechanical anchorage or transverse wrapping helped to postpone the failure and increased the ultimate capacity of the beam by delaying the concrete cover separation [53]. Furthermore, the use of steel plates at the end of the beam helped to increase the flexural capacity of the beams [54]. In the other study [55], a mechanically fastened EBR (MF-EBR) anchorage showed a better performance under instantaneous loading when compared to the NSM system.

Finally, although it is not common nowadays to face this issue, the effect of NSM CFRP-strengthening on the flexural performance of the RC beams internally reinforced with GFRP bars has also been studied in [56]. The results showed that despite the high degrees of deformability that may be expected in GFRP RC beams, strengthening with NSM CFRP strips appeared as an adequate strategy to provide higher stiffness at a service level than that of the unstrengthened element.

2.4.2 Instantaneous flexural behavior of NSM FRP-strengthened RC beams tested at service temperature

The performance of both EBR and NSM FRP-strengthened RC flexural members exposed to high service temperature has been hardly investigated, when compared to the amount of existing literature on their performance at room temperature and fire conditions. In this sense, for the EBR system, the application of a high service temperature up to 70 °C had a slight effect on the load capacity of the system. It should be mentioned that different bonded lengths and laminate widths were used for each temperature. Besides, even though the load capacity of the beams was not affected, a change in the failure interface took place for specimens with shorter bonded length tested at 70 °C [57]. In a similar study, the load capacity of EBR-strengthened beams tested at 80 °C decreased by 20%, when compared to the reference beam tested at room temperature. In addition, the failure mode changed from cohesion in concrete to adhesion at the concrete-epoxy interface [58].

Regarding the NSM FRP-strengthened RC flexural members, there is scarce work available in the literature. In this sense, results from the effect of temperature on the flexural response of the NSM FRP-strengthened slabs showed that the increase in the temperature up to 80 °C was followed by a 12% reduction in the ultimate capacity of the slab, and the failure mode changed from concrete crushing to cohesive failure at the epoxy [36]. In this experimental study, the maximum capacity of the system was observed at 40 °C, which was attributed to a possible post-curing in epoxy adhesive.

2.4.3 Failure modes in NSM technique

Failure modes of NSM FRP-strengthened RC beams include those traditionally observed for RC structures (i.e. concrete crushing, shear failure and steel reinforcement rupture), FRP rupture

and those failure modes related to a premature failure of NSM bonded joint, usually referred to as debonding failure modes. The classification of the different debonding failure modes is done on the basis of the location where debonding starts, as shown in Figure 2.8. Besides, bond failure may occur at different FRP-concrete interfaces, as shown in Figure 2.9.
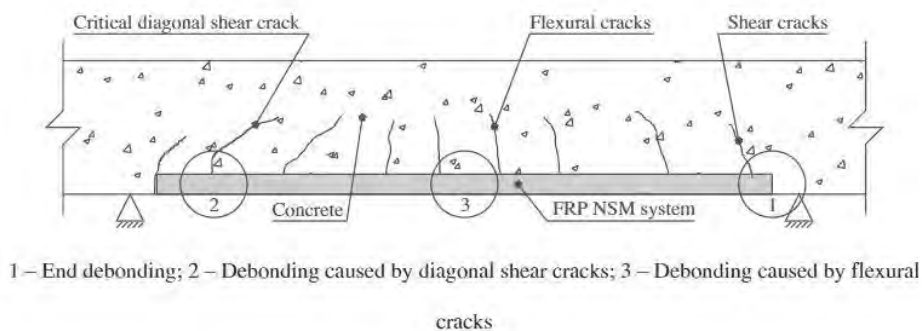
Figure 2.8. Principal debonding failure modes in a beam strengthened in flexure with a FRP NSM system [59].
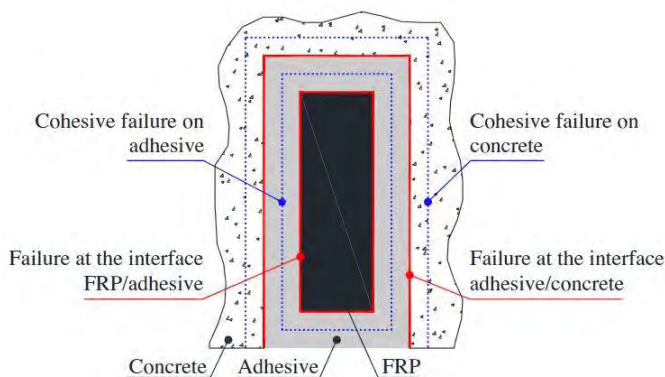
Figure 2.9. FRP-concrete interfaces for bond failure [59].

Concrete crushing

Concrete crushing is a very common failure mode in conventional RC beams without strengthening that takes place when concrete in compression reaches its maximum compressive strain [48,60-67], as shown in Figure 2.10a.

Shear failure

This type of failure normally occurs due to insufficient internal shear reinforcement. When the applied shear reaches the shear resistance of the section, the diagonal cracks in the shear span propagate until they reach to the compression face of the beam and, subsequently, the beam fails in shear [48,62,68,69], as shown in Figure 2.10b.

Steel reinforcement rupture

Steel reinforcement rupture takes place when steel in tension reaches its maximum tensile strain. This failure mode is very common in both unstrengthened and strengthened beams under fatigue loading. Besides, it is usual for strengthened beams that steel reinforcement rupture is then followed by bond failure or FRP rupture [48,65,67,69,70] as shown in Figure 2.10c.

FRP rupture

This type of failure mode happens in strengthened RC beams with good composite action and sufficient bonded length [48,61,63,64,68,71] and means that the maximum capacity of the strengthening system has been used [41]. FRP rupture usually takes place following yielding of the steel reinforcement, without failure in the compressed concrete. The representative view of this failure mode is shown in Figure 10d.

Interfacial debonding failure

The debonding failure happens due to lose of composite action at FRP-adhesive-concrete interfaces. This failure mode can be initiated in zones 1 and 2 in Figure 2.8. The failure mode is affected by many factors, including the FRP's geometry, the tensile steel and FRP reinforcement ratios, and the mechanical strength of the concrete substrate and the adhesive [48]. Besides, in flexural tests, the flexural cracks may intersect the epoxy cover, thus damaging the epoxy and facilitating the interface debonding. This failure mode is more common in NSM FRP-strengthened RC beams with short/limited bonded length [42,48,61,64,69-76]. An example of this failure mode is shown in Figure 2.10e.

Concrete cover separation

Concrete cover separation is more probable to occur for NSM strengthened RC members with the decrease of the distance between each grooves/FRP reinforcement and with the decrease of the tensile strengths of the concrete cover [1,41]. In many tests, bond cracks inclined at approximately 45° to the beam axis formed on the soffit of the beam. Upon reaching the edges of the beam's soffit, these cracks may propagate upwards on the beam sides maintaining a 45° inclination within the cover thickness. Then, they can propagate horizontally at the level of the steel tension bars [39,42,44,45,77,78]. For the strengthened specimens with significant distance between the end of the FRP and the supports, separation of concrete cover typically starts from the cut-off section and propagates inwards [45,46,75,79]. The example of strip and cover separation is shown in Figure 2.10f.
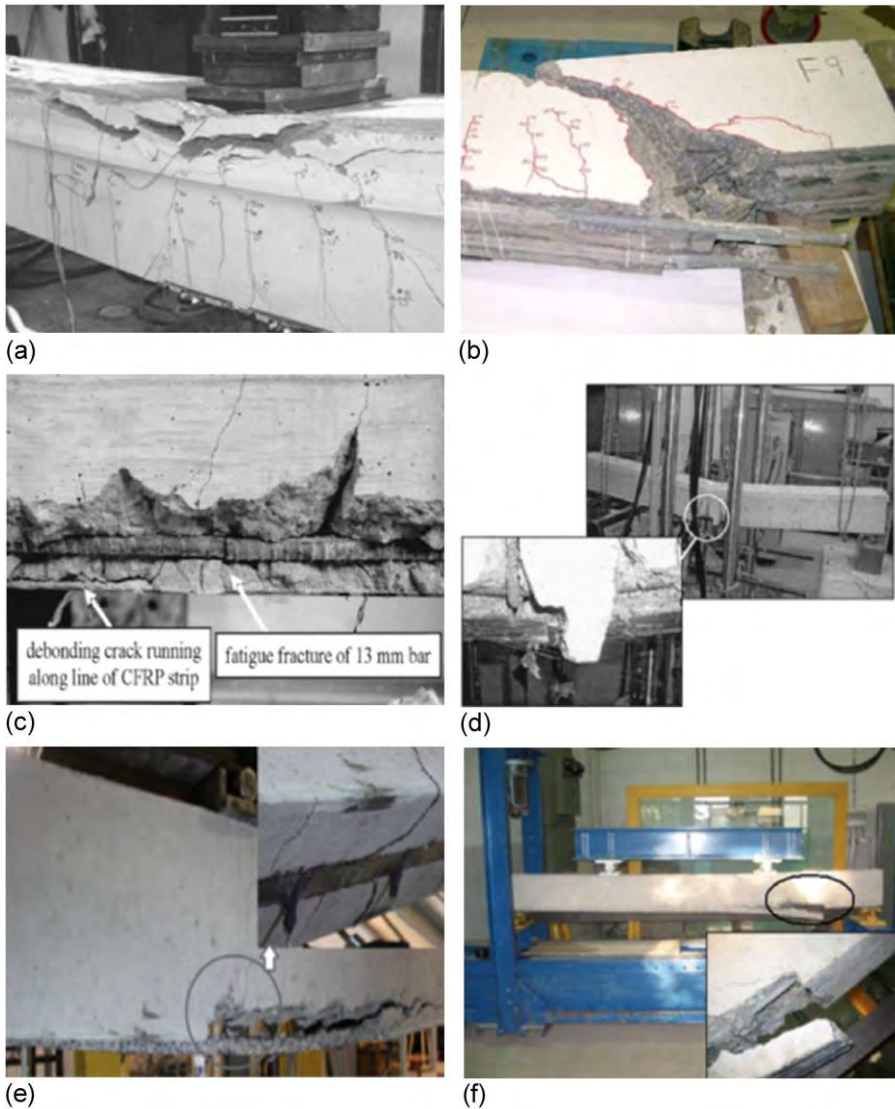
Figure 2.10. Failure modes of RC beams strengthened by NSM FRP: (a) Concrete crushing [66], (b) Shear failure [62], (c) Steel reinforcement rupture [65], (d) FRP rupture [61], (e) Interfacial debonding failure [64] and (f) Debonding failure due to concrete cover separation [75].

2.5 Long-term loading effects

RC elements are usually subjected to long-term loads that may have an effect on their structural performance. The time-dependent deflections in RC elements are, basically, due to creep and shrinkage of concrete [80-82]. Creep and shrinkage values are dependent on

environmental conditions (temperature and humidity), age of concrete, magnitude and duration of long-term load and material properties [83]. In concrete structures under service loading, excessive cracking or deflection are relatively common and this is normally due to failure in adequately accounting for the time-dependent deflections in the design process [84].

2.5.1 Creep phenomena in materials

Creep is a time-dependent deformation and can be defined as the increase of strain with time due to constant applied stress and temperature. As a result, there is a progressive increase in deflections, relaxation and redistribution of stresses and reduction of the material mechanical properties [85]. The shape of the creep curve and the duration of the creep stages strongly depend on the stress and temperature values. The creep rate depends on material properties, temperature, humidity, applied load and loading time [83].

Three materials are involved in the NSM FRP system namely concrete, FRP and adhesive. Therefore, the understanding of their time-dependent behavior is of paramount importance because the creep of these materials may cause time-dependent deformations in the strengthened element [86].

Creep of concrete

A typical time-dependent strain of concrete under constant stress (and temperature) is shown in Figure 2.11. Before applying any load (or stress), the strain increases due to shrinkage of concrete. Later, when an external long-term load (stress) is applied to the member, there is an associated jump in strain (the amount of the strain depends on the load level), and immediately after the application of the long-term stress, creep develops rapidly. A large portion of the final creep strain takes place at the beginning of the loading (first few months), and later the rate of the increase of concrete creep slows down [84]. It should be mentioned that the shrinkage strain of concrete is independent of the loading and it continues increasing by time. However, similar to creep strain, the rate of the increase of shrinkage strain slows down by time.
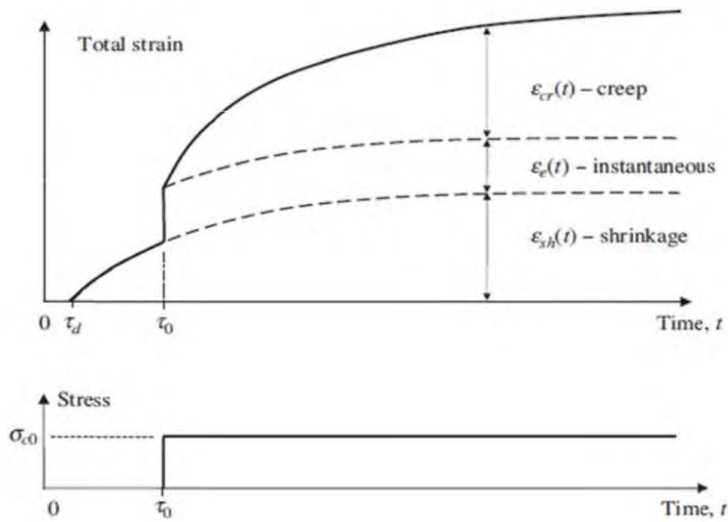
Figure 2.11. Time-dependent strain of concrete [84].

It should be mentioned that a large portion of the creep strain (deflection) is irrecoverable and will stay in the member permanently when the long-term load is removed, whilst a small portion of the creep strain/deflection will be recovered [10]. Figure 2.12 shows creep strain, creep recovery and irrecoverable creep.
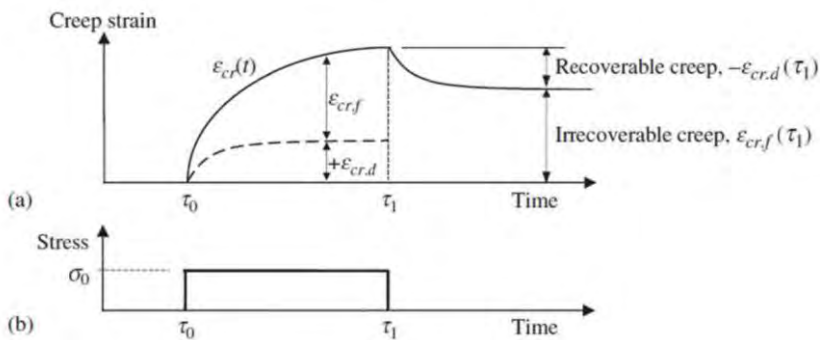
Figure 2.12. Recoverable and irrecoverable creep components: (a) Time-dependent concrete strain and (b) Compressive stress history [84].

There are several factors that can affect the creep of concrete, being compressive strength of concrete, long-term load level (stress level), environmental condition, concrete curing process, concrete age, cement type and admixture properties the most important ones [83]. According to the *fib* Model Code 2010 [83], under service conditions, in order to avoid a non-

linear creep in concrete, the maximum stress level should be limited to 40% of the compressive strength of concrete.

Several theoretical works exist to predict the time-dependent behavior of concrete [84,87-89]. Furthermore, there are many codes and guidelines available to calculate the creep strain in concrete, such as *fib* Model Code 2010 [83], ACI Committee 318 [90] and ACI Committee-209R-92 [91].

Creep of FRP

FRP materials can be also affected by creep when subjected to long-term loads. Following the approach stated for creep of concrete, creep effect of FRP materials can be predicted using an effective modulus of elasticity at time t after loading, $E_{FRP,e}$ (t, t_0), that can be calculated as:

$$E_{FRP,e}(t, t_0) = \frac{E_{FRP}(t_0)}{1 + \varphi_{FRP}(t, t_0)} \tag{2.1}$$

where t_0 is the age at the start of loading, E_{FRP} (t_0) is the modulus of elasticity of FRP at time t_0 and φ_{FRP} (t,t_0) is the FRP creep coefficient at time t after loading, that can be obtained from experimental data, as below:

$$\varphi_{FRP}(t, t_0) = \frac{\varepsilon_{FRP}(t, t_0) - \varepsilon_{FRP}(t_0)}{\varepsilon_{FRP}(t_0)} \tag{2.2}$$

where ε_{FRP} (t,t_0) is the strain in FRP at time t after loading and ε_{FRP} (t_0) is the instantaneous strain in FRP at loading time, respectively.

An alternative equation was suggested in [92] to calculate the FRP creep coefficient is:

$$\varphi_{FRP}(t, t_0) = \left(\frac{t}{t_0}\right)^m - 1 \tag{2.3}$$

where t is the age of the specimen at the moment considered in hours, t_0 reads 1 hour and m is the slope of the best-fit line relating log ε_{FRP} (t,t_0) and log (t/t_0).

The time-dependent behavior of the CFRP strips has been investigated in [93,94-97]. Yamaguchi et al [97] and Malvar [93] performed a study for a 50-year period and concluded that

the strength of the CFRP was reduced by 10%. Furthermore, Ascione *et al.* [95] showed that the creep strain of CFRP strips was almost negligible and, after 500 days loading, the creep strain in the CFRP strips was 2% higher than the instantaneous strain. The experimental data obtained from Ascione *et al.* [95] was used in Mazzotti *et al.* [96] to calibrate an equation to calculate the creep coefficient of CFRP strips with time, as below:

$$\varphi_{FRP}(t, t_0) = 0.02 \left(1 - exp^{\frac{-t}{130}}\right) \tag{2.4}$$

Creep deformations are dependent on the level of the long-term load, so that high levels of long-term load can eventually lead to the tensile failure of the FRP, which is known as creep rupture [98]. In this regard, Goertzen *et al.* [94] performed an experimental program based on tensile and flexural tests of CFRP dog-bone and rectangular specimens, to evaluate the effect of a high long-term load (77% of its ultimate strength). Experimental results showed no creep rupture, and the authors concluded that, under ambient conditions, CFRP are highly resistant to creep failure. Available standards, such as the *fib* Bulletin 90 [1] and the ACI 440.2R [99] consider that CFRP can withstand stress levels up to 80% of its tensile strength.

Creep of adhesive

Structural adhesives are designed to transfer the load from the structure to the FRP-strengthening system. Although different types of adhesive exist, epoxy adhesives are the most widely used in civil applications. Epoxy adhesives, however, present a viscoelastic behavior and, therefore, the evaluation of their time-dependent properties is of importance for assessing their long-term load-bearing performance [100].

Three stages can be considered in a typical creep curve for an epoxy adhesive [101] (see Figure 2.13): (i) the primary stage (reduced creep) in which the creep rate decreases to a certain value (minimum creep rate); (ii) the secondary stage, in which the creep rate is almost constant; and (iii) the tertiary stage, where the creep rate increases. At the end of the tertiary stage creep rupture of the specimen occurs [85].
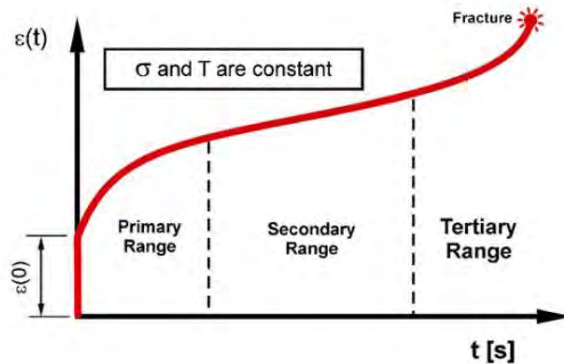
Figure 2.13. Three stages of creep [101].

Majda and Skrodzewicz [101] performed an experimental work on long-term tension tests at room conditions, where four different load levels were considered (i.e. 33%, 43%, 54% and 65% of ultimate instantaneous tensile strength of the epoxy adhesive). Experimental results showed that higher creep strains were obtained for larger levels of long-term load, leading to failure in the case of high long-term loading level. Same findings were observed in Meshgin *et al.* [102], who performed an experimental program on long-term shear tests (i.e. epoxy at the interface between the concrete and FRP) and applied a maximum long-term load level of 62% of ultimate instantaneous shear strength. In both cases, experimental results were used to obtain empirical expression to predict the adhesive behavior with time.

In a similar study, Costa and Barros [103] characterized the tensile creep behavior of an epoxy adhesive and observed that up to a long-term load level of 60% of the ultimate tensile strength, the adhesive can be assumed as a linear viscoelastic material.

The effect of environmental conditions on the creep behavior of an epoxy adhesive was studied in Emara et al. [7], who considered different levels of long-term load (20%, 40% and 60% of ultimate tensile strength) for specimens that were tested under different combinations of temperature and humidity (temperature equal to 20 °C and 40 °C, and relative humidity equal to 55% and 90%). The results showed that at 20 °C, a linear viscoelastic behavior was observed for all levels of loads. With an increase in the humidity to 90% (at 20 °C), the specimens tested under higher load level failed but still the creep was linear for the specimens tested under low and medium level of load. Moreover, with an increase in the temperature to 40 °C and humidity of 55%, the specimens at medium and higher load levels failed, but those specimens at lower

load level survived. Finally, all specimens tested at 40 °C and 90% of humidity failed and did not survive for 1000h.

Finally, the effect of the age of specimens at loading time was studied in Silva et al. [104]. Experimental results showed that the specimen with less age at loading time experienced higher creep strains. However, the recovery strain after unloading was similar for all of the specimens, regardless of their age at the time of loading.

2.5.2 Time-dependent flexural behavior of NSM FRP-strengthened RC beams

Most of the existing works in the literature are related to the time-dependent flexural behavior of the EBR FRP systems [81,82,105-110], whilst scarce literature exists on the NSM FRP system [111-114].

As for the case of EBR FRP systems, the majority of time-dependent deflections for the NSM CFRP systems occurs at the first stages of the long-term loading [111], even if the long-term load (equal to 33% of the ultimate load capacity of the specimens) is applied in two steps (40% of the long-term load for a duration of 78 days, and later 100% of the long-term load for a duration of 55 days). Besides, the residual flexural capacity of NSM CFRP-strengthened RC beams has been demonstrated to be inversely proportional to the long-term load applied [112]. However, no effect on the failure mode was observed as all specimens failed by end debonding. It should be mentioned that end debonding occurred in longer bonded lengths for the higher values of long-term load. It is also important to remark that these results correspond to the specific set of geometrical and mechanical properties, as well as test setup, of the corresponding study. Experimental results presented in [112] were used to validate analytical prediction on time-dependent strain in FRP [113].

Finally, Moawad et al. [114] experimentally studied the time-dependent behavior of different series of NSM CFRP-strengthened RC beams with different loading histories and sectional properties. According to experimental results, specimens with higher compressive strength of concrete experienced larger ratios of time-dependent deflections to instantaneous deflection. Besides, for the NSM FRP-strengthened specimens with compression steel reinforcement, the effectiveness of NSM strengthening was more pronounced, and creep deflections were reduced.

According to the literature, few works have been performed to evaluate the effect of long-term loading on the flexural performance of NSM CFRP-strengthened RC elements, and none of them account for evaluating the effect of high service temperature. Therefore, more work is needed to fully understand their performance.

2.6   Fatigue loading

Fatigue failure of a structural element is defined as the degradation in material by means of a progressive cracking under repeated or cyclic loading, being the applied load usually lower than the element ultimate capacity [115,116]. RC structures need to be designed to withstand not only the static loads but also fatigue loads (produced by vehicle vibration and traffic load in bridges, wind and wave load in marine structures and earthquake activities, among others), as fatigue loads may reduce the structure's service life. Regarding the fatigue loading, service life of RC structures directly depends on the stress range applied to steel reinforcement, the environmental conditions and the number of the cycles during the cyclic loading [116,117]. According to the literature, fatigue life decreases if the fatigue load level or/and the fatigue cycle amplitude are increased [67,118-120], and vice versa [121,122].

2.6.1   Fatigue behavior of NSM FRP-strengthened RC beams

Regarding the fatigue behavior of FRP-strengthened RC beams, a significant amount of work has been done for both the EBR strengthening system [118,119,123-133] and the NSM strengthening system [67,69,70,120-122,134,135].

The presence of the NSM FRP system has demonstrated to enlarge the fatigue life of RC members [67,69,120]. Besides, the inclusion of the NSM FRP system has no effect on the failure mode during the fatigue test, as both unstrengthened and strengthened beams have shown to fail by steel reinforcement rupture [67,69,120,121]. Nevertheless, unlike the EBR system, no debonding happens after steel reinforcement rupture, and the NSM FRP system gets involved in holding the integrity of system [136], thus showing a better performance when compared to the EBR system [55,65,136]. It should be mentioned that the reported trends are valid for the levels of fatigue loads applied in each experimental program.

Some studies exist to evaluate the influence of different types of the NSM bars and strips [67,69,120] and bonding material [121] on the fatigue performance of NSM FRP-strengthened flexural elements. According to the existing works, for a given load level, the fatigue performance of sandblasted rods was better than spirally wound rods [69]. Moreover, it was observed that for the same given load range, the fatigue life of specimens strengthened with NSM strips was larger than that of specimens strengthened with the NSM rods [120]. Regarding the effect of the bonding material, it has been shown that the use of cementitious adhesives resulted in a better fatigue performance, when compared to epoxy adhesive, and this was attributed to a better bond and stress transfer [121].

According to the literature, none of the existing works have addressed the effect of high service temperature on the fatigue performance of NSM CFRP-strengthened RC beams, so further investigation is still needed.

3   Methodology

The aim of this chapter is to present the methodology carried out to achieve the proposed objectives of the PhD thesis. The chapter is divided into five main sections: material characterization, production of NSM CFRP-strengthened RC beams and instantaneous, time-dependent and fatigue flexural behavior of NSM CFRP-strengthened RC beams.

3.1   Material characterization

The mechanical properties of all the materials involved in the NSM CFRP-strengthened RC beams (i.e. concrete, steel reinforcement, CFRP strips and epoxy adhesive) were determined according to the corresponding standards. Additionally, the T_g of the epoxy adhesive was also characterized and the influence of curing, post-curing and testing temperature on the mechanical properties of the epoxy adhesive was studied.

3.1.1   Concrete

In this PhD thesis, four different batches of concrete have been used. The first and second batches were used in the experimental campaign related to the short-term behavior of NSM CFRP-strengthened RC beams, whilst the third and the fourth batches were used for the study of the long-term and fatigue performance of NSM CFRP-strengthened RC beams, respectively.

Instantaneous mechanical characterization

In all concrete batches the maximum aggregate size was 12 mm, the consistency was fluid and the expected compressive strength of concrete was 30 MPa. The experimental compressive strength (f_c), tensile strength (f_t), and modulus of elasticity (E_c) of concrete were determined from cylindrical specimens (300 mm nominal height and 150 mm nominal diameter), according to UNE-EN 12390-3 [137], UNE-EN 12390-6 [138], and ASTM C469 [139] standards, respectively. It should be mentioned that batches 1 and 2 were characterized at the age of 36 and 37 days, respectively, whilst batches 3 and 4 were characterized at different ages, to track the evolution of the mechanical properties with time. Besides, splitting tensile strength ($f_{t,sp}$) tested according to UNE-EN 12390-6 [138] was transformed to tensile strength (f_t) following *fib* Model Code 2010 [83] formulation:

$$f_t = \alpha_{sp} f_{t,sp} \tag{3.1}$$

where α_{sp}=1. Details on the concrete batches and results of the mechanical properties are summarized in Table 3.1. For each test, three specimens were used.

Table 3.1. Details of concrete batches and mechanical properties.

Batch number	Cement type	Cement content (kg/m³)	w/c[a] ratio	Concrete age (days)	Compressive strength, f_c (MPa)	Tensile strength, f_t (MPa)	Modulus of elasticity, E_c (GPa)
1	I-42.5R	390	0.46	36	31.8 (6.6%)[b]	4.2 (2.3%)[b]	31.5 (7.8%)[b]
2	I-42.5R	333	0.48	37	40.8 (2.8%)[b]	5.2 (0.5%)[b]	29.4 (0.8%)[b]
3	I-42.5R	390	0.41	90	48.1 (2.3%)[b]	3.7 (6.0%)[b]	41.2 (5.3%)[b]
				200	48.3 (2.2%)[b]	3.7 (9.0%)[b]	41.9 (4.5%)[b]
				403	53.7 (0.8%)[b]	3.6 (9.4%)[b]	47.6 (1.9%)[b]
4	II-42.5R	320	0.50	31	32.2 (2.2%)[b]	3.1 (1.2%)[b]	37.7 (4.2%)[b]
				107	40.7 (2.2%)[b]	3.5 (6.8%)[b]	38.0 (5.6%)[b]
				150	41.1 (2.5%)[b]	3.8 (3.6%)[b]	39.9 (3.8%)[b]
				204	41.4 (4.8%)[b]	3.7 (8.3%)[b]	39.0 (7.6%)[b]

[a] Water to cement ratio.
[b] Coefficient of variation (CoV).

Representative photos of characterization test setups (compression test and splitting tension test) and failure modes are presented in Figure 3.1. Besides, representative stress-strain curves obtained in a compression test are shown in Figure 3.2.

(a)   (b)   (c)   (d)
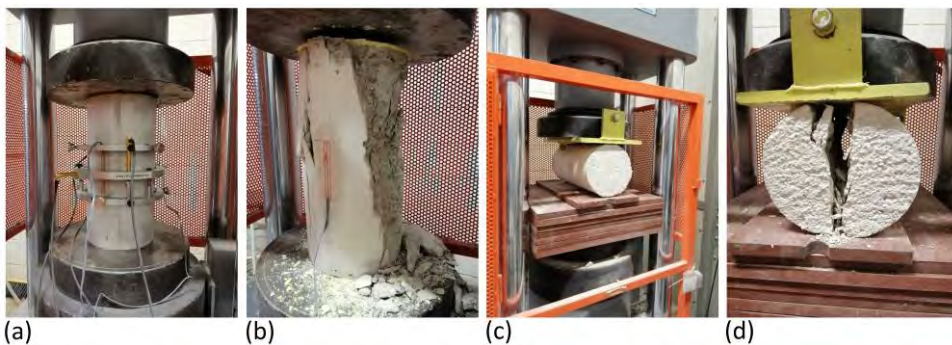
Figure 3.1. Concrete tests and failure modes: (a) Compression test, (b) Compression failure mode, (c) Splitting tension test and (d) Tension failure mode.
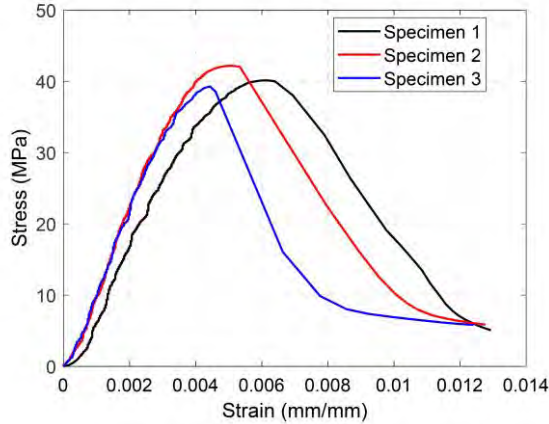
Figure 3.2. Representative stress-strain curves for concrete in batch 2.

Time-dependent behavior of concrete

Time-dependent properties of concrete in batch 3 were also determined for a correct analysis of the time-dependent behavior of NSM CFRP-strengthened RC beams. Time-dependent mechanical properties of concrete are affected by temperature and humidity. Therefore, laboratory conditions (temperature and humidity) were registered from the day of concrete casting and continued till the end of the experimental program. For the determination of time-dependent properties of concrete heated up to 50 °C, registers on the temperature on the surface of the flexural beams were also recorded along the long-term loading.

To measure free shrinkage strain in concrete (ε_{sh}), two concrete prisms, having the same beam section (180 × 140 mm) and 1 m length, were instrumented with an embedded strain gauge and left unloaded at the same temperature (20 °C and 50 °C) and humidity as beam specimens. The registration started immediately after the casting and continued till the end of the long-term loading. The specimen submitted to 50 °C was heated and isolated by the same means used for the flexural beams. Details on the heating and insulation system are described in details in Section 3.3.2. Figure 3.3 shows the shrinkage specimen with temperature. According to experimental measurements, maximum shrinkage at the end of long-term read 563 and 759 µε for the specimen at 20°C and 50 °C, respectively, which means having 35% larger free shrinkage because of temperature.

Figure 3.3. Shrinkage specimen at: (a) 20 °C and (b) 50°C.

In addition to shrinkage, the time-dependent behavior of concrete in batch 3 was also determined according to ASTM C512-02 [140]. To this end, four cylindrical specimens (150 mm diameter and 450 mm height) with an embedded strain gauge were manufactured and stacked in pairs on a loading frame, to be later loaded with a constant pressure of $0.35f_c$ (the same long-term load level as in the flexural beams). Each pair of specimens were kept at 20 °C and 50 °C.

Figure 3.4 shows the concrete creep test setup for the specimen at 50 °C. Due to technical issues during the lading of the concrete creep specimen subjected to 50 °C, the concrete creep coefficient was experimentally determined only for specimens at 20 °C, giving a value of 0.8. In order to obtain the concrete creep coefficient at 50 °C, the existing formulation from *fib* Model Code 2010 [83] was used, and a creep coefficient of 2.64 was obtained. For comparison purposes, analytical prediction on concrete creep coefficient of specimen subjected to 20 °C was also performed, obtaining a creep coefficient equal to 0.6.

Figure 3.4. Creep specimens at: (a) 20 °C and (b) 50°C.

3.1.2 Steel reinforcement

Similar to concrete, different batches of steel reinforcement (with same ribs geometry) were used in different experimental programs. Bars with different diameters (i.e. 6, 8, 10 and 12 mm) were used for the longitudinal steel reinforcement whilst the shear reinforcement consisted on stirrups with a diameter of 8 mm in all cases.

Tension tests were carried out following standard specifications UNE-EN ISO 15630-1 [141] to determine the yielding strength (f_y), the ultimate strength (f_u) and the modulus of elasticity (E_s) of steel bars of different batches. Figure 3.5 shows the tension test setup and typical failure mode of a steel reinforcing bar. Additionally, representative stress-strain curves of the tension test of steel reinforcing bars are shown in Figure 3.6. To avoid any damage to the extensometer (due to sudden failure), the extensometer was removed before reaching the ultimate tensile strength.
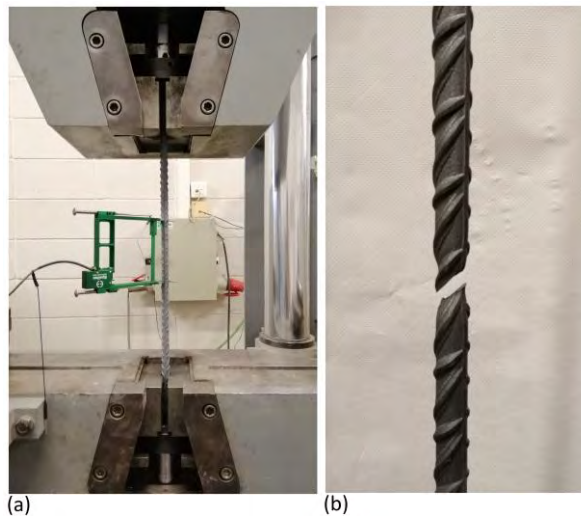
Figure 3.5. Tension test on steel reinforcing bar: (a) Test setup and (b) Failure mode.
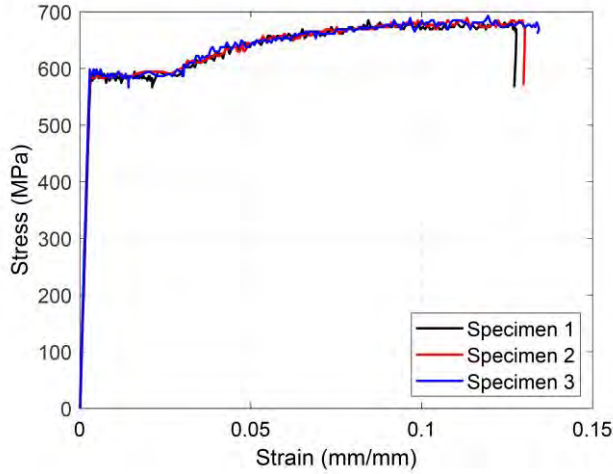
Figure 3.6. Representative stress-strain curves for a steel reinforcing bar (diameter of 10 mm) in batch 2.

Experimental results on steel reinforcing bar tensile properties are summarized in Table 3.2, where the average and CoV are based on measurements on a minimum of three specimens. First, second and third batches were used for the experimental program on instantaneous flexural behavior, long-term flexural behavior and behavior under fatigue loads of NSM CFRP-strengthened RC beams, respectively.

Table 3.2. Steel reinforcement mechanical properties.

Batch number	Bar diameter (mm)	Yielding strength, f_y (MPa)	Ultimate strength, f_u (MPa)	Modulus of elasticity, E_s (GPa)
1	8	568.9 (0.5%)[a]	676.6 (0.0%)[a]	201.9 (0.5%)[a]
	12	577.6 (1.1%)[a]	671.1 (1.0%)[a]	199.6 (0.4%)[a]
2	6	586.8 (0.9%)[a]	718.1 (1.4%)[a]	205.2 (1.0%)[a]
	8	604.8 (5.9%)[a]	721.7 (3.8%)[a]	208.9 (0.7%)[a]
	10	591.8 (0.8%)[a]	690.2 (0.3%)[a]	203.9 (0.9%)[a]
	12	562.2 (1.5%)[a]	700.7 (1.2%)[a]	202.5 (1.3%)[a]
3	6	553.8 (1.6 %)[a]	703.5 (1.9%)[a]	203.6 (0.8%)[a]
	8	536.7 (3.3%)[a]	698.1 (1.9%)[a]	196.4 (3.0%)[a]
	10	544.1 (2.9%)[a]	666.0 (1.6%)[a]	202.1 (5.5%)[a]

[a] Coefficient of variation (CoV).

3.1.3 CFRP strip

The CFRP strips used in this thesis were from *S&P C-laminates* provided by S&P Clever Reinforcement Ibérica Lda. The CFRP strips consisted on unidirectional carbon fibers (with a volume content fiber higher than 68%, according to the manufacturer datasheet) held together by an epoxy vinyl ester resin matrix [20]. CFRP specimens were characterized according to ISO 527-5 [142]. Tests were carried out in an MTS 810 testing machine under displacement control at a rate of 2 mm/min. The instrumentation consisted on two strain gauges bonded at each side of the CFRP strip and a load cell of 250 kN capacity. The CFRP strips had a cross-section of 1.4 × 10 mm and their tensile mechanical properties were obtained from five CFRP samples. An ultimate tensile strength ($f_{u,FRP}$) of 2251.4 MPa (CoV = 3.2%), an ultimate tensile strain ($\varepsilon_{u,FRP}$) of 0.0133 (CoV = 7.2%), and a modulus of elasticity (E_{FRP}) of 169.5 GPa (CoV = 6.3%) were obtained.

The CFRP strip tension test setup and typical failure mode are shown in Figure 3.7. Moreover, Figure 3.8 shows the stress-strain curve for the tested CFRP strips.
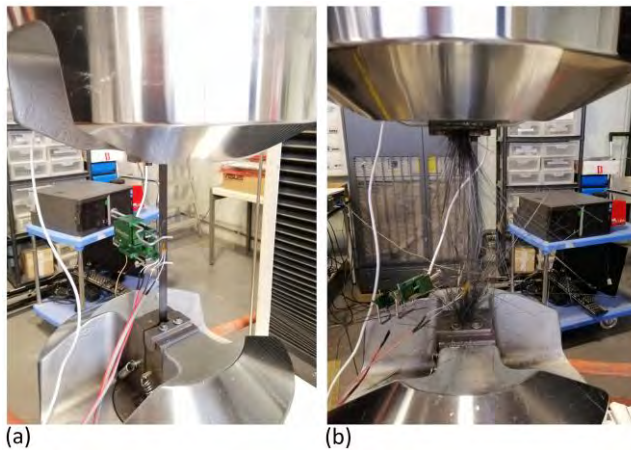
Figure 3.7. Tension test on CFRP strip: (a) Test setup and (b) Failure mode.
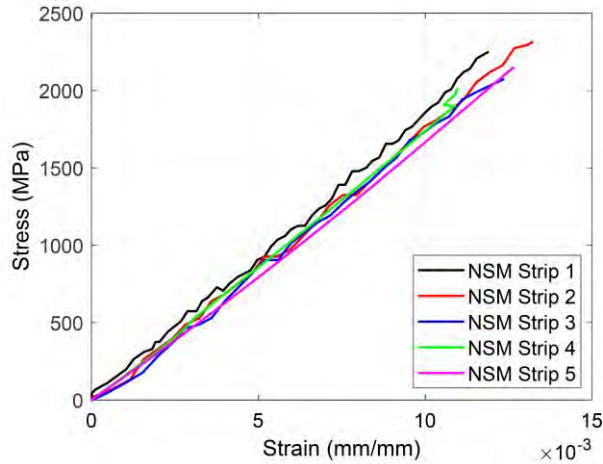
Figure 3.8. Stress-strain curve for CFRP strips.

3.1.4 Epoxy adhesive

The structural adhesive used in this thesis is a high performance, solvent-free, thixotropic, and grey two-component epoxy adhesive, under the commercial name of *S&P 220 HP*, specially developed for bonding CFRP to concrete. According to the manufacturer's product data sheet [143], the components A (resin) and B (hardener) should be mixed at a ratio of 2:1 by weight, and the suggested curing duration should be 7 days. However, a curing time of 12 days was imposed for all specimens in this PhD thesis.

Instantaneous tension tests

The instantaneous tensile properties of the epoxy adhesive were determined following ISO-527-1 [144] specifications. Dog-bone specimens with a section of 10 × 5 mm were tested in an MTS Insight testing machine at a displacement rate of 1 mm/min with a load cell of 5 kN. The instrumentation consisted on two strain gauges placed at both sides along with an axial extensometer. A tensile elastic modulus (E_{epoxy}) of 7.1 GPa (CoV=7.8%) and tensile strength ($f_{u,epoxy}$) of 30.4 MPa (CoV=4.3%) were obtained. Figure 3.9 shows the test setup and failure and the stress-strain curves obtained from tension tests.
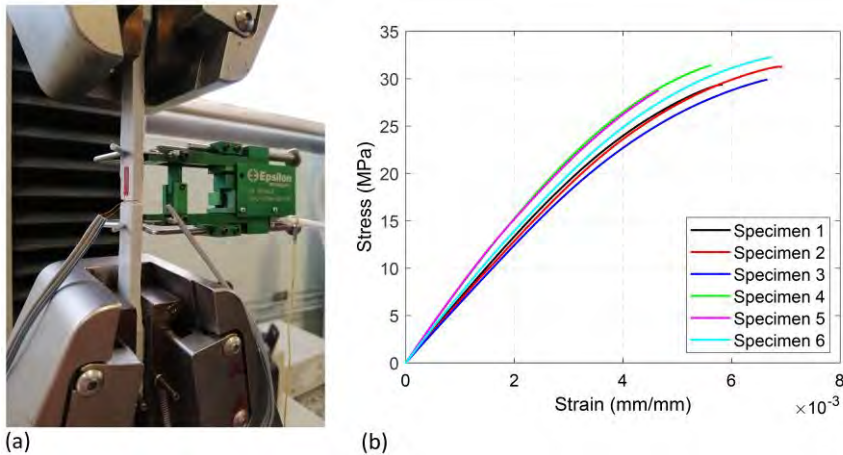
Figure 3.9. Tension test on epoxy dog-bone specimens: (a) Test setup and (b) Stress-strain curve for epoxy adhesive.

Glass transition temperature

The T_g of epoxy was determined based on two well-known available methods, namely differential scanning calorimetry (DSC) [145] and dynamic mechanical analysis (DMA) [146]. The DSC technique provides information about changes in physical, chemical, and heat capacity of the adhesive which may lead to important information about their thermal history (i.e. the temperature that epoxy undergoes), stability, processing conditions, progress of chemical reactions and possible changes in mechanical properties [145]. In this thesis, dynamic DSC tests were carried out using the DSC Q2000. A heating rate of 10 °C/min was applied using nitrogen as the purge gas at 50 mL/min. The temperature range was between 25 °C and 80 °C. To determine T_g, three temperatures were measured and reported: the extrapolated onset temperature (T_f), the mid-point temperature (T_m) and the extrapolated end temperature (T_e). The DMA test is an alternative method to determining the T_g and viscoelastic properties of polymeric materials. In this thesis, a METTLER TOLEDO DMA/SDTA861e analyzer with a 3-point bending test configuration and 45 mm between supports was utilized. The specimens were subjected to a heating rate of 2 °C/min within a temperature range of 30 to 100 °C. A 5 µm, constant displacement amplitude was applied at a frequency of 1 Hz. The T_g was obtained by analyzing the storage modulus (E'), the loss modulus (E''), and the loss factor ($tan\delta$) as functions of temperature. According to experimental tests, the T_g of the epoxy cured at laboratory conditions for 12 days ranged between 53.9 °C and 65.3 °C. Experimental results confirm that

T_g is not a unique temperature but can be defined as a range of temperatures, as stated elsewhere [147]. Further details regarding the determination of T_g of the epoxy resin are presented in Chapter 4 (Journal Paper A).

Effect of curing, post-curing and testing temperature on the mechanical properties of epoxy

The aim of this PhD thesis is to evaluate the effect of different service temperatures on the flexural performance of NSM CFRP-strengthened RC beams. Considering that the structural adhesive used in the PhD thesis is an epoxy, whose mechanical properties may vary when working temperature approaches its T_g, the evaluation of the effect of temperature on the epoxy adhesive mechanical properties is of vital importance. Therefore, a comprehensive experimental study was designed to address the effect of curing, post-curing and testing temperature on the instantaneous mechanical properties (tension and compression) of the epoxy adhesive. Besides, the effect of curing and post-curing temperatures on the value of T_g was also studied.

The experimental program included a total of four groups of specimens:

- Group 1. This Group comprised a total of 5 epoxy specimens, that were cured and post-cured at different temperatures (20 °C, 50 °C and 70 °C) to be later tested by DSC method to measure the epoxy T_g. Specimens cured at 50 °C and 70 °C were immediately moved to a thermal chamber after casting, to consider the effect of curing temperature from the very beginning of the casting.

- Group 2. This Group comprised a total of 48 specimens (24 dog-bone specimens for tensile characterization and 24 prisms for compressive characterization), that were cured at 20 °C to be later tested under tension and compression, following ISO 527-1 [144] and EN 196-1 [148], respectively. In order to study the effect of testing temperature on instantaneous mechanical properties, 1 day prior to testing, the specimens were heated up to different values of temperature (40 °C, 50 °C, 60 °C, 70 °C and 85 °C) and, after the stabilization of the testing temperature, the tests were performed. Some specimens included a one-day post-curing period before being heated and tested (the post-curing phase took place after 7 days of curing).

- Group 3. This Group comprised a total of 30 specimens (15 dog-bone specimens for tensile characterization and 15 prisms for compressive characterization), that were cured at three

different temperatures (-15 °C, 50 °C and 70 °C). After the curing period, the specimens were conditioned to 20 °C to be later tested under tension and compression. Similar to Group 2, some specimens included a one-day post-curing period. In this case, the post-curing phase took place after the curing period and before the testing.

- Group 4. This Group comprised a total of 30 specimens (15 dog-bone specimens for tensile characterization and 15 prisms for compressive characterization), that were cured at 20 °C to be later post-cured for 1 day at different temperatures (40 °C, 50 °C, 60 °C, 70 °C and 85 °C). Finally, specimens were cooled-down to 20 °C to be tested under tension and compression.

Tension tests were performed following ISO 527-1 [144], in an MTS Insight 100 testing machine at a displacement rate of 1 mm/min, and the instrumentation consisted on two strain gauges, an axial extensometer and a load cell of 100 kN. Compression tests were performed following EN 196-1 [148] in an MTS 810 testing machine under force control at a rate of 2400±200 N/s. The EN 196-1 [148] test standard was selected to ensure that results from the characterization tests and those reported in the manufacturer datasheet are comparable. In compression tests the instrumentation consisted on one strain gauge and a load cell of 250 kN.

Images on tension and compression tests setups are shown in Figure 3.10.

(a)   (b)
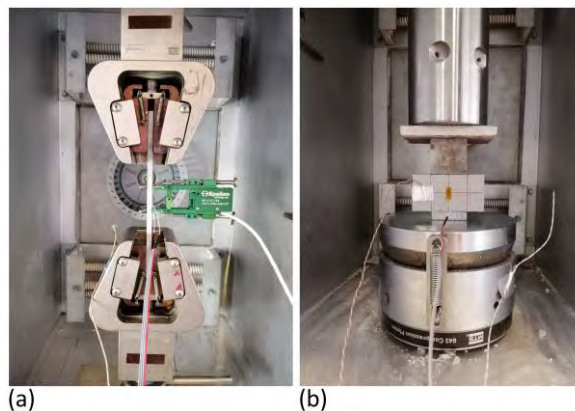
Figure 3.10. Epoxy tests setups: (a) Tension test and (b) Compression tests.

Further details regarding the experimental program, results and conclusions on the effect of curing, post-curing and testing temperature on the performance of the epoxy adhesive can be found in Chapter 5 (Journal Paper B).

Time-dependent behavior of epoxy adhesive

Time-dependent behavior of epoxy adhesive was also studied in order to evaluate the effect of different temperatures (20 °C and 50 °C) on the creep coefficient of epoxy adhesive (φ_{epoxy}), as it may have an effect on the time-dependent behavior of NSM CFRP-strengthened RC beams. To this end, dog-bone specimens with a cross-section of 5 × 10 mm were casted and cured for 12 days at 20 °C to be later tested under long-term loading inside a climatic chamber. The test setup consisted on a lever arm with a magnification factor of 4 that applied the gravity load onto the epoxy specimen (See Figure 3.11). Instrumentation included two strain gauges (placed at each side of the specimen, at the mid-section) and one temperature gauge that was glued on the surface of an epoxy dog-bone specimen that was left unloaded inside the chamber, under the same temperature conditions. Three levels of long-term load, causing 20%, 40% and 60% of the epoxy ultimate strain were applied to the specimens for a duration of 40 days (1000 h), which is similar to the duration used in the literature [7,101,103,104]. Two specimens were tested for each temperature and level of long-term load, thus giving a total of 12 specimens.

Figure 3.11. Time-dependent tension test setup for epoxy specimens.

According to experimental results, specimens tested at 50 °C failed after a few hours of loading, whilst specimens tested at 20 °C survived the 1000 h long-term loading. In these latter cases, the creep coefficient for epoxy tested under 60% of its ultimate strain almost doubled that of epoxy tested under 20%. Further details of the experimental configuration can be found in Chapter 6 (Journal Paper C) along with the presentation and discussion of results obtained from the tests carried out.

3.2 NSM CFRP-strengthened RC beams preparation

In this PhD thesis, all of the beams had the same dimensions, with a cross-section of 140 mm width and 180 mm height, and a total length of 2400 mm. Details on the preparation of the beams are summarized in the following subsections.

3.2.1 Steel reinforcement and mold preparation

The molds for the specimens were assembled, cleaned and located on their position. Later, according to the sketch of each experimental program, the steel cages (with longitudinal and shear reinforcements) were prepared. Following the steel preparation, one of the longitudinal tensile steel bars was instrumented with a strain gauge. To this end, the bar surface was polished, the strain gauge was glued and, finally, the strain gauge was covered by a waterproof material to protect it from wet environment during casting and curing of concrete. Figure 3.12 shows the preparation of steel reinforcement cages, the assembled molds and an installed strain gauge.

(a)　　　　　　　(b)　　　　　　　(c)
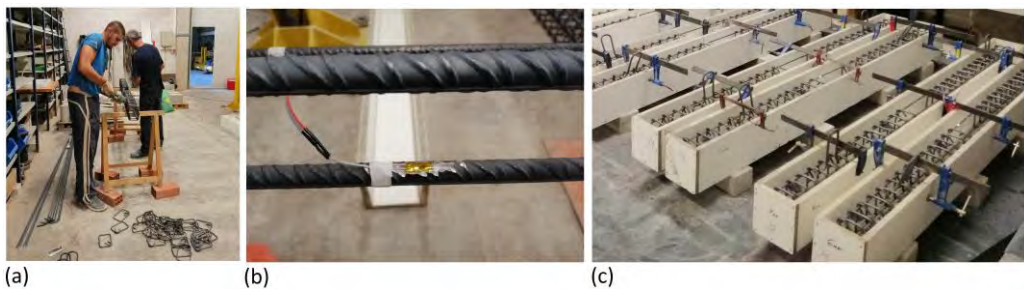
Figure 3.12. (a) Steel reinforcement preparation, (b) Strain gauge installation and (c) Placing the molds.

3.2.2 Concrete casting

After the preparation and placement of the steel reinforcement inside the molds, the concrete was cast. Ready-mixed concrete from a local supplier was used in this PhD thesis. Casting took place in laboratory conditions with conventionally vibrating procedure (see Figure 3.13). In addition to beam specimens, cylindrical control specimens (300 mm nominal height and 150 mm nominal diameter) were also cast in order to determine the instantaneous mechanical properties of the different batches of concrete. Moreover, a 1 m length prism,

having the same cross-section as that of the beams, was cast to measure the free concrete shrinkage in all batches. In this case, an embedded gauge was installed inside the mold prior to casting. Furthermore, for the time-dependent characterization of concrete in batch 3, four cylindrical specimens were cast (with an embedded gauge) to later determine the concrete creep, according to ASTM C512 [140] (see Figure 3.13c).

All specimens were unmolded after three days from casting and watering started from first day of casting and lasted a duration of about eight days.
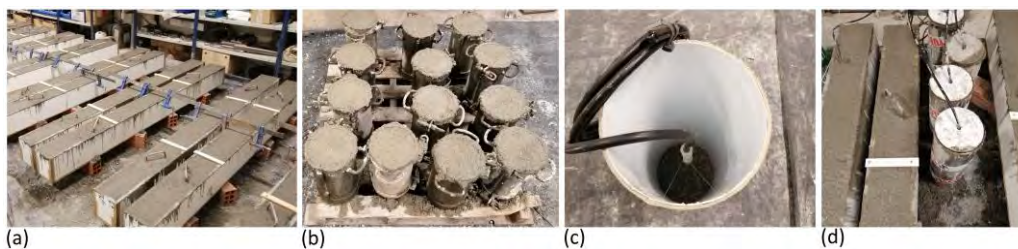
Figure 3.13. (a) Beam casting, (b) Control cylinder specimens, (c) Mold with embedded strain gauge for creep specimen and (d) shrinkage and creep cast specimens.

3.2.3 Groove cutting and introducing FRP strips

Three weeks after casting, the grooves were cut on the soffit of the beams in order to introduce the CFRP strips. Groove distances and groove sizes were based on *fib* Bulletin 90 recommendations [1]. In this PhD thesis, the beams were designed to have one, two or three grooves with dimensions of 6 × 15 mm. After cutting the grooves, they were cleaned by air compressor in order to avoid any weak layer of concrete.

The CFRP strips were cut and prepared to be introduced into the grooves. To this end, first the strain gauges and temperature gauges were installed to the surface of the CFRP strips and, similar to steel reinforcement, a waterproof material was used to protect them from the wet environment during the casting and curing of the epoxy adhesive.

Before the application of the epoxy adhesive, a plastic tape was placed in the soffit of the beam to enclose the bonded length. Later, the epoxy adhesive was mixed, according to the manufacturer instructions, and the grooves were filled with epoxy adhesive by steel blade and hand vibration, in order to remove air bubbles as much as possible. Finally, based on the design

sketch, the CFRP laminates were inserted into the grooves and the surface of the grooves were polished by steel blade to have a good finishing. A view of the groove cutting and epoxy application is shown in Figure 3.14.

(a)   (b)   (c)
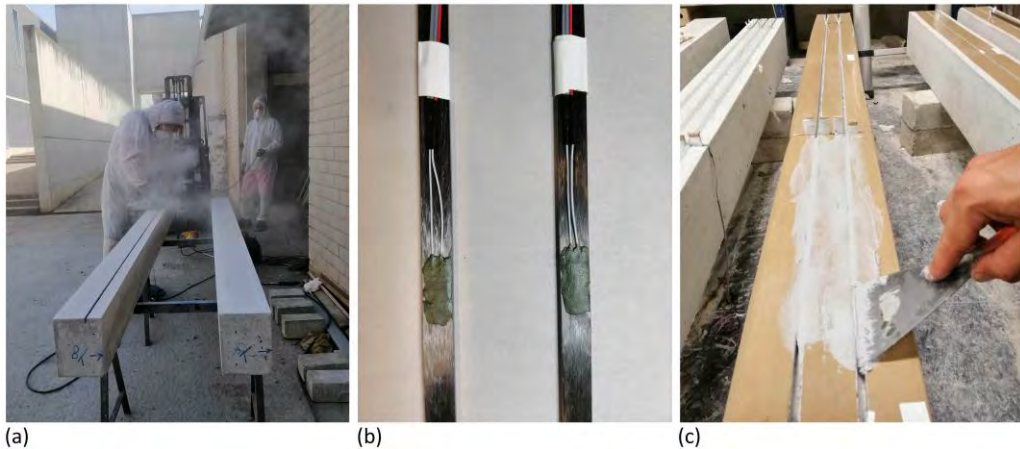
Figure 3.14. (a) Cutting of grooves, (b) Strain gauges on CFRP surface and (c) Application of the epoxy.

3.3   Instantaneous behavior of NSM CFRP-strengthened RC beams

The performance of the NSM strengthening system relies on the bond capacity of the joint between concrete and FRP material, which in turn depends on the properties of the adhesive. For civil applications it is typical to use epoxy adhesive as a bonding material. However, mechanical properties of epoxy adhesives can be affected by temperature near or beyond its T_g [8,9,149,150], which can lead to a premature debonding of the joint and, therefore, to a not complete exploitation of the strengthening system. There are some limitations on the working temperature of FRP-strengthening system. According to *fib* Bulletin 90 [1], the service temperature should be limited to 20 °C less than T_g of the epoxy adhesive. Furthermore, other studies [147,151-154] limited the service temperature to be 10 °C to 20 °C less than T_g in order to avoid any premature debonding of FRP sheets from concrete surfaces. It should be mentioned that these limitations apply to the EBR technique, where the adhesive is more exposed to environmental factors. Regarding the NSM technique, less information is available and no specific limitations have been stated.

As mentioned in Chapter 2, a very limited number of works have studied the flexural performance of NSM FRP-strengthened RC beams under service temperature different to laboratory conditions. Therefore, one of the main goals of this PhD thesis is to address this issue. To this end, an experimental program including 14 beams was designed to evaluate the effect of different temperatures (20 °C, 40 °C, 60 °C, 70 °C and 85 °C), CFRP ratios (0.06%, 0.12% and 0.18%) and compressive strengths of concrete (31.8 MPa and 40.8 MPa) on the instantaneous flexural behavior of NSM CFRP-strengthened RC beams. Furthermore, analytical predictions on the load-deflection curves are compared to experimental results. In these analytical predictions, the effect of shrinkage has been also included.

3.3.1 Instantaneous test setup

In this PhD thesis, a four-point bending test configuration was used in all the experimental programs. The beams had a total length of 2400 mm and a clear length (between supports) of 2200 mm. Furthermore, the shear span and loading span were 750 mm and 700 mm, respectively. All beams had a cross-section of 140 mm width and 180 mm height. Two ribbed steel bars with a diameter of 12 mm were used in the tension side of the beams and two ribbed steel bars with a diameter of 8 mm were used in the compression side of the beams. To avoid shear failure, shear reinforcement with a diameter of 8 mm and distance equal to 75 mm was used in all beams. For strengthened beams, CFRP strips with a cross-section of 1.4 × 10 mm and bonded length of 1950 mm were used. To allocate the CFRP strips, grooves having dimensions of 6 × 15 mm were cut in the soffit of the beam. The distance between the grooves was set based on *fib* Bulletin 90 [1] recommendations. The beams were strengthened by one, two or three CFRP strips. To initiate a crack at a specific position, all beams had a 5 mm wide and 15 mm deep notch at midspan.

The beams were placed on steel supports that were connected to the strong floor. An actuator with a capacity of 300 kN was used to apply the load to the beams through a steel spreader beam. The instantaneous flexural tests were performed under displacement control at a rate of 0.6 mm/min. Figure 3.15 shows the tests setup for instantaneous loading. This test setup was used in all the instantaneous flexural tests of the present PhD thesis (i.e. those corresponding to experimental programs on instantaneous and long-term NSM CFRP-

strengthened RC beams). Further details on the test setup can be found in Journal Paper A (Chapter 4) and in all instantaneous tests presented in Journal Paper C (Chapter 6).
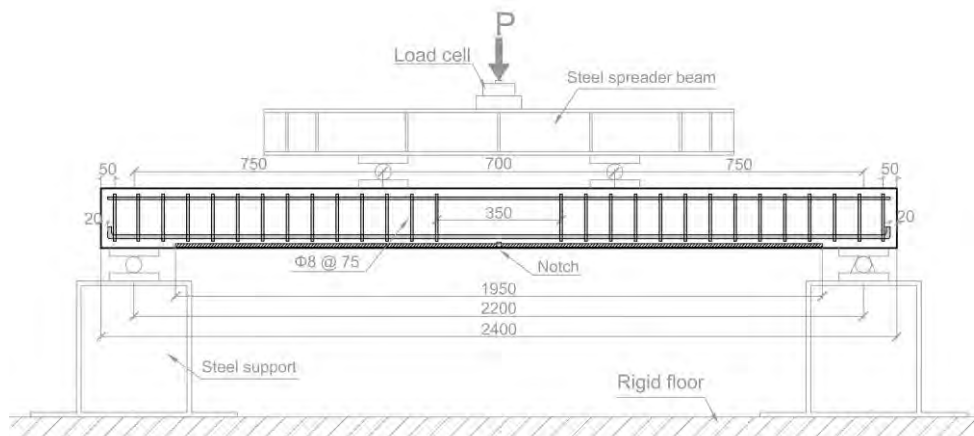
Figure 3.15. Tests setup for instantaneous loading (dimensions in mm).

3.3.2 Instantaneous test instrumentation

Five linear vertical displacement transducers (LVDTs) were used in the soffit of the beam to measure the deflections (LVDT1 at midspan and LVDTs 2-5 under the loading points). Furthermore, to measure the supports settlement, two LVDTs were used in both supports (LVDT6 and LVDT7). Moreover, only in the strengthened beams, two LVDTs (connected to the concrete and touching the end of the CFRP strip) were used to measure the possible slip between CFRP and concrete (LVDT8 and LVDT9). To register the strain variation during the loading process, one strain gauge was installed on the surface of the FRP at midspan. Furthermore, to evaluate the bond behavior between the CFRP strip and concrete, 14 additional strain gauges were also installed along the strengthening strip for two specimens.

Prior to testing, the beams were heated up to target temperature using heating blankets that were attached to the soffit of the beam. A proportional integral derivative (PID) controller was utilized for the heating process, and Type-T thermocouples, installed between the heating blanket and the soffit of the beam, were used as temperature controller sensor. To record and monitor the temperature variation during the heating process and flexural testing, different temperature gauges were glued on the concrete surface at the top and bottom of the beam, on the surface of the CFRP and on the surface of epoxy adhesive. The tests started when the

average temperature in the soffit of the beam was stabilized to the target value, almost 24 hours after the heating process started. Further details on the heating process can be found in Journal Papers A, C and D, in Chapters 4, 6 and 7, respectively.

3.3.3 Analytical predictions and shrinkage effect

An analytical work was performed to predict the instantaneous load-deflection responses of the specimens. The model considers crack section analysis, and applies equilibrium of forces and moments to get the theoretical moment-curvature responses of the uncracked and cracked sections. In this analysis, the following assumptions were considered: (i) strain compatibility; (ii) Bernoulli's hypothesis; (iii) perfect bond, and (iv) the parabola–rectangle stress–strain curve defined in Eurocode 2 [155]. The beam moment-curvature response is derived as the interpolation between cracked and uncracked sections, according to CEB-FIP Model Code 1990 [156]. Finally, the analytical load-deflection curve is obtained from integration of curvatures.

The schematic uncracked section considered for uncracked section analysis is shown in Figure 3.16. The neutral axis depth of the uncracked section ($d_{n,ucr}$) can be obtained by calculation of the first moment of inertia, as below:

$$
\begin{aligned}
(n_s - 1)A_{s1}\big(d_{n,ucr} - d_{s1}\big) + \big(0.5bd_{n,ucr}^2\big) - (n_s - 1)A_{s2}\big(d_{s2} - d_{n,ucr}\big) \\
- (n_{FRP} - 1)A_{FRP}\big(d_{FRP} - d_{n,ucr}\big) - \big(0.5b\big(h - d_{n,ucr}\big)^2 = 0
\end{aligned}
\tag{3.2}
$$

where n_s and n_{FRP} are steel and FRP modular ratios, respectively; A_{s1}, A_{s2} and A_{FRP} are the area of compression steel reinforcement, tension steel reinforcement and FRP strips, respectively; b and h are the width and height of the section, respectively; and d_{s1}, d_{s2} and d_{FRP} are effective depth of compression steel reinforcement, tension steel reinforcement and FRP strips, respectively.

After calculating the neutral axis depth of the uncracked section, the moment of inertia for the uncracked section (I_{ucr}) can be calculated as follows:

$$I_{ucr} = \frac{bd_{n,ucr}^3}{3} + \frac{b(h - d_{n,ucr})^3}{3} + (n_s - 1)A_{s2}(d_{s2} - d_{n,ucr})^2$$
$$+ (n_s - 1)A_{s1}(d_{n,ucr} - d_{s1})^2$$
$$+ (n_{FRP} - 1)A_{FRP}(d_{FRP} - d_{n,ucr})^2$$

(3.3)

The cracking moment (M_{cr}) of the section can be calculated as:

$$M_{cr} = f_t \frac{I_{ucr}}{h - d_{n,ucr}}$$

(3.4)

where f_t is the tensile strength of concrete.

The moment capacity of the uncracked section ($M_{n,ucr}$) can be obtained as below:

$$M_{n,ucr} = \kappa_{ucr} E_c I_{ucr}$$

(3.5)

where E_c is modulus of elasticity of concrete and κ_{ucr} is the curvature of the uncracked section, that can be obtained as:

$$\kappa_{ucr} = \frac{\varepsilon_t}{d_{n,ucr}}$$

(3.6)

where ε_t is the concrete tensile strain.
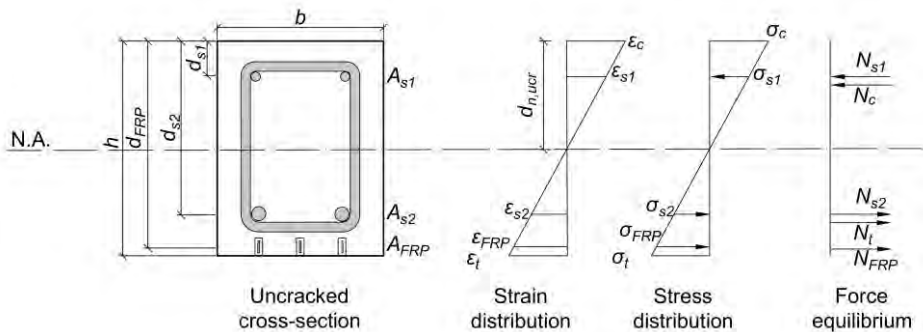
Figure 3.16. Uncracked section analysis.

46

The schematic cracked section to be considered for the cracked section analysis is shown in Figure 3.17. Based on the strain compatibility, the following equation can be written:

$$\frac{\varepsilon_c}{d_{n,cr}} = \frac{\varepsilon_{s2}}{d_{s2} - d_{n,cr}} = \frac{\varepsilon_{s1}}{d_{n,cr} - d_{s1}} = \frac{\varepsilon_{FRP}}{d_{FRP} - d_{n,cr}} \tag{3.7}$$

where ε_c, ε_{s1}, ε_{s2} and ε_{FRP} are corresponding strain in compression concrete, compression steel reinforcement, tension steel reinforcement and FRP strips, respectively and $d_{n,cr}$ is neutral axis depth of cracked section.

From force equilibrium, the following equation can be written:

$$N_c + N_{s1} - N_{s2} - N_{FRP} = 0 \tag{3.8}$$

where N_c, N_{s1}, N_{s2} and N_{FRP} are the forces resulting from the compression concrete stress block, the compression steel reinforcement, the tension steel reinforcement and the FRP strip, respectively.

$$N_c = \alpha f_c b d_{n,cr} \tag{3.9}$$

where f_c is the compressive strength of concrete and α is a parameter to determine the force resulting from the concrete compression stress block and can be obtained as below:

$$0 < \varepsilon_c < 0.002 \rightarrow \begin{cases} \alpha = \dfrac{1000\varepsilon_c}{12}(6 - 1000\varepsilon_c) \\ \lambda = \dfrac{8 - 1000\varepsilon_c}{4(6 - 1000\varepsilon_c)} \end{cases} \tag{3.10}$$

$$0.002 < \varepsilon_c < \varepsilon_{c,max} \rightarrow \begin{cases} \alpha = \dfrac{3000\varepsilon_c - 2}{3000\varepsilon_c} \\ \lambda = \dfrac{1000\varepsilon_c(3000\varepsilon_c - 4) + 2}{2000\varepsilon_c(3000\varepsilon_c - 2)} \end{cases} \tag{3.11}$$

where λ is a parameter to modify the neutral axis depth in the concrete compression stress block. In this PhD thesis, $\varepsilon_{c,max}$ was considered based on registers on concrete compression strain in each tested beam.

$$N_{s1} = A_{s1}E_s\varepsilon_{s1} \tag{3.12}$$

$$N_{s2} = A_{s2}E_s\varepsilon_{s2} \tag{3.13}$$

$$N_f = A_{FRP}E_{FRP}\varepsilon_{FRP} \tag{3.14}$$

where E_s and E_{FRP} are the modulus of elasticity of steel reinforcement and FRP strips, respectively.

Substituting Eqs. 3.7 and 3.9-3.14 in Eq. 3.8 allows to determine the neutral axis depth of cracked section ($d_{n,cr}$). Subsequently, the strain and stress at any height of the section can be obtained. Finally, the moment capacity of the cracked section ($M_{n,cr}$) can be calculated as below:

$$M_{n,cr} = \sigma_{s2}A_{s2}\big(d_{s2} - \lambda d_{n,cr}\big) + \sigma_{FRP}A_{FRP}\big(d_{FRP} - \lambda d_{n,cr}\big) + \sigma_{s1}A_{s1}\big(d_{n,cr} - d_{s1}\big) \tag{3.15}$$

where σ_{s1}, σ_{s2}, and σ_{FRP} are corresponding stresses in compression steel reinforcement, tension steel reinforcement and FRP strips, respectively.
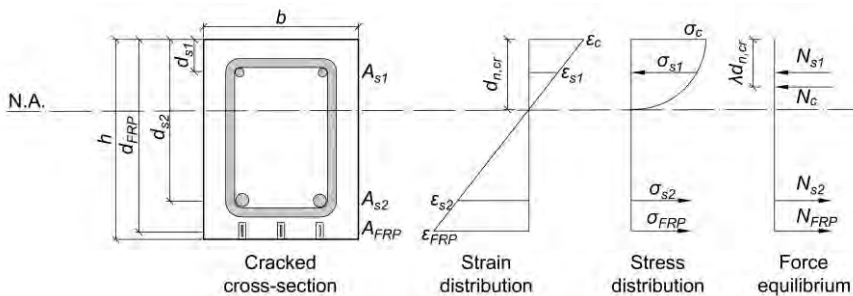
Figure 3.17. Cracked section analysis.

Based on these calculations, theoretical moment–curvature relationships for uncracked and cracked sections can be found. Then, the beam moment–curvature relationship can be derived

as the interpolation between cracked and uncracked sections, according to CEB-FIP Model Code 1990 [156]. Finally, the integration of curvatures allows to obtain the beam load-deflection curves.

It should be mentioned that, in the analytical predictions, the effect of temperature on concrete properties is considered following the equations proposed in *fib* Model Code 2010 [83]:

$$f_c(T) = f_c(1.06 - 0.003.T) \qquad (3.16)$$

$$f_t(T) = f_t(1.06 - 0.003.T) \qquad (3.17)$$

$$E_c(T) = E_c(1.06 - 0.003.T) \qquad (3.18)$$

where $f_c(T)$, $f_t(T)$ and $E_c(T)$ are the compressive strength, the tensile strength and the modulus of elasticity of concrete at temperature T (in °C), respectively. Moreover, f_c, f_t and E_c are the compressive strength, the tensile strength and the modulus of elasticity of concrete at T=20 °C, respectively.

Effect of shrinkage on short-term response of RC beams

In this section, the effect of concrete shrinkage on the instantaneous flexural behavior of the NSM CFRP-strengthened RC beams is presented. Concrete shrinkage can be defined as a reduction in its volume due to moisture loss. This process begins after casting at an early age of the concrete and continues for a long time. Concrete shrinkage depends on the water/cement ratio, ambient humidity, shape of aggregates, mixture properties, curing method and temperature and geometry of specimens, among the other parameters [83]. Unlike the plane concrete, where shrinkage can happen freely without any restrictions, in reinforced concrete, the internal reinforcement restrains free shrinkage, thus causing tensile and compressive loads to appear in concrete and reinforcement, respectively. As a result, unsightly micro cracks appear in concrete. In addition to these premature cracks, in those cases where non-uniform distribution of reinforcement in section depth exists, an additional curvature can also be observed [89].

According to the literature [89,157-159], shrinkage is not only an important parameter in time-dependent deflections of the RC flexural members, but it also has a significant effect on their instantaneous response. Premature cracks appearing due to the tensile stresses in concrete cause a reduction in the cracking moment of the flexural element and a shift on the bare bar response, therefore increasing deflections.

Figure 3.18 shows the moment-curvature relationships of an RC flexural member. In this figure, the black lines show the theoretical cracked and uncracked flexural responses (along with interpolation between them) of a beam without shrinkage (ε_{sh}=0). The red lines correspond to the (theoretical) actual state of a beam with shrinkage (ε_{sh}≠0), that derives in a shift of the origin point to the bottom-left side. Finally, the blue lines correspond to the behavior observed in the laboratory when a beam with shrinkage (ε_{sh}≠0) is tested under short-term conditions.
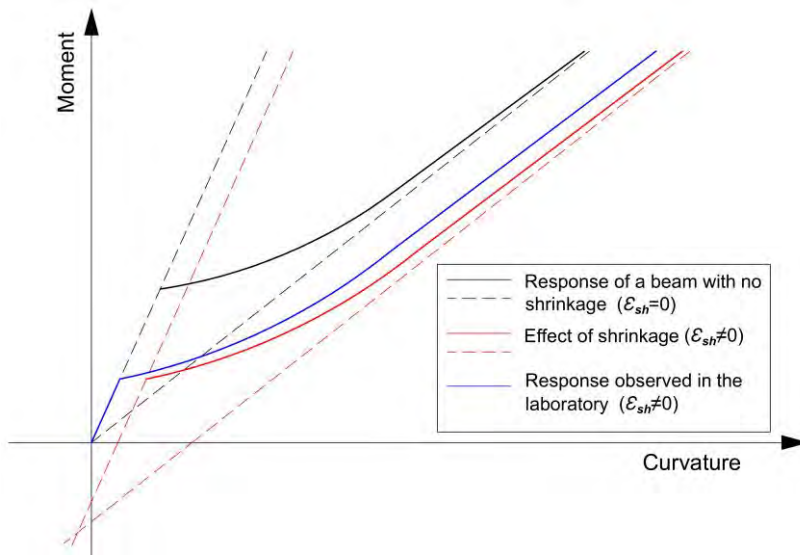
Figure 3.18. Moment-curvature of beam with and without shrinkage.

Further details on the analytical work for the inclusion of the effect of shrinkage on the load-deflection response of a beam, along with comparison with experimental results, can be found in Journal Paper A in Chapter 4.

3.4 Time-dependent behavior of NSM CFRP-strengthened RC beams

Real-life RC structures are usually subjected to long-term loads (dead weight of structure, weight of the installations and load from users) that can influence the long-term performance (time-dependent deflections, loading capacity and failure mode) of the elements [80-82]. The effect of long-term loading on the performance of the element depends on many factors such as material properties, environmental conditions, age of concrete and magnitude of long-term load [83]. Within material properties, creep and shrinkage of concrete, which are dependent on environmental conditions, are of major importance [83].

Besides, RC structures are normally exposed to temperature variations during the different seasons of the year in their useful life. As stated in the literature, epoxy adhesives are the most common ones in the NSM strengthening system. Due to their nature, special attention should be given when working temperature approaches their T_g, as mechanical properties may vary, thus affecting the performance of the strengthening system. In this scenario, both long-term loads and high service temperature (near or beyond the T_g of the epoxy adhesive) may have an effect on the performance of NSM FRP-strengthened RC elements, which highlights the importance of analyzing the combination of both phenomena [7-9].

As mentioned in Chapter 2, there are few works regarding the flexural behavior of NSM FRP-strengthened RC beams and, to the best of author knowledge, none of them accounts for the effect of high service temperature on their time-dependent behavior. This is, therefore, one of the aims of this PhD thesis. To this end, an experimental program including 23 beams was conducted to investigate the effect of different parameters such as: different temperatures (20 °C and 50 °C), steel reinforcement ratios (ρ_s = 0.79% and ρ_s = 1.14%) and CFRP ratios (0.06% and 0.18%) on the flexural time-dependent behavior of NSM CFRP-strengthened RC beams. The time-dependent behavior of the materials (concrete and epoxy adhesive) under different temperatures is also analyzed. Furthermore, an analytical work, based on the age-adjusted effective modulus method (AEMM) [83,84], is presented to predict the time-dependent deflections.

3.4.1   Long-term test setup

As stated in Section 3.2, loading configuration, dimensions of the beams and CFRP bonded length are common for the whole PhD thesis, and the internal and external reinforcement were changed according to the experimental program.

This experimental program included 23 beams divided into three series: 10 beams were tested under short-term loading (Series 1), to act as reference beams; 10 beams were tested under long-term loading (series 2); and 3 beams were resting in the laboratory for ageing, to be latter tested under short-term loading (at the end of the long-term loading period) (Series 3). The comparison of beams in Series 3 and the post long-term performance of beams in Series 2 allowed to evaluate the ageing effect.

The test setup for the instantaneous tests (specimens in Series 1 and 3, and post long-term of specimens in Series 2) is the same as the one presented in section 3.3.1 and Figure 3.15. For the long-term test, the beams were placed in the long-term loading frame and concrete blocks and steel plates were used as deadweight to simulate the long-term loading. In this setup, the loading and shear span were equal to those of instantaneous test (i.e. 700 mm and 750 mm, respectively).

Prior to the long-term test, beams were subjected to pre-loading in order to ensure a level of cracking corresponding to the service load. The pre-loading stage consisted on two loading/unloading cycles up to service load level, P_{ser}, and the test setup for instantaneous test was applied. The service load was calculated by limiting the stress in compressed concrete ($\sigma_c<0.6f_c$) and steel reinforcement ($\sigma_s<0.8f_y$) [155]. After the pre-loading, specimens were moved to the long-term loading frames and the long-term load was applied for a duration of 200 days. The long-term load was chosen so as to obtain a concrete compressive stress of $0.35f_c$, so that linear creep behavior of concrete was ensured by being under the *fib* Model Code 2010 limitation [83].

After finishing the long-term tests, the specimens were tested under short-term loading to evaluate their residual flexural strength.

3.4.2 Long-term test instrumentation

Instrumentation for the long-term tests consisted on one linear vertical displacement transducer (LVDT) placed in the midspan of the beam to measure the evolution of the central deflection along long-term tests. In short-term tests, in addition to midspan LVDT, two more LVDTs were also used to measure the support settlements. In all cases, instantaneous and long-term tests, one strain gauge was installed in the midspan of the specimens to register the strain at the top fiber of concrete (SG_C).

Similar to the case of the instantaneous tests with temperature (Section 3.3.2), specimens submitted to 50 °C were heated with heating blankets (installed to the soffit of the beam), and a PID controller was used to control the heating process, where Type-T thermocouples were used as temperature controller sensor. Additionally, an isolation system, consisting of rock wool with aluminum foil, was used in order to speed the heating process and ensure a uniform constant temperature along the long-term loading (see Figure 3.19b). A set of temperature gauges was installed to track and register the temperature variation on the surface of different materials (concrete, epoxy and CFRP strips).

The general view of test setup in both short-term and long-term tests is shown in Figure 3.19.

(a)   (b)
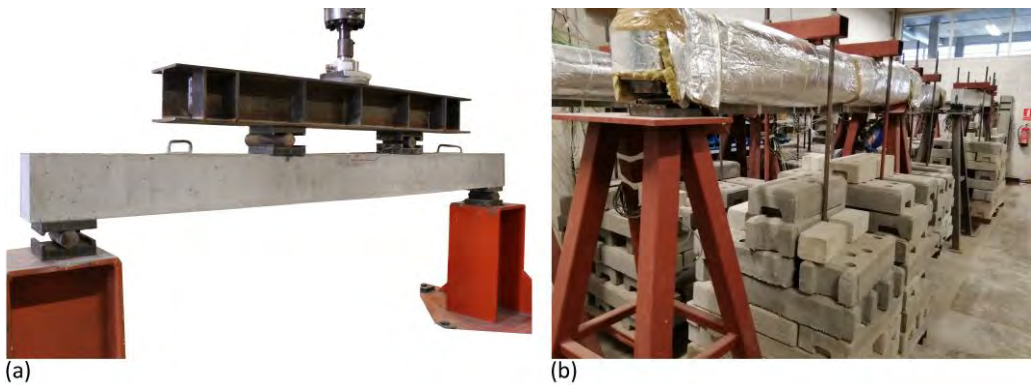
Figure 3.19. Tests setups: (a) Short-term test and (b) Long-term tests.

Further details on the long-term flexural program can be found in Journal Paper C in Chapter 6.

3.4.3 Analytical predictions

An analytical procedure, based on the AEMM outlined in Gilbert [84], was used to predict the time-dependent deflections of NSM CFRP-strengthened RC beams. In this method, a cross-section analysis was performed to determine the effect of creep and shrinkage on the evolution of stresses, strains and curvatures by time. For analytical predictions, average values for registers of temperature and humidity during the long-term load were used for determining the values of concrete creep coefficient, φ_c (t,t_0), and concrete shrinkage, ε_{sh} (t,t_0), following *fib* Model Code 2010 [83] predictions. Moreover, the effect of temperature on the mechanical properties of concrete was considered following *fib* Model Code 2010 [83] as it outlined in Section 3.3.3 through Eqs. 3.16-3.18. The detailed procedure regarding the analytical predictions can be found in Journal Paper C in chapter 6.

3.5 Fatigue behavior of NSM CFRP-strengthened RC beam

To complete the analysis on the effect of temperature on the performance of NSM CFRP-strengthened RC beams, a final experimental program including fatigue loads was also designed. Fatigue failure of a structural element is defined as a progressive cracking/degrading in the material up to fracture under repeated loading. Unlike short-term loading, fatigue loading causes a reduction in stiffness of the system due to stress/strain accumulation in the material that may lead to a failure in the system before reaching its ultimate capacity [116]. Civil structures should not only be designed to resist short-term and long-term loads. These structures also undergo vehicle vibration (in road pavements and bridges) and wind and wave actions (in marine structures), so that fatigue (cycling loading) is also present in their life [116].

As it was mentioned before, the performance of NSM FRP-strengthened RC elements may be affected by temperature, as mechanical properties of epoxy adhesive, typically used in this strengthening technique, may change when temperature approaches its T_g. Therefore, the evaluation of the performance of this NSM FRP-strengthened elements under the combined action of high service temperature (near or beyond the T_g of the epoxy adhesive) and fatigue loads is of huge importance for a correct design of civil structures.

There is considerable work in the literature regarding to the flexural performance of the NSM FRP-strengthened RC beams [55,65,67,69,70,120-122,134-136] under fatigue loading, but none

of them evaluates the effect of high service temperature on fatigue performance of this system. Therefore, the last experimental program of this PhD thesis was designed to investigate the effect of high service temperature on the fatigue flexural performance of the NSM CFRP-strengthened RC beams.

3.5.1 Fatigue test setup

In this experimental program, beams with the same dimension as those considered in previous experimental programs were used. Similarly, the same test setup as those of previous tests was also imposed (same CFRP bonded length, clear span, loading span and shear span). Steel supports, connected to the strong floor, were used to place the beams, and a dynamic actuator, with a capacity of 125 kN, was used to apply the load to the beam through a steel spreader beam. The dynamic actuator was held by a strong frame that was connected to the strong floor, to minimize the vibration effect during fatigue loading. A general view of fatigue test is shown in Figure 3.20.
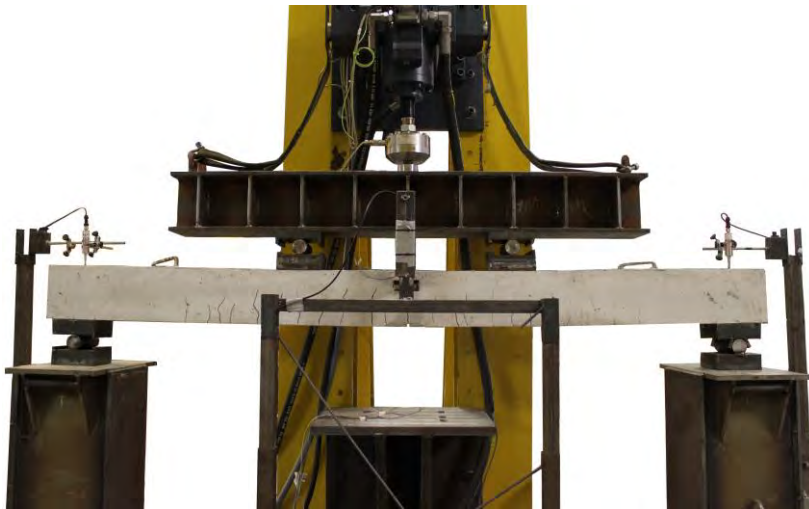
Figure 3.20. General view of fatigue test setup.

This experimental program included 11 beams divided into two series: 3 beams were tested under short-term loading at 20 °C (Series 1), to act as reference beams and 8 beams were tested under fatigue loading (Series 2). The beams in Series 2 were divided in two groups, according to the temperature applied during the fatigue test (20 °C and 70 °C). In each of these two groups, two different CFRP ratios (0.06% and 0.18%) and two different *R* ratios (0.57 and 0.38) were

investigated. It should be mentioned that *R* ratio is defined as the ratio between minimum load and maximum load of a fatigue cycle.

Similar to previous sections, the instantaneous flexural tests were performed under displacement control at a rate of 0.6 mm/min until failure of the beam. For the fatigue tests, the application of the fatigue load was preceded by a loading stage (up to the maximum fatigue load to be applied in the fatigue cycles) and an unloading stage (until the average load to be applied in the fatigue cycles). The loading-unloading stages were also performed under displacement control at a rate of 0.6 mm/min. Thereafter, the fatigue load was applied through a sinusoidal loading path with a frequency of 2 Hz. The fatigue test duration was programmed to 2 million cycles or failure of the beam, whichever occurs first.

3.5.2 Fatigue test instrumentation

In fatigue tests, similar to long-term experimental program, one linear vertical displacement transducer (LVDT) is used in the midspan of the beam, to measure the midspan deflection. Furthermore, two more LVDTs were also used to measure the support settlements. Besides, strain gauge was installed at the concrete top fiber in the midspan of the specimens to register the strain of concrete (SG_C). In those specimens to be tested at 70 °C (specimens of Group 2 in Series 2), the same heating system used in the long-term experimental program was applied, and the heating process started almost 24 hours prior to fatigue testing (until stabilization of the temperature at the soffit of the beam). The evolution of temperature during the fatigue tests was possible due to the temperature gauges installed on the top and bottom of concrete surface, on CFRP surface and on epoxy adhesive surface. Further details on the fatigue test setup can be found in Journal Paper D in Chapter 7.

PART III: Publications and discussion

4 Paper A: Experimental study of the effect of high service temperature on the flexural performance of near-surface mounted (NSM) carbon fiber-reinforced polymer (CFRP)-strengthened concrete beams

Younes Jahani[1]*, Marta Baena[1], Javier Gómez[1], Cristina Barris[1] and Lluís Torres[1]

[1]AMADE, Polytechnic School, University of Girona, 17003, Girona, Spain

*Corresponding author

Experimental Study of the Effect of High Service Temperature on the Flexural Performance of Near-Surface Mounted (NSM) Carbon Fiber-Reinforced Polymer (CFRP)-Strengthened Concrete Beams

Younes Jahani *, Marta Baena, Javier Gómez, Cristina Barris and Lluís Torres

AMADE, Polytechnic School, University of Girona, 17003 Girona, Spain; marta.baena@udg.edu (M.B.); javier.gomez@udg.edu (J.G.); cristina.barris@udg.edu (C.B.); lluis.torres@udg.edu (L.T.)
* Correspondence: younes.jahani@udg.edu; Tel.: +34-972-418-817

Abstract

This paper presents a study of the effect of high service temperature (near or beyond glass transition temperature (T_g) of structural epoxy adhesive) on the behavior of near-surface mounted (NSM) carbon fiber-reinforced polymer (CFRP)-strengthened reinforced concrete (RC) beams. The study includes experimental work as well as analytical and numerical analysis. To this end, fourteen beams have been tested up to failure in two different series. In series 1, specimens with three different CFRP ratios have been tested at two different temperatures (i.e., 20 °C and 40 °C). In series 2, and with the aim of evaluating the effect of higher temperatures, only one CFRP ratio was tested under four different temperatures (i.e., 20 °C, 60 °C, 70 °C, and 85 °C). Experimental results are evaluated in terms of load-deflections, failure modes, and bond performance. Furthermore, the experimental load-deflection curves are satisfactorily compared to both analytical predictions and finite element (FE) numerical simulations. In both cases, shrinkage and temperature effects on the short-term response of flexural elements have been accounted for. No significant reduction in stiffness and ultimate load was observed for specimens being tested up to 60 °C (in the range of epoxy T_g), showing FRP rupture failure in all of them. For specimens under 70 °C and 85 °C, the failure mode changed from FRP rupture to FRP end debonding and concrete crushing, respectively.

Keywords: NSM strengthening, carbon fiber reinforced polymer, epoxy adhesive, temperature, experimental, shrinkage

4.1 Introduction

In the past decades, fiber-reinforced polymer (FRP) materials have been produced in different configurations and have been widely used for different purposes, such as the strengthening of reinforced concrete (RC) structures. Currently, externally bonded reinforcement (EBR) and near-surface mounted (NSM) are the two most used strengthening techniques in civil structures. In the EBR technique, the FRP is bonded to the previously prepared concrete surface, usually with an epoxy resin, while in the NSM technique, a groove is cut in the concrete cover and the FRP bar or strip is inserted and bonded using groove filler, which is typically an epoxy adhesive or a cement grout. The improvement of the bond performance, along with higher protection against potential aggressive environmental exposure and vandalism actions, are some of the advantages of the NSM technique [5,6,30].

The performance of the NSM strengthening system relies on the bond capacity of the joint between concrete and FRP material, which in turn depends on the properties of the adhesive (usually epoxy resin), among other parameters. Typically, epoxy adhesives can be affected by temperature, as near or beyond the glass transition temperature (T_g), their mechanical properties may change [8,9,149,150]. This may lead to a decrease of its performance and premature debonding and therefore to a not complete exploitation of the strengthening system. In this sense, some limitations on the working temperature of these strengthening systems exist. According to *fib* Bulletin 90 [1], to avoid any considerable change in the adhesive properties in the service condition, the maximum temperature should be 20 °C less than T_g. In this same line, Michels et al. [147] summarized the various design codes provisions to define the service temperature in FRP-strengthened RC structures to be 10 °C to 20 °C less than T_g, whilst Klamer et al. [151] suggested the service temperature to be limited to 10 °C less than T_g. Furthermore, Ferrier et al. [152] limited the service temperature to be 15 °C less than T_g for avoiding temperature effects in the creep of epoxies with lower range of T_g ($T_g < 55$ °C). Moreover, other studies [153,154] limited the maximum temperature to 10 °C less than T_g to avoid premature debonding of FRP sheets from concrete surface. These limitations are related to the EBR technique, while for the NSM technique, less information is available, and no specific limitation has been stated.

Focusing on the existing experimental work, the flexural behavior of NSM strengthened concrete beams under room temperature have been widely studied in the literature [43,47,49,53-56], while the structural performance of this technique under elevated temperature and high service temperature is still an open topic that needs detailed research. The fire resistance of FRP-strengthened RC flexural elements has been analyzed in different studies [160–169]. Results from these works showed that the efficiency of the NSM method was better than EBR technique, and the thicker layers of the insulation system helped significantly reduce the temperature in the concrete and the adhesive. As a result, failure in the interface between laminate and concrete was postponed and, therefore, the durability of the system increased. A deep state-of-the-art review on the performance of FRP-strengthened RC elements exposed to fire conditions can be found in [170].

Compared to fire resistance, the performance of FRP-strengthened RC flexural elements exposed to high service temperature has been hardly investigated. The behavior of four different EBR strengthened RC beams under three different temperatures (i.e., 20, 50, and 70 °C), was studied and analyzed in [57]. Results showed that the failure load of the specimens was not significantly affected by temperature. However, a change in the failure interface took place for specimens with shorter anchorage length exposed to higher temperature (70 °C). Similar results were obtained in [58], who applied temperatures in the range of 20 °C to 80 °C and concluded that the load capacity of EBR-strengthened beams subjected up to 62 °C was slightly decreased, whilst the application of larger temperatures (from 70 °C on) resulted in a reduction in load capacity of approximately 20% of its nominal capacity at room temperature. Moreover, the application of larger temperatures made the failure mode change from cohesive in concrete to adhesive at the concrete-epoxy interface. Moving from beams to slabs, Silva et al. [36] studied the flexural performance of concrete slabs strengthened with the NSM technique under service temperature (up to 80 °C). According to this work, the maximum ultimate load capacity was observed in a slab under 40 °C, which was attributed to possible post-curing in epoxy adhesive, and the increase in the temperature up to 80 °C was followed by a decrease of the ultimate capacity of the slab of about 12%. In addition, the specimens subjected to 80 °C failed by cohesive failure at the epoxy, while in the rest of the specimens, the failure mode was concrete crushing. Focusing on EBR adhesive double lab joints with a wet lay-up system, Ferrier et al. [171] investigated the effect of temperature (ranging from −40 °C to 120 °C). According to the

experimental results, the increase of temperature was followed by an increase of the slip between joint elements that made the specimens failed at lower loads.

In addition to experimental work, finite element methods have been also widely used to simulate the FRP-strengthened beams and columns under different loading and environmental conditions [172-179]. In these studies, different types of FRP material (i.e., carbon, glass, and basalt) have been considered as NSM or EBR reinforcement, and both the flexural and shear performance of the strengthened members have been validated. It should be noted that these studies correspond to specimens under room and fire conditions.

According to the literature, it is seen that there are a limited number of studies related to the flexural performance of NSM FRP-strengthened RC beams under high service temperature, which justifies the need for further research in this field. The present work aims at studying the effect of relatively high service temperature (near and beyond T_g) on the flexural performance of NSM carbon FRP (CFRP)-strengthened RC beams when different strengthening ratios of CFRP are used. For this purpose, an experimental program has been carried out, and results are analyzed in terms of flexural behavior, failure modes, and bond performance along the FRP laminate. Additionally, experimental results are also compared to analytical predictions and numerical simulations with the finite element method. The influence of shrinkage and temperature on the short-term response of the specimens was included in both analytical calculations and numerical predictions.

4.2 Experimental program

4.2.1 Experimental test setup

The experimental program included fourteen specimens divided into two series (Table 4.1). Series 1 included eight beams, which were distributed as follows: two control beams (exposed to 20 °C and 40 °C) and six NSM CFRP-strengthened beams (exposed to 20 and 40 °C) with three different ratios of CFRP. In series 2, unlike series 1, only one CFRP-strengthening ratio was used, and four different temperatures were applied (20 °C, 60 °C, 70 °C, and 85 °C). The beams were tested under a four-point bending configuration (Figure 4.1). The beams had a rectangular cross-section of 140 × 180 mm and a total length of 2400 mm. The clear span was 2200 mm and the shear span was 750 mm, thus leading to a flexural span of 700 mm. Two ribbed steel bars with

a diameter of 12 mm were utilized as longitudinal reinforcement on the tension side, while two ribbed steel bars with the diameter of 8 mm were used on the compression side. The shear span and some portion of the flexural span were reinforced with Φ8 mm steel stirrups every 75 mm to avoid shear failure. All beams had a 5 mm wide and 15 mm deep notch at midspan (to act as a crack initiator at this specific position).

The same CFRP strip, having a thickness of 1.4 mm and a width of 10 mm, was used in all the strengthened beams, but different configurations of the strengthening system were considered (see Figure 4.1). The bonded length of the CFRP strips was 1950 mm for all specimens. Grooves of size 6 × 15 mm were cut using a sawing machine. After cutting them, the grooves were completely cleaned with air pressure to make sure there was no dust inside the grooves.

The specimens were designated as X-Y-Z, where X denotes the type of beam (CB for control beams with no strengthening system, SB1S for beams strengthened with one CFRP strip, SB2S for beams strengthened with two CFRP strips, and SB3S for beams strengthened with three CFRP strips), Y indicates the series of specimens, and Z is the temperature applied to the beam (where R refers to room temperature equal to 20 °C). For example, SB1S-1-R refers to the strengthened beam with one strip in series 1 of specimens at 20 °C. Details of the specimens are shown in Table 4.1.
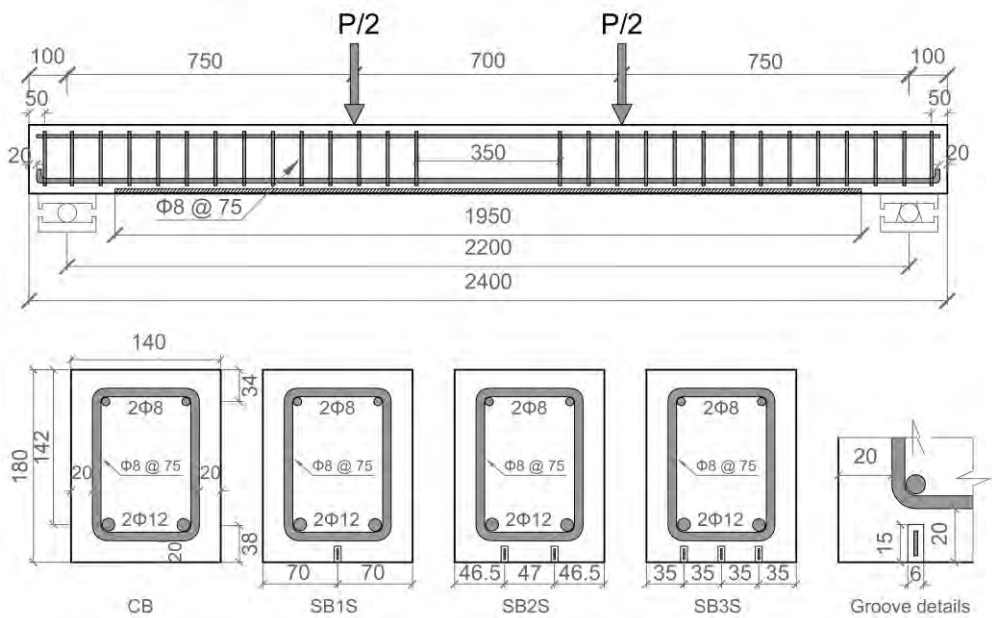
Figure 4.1. Beam details (dimensions in mm).

Table 4.1. Details of the tested specimens.

Experimental campaign	Beam ID	Test temperature (°C)	compressive strength of concrete (MPa)	FRP dimension (mm²)	No. of strips	CFRP area (mm²)
Series 1	CB-1-R	20	31.8	-	-	-
	CB-1-40	40		-	-	-
	SB1S-1-R	20		1.4 × 10	1	14
	SB1S-1-40	40		1.4 × 10	1	14
	SB2S-1-R	20		1.4 × 10	2	28
	SB2S-1-40	40		1.4 × 10	2	28
	SB3S-1-R	20		1.4 × 10	3	42
	SB3S-1-40	40		1.4 × 10	3	42
Series 2	CB-2-R	20	40.8	-	-	-
	CB-2-70	70		-	-	-
	SB2S-2-R	20		1.4 × 10	2	28
	SB2S-2-60	60		1.4 × 10	2	28
	SB2S-2-70	70		1.4 × 10	2	28
	SB2S-2-85	85		1.4 × 10	2	28

Beams to be tested at high temperature were submitted to a heating process before instantaneous testing. The heating was applied on the tension face of the beam by using silicone rubber fiberglass-reinforced heating blankets. An insulating support was used to hold the heating blankets in contact with the tension face of the beam. A proportional integral derivative (PID) controller was utilized for the heating process, and Type-T thermocouples, located between the heating blankets and the concrete surface, were used as temperature controlling sensors. The evolution of temperature with time at different locations is shown in Figure 4.2. Tests started after the stabilization of temperature (see Figure 4.2), which remained constant along the test. Temperature strain gauges located at different points of the beam section allowed the registering of temperature along both the heating process and flexural test.
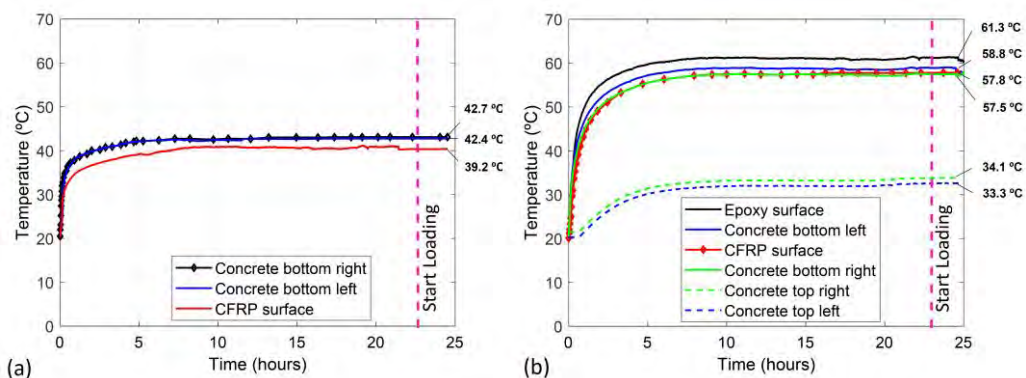
Figure 4.2. Evolution of temperature with time at different locations of specimens: (a) SB3S-1-40 and (b) SB2S-2-60 (before and during loading).

In all the cases, a hydraulic jack applied the load onto the specimens through a spreader beam. The load was applied under displacement control mode at a rate of 0.6 mm/min.

4.2.2   Instrumentation

Five linear vertical displacement transducers (LVDTs) were used to record the vertical displacements, and two other LVDTs were utilized to measure the settlement of the supports. Due to the use of heating blankets in the soffit of the beam, two LVDTs were installed to the side faces of the beam under each loading point. Furthermore, end slips of the NSM CFRP strip were measured with two horizontal LVDTs (see Figure 4.3a). The measurements from horizontal LVDTs were almost negligible in all specimens.

A strain gauge was installed at the midspan section of specimens on FRP surface (SG_f) to assess strain variation with load. Furthermore, to evaluate the bond behavior between the CFRP strip and concrete, 14 additional strain gauges (SG_{f1} to SG_{f14}) were installed along the strengthening strip for SB1S-1-R and SB1S-1-40 specimens (see Figure 4.3b). To avoid reducing the bonded surface, the strain gauges were installed in both sides of the strip (i.e., alternate in front and back of the strip).
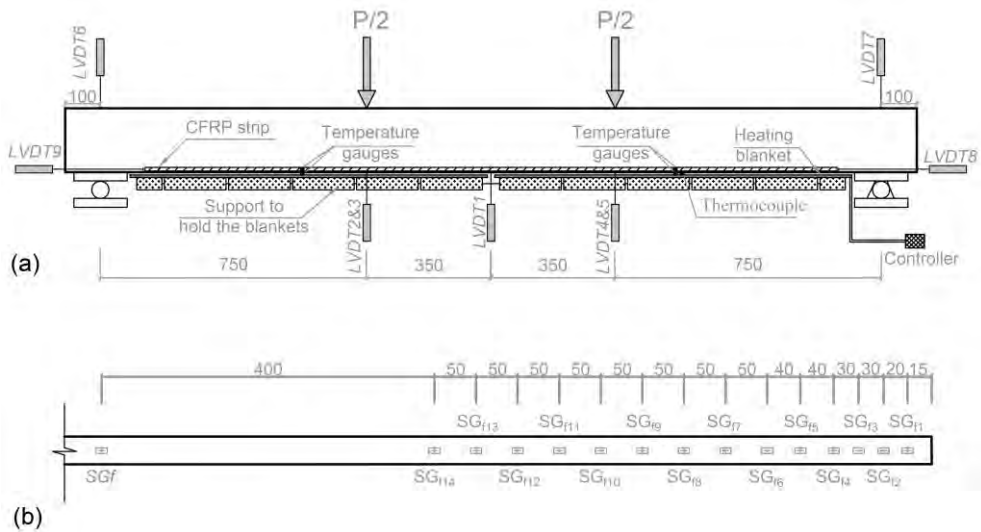
Figure 4.3. Test configuration: (a) Position of linear vertical displacement transducers (LVDTs), temperature gauges, thermocouples, and heating system and (b) Strain gauges along the CFRP laminate in specimens SB1S-1-R and SB1S-1-40 (dimensions in mm).

Moreover, to record the temperature variation, temperature gauges (thermocouples) were installed in specimens under temperature at the surface of the concrete at the top and soffit of the beam and inside the groove. The temperature variations were recorded during the heating process as well as during the flexural tests. The position of the thermocouples is shown in Figure 4.3a. A general overview of test scene, along with the elements of the heating system (PID controller and heating blanket) is shown in Figure 4.4.
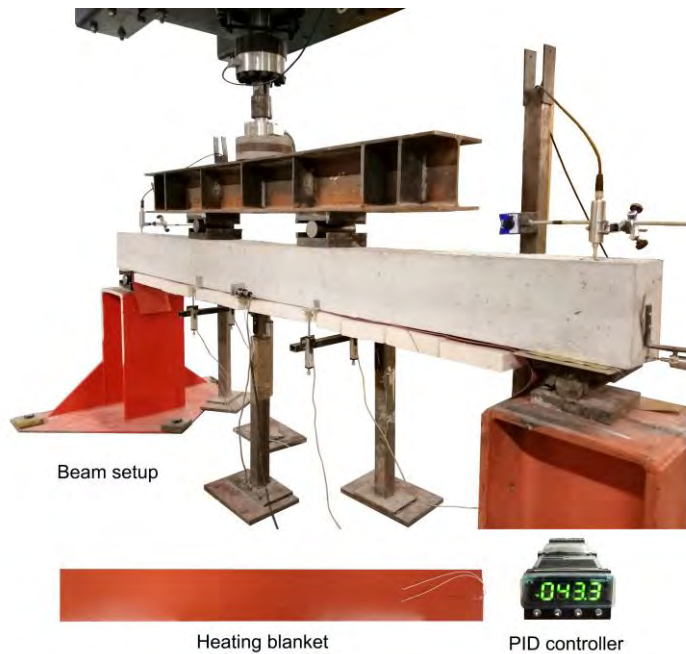
Figure 4.4. General overview of test scene and elements of the heating system.

4.2.3 Materials

The specimens were cast in laboratory conditions with conventionally vibrating procedure. Two different concrete batches were used. For concrete of series 1, the cement type was I-42.5R, with a content of 390 kg/m³, the maximum aggregate size was 12 mm, and the water/cement relationship was 0.46. For concrete of series 2, the cement type was I-42.5R, with a content of 333 kg/m³, the maximum aggregate size was 10 mm, and the water/cement relationship was 0.48. In both series, a viscosity modifier and underwater admixture were used to improve workability. The experimental compressive strength (f_c), tensile strength (f_t), and modulus of elasticity (E_c) of concrete were determined from three cylinder tests (300 mm high and 150 mm diameter) according to UNE-EN 12390-3:2003 [137], UNE-EN 12390-6:2010 [138], and ASTM C469-87 [139] standards, respectively. According to the test results, for series 1 of specimens, f_c of 31.8 MPa (CoV = 6.6%), f_t of 4.2 MPa (CoV = 2.3%), and E_c of 31.5 GPa (CoV = 7.8%) were obtained. Furthermore, for series 2 of specimens, f_c, f_t, and E_c were 40.8 MPa (CoV = 2.8%), 5.2 MPa (CoV = 0.5%), and 29.4 GPa (CoV = 0.8%), respectively.

The mechanical properties of steel bars were obtained from tension tests based on UNE-EN ISO 15630-1 [141]. The yielding stress (f_y) and the modulus of elasticity (E_s) were 573.2 MPa (CoV = 1.1%) and 200.8 GPa (CoV = 0.7%), respectively.

67

The CFRP laminates used in the experimental work consisted on unidirectional carbon fibers (with a volume content fiber higher than 68%) held together by an epoxy vinyl ester resin matrix [20]. The mechanical properties were obtained according to ISO 527-5:2009 [142] recommendations. An ultimate tensile strength ($f_{u,FRP}$) of 2251.4 MPa (CoV = 3.2%), an ultimate tensile strain ($\varepsilon_{u,FRP}$) of 0.0133 (CoV = 7.2%), and modulus of elasticity (E_{FRP}) of 169.5 GPa (CoV = 6.3%) were obtained.

A two-component epoxy adhesive was used to bond the CFRP strip to a concrete groove. According to the manufacturer's product guide specification [143], the components A and B should be mixed at a ratio of 2:1 by weight. In addition, the proposed curing time was 7 days. However, in this study, the specimens were tested after 12 days of epoxy curing at room temperature.

Mechanical properties of the epoxy adhesive were assessed according to ISO-527-1 [144]. A tensile elastic modulus (E_{epoxy}) of 7.1 GPa (CoV = 7.8%) and tensile strength ($f_{u,epoxy}$) of 30.4 MPa (CoV = 4.3%) were obtained.

As mentioned previously, the aim of this study is to evaluate the effect of high service temperature on the flexural behavior of NSM CFRP-strengthened beams. Therefore, characterization of the glass transition temperature (T_g) of the epoxy adhesive is of interest. According to the literature, there are two different well-known methods to obtain T_g of the adhesive: differential scanning calorimetry (DSC) [145] and dynamic mechanical analysis (DMA) [146]. The DSC technique provides information about changes in physical, chemical, and heat capacity of the adhesive. In this experimental program, isothermal DSC tests were carried out using the DSC Q2000. A heating rate of 10 °C/min was applied using nitrogen as the purge gas at 50 mL/min. The temperature range was between 25 °C and 80 °C. To determine T_g, three temperatures were measured: the extrapolated onset temperature (T_f), the mid-point temperature (T_m), and the extrapolated end temperature (T_e). The DMA test is an alternative method to determining the T_g and viscoelastic properties of polymeric materials. In this study, a METTLER TOLEDO DMA/SDTA861e analyzer with a 3-point bending test configuration and 45 mm between supports was utilized. The specimens were subjected to a heating rate of 2 °C/min within a temperature range of 30 °C to 100 °C. A 5 µm, constant displacement amplitude was applied at a frequency of 1 Hz. T_g was obtained by analyzing the storage modulus (E'), the loss modulus (E''), and the loss factor ($tan\delta$) as functions of temperature. In the present work, both methods (DSC and DMA) were utilized to determine the T_g after 12 days of curing time at room

temperature. According to the test results, presented in Table 4.2, T_g cannot be considered as a unique temperature, but rather, it should be considered as a range of temperatures, as stated elsewhere [147]. The results of DSC and DMA tests are plotted in Figures 4.5 and 4.6, respectively. According to these results, T_g was in the range of 53.9 °C –65.3 °C.

Table 4.2. Results of DSC and DMA methods.

Methodology	DSC			DMA		
	T_f	T_m	T_e	Storage Modulus (E')	Loss Modulus (E'')	Loss Factor ($tan\delta$)
T_g (°C)	53.9	55.2	55.9	56.2	57.7	65.3
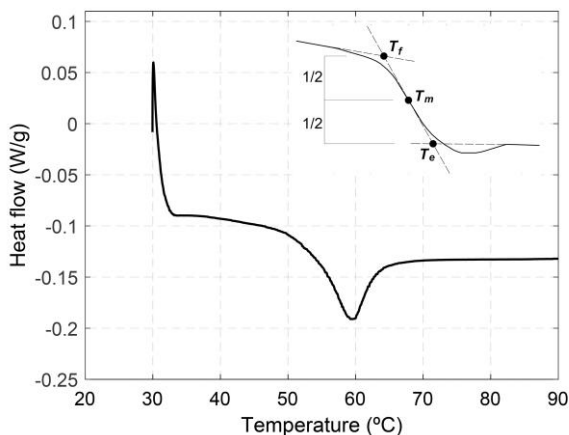
Figure 4.5. Differential scanning calorimetry (DSC) test results.
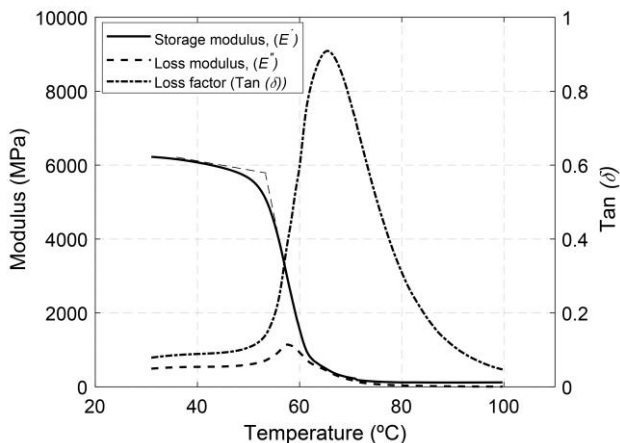
Figure 4.6. Dynamic mechanical analysis (DMA) test results.

4.3 Results and Discussion

In this section, experimental results are presented and discussed in terms of load-deflection curve, failure mode, and strain distribution along the CFRP strips. Analytical predictions for the load-deflection relationship are also presented.

In the analytical work, equilibrium of forces and moments is applied, where the following assumptions have been considered: (i) strain compatibility; (ii) Bernoulli's hypothesis; (iii) perfect bond, and (iv) the parabola-rectangle stress-strain curve defined in Eurocode 2 [155]. Based on this, theoretical moment–curvature is determined for uncracked and cracked sections and, finally, the moment–curvature relationship is derived as the interpolation between cracked and uncracked sections, according to CEB-FIP Model Code 1990 [156]. Afterwards, an analytical load–deflection curve is obtained from an integration of curvatures. It should be noted that shrinkage previous to loading has been found to affect the load-deflection behavior of RC members [89,157-159]. This influence has also been experienced in the NSM FRP-strengthened beams included in this work. Therefore, a systematic procedure is applied to account for this effect in the analytical predictions for their load–deflection relationship.

4.3.1 Shrinkage Effects on Instantaneous Deflection of Concrete Beams

Concrete shrinkage is a reduction in its volume due to moisture loss. This reduction starts after casting the concrete and depends on the water/cement ratio, ambient humidity, shape of aggregates, mixture properties, curing method and temperature, and geometry of specimens, among other parameters. In plain concrete without reinforcement, this shortening would happen without any restrictions. However, in the case of reinforced concrete, the presence of the embedded reinforcement acts as an impediment to free shrinkage. As a result of the restrain provided by the reinforcement, compressive and tensile loads appear in the reinforcement and the concrete, respectively, therefore causing unsightly cracks in concrete. Additionally to these premature cracks, in those cases where non-uniform distribution of reinforcement in section depth exists, an additional curvature can be observed [89].

Shrinkage is an important parameter in predicting the long-term deflection of RC flexural members, although depending on the amount of shrinkage and reinforcement ratio, it may have a significant influence even in the short-term behavior of RC elements [89,157-159]. Considerable shrinkage can be developed in concrete elements before testing unless special attention to the curing method and conditions is paid. With increasing the shrinkage at early

age of concrete, tensile stresses are developed in concrete due to the restrain caused by internal reinforcement. This causes a reduction in the cracking moment of the flexural element and a shift on the bare bar response and therefore an increase in deflections.

In this work, shrinkage before flexural loading was assessed since shrinkage strain recorded from the day of casting was significantly higher for specimens in series 2 (344 µε) when compared to that of series 1 (88 µε).

The original uncracked and cracked responses (moment-curvature relationships) of a flexural specimen without considering the shrinkage are shown in Figure 4.7 (black lines). The corresponding uncracked and cracked additional curvatures due to shrinkage can be calculated according to [84]:

$$\varphi_{ucr} = \frac{A_{ucr}\Delta M_{ucr} + B_{ucr}\Delta N_{ucr}}{E_c(A_{ucr}I_{ucr} - B_{ucr}^2)} \tag{4.1}$$

$$\varphi_{cr} = \frac{A_{cr}\Delta M_{cr} + B_{cr}\Delta N_{cr}}{E_c(A_{cr}I_{cr} - B_{cr}^2)} \tag{4.2}$$

where E_c is the modulus of elasticity of concrete, A_{ucr} is the area of uncracked transformed section, and B_{ucr} and I_{ucr} are the first and second moments of inertia of the area of the uncracked transformed section, respectively. Moreover, A_{cr}, B_{cr}, and I_{cr} are the corresponding values for the cracked transformed section. Furthermore, ΔM and ΔN are the restraining moment and axial force against shrinkage.

$$\Delta N_{ucr} = -E_c\varepsilon_{sh}A_{c,ucr} \tag{4.3}$$

$$\Delta M_{ucr} = E_c\varepsilon_{sh}B_{c,ucr} \tag{4.4}$$

$$\Delta N_{cr} = -E_c\varepsilon_{sh}A_{c,cr} \tag{4.5}$$

$$\Delta M_{cr} = E_c\varepsilon_{sh}B_{c,cr} \tag{4.6}$$

where ε_{sh} is the shrinkage in concrete and A_c and B_c are the area of concrete and the first moment of inertia of the area of concrete (ignoring steel as shrinkage takes place only in concrete).

To account for the effect of shrinkage, these uncracked (φ_{ucr}) and cracked (φ_{cr}) additional curvatures are applied, so that the black dash lines in Figure 4.7 are shifted to the right (red dash lines). To find the additional moment due to shrinkage (ΔM_{sh}), the intersection point between red dash lines is obtained (point B). This means that if shrinkage of the flexural element is accounted for, point B should be the origin of the moment-curvature response. Hence, a reduction in the cracking moment equal to ΔM_{sh} should be applied (moving from black solid line to red solid line in Figure 4.7). Then, point A should be shifted to the origin of the absolute

coordinate system (moving from the red solid line to the blue solid line in Figure 4.7). Finally, the blue solid line is the final moment-curvature response of the beam when shrinkage effects are considered. It can be observed that if shrinkage is accounted for, the cracking moment reduces from M_{cr} to $M_{cr,sh}$ and additional deflections appear due to an extra curvature.
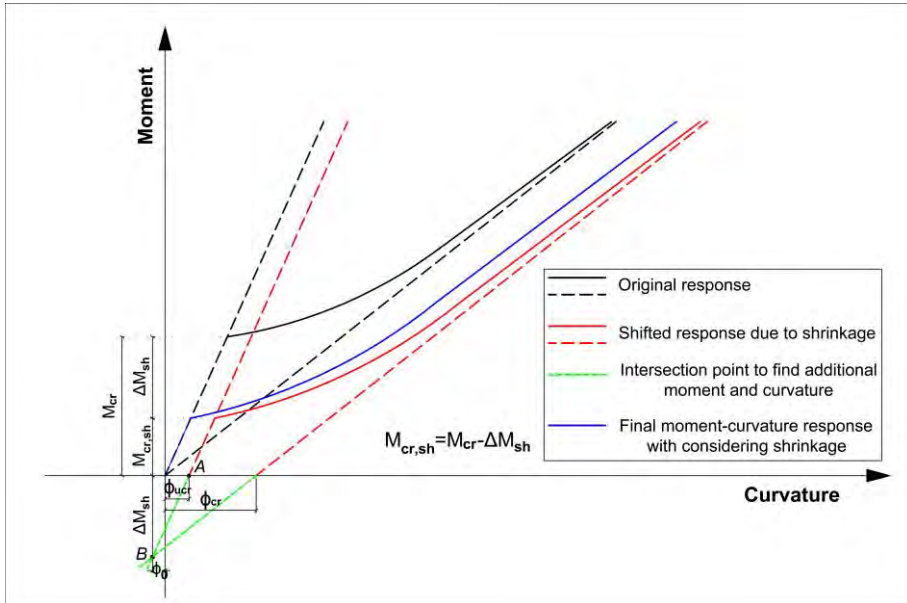
Figure 4.7. Flexural response of beam with and without shrinkage.

Representative comparisons between the analytical predictions of load-deflection curves for beams (both unstrengthened and strengthened) of the present work, with and without considering the effect of shrinkage are presented in Figure 4.8. A larger difference between the two predictions exists for those beams of series 2, as expected.
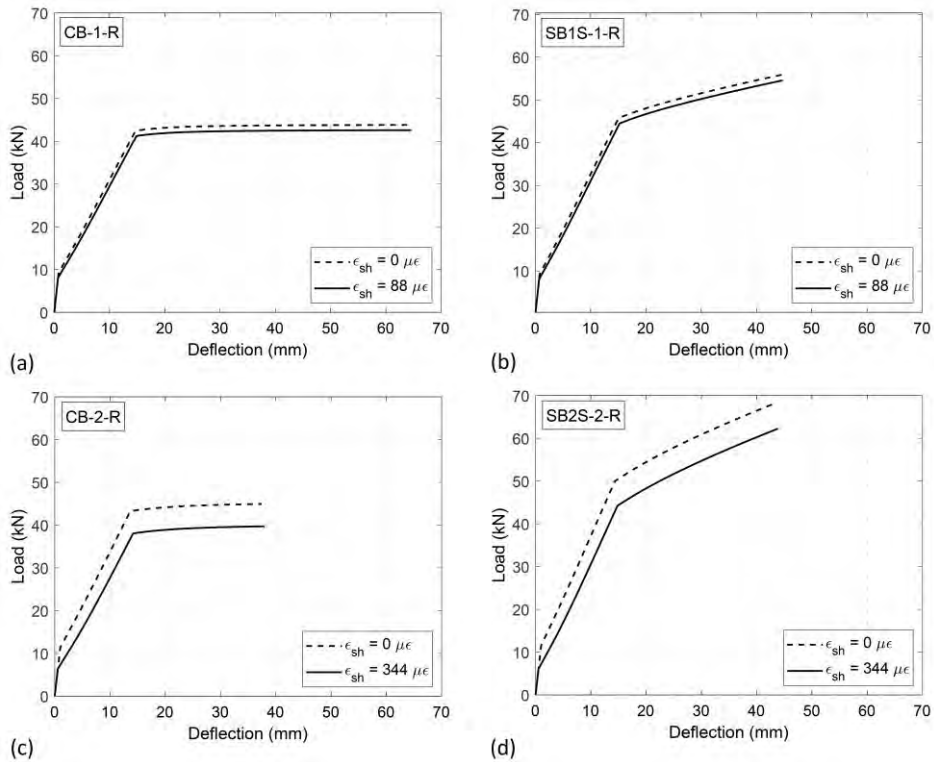
Figure 4.8. Analytical predictions of load-deflection curves with and without accounting for the shrinkage effect for specimens: (a) CB-1-R, (b) SB1S-1-R, (c) CB-2-R and (d) SB2S-2-R.

4.3.2 Load–Deflection Curves

The experimental load versus midspan deflection of the specimens of the present work is presented in Figure 4.9. As a general description, an initial linear behavior is observed that represents the elastic behavior of the flexural element. Once the cracking load is attained, the stiffness of the system decreases, and the load can be further increased until the yielding load; after this yielding load, the stiffness drops dramatically. From the yielding point onwards, no considerable increase in the ultimate capacity of control RC beams (unstrengthened) is found, whilst the ultimate capacity of strengthened beams is increased. In this sense, with the increase in the strengthening level (i.e., CFRP ratio), a slight increase of the cracking load was observed (see Table 4.3). In the strengthened specimens, the stiffness of load-deflection curves was relatively higher than in the RC beams, as expected. Moreover, the yielding (P_y) and ultimate (P_u) loads of the strengthened specimens were accordingly increased, irrespective of the applied temperature (see Figure 4.9).
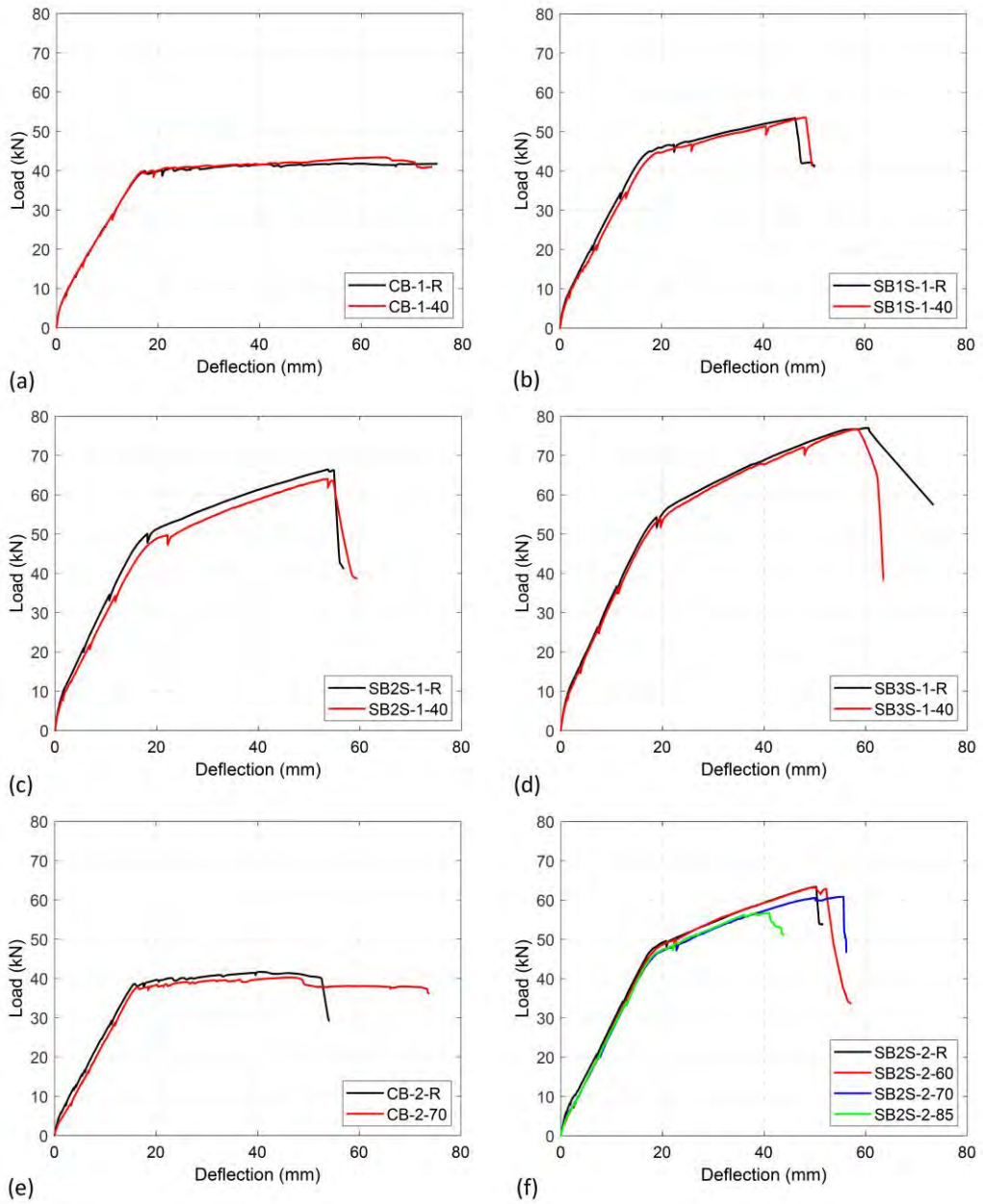
Figure 4.9. Effect of temperature on the experimental load–deflection curves of specimens: (a) CB-1, (b) SB1S-1, (c) SB2S-1, (d) SB3S-1, (e) CB-2 and (f) SB2S-2.

Table 4.3. Experimental results and analytical predictions.

Beam ID	Cracking load, P_{cr} (kN)		Yielding load, P_y (kN)		Ultimate load, P_u (kN)		Ultimate FRP strain, $\varepsilon_{u,FRP}$ (mm/mm)	Failure mode[1]	
	Exp.	Analyt.	Exp.	Analyt.	Exp.	Analyt.	Exp.	Exp.	Analyt.
CB-1-R	6.53	7.98	39.90	41.29	41.87	42.59	-	CC	CC
CB-1-40	5.51	7.48	39.68	41.07	43.39	42.23	-	CC	CC
SB1S-1-R	7.11	7.97	44.90	44.68	53.44	54.57	0.0139	FR	FR
SB1S-1-40	6.07	7.47	44.69	44.36	53.63	54.39	0.0142	FR	FR
SB2S-1-R	7.21	7.96	49.40	47.90	66.50	65.04	0.0132	FR	FR
SB2S-1-40	6.12	7.46	49.27	47.68	64.06	64.19	0.0134	FR	FR
SB3S-1-R	7.56	7.95	56.80	51.29	77.04	74.74	0.0127	FR	FR
SB3S-1-40	6.41	7.45	55.60	51.03	76.77	73.39	0.0124	FR	FR
CB-2-R	3.69	6.17	38.59	38.12	41.71	39.72	-	CC	CC
CB-2-70	2.12	4.66	37.76	37.64	40.26	39.14	-	CC	CC
SB2S-2-R	4.79	5.67	48.21	44.51	63.36	62.27	0.0131	FR	FR
SB2S-2-60	2.09	4.45	47.88	43.99	63.39	59.35	0.0119	FR	FR
SB2S-2-70	1.82	4.15	46.70	43.80	60.86	56.21	0.0103	ED	FR
SB2S-2-85	1.68	3.69	46.47	43.70	56.72	55.24	-[2]	CC	FR

[1] Failure modes. CC: concrete crushing after steel yielding; FR: FRP rupture; ED: end debonding.

[2] strain gauge failed during the loading

According to Figure 4.9, small differences can be observed between the load-deflection curves of specimens in series 1 when the temperature was increased from 20 °C to 40 °C. In this sense, the application of 40 °C derived in a slight reduction of the stiffness in load–deflection curves, which is in accordance with results presented in [36,57,58]. This reduction in stiffness was followed by a slight decrease in the ultimate capacity of the beams. In series 2, the application of a temperature that is approaching and even exceeding the epoxy T_g (i.e., 60 °C to 85 °C) generated a small reduction in the stiffness of the specimens. Moreover, the ultimate capacity of the beams in this series decreased by 3.48%, 3.95%, and 10.45% for CB-2-70, SB2S-2-70, and SB2S-2-85, respectively. No change was observed in SB2S-2-60 specimen. In unstrengthened beams, the increase in the temperature derived in a reduction of the cracking load and stiffness of system (see Figure 4.10). This reduction has been also observed in strengthened beams, where the increase in the temperature (near or beyond T_g) was followed

by bond decrease and, subsequently, the efficiency of strengthening system was slightly reduced, thus making beams more susceptible to premature debonding.

(a)   (b)
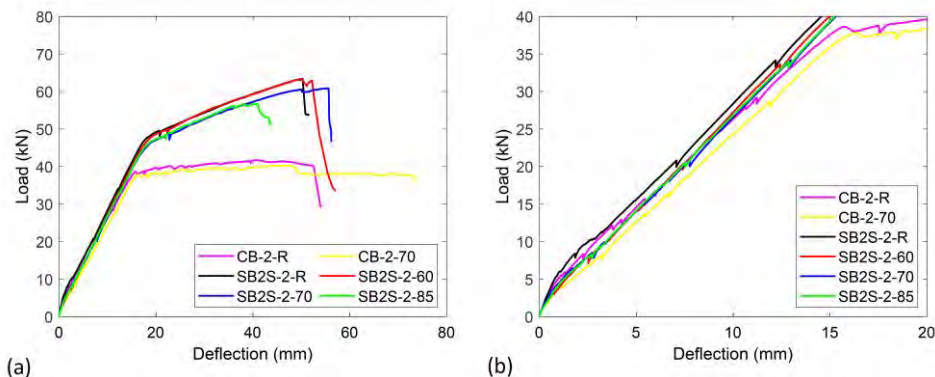
Figure 4.10. Effect of temperature on the experimental load–deflection curves of series 2 of specimens: (a) Total view and (b) Zoom in view.

Experimental results in terms of cracking load (P_{cr}), yielding load (P_y), ultimate load (P_u), ultimate CFRP strain ($\varepsilon_{u,FRP}$), and failure modes are presented and compared to analytical predictions in Table 4.3. For the analytical predictions, the effect of temperature on normal weight concrete properties is considered following the equations proposed in *fib* Model Code 2010 [83], which is said to be valid for temperatures ranging approximately from 0 °C to 80 °C:

$$f_c(T) = f_c(1.06 - 0.003T)$$
(4.7)

$$f_t(T) = f_t(1.06 - 0.003T)$$
(4.8)

$$E_c(T) = E_c(1.06 - 0.003T)$$
(4.9)

where $f_c(T)$, $f_t(T)$, and $E_c(T)$ are the compressive strength, the tensile strength, and the modulus of elasticity of concrete at temperature T (in °C), respectively. Moreover, f_c, f_t, and E_c are the compressive strength, the tensile strength, and the modulus of elasticity of concrete at T = 20 °C, respectively.

The mechanical properties of steel reinforcement and CFRP strips were not modified to include any effect of temperature because they are not sensitive to this range of temperatures [164,165,170,180]. For CFRP material, the ultimate strain (stress) value obtained from experimental results was used in analytical predictions.

To complement the comparison between experimental results and analytical predictions presented in Table 4.3, experimental and analytical load-deflection curves are compared in Figure 4.11. According to the figure, good agreement between experimental results and analytical predictions can be observed in terms of the cracking load, yielding load (and their

76

corresponding deflections), and stiffness of the system before and after cracking load and after yielding load, thus meaning that shrinkage and temperature were correctly accounted for in the analytical work. However, it should be noted that some differences exist between experimental and analytical ultimate load and deflections.
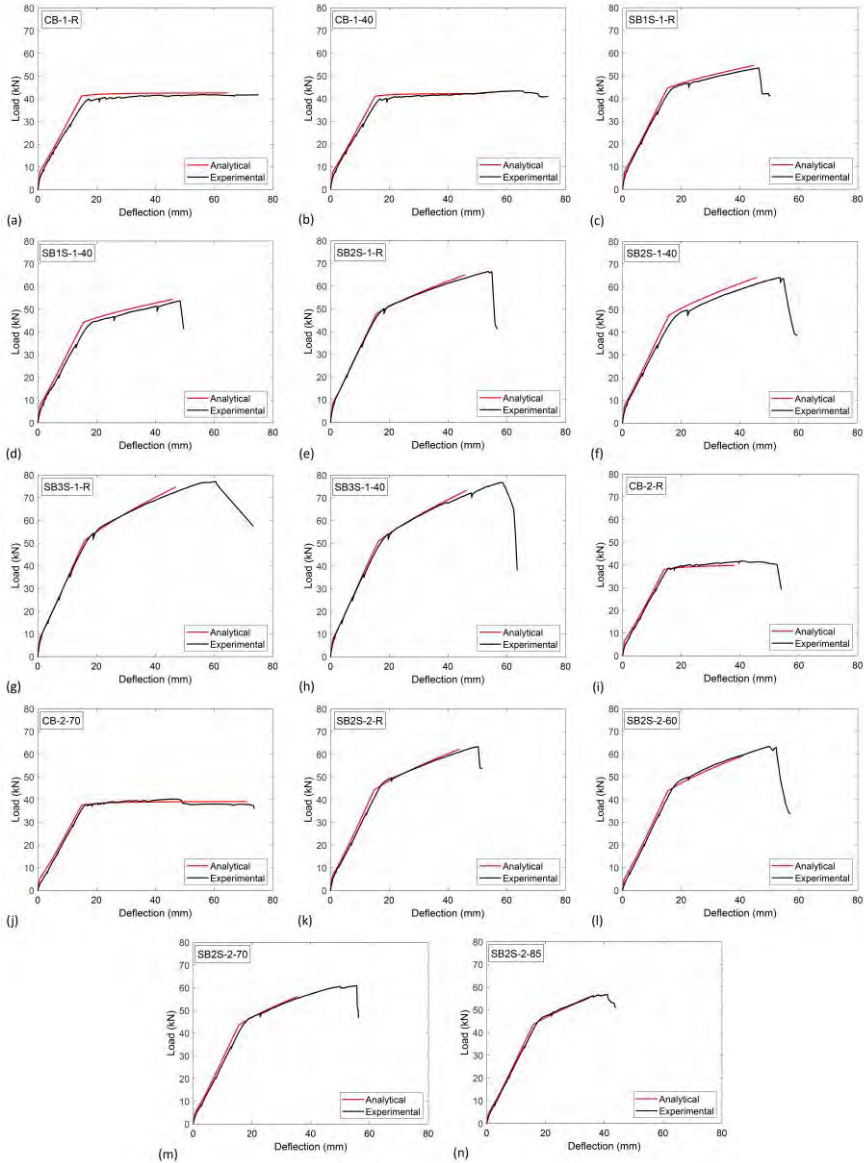
Figure 4.11. Comparison between experimental and analytical predictions on load-deflection curves of specimens: (a) CB-1-R, (b) CB-1-40, (c) SB1S-1-R, (d) SB1S-1-40, (e) SB2S-1-R, (f) SB2S-1-40, (g) SB3S-1-R, (h) SB3S-1-40, (i) CB-2-R, (j) CB-2-70, (k) SB2S-2-R, (l) SB2S-2-60, (m) SB2S-2-70 and (n) SB2S-2-85.

4.3.3 Failure Mode

According to Table 4.3, control unstrengthened beams of both series (i.e., CB-1 and CB-2, at different temperatures) failed by concrete crushing in the compression zone of the beam after steel yielding. On the other hand, FRP rupture (after yielding of steel reinforcement) was the failure mode of all strengthened beams of series 1. This means that with the application of 40 °C, the anchorage length of the CFRP strips was long enough to avoid FRP debonding failure, and the effect of the application of temperatures within this range is negligible. In series 2 of specimens, the application of 60 °C (i.e., specimen SB2S-2-60) resulted in FRP rupture failure mode, while the application of 70 °C (i.e., specimen SB2S-2-70) lead to failure by CFRP end debonding. To conclude, in specimen SB2S-2-85 (i.e., application of 85 °C), concrete was initially crushed in the compression zone of the section and, as a result, the load suddenly dropped without end debonding. This unexpected behavior can be due to a change in concrete mechanical properties, FRP, and epoxy at high service temperatures. As a general comment regarding the failure mechanism of the specimens, the increase in the temperature may be followed by a reduction of the efficiency of the strengthening system and, subsequently, it can lead to changes in the failure mechanism of the system (changing from FRP rupture to FRP debonding or even concrete crushing). Representative images of experienced failure modes are shown in Figure 4.12. It should be noted that in those cases where FRP rupture took place, it was subsequently followed by the detachment of the concrete around the FRP laminate.

Figure 4.12. Experimental failure modes.

As previously mentioned, *fib* Bulletin 90 [1] recommends limiting the maximum temperature to avoid premature failure in EBR-strengthened systems. According to experimental observations, as long as the temperature is sufficiently lower than T_g, no premature failure was observed. On the contrary, the application of a temperature exceeding the T_g resulted in end

debonding failure mode (i.e., specimen SB2S-2-70). It should be noted that no premature failure (i.e., end debonding) occurred when temperature in the range of T_g was applied (T = 60 °C), thus showing a good performance related to end debonding for the NSM strengthening system. Nevertheless, it must be noted that additional experimental work is needed to confirm the findings of the experimental program presented in this communication.

4.3.4 Strain Distribution along the CFRP Strip

The distribution of strains along the CFRP strips can give useful information about the bond behavior (i.e., the force distribution between the CFRP and concrete interface) and its influence on cracking phenomena. Instrumentation with strain gauges presented in Figure 4.3b allowed the register of strains at several sections along the CFRP strip in SB1S-1-R and SB1S-1-40 specimens. Experimental strain distributions along half of the CFRP laminate of these specimens are plotted at different levels of load in Figure 4.13. Experimental results show that the increase in temperature was followed by an increase of strains in the strip. In addition, in both specimens, the strain in the CFRP strip increased dramatically after yielding of the longitudinal steel reinforcement. The available fluctuation in the strain distributions may be related to the appearance and opening of new cracks.
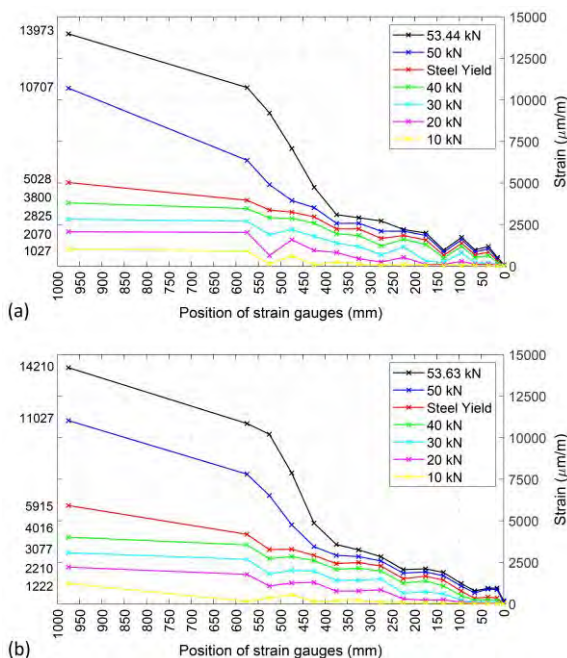
Figure 4.13. Strain distributions along one half of the CFRP strip at different levels of load for specimens: (a) SB1S-1-R and (b) SB1S-1-40.

4.4 Finite Element Analysis

Nonlinear finite element (FE) analysis of control and CFRP-strengthened beams subjected to four-pointed loads was carried out to compare with the results obtained from the experimental work. A three dimensional FE model was created using the well-known commercial FE program ABAQUS [181].

4.4.1 Description of FE Model

FE models include concrete, steel reinforcements (longitudinal and stirrups), CFRP strips, and epoxy. Concrete and epoxy are modeled by an eight-node linear hexahedral solid element with reduced integration (C3D8R), steel reinforcements are modeled by a two-node linear 3D truss element (T3D2), and FRP strips are modeled by a two-node linear beam (B31). A mesh convergence analysis was performed to select the optimum mesh sizes for different parts involved in the FE model. In this study, it was observed that the meshing refinement was not sensitive after having the maximum mesh size of 25 mm for all elements except epoxy that had 10 mm mesh size. By taking advantage of symmetry in two perpendicular planes, only a quarter of the beam was modeled. Boundary conditions of the experimental test set-up were considered. Finite element mesh along with the boundary conditions is shown in Figure 4.14.

Figure 4.14. Finite element mesh of simulated beam (one quarter).

Considering perfect bond, steel reinforcements and CFRP strips are embedded inside the concrete and epoxy, respectively. In order to address this condition, the embedded region function of ABAQUS is used. Moreover, the tie constraint function is assumed to simulate the interaction in the interface between epoxy and concrete. The selection of these interfacial behaviors is based on the fact that the bond was good enough and bond failure took place only in one of the beams of the present experimental program (i.e., specimen SB2S-2-70). As a result of this, specimen SB2S-2-70 is not included in the numerical simulations.

Similar to the case of analytical predictions presented in Section 4.3.1, the effect of shrinkage is also addressed in the numerical simulations. To this end, an initial extra deflection due to shrinkage (calculated following Section 4.3.1) is applied to the middle of the beam in a separate step. Afterwards, the main flexural load is applied in a displacement control mode through a rigid plate to avoid any extra deformation along the loading.

4.4.2   Materials Definition

Steel reinforcement is modeled as an isotropic bilinear elasto-plastic material, while epoxy is modeled as isotropic linear elastic material and CFRP is modeled as brittle material (with ultimate strain value obtained from experimental results). Moreover, to simulate the inelastic behavior of concrete, concrete damage plasticity (CDP) is used. This continuum, plasticity-based, damage model for concrete is applicable to different loading conditions and can be utilized for concrete with embedded reinforcement [181]. This model assumes that the two main failure mechanisms are tensile cracking and compressive crushing. Therefore, the evolution of the failure surface is controlled by two hardening variables linked to the failure mechanisms under tension and compression loading. The required material parameters for the definition of the CDP model are dilation angle (ψ), flow potential eccentricity (ϵ), the ratio of the biaxial compressive stress to the uniaxial compressive stress (σ_{b0}/σ_{c0}), the ratio of the second stress invariant on the tensile meridian to that on the compressive meridian (K_c), and viscosity (μ). In this numerical study, these parameters are considered as $\psi = 36°$, $\epsilon = 0.1$, $\sigma_{b0}/\sigma_{c0} = 1.16$, $K_c = 0.67$, and $\mu = 0.0005$.

The concrete stress-strain compression relationship is modeled according to Eurocode 2 [155]. Moreover, the tensile post-cracking behavior of concrete is modeled according to Torres et al. [182], where α_1 and α_2 are two dimensionless coefficients that define the tensile post-cracking stress-strain relationship of concrete (see Figure 4.15). In this study, based on the loading condition, α_1 was assumed to be equal to 0.4 and based on section properties, α_2 was assumed to be in the range of 13 to 15.
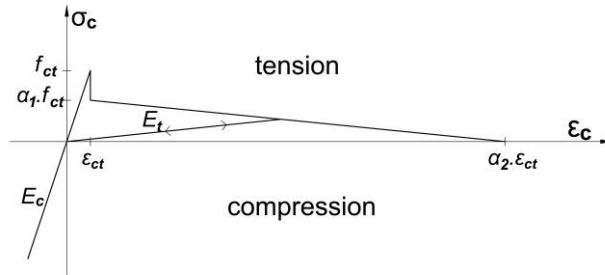
Figure 4.15. Equivalent stress-strain relationship for tensioned concrete [182].

The effect of temperature is applied directly in the definition of materials' properties, following the same strategy as in the analytical work (see Section 4.3.2). The effect of temperature on epoxy material is considered according to the experimental results presented in [8]. This assumption is based on the fact that the possible effect of the heating process, taking place before the main flexural test, is not included in the experimental load-deflection responses obtained in the laboratory (i.e., the system is zeroed before testing).

4.4.3   FE Results

The comparison between numerical predictions and experimental results is presented in Figure 4.16 and Table 4.4. In all cases, the FE model reasonably predicts the experimental behavior of beams under flexural load. Slightly higher initial stiffness is observed in the numerical simulation when compared to experimental curves, with a mean difference in deflections of 7.15% observed at the service load level [1]. In terms of yielding and ultimate loads, differences of only 3% and 2.9% are observed, respectively, with the same failure mode in both experimental work and numerical simulations. In this sense, it should be highlighted that concrete crushing was the predicted failure mode in the numerical simulation of specimen SB2S-2-85, which coincides with experimental observation. This would confirm that the negative effect of temperature on the mechanical properties of concrete and epoxy leads to an unexpected concrete crushing failure mode.

Table 4.4. Comparison between numerical predictions and experimental results.

Beam ID	Service load (kN)	Deflection at service load, d_{ser} (mm)		Diff. (%)	Yielding load, P_y (kN)		Diff. (%)	Ultimate load, P_u (kN)		Diff. (%)	Failure mode[1]	
		Exp.	Numeric.		Exp.	Numeric.		Exp.	Numeric.		Exp.	Numeric.
CB-1-R	20.57	7.04	5.99	14.91	39.90	39.15	1.88	41.87	41.22	1.55	CC	CC
CB-1-40	19.82	6.65	6.07	8.72	39.68	39.11	1.44	43.39	40.75	6.08	CC	CC
SB1S-1-R	21.37	6.70	5.93	11.49	44.90	43.39	3.36	53.44	55.86	4.53	FR	FR
SB1S-1-40	20.59	7.01	5.94	15.26	44.69	43.18	3.38	53.63	53.73	0.19	FR	FR
SB2S-1-R	22.12	6.10	5.82	4.59	49.40	49.99	1.19	66.50	68.20	2.56	FR	FR
SB2S-1-40	21.32	6.60	5.78	12.42	49.27	48.83	0.89	64.06	66.07	3.14	FR	FR
SB3S-1-R	22.85	6.02	5.67	5.81	56.80	54.11	4.74	77.04	78.77	2.25	FR	FR
SB3S-1-40	22.01	5.97	5.51	7.71	55.60	53.76	3.31	76.77	74.38	3.11	FR	FR
CB-2-R	26.28	9.98	9.99	0.10	38.59	36.95	4.25	41.71	40.78	2.23	CC	CC
CB-2-70	24.64	10.20	10.05	1.47	37.76	36.38	3.65	40.26	39.60	1.64	CC	CC
SB2S-2-R	29.20	10.31	9.55	7.37	48.21	47.49	1.49	63.36	64.24	1.39	FR	FR
SB2S-2-60	27.04	9.94	9.65	2.92	47.88	45.71	4.53	63.39	58.72	7.37	FR	FR
SB2S-2-85	25.63	9.52	9.51	0.11	46.47	44.34	4.58	56.72	55.55	2.06	CC	CC
		Mean diff. (%)		7.15	Mean diff. (%)		2.98	Mean diff. (%)		2.93		

[1] Failure modes. CC: concrete crushing after steel yielding; FR: FRP rupture.

Figure 4.16. Comparison between experimental and numerical work of specimens: (a) CB-1-R, (b) CB-1-40, (c) SB1S-1-R, (d) SB1S-1-40, (e) SB2S-1-R, (f) SB2S-1-40, (g) SB3S-1-R, (h) SB3S-1-40; (i) CB-2-R, (j) CB-2-70, (k) SB2S-2-R, (l) SB2S-2-60 and (m) SB2S-2-85.

4.5 Conclusions

In the present work, an experimental program to study the influence of high service temperature on the flexural performance of NSM CFRP-strengthened RC beams is presented. The experimental results are compared to analytical and numerical predictions. Based on the data presented, the following conclusions can be drawn:

- No considerable differences can be observed in the load-deflection curve when specimens are subjected to 40 °C (i.e., series 1). This behavior can be attributed to 40 °C being far below the T_g of the epoxy resin.

- In series 2, as a result of the increase in temperature near or beyond the T_g, the stiffness and the ultimate load of strengthened and unstrengthened specimens decreased. The interface bond capacity between epoxy and concrete could have been affected, and the efficiency of the strengthening system showed some reduction, thus making the beam to be more prone to experience end deboning failure.

- In both series of specimens, the failure mode of the control unstrengthened beams was concrete crushing after steel yielding. For the strengthened beams under 20 °C, 40 °C, and 60 °C, the failure mode was FRP rupture. With the increase of temperature up to 70 °C, the beam failed by end debonding. Finally, specimens under 85 °C experienced concrete crushing and, as a result, the load suddenly dropped without giving place to end debonding. This failure mode can be attributed to the reduction in mechanical properties of concrete and epoxy when submitted to higher temperature.

- No end debonding or significant reduction in ultimate load occurred for specimens being tested up to 60 °C, thus showing a good performance of the NSM strengthening system.

- The application of temperature exceeding the epoxy T_g generated a small reduction in the stiffness of the specimen and a decrease by 3.48%, 3.95%, and 10.45% in the ultimate capacity of beams CB-2-70, SB2S-2-70, and SB2S-2-85, respectively.

- The effect of temperature on the experimental bond behavior of specimen at 40 °C was studied in one of the strengthened beams (i.e., SB1S-1 specimens). With the increase in the temperature, strains (and stresses) in the CFRP strip increased.

- A systematic procedure was applied to consider the effect of shrinkage in short-term response of the specimens. It was observed that the increase in the concrete shrinkage resulted in a reduction of the elements' stiffness and cracking load. Good agreement was observed between analytical predictions and experimental results.

- A simple but trustable FE model accounting for initial shrinkage and effects of temperature was created to be compared with experimental work. In all cases, numerical models correctly predict the experimental load–deflection responses and failure modes.

5 Paper B: Influence of curing, post-curing and testing temperatures on mechanical properties of a structural adhesive

Younes Jahani[1]*, Marta Baena[1], Cristina Barris[1], Ricardo Perera[2] and Lluís Torres[1]

[1]AMADE, Polytechnic School, University of Girona, 17003, Girona, Spain

[2]Department of Mechanical Engineering, Technical University of Madrid, 28006 Madrid, Spain

*Corresponding author

Influence of curing, post-curing and testing temperatures on mechanical properties of a structural adhesive

Younes Jahani [a,*], Marta Baena [a], Cristina Barris [a], Ricardo Perera [b], Lluís Torres [a]

[a] AMADE, Polytechnic School, University of Girona, 17003 Girona, Spain
[b] Department of Mechanical Engineering, Technical University of Madrid, 28006 Madrid, Spain

Abstract

Structural cold-curing adhesives are widely used to strengthen reinforced concrete (RC) structures with fiber reinforced polymers (FRPs). The performance of these adhesives, and therefore the performance of the strengthening system, may be affected by temperature, as ambient-cured structural adhesives usually have low glass transition temperature (T_g). This paper presents a comprehensive experimental investigation on the influence of temperature on mechanical properties and T_g of a structural epoxy adhesive. The experimental program was divided in four groups of specimens. In Group 1, the effect of curing and post-curing temperature on T_g of the epoxy adhesive was investigated. In Groups 2-4, the effects of testing temperature, curing temperature and post-curing temperature, respectively, on adhesive mechanical properties were studied. Experimental results confirm that curing and post-curing temperature affected T_g differently depending whether the applied temperature was below or beyond the epoxy T_g. Similar behavior was observed in the mechanical properties of the epoxy, as they showed improvements when curing process (curing and post-curing) temperature was below T_g and they were negatively affected when curing process temperature was beyond T_g. Besides, tensile and compressive mechanical properties were negatively affected by testing temperatures beyond 20 °C.

Keywords: Epoxy adhesive, Temperature, Curing, Post-curing, T_g, Mechanical properties

5.1   Introduction

Structural epoxy adhesives are widely used to bond fiber-reinforced polymers (FRPs) to concrete in both externally bonded reinforcement (EBR) and near-surface mounted (NSM) strengthening techniques [5,30]. The performance of the strengthened structure will depend

on the bonded joint, whose behavior has been acknowledged to be partially governed by the mechanical properties of the adhesive [154,183,184].

In civil engineering applications adhesive joint is typically cured at ambient temperature. Accordingly, cold-curing adhesives are the most widely used, as its use is easier and they present good mechanical properties after the required curing time (which depends on the curing agent and temperature). It is a feature of commonly used ambient-cured structural adhesives to have glass transition temperatures (T_g) ranging between 40 °C to 70 °C [185]. Being T_g defined as the temperature range where a thermosetting polymer changes from a glassy to a rubbery state, (i.e. the temperature ranges over which the mobility of the polymer chains increases significantly) [149], these relatively low values of T_g can be a limiting factor because these adhesives can exhibit substantial changes in their mechanical properties if working temperature approaches its T_g [7,8,186-190]. As a consequence of the reduction in the adhesion strength of the epoxy as the T_g range is approached, a reduction in the stiffness and ultimate capacity of the FRP-strengthened element can take place and the failure mode can change [36,57,58,171,186,191].

A reduced number of studies have investigated the influence of testing temperature on the mechanical properties of cold-curing epoxy adhesive typically used in civil engineering [7,8,36,57,58,171,187-192]. Firmo et al. [8] presented an experimental work to assess the mechanical properties of a commercial epoxy adhesive typically used in civil engineering at different temperatures (from 20 °C to 120 °C). The results showed that mechanical properties were significantly affected by testing temperatures larger than T_g (T_g=47 °C), as the shear and the tensile strength of epoxy were reduced to around 30% of their corresponding ambient strengths. Additionally, the shear and the tensile modulus were almost negligible for tests at 50 °C. These results are similar to those obtained in other studies on epoxy adhesives with larger T_g values used in other applications, such as aerospace industry [187-189]. As an example, Banea et al. [187,188] investigated the effect of testing temperature on the mechanical properties of an epoxy adhesive having a T_g value equal to 150 °C. In these studies, four different temperatures were applied during testing (i.e. room temperature, 100, 150 and 200 °C), and experimental results showed a reduction in the tensile strength and an increase in the ductility when testing temperature was increased. The maximum reduction was observed for testing temperatures near to and beyond T_g, where the adhesive was in rubbery state. Similarly, Wu [189] studied the influence of testing temperature on mechanical properties of an epoxy whose

T_g equals 177 °C. According to their experimental results, increasing the testing temperature produced a decrease in both the tensile strength and the elastic modulus. It should be noted that the rate of loss of the mechanical properties was sharply increased for testing temperature beyond T_g. Besides, Reis [190] presented a comparative study on the effect of testing temperature (ranging from 23 °C to 90 °C) on compressive strength of epoxy polymer mortar and unsaturated polyester mortar (mixture of a quartz foundry sand with the thermoset resin binder). Although both materials experienced a decrease in their mechanical properties when testing temperature was increased, epoxy polymer mortars were more sensitive to temperature changes than unsaturated polyester mortars. This temperature dependency was related to the T_g of the resins used.

In addition to testing temperature, curing and post-curing procedures can also affect the structural performance of an epoxy adhesive, in terms of the value of T_g and the epoxy mechanical properties [150,193-201]. Michels et al. [150] studied the effect of different curing conditions and mixing processes on mechanical properties of three different epoxy adhesives. Specimens exposed to accelerated curing (consisting in exposing the epoxy specimens to an elevated temperature, 90 °C, for a period of 25 minutes just after casting) showed higher porosity, which appeared to be the cause of their apparent lower tensile properties. The higher porosity can be attributed to a faster development of strength and stiffness, that finally affects to the cross-linking process, thus showing the influence of the cure-kinetics. Mixing the epoxy under vacuum reduced the porosity of both specimens (with and without accelerated curing) leading to higher tensile properties. Similar results were obtained in Cruz et al. [193]. It has been shown in the literature that longer curing times are needed for lower curing temperatures. This effect, which is of high importance in cold-curing epoxy adhesives, is a consequence of the vitrification of the network that takes place when the resin is cured at a temperature below the ultimate glass transition of the completely cross-linked resin. As a result, the resin is in a glassy but uncured state, so that cross-linking reaction has slowed down dramatically and it may take a long time before the ultimate properties of the adhesives are reached. This dependency was confirmed for cold-curing epoxy adhesives in Lapique and Redford [194] and Moussa et al. [195]. For the case of Lapique and Redford [194], they obtained same mechanical properties with 4 hours curing at 64 °C and 28 days curing at room temperature. For the case of Moussa et al. [195], epoxy cured at low temperatures of 5 °C to 10 °C required a 3-days curing period for attaining the full curing, whereas few hours (3.7 h to 1.6 h) were needed for curing temperatures

in the range of 35 °C to 60 °C. Lahouar et al [196] investigated the evolution of epoxy T_g under four different curing temperatures (i.e. 20 °C, 50 °C, 82 °C and 108 °C). According to their results on DSC tests, the T_g increased gradually by increasing the curing temperature. However, this increase in T_g had an upper bound value, as curing beyond 82 °C had no effect on T_g. This upper bound value corresponds to the glass transition temperature of the fully cured network ($T_{g\infty}$), at which the resin reaches its maximum degree of cross-linking. The existence of a T_g upper bound value ($T_{g\infty}$) was also confirmed in a study from Carbas et al. [197], who studied the effect of the curing temperature on the mechanical properties and T_g of three different structural epoxy adhesives. For each adhesive, samples of the bulk adhesive were cured at various temperatures and T_g was measured by a dynamic mechanical analysis using an in-house developed apparatus. It should be mentioned that the main concern of the applied method is related to thermodynamics and the existence of a temperature gradient in the adhesive. Therefore, the speed of the test should be a compromise value that ensures a homogeneous temperature distribution in the specimen and avoids causing a post-curing in the specimen. Once T_g was determined at various curing temperatures, $T_{g\infty}$ could be determined. In addition to the determination of the $T_{g\infty}$ values for the three adhesives, results of their experimental program confirmed that, as far as the curing temperature was below $T_{g\infty}$, any increase in the curing temperature derived in an increase in the mechanical properties and T_g. On the contrary, for curing temperatures above $T_{g\infty}$, the mechanical properties and T_g decreased. Although these findings are in agreement with [198-200], it should be mentioned that T_g is a kinetic parameter that depends on the heating rate and on the measurement conditions [197]. Experimental work presented in [197] was complemented with a second program presented in Carbas et al. [201], where the effect of post-curing was analyzed. Post-curing process can be of high importance for the case of cold-curing epoxy adhesives. It may be the case that an un-complete cure in the epoxy resin exists because of the longer curing time needed, especially if they are cured at ambient temperature. In this case, the reactivation of the cross-linking process of the epoxy can take place if a post-curing process is applied. In this sense, experimental results presented in [201] showed that the effect of post-curing at temperature below $T_{g\infty}$ depended on whether the cross-linking process was complete or not. Finally, post-curing above $T_{g\infty}$ produced thermal degradation that caused a progressive decrease in mechanical properties and T_g. According to the literature [9,149,150,194,196,197,202], cross-linking plays an important role in the mechanical performance of an epoxy. In this sense, results presented in Michel and Ferrier [149]

confirmed that cross-linking of an epoxy resin is found to be an irreversible process, so that larger T_g values are obtained when curing at higher temperatures and its value does not change when the polymer is exposed back to a lower temperature. Similar results were obtained in [150].

This paper presents part of a larger experimental program on the flexural behavior of NSM FRP-strengthened Reinforced Concrete (RC) beams tested at different temperatures. Specifically, the main objective of this paper is the assessment of a commercial structural epoxy adhesive commonly used for RC strengthening and retrofitting with FRP materials. To this end, a comprehensive experimental program was performed to evaluate the influence of the temperature on mechanical properties (namely the uniaxial tensile strength ($f_{u,epoxy}$), the tensile elastic modulus (E_{epoxy}), the uniaxial ultimate compressive load ($F_{cu,epoxy}$), the uniaxial compressive strength ($\sigma_{cu,epoxy}$)) and T_g of a structural epoxy adhesive. Different curing temperatures, post-curing temperatures and testing temperatures have been considered. The experimental program is described and the main results are presented and discussed.

5.2 Experimental program

5.2.1 Material

The adhesive used in this study is a high performance, solvent-free, thixotropic, and grey two-component epoxy adhesive specially developed for bonding carbon FRP (CFRP) on concrete, that is traded under the commercial name of *S&P 220 HP*. According to the manufacturer's product data sheet [143], the components A (Bisphenol A and Bisphenol F based resin) and component B (hardener, with a mixture of amines) should be mixed at a ratio of 2:1 by weight, and the suggested curing duration is 7 days. Furthermore, the nominal elastic modulus, compressive strength and T_g of epoxy declared by the manufacturer are 7.1 GPa, 81 MPa and 58.2 °C, respectively. The mixture of epoxy adhesive is shown in Figure 5.1.

Figure 5.1. Epoxy adhesive mixture.

5.2.2 Specimens curing process and testing configuration

In this experimental program, 4 groups of specimens were considered. Group 1 comprised those specimens used for determining the effect of curing and post-curing temperature on T_g of the epoxy adhesive. Groups 2, 3 and 4 comprised those specimens used for evaluating the effect of testing temperature (Group 2), curing temperature (Group 3) and post-curing temperature (Group 4) on mechanical properties of the epoxy adhesive. The specimens were designated as X-Y-Z. In this designation X indicates the testing group, so that TG refers to specimens tested to determine the T_g (i.e. Group 1), TT refers to specimens tested to study the influence of testing temperature on epoxy mechanical properties (i.e. Group 2), CT refers to specimens tested to analyze the influence of curing temperature on epoxy mechanical properties (i.e. Group 3) and PT refers to specimens tested to determine the influence of post-curing temperature on epoxy mechanical properties (i.e. Group 4). In the proposed specimens' designation, Y indicates the curing process type (C for curing and PC for post-curing) for specimens of Group 1 and refers to mechanical test type (TEN for tension test and COM for compression test) for specimens of Groups 2-4. Finally, Z denotes the temperature. For example, TG-C-50, refers to a specimen that was cured at 50 °C and tested in order to determine the value of T_g (Group 1). Similarly, PT-TEN-70 refers to a specimen that was post-cured at 70 °C and tested in order to analyze the effect of post-curing temperature (Group 4) on tensile properties of the epoxy adhesive. It should be mentioned that the asterisk symbol appearing in some specimens' designation shows one extra day of post-curing. All specimens were tested at the age of 12 days. Curing and post-curing periods with target temperature different from 20 °C lasted 7 days and 1 day, respectively. Details on the curing process and testing configuration of each group are presented below and summarized in Table 5.1.

Group 1: effect of curing and post-curing temperature on T_g

This group includes a total of 5 specimens, whose curing and post-curing temperatures varied with the aim at analyzing its effect on the T_g of the epoxy adhesive. One specimen was cured at room temperature (20 °C) for 12 days as a reference sample (TG-C-20) (see black line in Figure 5.2a). Two other specimens were cured for 7 days under the target temperature (50 °C and 70 °C) to be later left 5 more days at 20 °C before testing the T_g (TG-C-50 and TG-C-70) (see blue line in Figure 5.2a). To conclude, two specimens were initially cured for 9 days at 20 °C, after which a post-curing process of one-day under the target temperature (50 °C and 70 °C) was applied, that was finally followed by a cooling-down process for 2 days at 20 °C prior to T_g testing (TG-PC-50 and TG-PC-70) (see red line in Figure 5.2a).

Group 2: effect of testing temperature on mechanical properties

This group includes a total of 48 specimens whose testing temperatures varied to evaluate its effect on epoxy adhesive mechanical properties. The specimens were cured at 20 °C for 11 days (see black line in Figure 5.2b). After this curing process, specimens were heated to the target temperature for one-day (20 °C, 40 °C, 50 °C, 60 °C, 70 °C and 85 °C) to be finally tested under tension and compression. It should be mentioned that the one-day heating process previous to testing should be considered as a one-day post-curing process. Furthermore, two additional configurations (marked with asterisk symbol) were considered where an additional one-day post-curing at the target temperature (50 °C and 70 °C) was applied (see red line in Figure 5.2b).

Group 3: effect of curing temperature on mechanical properties

This group includes a total of 30 specimens whose curing temperature varied with the aim at evaluating its effects on epoxy adhesive mechanical properties. Immediately after being cast, specimens were moved to the chamber to be cured at different target temperatures (-15 °C, 50 °C and 70 °C) for a period of 7 days. After this curing phase, specimens were left at 20 °C for 5 days before testing (see black line in Figure 5.2c). As in previous group, two additional configurations (marked with asterisk symbol) were exposed to a one-day post-curing at target temperature (50 °C and 70 °C) and cooled-down again at 20 °C (see red line in Figure 5.2c).

Group 4: effect of post-curing temperature on mechanical properties

This group includes a total of 30 specimens that were post-cured at different temperatures to evaluate its effect on epoxy adhesive mechanical properties. In this last group, the specimens

were cured at 20 °C for 9 days, to be later exposed to a one-day post-curing at different target temperatures (40 °C, 50 °C, 60 °C, 70 °C and 85 °C) and a final cooling-down at 20 °C before testing (see Figure 5.2d).
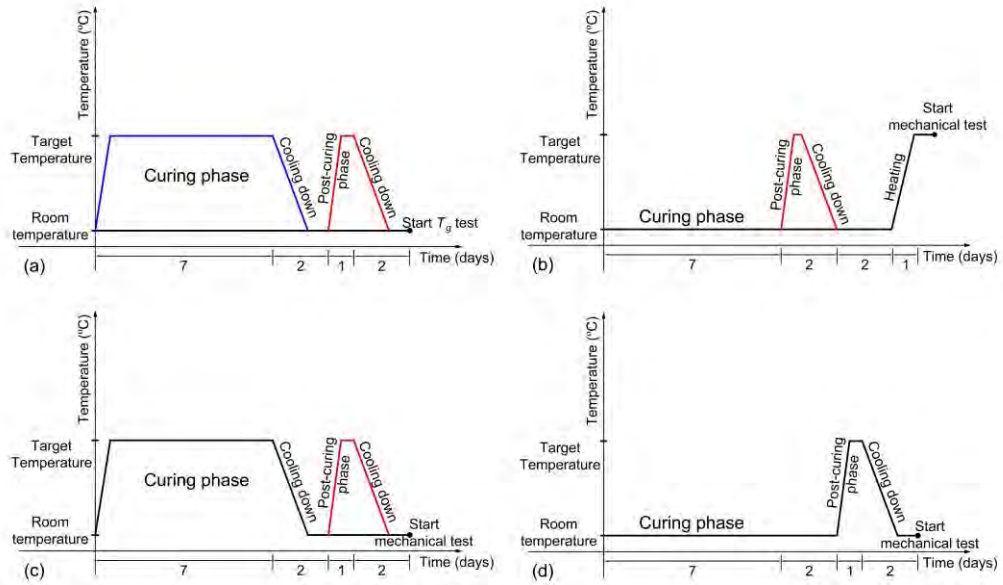
Figure 5.2. Diagram of the curing processes: (a) Group 1, (b) Group 2, (c) Group 3 and (d) Group 4.

Table 5.1. Details of the experimental program.

Group	Specimen ID	Number of specimens	Curing process	Curing process temperature (°C)	Test	Testing temperature (°C)
Group 1	TG-C-20	1	See Figure 5.2a	20	Glass transition temperature of epoxy	According to standard
	TG-C-50	1		50		
	TG-C-70	1		70		
	TG-PC-50	1		50		
	TG-PC-70	1		70		
Group 2	TT-TEN-20	3	See Figure 5.2b	20	Tensile strength and elastic modulus	20
	TT-TEN-40	3		20		40
	TT-TEN-50	3		20		50
	TT*-TEN-50	3		50		50
	TT-TEN-60	3		20		60
	TT-TEN-70	3		20		70
	TT*-TEN-70	3		70		70
	TT-TEN-85	3		20		85
	TT-COM-20	3		20	Compressive strength	20
	TT-COM-40	3		20		40
	TT-COM-50	3		20		50
	TT*-COM-50	3		50		50
	TT-COM-60	3		20		60
	TT-COM-70	3		20		70
	TT*-COM-70	3		70		70

	TT-COM-85	3		20		85
	CT-TEN-(-15)	3		-15		20
	CT-TEN-50	3		50	Tensile strength	20
	CT*-TEN-50[1]	3		50	and elastic	20
	CT-TEN-70	3		70	modulus	20
Group 3	CT*-TEN-70[2]	3	See Figure 5.2c	70		20
	CT-COM-(-15)	3		-15		20
	CT-COM-50	3		50	Compressive	20
	CT*-COM-50[1]	3		50	strength	20
	CT-COM-70	3		70		20
	CT*-COM-70[2]	3		70		20
	PT-TEN-40	3		40		20
	PT-TEN-50	3		50	Tensile strength	20
	PT-TEN-60	3		60	and elastic	20
	PT-TEN-70	3		70	modulus	20
	PT-TEN-85	3		85		20
Group 4	PT-COM-40	3	See Figure 5.2d	40		20
	PT-COM-50	3		50	Compressive	20
	PT-COM-60	3		60	strength	20
	PT-COM-70	3		70		20
	PT-COM-85	3		85		20

[1]Curing at 50 °C for 7 days and later exposed to a one-day post-curing at 50 °C.
[2]Curing at 70 °C for 7 days and later exposed to a one-day post-curing at 70 °C.

5.2.3 Test procedures

Differential scanning calorimetry test

The differential scanning calorimetry (DSC) technique [145] was used to calculate the T_g of the epoxy adhesive after different curing and post-curing conditions (Group 1 of the experimental campaign). For each curing condition, one specimen was tested. The DSC technique provides information about changes in physical, chemical, and heat capacity of the adhesive which may lead to important information about their thermal history (i.e. the temperature that epoxy undergoes), stability, processing conditions, progress of chemical reactions and possible changes in mechanical properties [145]. The dynamic DSC tests were carried out using the DSC Q2000 machine. A heating rate of 10 °C/min was applied using nitrogen as the purge gas at 50 mL/min. The temperature range was between 20 °C and 80 °C. To determine T_g, and according to ASTM E1356-08 [145], the extrapolated onset temperature (T_f) and the extrapolated end temperature (T_e) were measured. The mid-point temperature (T_m), computed as the mean between T_f and T_e, is the most commonly used as the glass transition temperature [145].

Tension test

Tensile properties of the epoxy adhesive were determined following ISO-527-1 [144] specifications. To this end, dog-bone specimens were manufactured following the geometry and dimensions shown in Figure 5.3a and tested under displacement-control at a speed of 1 mm/min. For each curing condition, three specimens were tested. The test setup is shown in Figure 5.3b. As mentioned in section 5.2.2, specimens of Group 2 were heated to the target testing temperature for a duration of 24 hours prior to testing and, once temperature was stabilized, the test was performed. To allow the curing process, a thermal chamber was mounted on the testing machine (see Figure 5.3b). Two strain gauges located at the back and front sides of the specimens and one axial extensometer with a 25 mm gauge length were used to measure the strain during the tension tests. Furthermore, two thermocouples (one to measure the environmental temperature inside the thermal chamber and the other glued on the surface of specimen) were used to measure the temperature before and during the test. In each specimen, registers of loads were transformed to stresses by using the mean cross-section area from three different measurements. The tensile elastic modulus was obtained from the

slope of axial stress-strain curve between 0.05% and 0.25% of the maximum tensile strain [144]. Details of the specimens and test setup are shown in Figure 5.3.
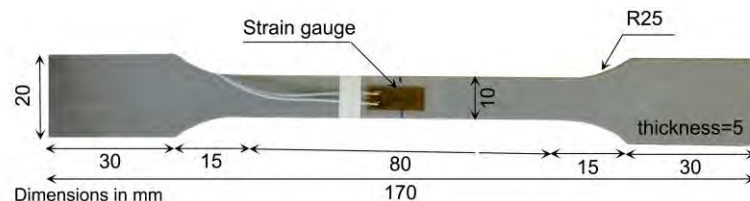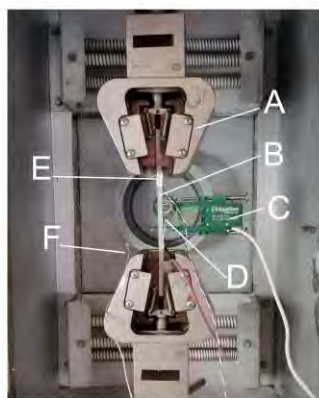
Figure 5.3. Details of the tension test: (a) Specimen dimensions and (b) Test setup inside the thermal chamber.

Compression test

The compressive strength of the epoxy adhesive was determined according to EN 196-1 [148], with the aim at following the same standard used by the epoxy manufacturer. According to EN 196-1 [148], 80 mm length prism having a 40x40 mm^2 cross-section should be used for determining the epoxy compressive strength (see Figures 5.4a and 5.4b). During the compression test, the load should be increased smoothly, under force-control, at a ratio of 2400±200 N/s until fracture. Similar to tension tests, also for compression specimens, three specimens were considered for each curing condition. The test setup is shown in Figure 5.4c. Two centralized steel plates, with dimensions of 40x40 mm^2, were placed at the top and the bottom of the specimen to transfer the load. Moreover, a spherical hinge was located at one loading side to avoid the effect of any possible eccentricity during loading. Similar to tension tests, a thermal chamber was mounted on the testing machine for the curing process (see Figure 5.4c). One strain gauge was installed to measure the evolution of specimen's longitudinal strain.

However, data obtained from the strain gauge were not reliable due to the earlier detachment and peeling in the surface that took place during the loading. Therefore, only the ultimate compressive strength of specimens was finally evaluated. Similar to tension tests, two thermocouples (one to measure the environmental temperature and the other glued on the surface of the specimen) were used to record the temperature before and during the test. The compressive strength of epoxy was calculated by dividing the ultimate load by initial contacted surface area. Due to possible unavoidable variations in dimensions of the specimens, measurements of the area were taken for each specimen prior to testing. Details of the specimen and test setup are shown in Figure 5.4.
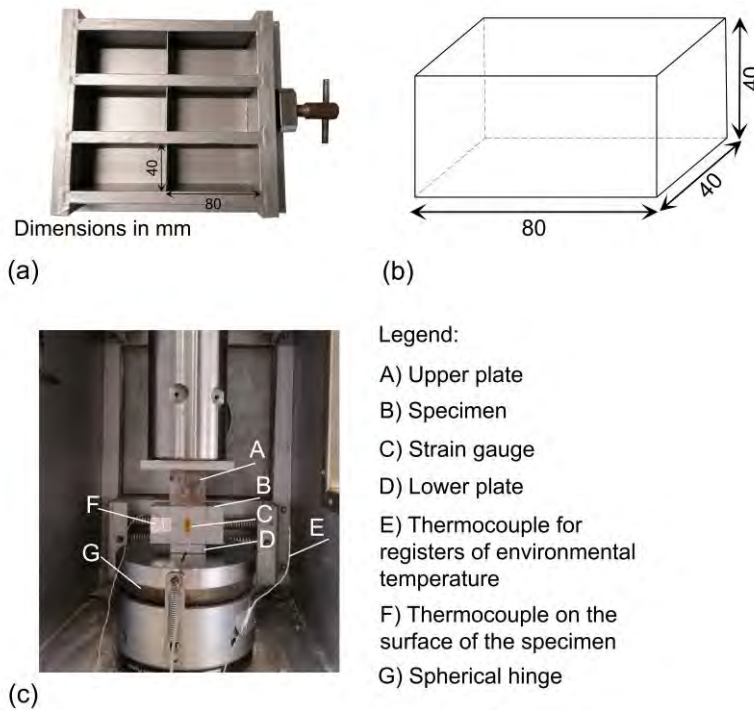
Figure 5.4. Details of the compression test: (a) Typical mould, (b) Specimen dimensions and (c) Test setup inside the thermal chamber.

5.3   Results and discussions

5.3.1   Effect of curing and post-curing temperature on T_g

Results of the DSC tests performed on specimens of Group 1 are presented in Figure 5.5a in the form of curves showing the variation of the heat flow versus temperature. It is acknowledged that the change of the heat flow versus temperature curve is related to an

absorption of energy and can, therefore, be an indicator of a possible change in the physical state of the resin. Considering that the T_g is defined as the temperature at which the physical state of the resin changes from the glassy state into the rubbery state, it has been accepted that T_g is in the range of the temperatures limiting the change in the baseline of the curve. It should be mentioned that in some of the curves presented in Figure 5.5a, an enthalpy relaxation peak can be observed immediately after the T_g range. This is an indication that physical aging has occurred [203]. It is worth noting that physical aging occurs in an amorphous polymer held below its T_g. According to experimental results presented in Table 5.2, the T_g value of the epoxy cured at room temperature (specimen TG-C-20) was 54.9 °C. Based on this, two different behaviors can be observed in Figure 5.5a: curing or post-curing the specimens at a temperature below epoxy T_g (i.e. specimens cured (and post-cured) at 50 °C of the present experimental program) resulted in a shift to the right of the peak in the heat flow versus temperature curve; contrarily, curing or post-curing the specimens at a temperature beyond epoxy T_g (i.e. specimens cured (and post-cured) at 70 °C of the present experimental program) resulted in a shift to the left of the peak in the heat flow versus temperature curve. This shifts to the right and left are therefore indicating an increase and reduction of the T_g value, respectively. These two different trends can also be observed in Figure 5.5b, where the dashed line represents the T_g value of the specimen cured at room temperature (TG-C-20), and the black and red solid lines represent the evolution of T_g for specimens that were cured and post-cured, respectively. When curing or post-curing of an adhesive takes place at a temperature below $T_{g\infty}$, T_g increases as the curing temperature increases. On the contrary, when curing or post-curing of an adhesive takes place at a temperature above $T_{g\infty}$, T_g decreases as the curing temperature increases [195,197,199]. This change in epoxy T_g is due to possible variations in the degree of cross-linking (i.e. possible thermal degradation or oxidative cross-linking) in the epoxy adhesive [9,149,189,201,202]. Based on this, and according to experimental results, for the epoxy adhesive studied in this paper, the curing temperature that leads to the fully cured network ($T_{g\infty}$) should be between 50 °C and 70 °C. Table 5.2 summarizes the experimental values of the T_g and its percentages of variation with respect to reference specimen (specimen TG-C-20).
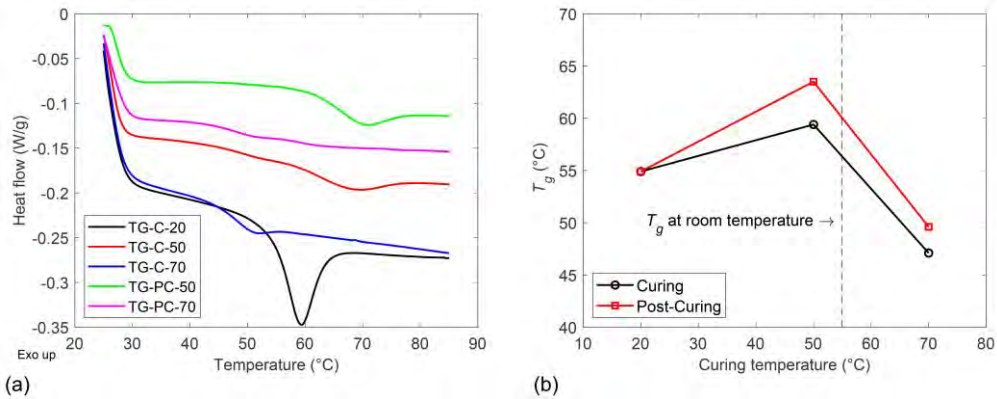
Figure 5.5. (a) Results from DSC tests and (b) Evolution of T_g as a function of the curing and post-curing temperatures.

Table 5.2. Experimental values of T_g from DSC tests.

Specimens ID	TG-C-20	TG-C-50	TG-C-70	TG-PC-50	TG-PC-70
T_g (°C)	54.9	59.4	47.1	63.5	49.6
Difference with T_g at 20 °C (%)	-	8	-14	16	-10

5.3.2   Effect of testing temperature on mechanical properties

In this section, results from tension and compression tests on specimens of Group 2 are presented and analyzed to study the effect of testing temperature on mechanical properties of the epoxy adhesive.

Regarding to the tension tests, Figure 5.6a shows the axial tensile stress versus strain curves, for one representative specimen of each testing temperature. From Figure 5.6a it can be observed that specimen tested at room temperature (TT-TEN-20) showed an almost perfect linear behavior up to failure. With the application of higher testing temperature (but still below T_g), the initial linear behavior was followed by a non-linear one before specimen's failure. Lately, when testing temperature was beyond T_g, the stress-strain curves became highly non-linear and properties were greatly affected, as a result of the rubbery behavior of the epoxy. Same behavior was observed in [8,187-190].
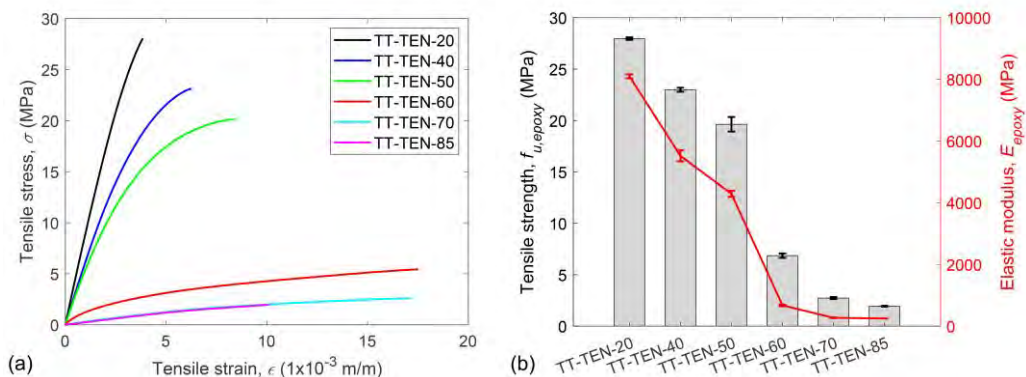
Figure 5.6. Effect of testing temperature on tensile mechanical properties of the epoxy resin: (a) Representative stress-strain curves and (b) Evolution of tensile strength and elastic modulus.

Experimental results in terms of tensile strength and elastic modulus are presented in Table 5.3 and Figure 5.6b. It can be observed that, the increase of the testing temperature was followed by a monotonic decrease in tensile strength and elastic modulus, with the most remarkable reduction taking place when testing temperature changed from 50 °C to 60 °C (epoxy T_g being within this range of temperatures). From this testing temperature on, the elastic modulus was almost negligible. These results are in agreement with previous studies on cold-curing epoxy adhesives [8,192].

According to the test matrix (Table 5.1), two additional configurations were considered whose curing included a one-day post-curing (specimens TT*-TEN-50 and TT*-TEN-70 in Table 5.1 and red line in Figure 5.1b). As mentioned before, the process of heating prior to testing should be considered as a post-curing and therefore, in specimens TT*-TEN-50 and TT*-TEN-70 two cycles of post-curing were applied. According to the experimental results, no significant effect of an extra cycle of post-curing was observed in the tensile strength and elastic modulus of the epoxy resin (see Figure 5.7 and Table 5.3). This might be a sign of the resin achieving a stable situation after the first post-curing, so that no additional evolution of the mechanical properties was possible. A representative typical failure mode under tension test (rupture near to the midspan of the specimens) is shown in Figure 5.8a.

Table 5.3. Tensile strength and elastic modulus for specimens tested at different temperatures (average ± standard deviation).

Specimens ID	Tensile strength, $f_{u,epoxy}$ (MPa)	$f_{u,epoxy}/f_{u,epoxy\_20}$ [1]	Elastic modulus, E_{epoxy} (MPa)	E_{epoxy}/E_{epoxy_20} [1]
TT-TEN-20	28.0 ± 0.1	-	8102.4 ± 67.0	-
TT-TEN-40	23.0 ± 0.2	0.82	5520.8 ± 179.0	0.68
TT-TEN-50	19.6 ± 0.7	0.70	4289.6 ± 100.7	0.53
TT*-TEN-50	19.7 ± 0.3	0.70	4128.7 ± 0.1	0.51
TT-TEN-60	6.9 ± 0.2	0.25	673.2 ± 24.5	0.08
TT-TEN-70	2.7 ± 0.1	0.10	271.5 ± 12.9	0.03
TT*-TEN-70	2.8 ± 0.0	0.10	273.9 ± 2.1	0.03
TT-TEN-85	1.9 ± 0.0	0.07	247.5 ± 1.8	0.03

[1]Defined as the ratio between the property value under the specific curing process and the reference property value (i.e. TT-TEN-20 tested at 20 °C)

Figure 5.7. Effect of additional post-curing on tensile mechanical properties of specimens in Group 2: (a) Representative stress-strain curves and (b) Evolution of tensile strength and elastic modulus.
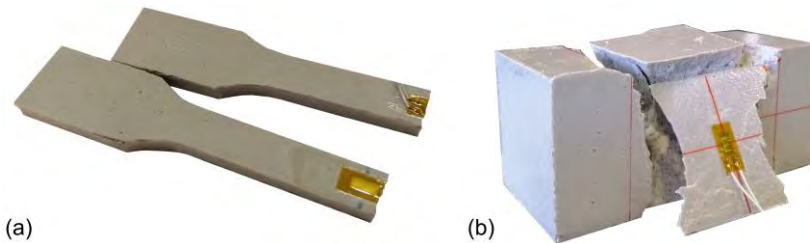
Figure 5.8. Typical failure modes: (a) Tension test and (b) Compression test.

In addition to tensile properties, behavior under compression was also evaluated under different testing temperatures. Figure 5.9a shows the compressive load versus deflection curves for one representative specimen of each testing temperature. Although one strain gauge was installed in every specimen, the peeling of specimen external surface invalidated the registered data. Therefore, deflections presented in Figure 5.9a correspond to the movement between grips of testing machine. In general, as observed in tension tests, the increase in the testing temperature was followed by a more flexible response and a decrease of the ultimate compressive load.
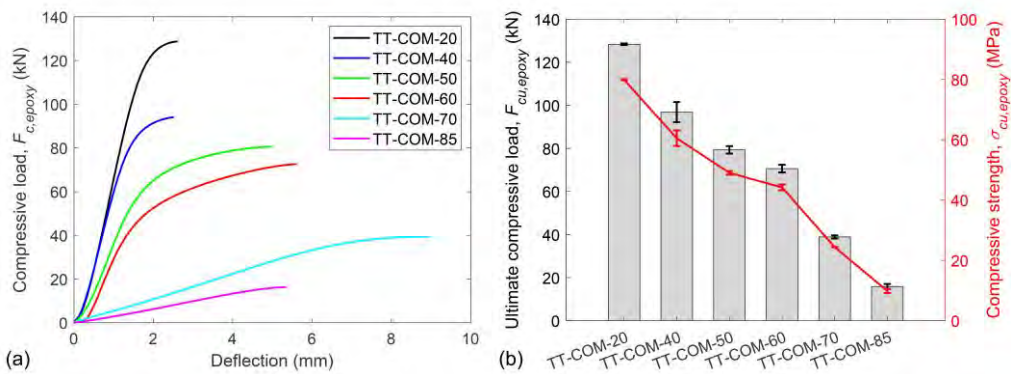
Figure 5.9. Effect of testing temperature on compressive mechanical properties of the epoxy resin: (a) Representative load-deflection curves and (b) Compressive strength and ultimate compressive load.

Averaging the experimental value of ultimate compressive load over the initial area of contact allowed determining the compressive strength of each specimen. Experimental results of compressive properties (ultimate compressive load and compressive strength) are presented in Table 5.4 and Figure 5.9b. According to these results, compressive strength was almost halved for testing temperatures equal to 60 °C, and the reduction rate highly increased beyond 60 °C.

With the aim at analyzing the possible effect of the inclusion of an extra cycle of post-curing phase in the curing process of the specimens, and similar to what was done for tension tests, two additional configurations were considered (specimens TT*-COM-50 and TT*-COM-70 in Table 5.1 and red line in Figure 5.1b). According to experimental results presented in Table 5.4 and Figure 5.10, the extra cycle of post-curing resulted in a small variation in the ultimate compressive load and compressive strength, which can be attributed to typical scatter in experimental results.

A representative typical failure mode of the compressive specimens is shown in Figure 5.8b.

Table 5.4. Ultimate compressive load and compressive strength for specimens tested at
different temperatures (average ± standard deviation).

Specimens ID	Compressive load, $F_{cu,epoxy}$ (kN)	$F_{cu,epoxy}/F_{cu,epoxy\_20}$[1]	Compressive strength, $\sigma_{cu,epoxy}$ (MPa)	$\sigma_{cu,epoxy}/\sigma_{cu,epoxy\_20}$[1]
TT-COM-20	128.4 ± 0.4	-	79.9 ± 0.1	-
TT-COM-40	96.9 ± 4.7	0.75	60.5 ± 2.6	0.76
TT-COM-50	79.3 ± 1.7	0.62	49.0 ± 0.6	0.61
TT*-COM-50	82.2 ± 0.7	0.64	51.8 ± 0.5	0.65
TT-COM-60	70.6 ± 1.8	0.55	44.2 ± 1.0	0.55
TT-COM-70	38.9 ± 0.7	0.30	24.4 ± 0.1	0.31
TT*-COM-70	36.1 ± 1.6	0.28	22.4 ± 0.7	0.28
TT-COM-85	15.9 ± 1.2	0.12	9.9 ± 0.7	0.12

[1]Defined as the ratio between the property value under the specific curing process and the reference
property value (i.e. TT-COM-20 tested at 20 °C)

Figure 5.10. Effect of additional post-curing on compressive mechanical properties of
specimens in Group 2.

5.3.3 Effect of curing temperature on mechanical properties

With the aim at analyzing the effect of curing temperature on the mechanical properties of
the epoxy resin, results on specimens of Group 3 are presented and discussed in this section.

Experimental results in terms of tensile strength and elastic modulus of epoxy cured at
different temperatures are presented in Figure 5.11 and Table 5.5, and compared to results on

specimens TT-TEN-20, belonging to Group 2, which were cured and tested at 20 °C. From this comparison it can be observed that curing the specimens at -15 °C (CT-TEN-(-15)) had no significant effect on epoxy tensile strength and had some detrimental effects on the elastic modulus. The application of -15 °C during curing, in fact, postponed the initiation of curing, as 7 days after being casted, epoxy resin was still soft. Same observations were reported in [149,204]. These observations suggest that, due to cold temperature postponing the initiation of curing, suitable considerations should be taken into account in the cold weather regions to facilitate the adhesive curing process.

According to experimental results on tensile strength and elastic modulus, the increase of curing temperature below $T_{g\infty}$ promotes the increase of cross-linking, which results in the increase of the performance of the adhesive (specimen CT-TEN-50). On the contrary, curing at temperatures above $T_{g\infty}$ possibly produces thermal degradation on the adhesive, which results in a decrease of its mechanical properties (specimen CT-TEN-70). These results confirm that mechanical properties and the T_g properties have similar behaviors.

Figure 5.11. Effect of curing temperature on tensile mechanical properties of the epoxy resin: (a) Representative stress-strain curves and (b) Evolution of tensile strength and elastic modulus.

In addition to previous specimens, two more configurations were also tested whose curing process was followed by a one-day post-curing (specimens CT*-TEN-50 and CT*-TEN-70). Experimental results on tension tests presented in Table 5.5 and Figure 5.12 revealed that the post-curing process did not highly affect the mechanical properties of the adhesive used in this experimental program. It should be mentioned that a large scatter in experimental results on elastic modulus can be observed for the specimen with an additional post-curing (specimens CT*-TEN-50 and CT*-TEN-70). These results, along with experimental results on specimens of Group 2 having an additional post-curing process (TT*-TEN-50 and TT*-TEN-70), indicate that

the application of a post-curing process at a temperature equal to that of the curing process produces no evolution in mechanical properties, because of the stability in the epoxy resin.
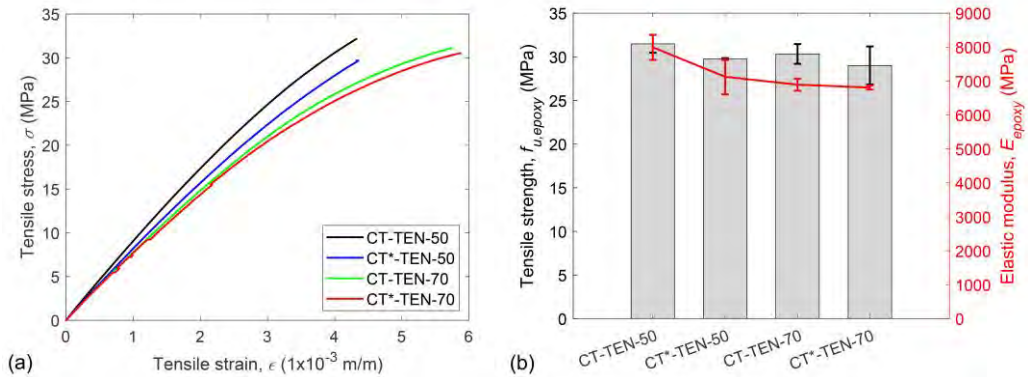
Figure 5.12. Effect of additional post-curing on tensile mechanical properties of specimens in Group 3: (a) Representative stress-strain curves and (b) Evolution of tensile strength and elastic modulus.

Table 5.5. Tensile strength and elastic modulus for specimens cured at different temperatures (average ± standard deviation).

Specimens ID	Tensile strength, $f_{u,epoxy}$ (MPa)	$f_{u,epoxy} / f_{u,epoxy\_20}$ [1]	Elastic modulus, E_{epoxy} (MPa)	E_{epoxy} / E_{epoxy_20} [1]
CT-TEN-(-15)	27.7 ± 0.7	0.99	7601.9 ± 56.3	0.94
TT-TEN-20	28.0 ± 0.1	-	8102.4 ± 67.0	-
CT-TEN-50	31.5 ± 1.0	1.13	7992.0 ± 372.8	0.99
CT*-TEN-50	29.8 ± 0.1	1.06	7124.9 ± 516.1	0.88
CT-TEN-70	30.3 ± 1.1	1.08	6892.5 ± 176.4	0.85
CT*-TEN-70	29.0 ± 2.2	1.04	6808.0 ± 60.2	0.84

[1]Defined as the ratio between the property value under the specific curing process and the reference property value (i.e. TT-TEN-20 tested at 20 °C)

Compression tests were also performed to study the possible influence of curing temperature on the compressive mechanical properties of the epoxy resin. Results of these tests are presented in Table 5.6 and Figure 5.13a. The increase in the curing temperature to values below epoxy T_g (i.e. up to 50 °C of the present experimental program) resulted in a monotonic increase of epoxy ultimate compressive load and compressive strength. On the other hand, when curing temperature was beyond epoxy T_g (i.e. 70 °C), a decrease in the compressive mechanical properties was observed. Besides, and according to results on additional specimens with one-

day post-curing (specimens CT*-COM-50 and CT*-COM-70), no significant differences were observed between compressive mechanical properties of specimens with and without the post-curing process (see Figure 5.13b).
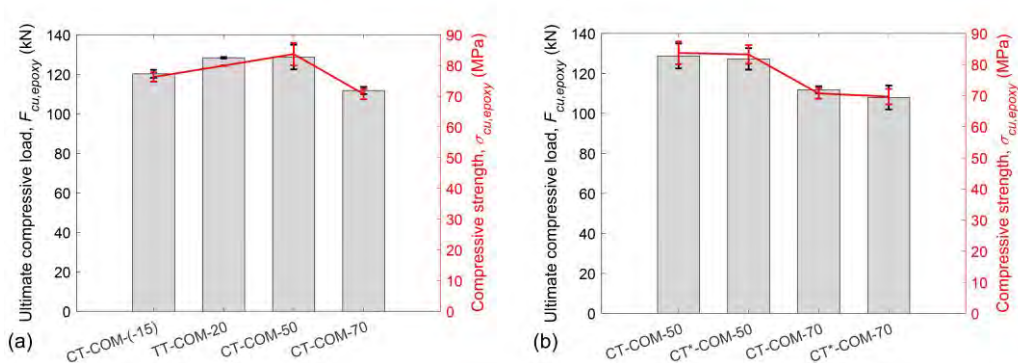
Figure 5.13. (a) Effect of curing temperature on compressive mechanical properties of the epoxy resin and (b) Effect of additional post-curing on compressive mechanical properties of specimens in Group 3.

Table 5.6. Ultimate compressive load and compressive strength for specimens cured at different temperatures (average ± standard deviation).

Specimens ID	Compressive load, $F_{cu,epoxy}$ (kN)	$F_{cu,epoxy} / F_{cu,epoxy\_20}$[1]	Compressive strength, $\sigma_{cu,epoxy}$ (MPa)	$\sigma_{cu,epoxy} / \sigma_{cu,epoxy\_20}$[1]
CT-COM-(-15)	120.2 ± 2.0	0.94	76.2 ± 1.5	0.95
TT-COM-20	128.4 ± 0.4	-	79.9 ± 0.1	-
CT-COM-50	128.7 ± 6.2	1.00	83.7 ± 3.6	1.05
CT*-COM-50	127.2 ± 5.4	0.99	83.2 ± 3.0	1.04
CT-COM-70	111.8 ± 1.8	0.87	70.7 ± 1.7	0.88
CT*-COM-70	107.9 ± 6.0	0.84	69.7 ± 2.5	0.87

[1]Defined as the ratio between the property value under the specific curing process and the reference property value (i.e. TT-COM-20 tested at 20 °C)

5.3.4 Effect of post-curing temperature on mechanical properties

In this section, results on mechanical properties of specimens of Group 4 are presented and discussed, with the aim at analyzing the effect of a post-curing process at different temperatures (ranging from 20 °C to 85 °C) on mechanical properties of specimens that were previously cured

at room temperature (i.e. 20 °C). Therefore, specimens TT-TEN-20 and TT-COM-20, from Group 2, are considered as the reference ones.

Experimental results on tensile properties of specimens in Group 4 are presented in Figure 5.14 and Table 5.7, where the mean value and standard deviation are also included. As highlighted in the literature [189,200,201,205], epoxy adhesives cured at ambient temperature may suffer from a not complete cross-linking, that can be reactivated with a post-curing process. This was confirmed by experimental results of Group 4, as tensile strength monotonically increased with the increase in the post-curing temperature, and elastic modulus tended to a constant value. However, for post-curing temperatures larger than 60 °C, an abrupt decay in tensile strength and a more sharped reduction on elastic modulus were observed in specimens post-cured at 70 °C, thus indicating that $T_{g\infty}$ of the adhesive might be in the range of 60 °C to 70 °C. Finally, results on elastic modulus for specimens post-cured at 85 °C continued their downward trend, whilst a groundless increase in tensile strength was observed.

Figure 5.14. Effect of post-curing temperature on tensile mechanical properties of the epoxy resin: (a) Representative stress-strain curves and (b) Evolution of tensile strength and elastic modulus.

Table 5.7. Tensile strength and elastic modulus for specimens post-cured at different temperatures (average ± standard deviation).

Specimens ID	Tensile strength, $f_{u,epoxy}$ (MPa)	$f_{u,epoxy}/f_{u,epoxy\_20}$ [1]	Elastic modulus, E_{epoxy} (MPa)	E_{epoxy}/E_{epoxy_20} [1]
TT-TEN-20	28.0 ± 0.1	-	8102.4 ± 67.0	-
PT-TEN-40	29.5 ± 1.6	1.05	7896.9 ± 625.5	0.97
PT-TEN-50	30.3 ± 1.8	1.08	7834.9± 119.8	0.97
PT-TEN-60	31.3 ± 0.7	1.12	7668.1 ± 566.6	0.95
PT-TEN-70	28.0 ± 1.6	1.00	7212.0 ± 548.1	0.89
PT-TEN-85	30.0 ± 1.5	1.07	6584.8 ± 95.3	0.81

[1]Defined as the ratio between the property value under the specific curing process and the reference property value (i.e. TT-TEN-20 tested at 20 °C)
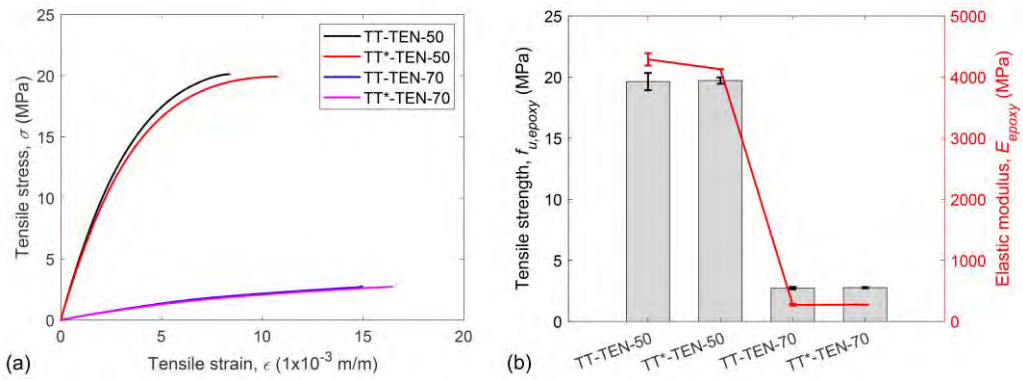
The effect of post-curing on compressive mechanical properties of the epoxy adhesive is shown in Figure 5.15 and Table 5.8. From Figure 5.15 it can be observed that the increase in the post-curing temperature from 20 °C to 40 °C resulted in an increase in the ultimate compressive load and compressive strength. On the other hand, for post-curing temperatures beyond 40 °C, a decrease in the compressive mechanical properties took place, with no meaningful changes and results falling within the same range of reference specimen (TT-COM-20).
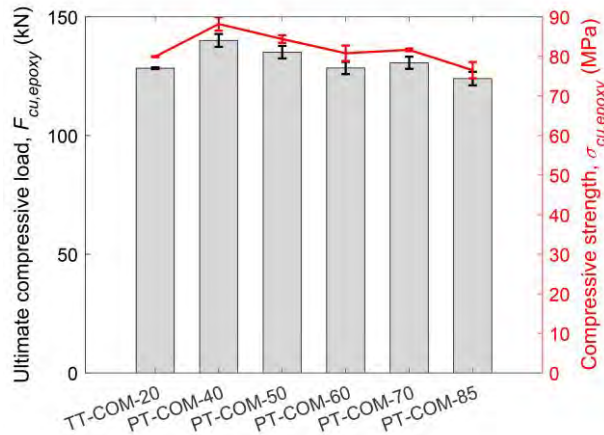
Figure 5.15. Effect of post-curing temperature on compressive mechanical properties of the epoxy.

Table 5.8. Ultimate compressive load and compressive strength for specimens post-cured at different temperatures (average ± standard deviation).

Specimens ID	Compressive load, $F_{cu,epoxy}$ (kN)	$F_{cu,epoxy}$ /$F_{cu,epoxy\_20}$[1]	Compressive strength, $\sigma_{cu,epoxy}$ (MPa)	$\sigma_{cu,epoxy}$ /$\sigma_{cu,epoxy\_20}$[1]
TT-COM-20	128.4 ± 0.4	-	79.9 ± 0.1	-
PT-COM-40	140.1 ± 2.7	1.09	88.2 ± 1.7	1.10
PT-COM-50	135.1 ± 2.6	1.05	84.2 ± 1.0	1.05
PT-COM-60	128.4 ± 2.6	1.00	80.8 ± 1.9	1.01
PT-COM-70	130.6 ± 2.6	1.02	81.7 ± 0.3	1.02
PT-COM-85	124.0 ± 2.8	0.97	76.5 ± 2.1	0.96

[1]Defined as the ratio between the property value under the specific curing process and the reference property value (i.e. TT-COM-20 tested at 20 °C)

5.4 Conclusion

In the present work, a comprehensive experimental program was performed to evaluate the effect of temperature (i.e. testing temperature, curing temperature and post-curing temperature) on the mechanical properties and the T_g of an epoxy adhesive.

From the analysis of the effect of temperature on the measured T_g of the epoxy adhesive (specimens in Group 1), it can be concluded that curing and post-curing temperature affected T_g differently depending whether the applied temperature was below or beyond the epoxy $T_{g\infty}$.

From the analysis of the effect of testing temperature on mechanical properties of the epoxy adhesive (specimens in Group 2), the following conclusions can be drawn:

- The falling trend in tensile mechanical properties experienced the largest decrease when testing temperature exceeded the T_g of the epoxy adhesive. Besides, for testing temperatures beyond 60 ° C, due to complete rubbery state of the epoxy, the elastic modulus was almost negligible. For the compression tests, this large reduction took place at the temperature equal 70 °C.
- The inclusion of an extra cycle of post-curing barely affected the mechanical properties of epoxy specimens.

From the analysis of the effect of curing temperature on mechanical properties of the epoxy adhesive (specimens in Group 3), the following conclusions can be drawn:

- Curing temperatures below $T_{g\infty}$ resulted in larger mechanical properties because of the cross-linking promotion. On the other hand, curing temperatures beyond $T_{g\infty}$ produced a possible thermal degradation on the adhesive that resulted in a decrease of its mechanical properties.
- No significant effect of an additional post-curing process was observed. This may be due to stabilization of epoxy because of post-curing at the same curing temperature.

From the analysis of the effect of post-curing temperature on mechanical properties of the epoxy adhesive (specimens in Group 4), the following conclusions can be drawn:

- Post-curing the epoxy at a temperature below the temperature that leads to a fully cured network (near to $T_{g\infty}$) enhanced the mechanical properties because of the reactivation of cross-linking of the non-complete cured epoxy adhesive.
- The largest benefit of post-curing on epoxy compressive strength took place for post-curing temperature equal to 40 °C.

The increase in the mechanical properties of epoxy at curing or post-curing temperatures below or near to the T_g of epoxy can be attributed to the fact that the degrees of cross-linking between the epoxy's molecules has increased, thus having the consequence of an increase in T_g.

6 Paper C: Time-dependent behavior of NSM CFRP-strengthened RC beams under different service temperatures

Younes Jahani[1], Marta Baena[1*], Alba Codina[1], Cristina Barris[1] and Lluís Torres[1]

[1]AMADE, Polytechnic School, University of Girona, 17003, Girona, Spain

[*]Corresponding author

Time-dependent behavior of NSM CFRP-strengthened RC beams under different service temperatures

Younes Jahani, Marta Baena *, Alba Codina, Cristina Barris, Lluís Torres

AMADE, Polytechnic School, University of Girona, 17003 Girona, Spain

Abstract

The use of fiber-reinforced polymer (FRP) for flexural strengthening of reinforced concrete (RC) beams has become a popular strengthening technique. Significant amount of work is available on the short-term flexural behavior of RC beams strengthened with near-surface mounted (NSM) technique. However, their time-dependent flexural behavior, specifically under high service temperature, has not yet been addressed. This paper presents an experimental work to evaluate the time-dependent behavior of NSM carbon FRP (CFRP)-strengthened RC beams. The experimental program included 23 beams, where the effect of different parameters such as strengthening (CFRP) ratio, steel reinforcement ratio and applied temperature (20 °C and 50 °C) have been considered. Experimental results show that the effect of strengthening ratio is significant on the flexural short-term response of the beams, while minor effects are found on the time-dependent deflections. On the other hand, increasing the service temperature has no significant effect on the short-term tests, but it produces a large increase in the time-dependent deflection of the specimens. Finally, an analytical procedure for the prediction of time-dependent deflections, which is based on the age-adjusted effective modulus method (AEMM), is presented. Good agreement between the experimental results and analytical predictions on time-dependent deflections is shown.

Keywords: NSM FRP-strengthening, long-term load, service temperature, time-dependent deflections

6.1 Introduction

Strengthening of reinforced concrete (RC) structures may become necessary due to different reasons such as increase in the service loads, design code changes, earthquake activities, deficiencies resulting from environmental effects (e.g. corrosion), changes in the occupancy of

buildings, etc. [2,3]. In the last decades, fiber-reinforced polymer (FRP) materials have been accepted to be used in two of the principal strengthening techniques for RC elements, namely externally bonding reinforcement (EBR) and near-surface mounted (NSM) systems. In the EBR reinforcing technique, the FRP sheets or laminates are bonded to the tensile concrete surface of the damaged member. In the NSM technique, grooves are cut in the tensile face of the RC element where the FRP strips/bars are inserted and bonded. Therefore, due to the confinement provided by surrounding concrete and epoxy, NSM FRP-strengthening technique is less exposed to aggressive environment (and other detrimental effects) and less prone to premature debonding [5,6,30,48].

RC elements are usually subjected to long-term loads that can affect their structural performance in terms of time-dependent deflections, loading capacity and failure mode [80-82,206]. Time-dependent deflections are a function of the loading history (and its effect on the concrete mechanical properties), age of concrete at the time of loading, the magnitude and duration of the long-term load and material properties. Within material properties, creep and shrinkage of concrete, which are dependent on environmental conditions, are of main importance [83].

Significant amount of work has been done to study the time-dependent behavior of EBR FRP-strengthened RC elements [82,105-110], where different amounts of carbon FRP (CFRP) ratio and long-term load levels were considered. The results showed that larger time-dependent deflections were obtained when higher levels of long-term load were applied. Besides, the contribution of CFRP-strengthening systems to RC elements under flexural long-term loading was not significant when compared to elements under flexural instantaneous loading [82,107].

Unlike the EBR FRP-strengthened system, few works exist in the literature regarding the time-dependent behavior of NSM FRP-strengthened RC beams [111-114]. Sena-Cruz et al. [111], experimentally studied the time-dependent behavior of slab specimens strengthened with NSM CFRP strips. The load was applied in two steps, first 40% of long-term load was applied for a duration of 78 days, later the load increased to 100% for a duration of 55 days. The results showed that the majority of time-dependent deflection occurred at the first step of the loading. Moawad et al. [114] experimentally studied the time –dependent behavior of different series of NSM CFRP-strengthened RC beams with different loading histories and sectional properties. Results showed the influence of the loading sequences and levels of loading in combination with the other parameters. The specimens with higher concrete strength resulted in a larger ratio of

time-dependent deflections to instantaneous deflection. Moreover, for the strengthened specimens with compression steel reinforcement, the effectiveness of NSM strengthening was more pronounced in reducing the deflections. Finally, the effect of the long-term load on the residual flexural capacity of NSM CFRP-strengthened RC beams was experimentally studied [112] and an analytical work to predict the time-dependent response of the specimens was presented [113]. With increase in the long-term load, the residual capacity of beams decreased. Furthermore, all specimens failed by end debonding, but for higher long-term load, the end debonding occurred in longer bonded length with larger bond deterioration. In addition, the same trend in time-dependent strain evolution in FRP was observed from both experimental data and analytical procedures.

The structures under long-term loading are usually exposed to temperature variation during the different seasons of the year. Being epoxy adhesives the most common ones used in NSM strengthening, and due to their nature, special attention should be given to high service temperature (near or beyond the glass transition temperature, T_g, of the epoxy adhesive) [7-9,207]. In this sense, the instantaneous behavior of NSM FRP-strengthened RC beams under room temperature [49,55,56,75,76,208-211] and elevated temperature (fire conditions) [161,163,165,166,169] has received considerable attention, but less work has been done on the effect of high service temperature [36,37,191].

According to the literature, few works have been performed to study the time-dependent behavior of NSM FRP-strengthened RC members, and, to the best of authors knowledge, none of them account for the effect of high service temperature on the time-dependent deflections and structural performance. Therefore, the purpose of the present study is to investigate the time-dependent behavior of NSM CFRP-strengthened RC beams subjected to room temperature (20 °C) and high service temperature (50 °C). To this end, a total of 23 beams were cast, where the effect of different parameters was considered (i.e. level of strengthening (CFRP ratio), steel reinforcement ratio and applied temperature (20 °C and 50 °C)). Experimental results are presented and discussed in terms of instantaneous load-deflection curves, time-dependent and total deflections, time-dependent strain in concrete, failure modes, residual flexural strength of tested specimens and aging effect. Furthermore, an analytical procedure to predict the time-dependent deflection in NSM CFRP-strengthened RC beams is presented. The analytical procedure is based on the age-adjusted effective modulus method (AEMM) [83,84].

6.2   Experimental program

6.2.1   Test matrix and test setup

The experimental program included 23 RC beams distributed in three series as follows (see Table 6.1): 10 beams were tested under short-term load and were considered as reference specimens (Series 1), 10 beams were tested under long-term load to examine their time-dependent behavior (Series 2) and, finally, 3 beams were cast and rested in the laboratory (without any loading) to be tested at the end of the long-term experimental program. Series 1 and Series 2 were divided into two groups to evaluate the effect of steel reinforcement ratio (ρ_s = 0.79% and 1.14% for Group 1 and 2, respectively). Group 1 included two control beams and four NSM CFRP-strengthened RC beams, with two different amounts of CFRP-strengthening, subjected to 20 °C and 50 °C. In Group 2, two control beams and two NSM CFRP-strengthened RC beams, strengthened with three CFRP strips, were subjected to 20 °C and 50 °C.

Specimens' designation reads X-Y-Z-T, where X indicates the type of loading (ST standing for short-term load, LT standing for long-term load and AG meaning aging effect). Moreover, Y denotes the type of beam (CB meaning control beam, and SB1S and SB3S referring to strengthened beams with one and three CFRP strips, respectively). Furthermore, Z indicates the Group that specimen belongs to (i.e. thus indicating the steel reinforcement ratio). Finally, T stands for the testing temperature. For instance, ST-CB-1-20, refers to the control beam in Group 1 (ρ_s = 0.79%) tested under short-term loading at 20 °C. Furthermore, LT-SB3S-2-50 refers to a beam strengthened with three CFRP strips from Group 2 (ρ_s = 1.14%) and tested under long-term loading at 50 °C.

The beams were tested under a four-point bending configuration (see Figure 6.1). The sectional dimensions of the beams were 140 × 180 mm and the total and clear length of specimens were 2400 mm and 2200 mm, respectively. Specimens in Group 1 were reinforced with two steel rebars with a diameter of 10 mm and two steel rebars with a diameter of 6 mm in the tension and compression side of the beam, respectively (ρ_s = 0.79%).

Table 6.1. Text matrix for long-term loading.

Series	Loading type	Group	Beam ID	Testing Temperature (°C)	Steel reinforcement ratio, ρ_s (%)	No. of CFRP strips	Total CFRP area (mm²)
Series 1	Short-term	Group 1	ST-CB-1-20	20	0.79	-	-
			ST-CB-1-50	50		-	-
			ST-SB1S-1-20	20		1	14
			ST-SB1S-1-50	50		1	14
			ST-SB3S-1-20	20		3	42
			ST-SB3S-1-50	50		3	42
		Group 2	ST-CB-2-20	20	1.14	-	-
			ST-CB-2-50	50		-	-
			ST-SB3S-2-20	20		3	42
			ST-SB3S-2-50	50		3	42
Series 2	Long-term	Group 1	LT-CB-1-20	20	0.79	-	-
			LT-CB-1-50	50		-	-
			LT-SB1S-1-20	20		1	14
			LT-SB1S-1-50	50		1	14
			LT-SB3S-1-20	20		3	42
			LT-SB3S-1-50	50		3	42
		Group 2	LT-CB-2-20	20	1.14	-	-
			LT-CB-2-50	50		-	-
			LT-SB3S-2-20	20		3	42
			LT-SB3S-2-50	50		3	42
Series 3	Aging	Group 1	AG-CB-1-20	20	0.79	-	-
			AG-SB1S -1-20	20		1	14
			AG-SB3S-1-20	20		3	42

In Group 2, rebars with a diameter of 12 mm and 8 mm were used in tension and compression side of the beam, respectively (ρ_s = 1.14%). To avoid shear failure, stirrups with a diameter of 8 mm were placed every 75 mm in all beams. Furthermore, to strengthen the beams in flexure, and following *fib* Bulletin 90 [1] recommendations, grooves with dimensions of 6 × 15 mm were cut in the soffit of the beams, and strips with dimensions of 1.4 × 10 mm were introduced using an epoxy adhesive. Moreover, a 5 × 15 mm notch was created in the midspan of all beams to act as a crack initiator. For Series 1 and 3 (short-term load before and after aging), the flexural test was performed under displacement control at a rate of 0.6 mm/min, whereas for Series 2 (long-term load), concrete blocks and steel plates were used as deadweight (see Figure 6.1b).
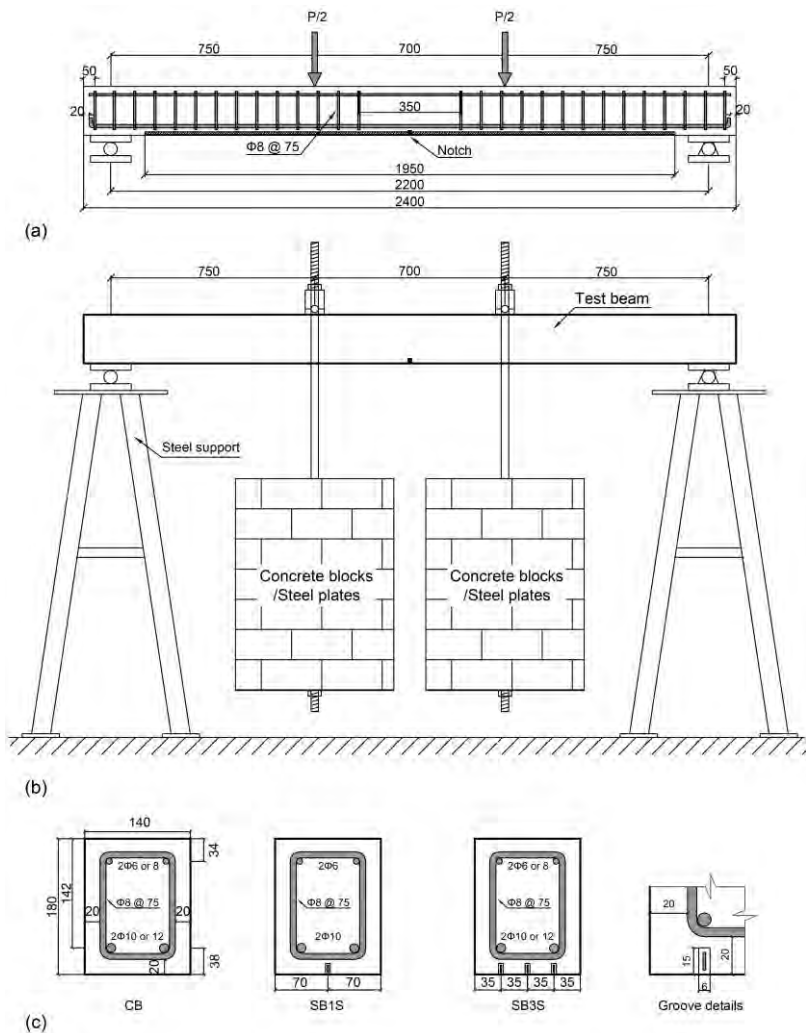
Figure 6.1. Details of the tested beams: (a) Short-term setup, (b) Long-term setup and (c) Beam sections (dimensions in mm).

120

6.2.2 Instrumentation

Beam instrumentation is shown in Figure 6.2. A set of linear vertical displacement transducers (LVDTs) were placed in the beam to register the movement of the beam. One LVDT was used in the midspan of the beam to measure the central deflection (LVDT1). In Series 1 and 3 (subjected to short-term loading), two LVDTs (LVDT 2 and 3) were placed at supports sections to measure the supports settlement. In addition to LVDTs, one strain gauge was installed in the midspan of the specimens to register the strain at the top fiber of concrete (SG_C).
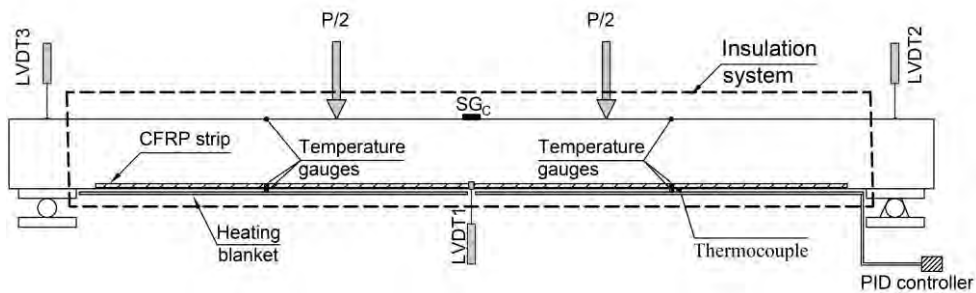
Figure 6.2. Beams instrumentation: Position of the linear vertical displacement transducers (LVDTs), concrete strain gauges, temperature gauges, heating system and insulation system.

In those specimens subjected to the temperature, heating blankets (installed to the soffit of the beam) were used to heat up the beams up to the target temperature (i.e. 50 °C). The heating process was controlled by proportional integral derivative (PID) controller, and Type-T thermocouples, installed between the heating blanket and the soffit of the beam, were used as temperature controller sensor. In order to ensure a better heat distribution along the beam, an isolation system was used. To monitor and record the temperature during the heating process and flexural testing, different temperature gauges were installed on concrete surface at the top and bottom of the beam, on the surface of the CFRP (it was installed before introducing FRP into the grooves) and on the surface of epoxy adhesive (see Figure 6.2). The beams were left to be heated-up for 24 hours prior to testing (in both short-term and long-term load) until the average temperature in the soffit of the beam was stabilized to the target value. A general view of short-term and long-term load setup is shown in Figure 6.3.
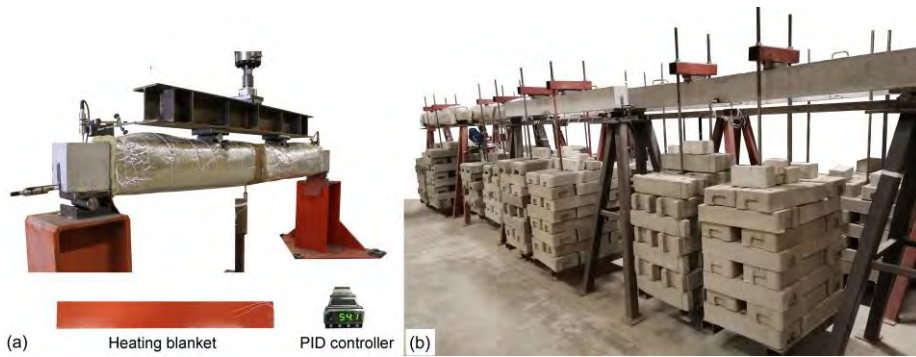
Figure 6.3. General view of experimental setup and heating system: (a) Short-term load setup and (b) Long-term load setup.

6.2.3 Temperature and humidity

Registration of laboratory conditions (temperature and humidity) started the day of concrete casting and continued till the end of the experimental program. An average temperature and humidity of 19.6 °C and 64% were registered, respectively (see Figure 6.4a). In addition, the evolution of temperature and humidity of beams under 50 °C was registered during the heating (24 hours prior to testing) until the end of the long-term loading. Average values for temperature and humidity read 50.4 °C and 16%, respectively (see Figure 6.4b).
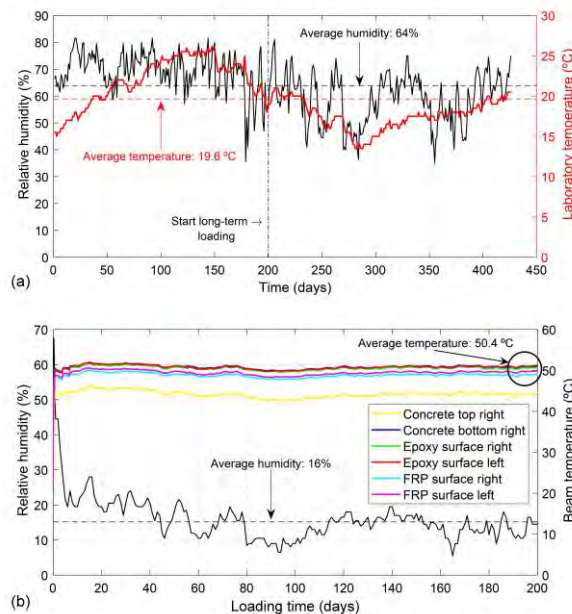
Figure 6.4. Registers on temperature and humidity: (a) Laboratory condition and (b) Inside the beam at 50 °C.

6.2.4 Materials

Concrete

The specimens were cast in the structural laboratory with ready-mix concrete. The cement type was I-42.5R, with a content of 390 kg/m³. The maximum aggregate size was 12 mm, and the water/cement ratio was 0.41. A viscosity modifier and underwater admixture were used to improve workability. In order to determine the mechanical properties of concrete, cylinder specimens with 300 mm nominal height and 150 mm nominal diameter were used. The compressive strength (f_c), tensile strength (f_t) and modulus of elasticity (E_c) of the concrete were determined according to UNE-EN 12390-3 [137], UNE-EN 12390-6 [138], and ASTM C469 [139] standards, respectively. The mechanical properties of concrete at different ages is summarized in Table 6.2.

Table 6.2. Concrete mechanical properties.

Concrete age (days)	Compressive strength, f_c (MPa)	Tensile strength, f_t (MPa)	Modulus of elasticity, E_c (GPa)
90[a]	48.1 (2.3%)[d]	3.7 (6.0%)[d]	41.2 (5.3%)[d]
200[b]	48.3 (2.2%)[d]	3.7 (9.0%)[d]	41.9 (4.5%)[d]
430[c]	53.7 (0.8%)[d]	3.6 (9.4%)[d]	47.6 (1.9%)[d]

[a] Age at short-term test of Series 1

[b] Age at long-term test of Series 2

[c] Age at residual flexural test of Series 2 and short-term test of Series 3

[d] Coefficient of variation (CoV) indicated in brackets.

The time-dependent behavior of the concrete was determined according to ASTM C512-02 [140]. To this end, four cylindrical specimens (150 mm diameter and 450 mm height) with an embedded strain gauge were manufactured. Two of the four cylinders were kept at 20 °C and the other two were heated up to 50 °C. Each pair of concrete cylinders was stacked on a loading frame and loaded with a long-term load level of $0.35f_c$ (the same long-term load level in all specimens). The long-term load was applied at the same time as the beams.

To measure free shrinkage strain in concrete (ε_{sh}), two concrete prisms, having the same concrete beam section (180 × 140 mm) and 1 m length, were instrumented with an embedded strain gauge and left unloaded at the same temperature and humidity as beam specimens. The strain evolution with time for both shrinkage specimens (at 20 °C and 50 °C) is shown in Figure 6.5a. For the specimen submitted to 50 °C, heating started at the same time as heating of the

long-term specimens (Series 2). The effect of heating on concrete shrinkage is clearly visible. In the shrinkage specimen subjected to 50 °C, the thermal strain was also considered in the strain registration. Registers of maximum shrinkage at the end of long-term loading are summarized in Table 6.3, with shrinkage corresponding to the heated specimen being 35% higher than that of the specimen at laboratory conditions.

The concrete creep coefficient was obtained according to Eq. (6.1):

$$\varphi_c(t, t_0) = \frac{\varepsilon_c(t, t_0) - \varepsilon_{cs}(t, t_0) - \varepsilon_{ci}(t_0)}{\varepsilon_{ci}(t_0)} \tag{6.1}$$

where t is the loading time, t_0 is the concrete age at the start of loading, $\varphi_c(t,t_0)$ is the concrete creep coefficient, $\varepsilon_c(t,t_0)$ is the total concrete strain, $\varepsilon_{cs}(t,t_0)$ is the concrete shrinkage strain and $\varepsilon_{ci}(t_0)$ is the instantaneous concrete strain caused by the long-term load.

Due to technical issues in the setup of the concrete creep specimen subjected to 50 °C, the concrete creep coefficient was experimentally determined only for specimens at 20 °C (see Figure 6.5b). Existing formulation from *fib* Model Code 2010 [83] was used to estimate the concrete creep coefficient for the concrete at 50 °C. Experimental values and analytical prediction of concrete creep coefficient are presented in Table 6.3. For comparison purposes, analytical prediction on concrete creep coefficient of specimen subjected to 20 °C is also included.
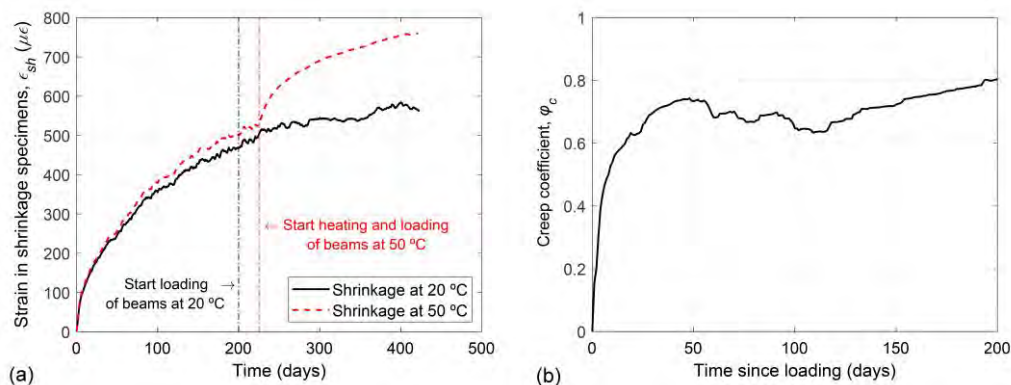
Figure 6.5. Experimental time-dependent behavior of concrete: (a) Strain in shrinkage specimens at 20 and 50 °C and (b) Creep coefficient at 20 °C.

Table 6.3. Concrete creep coefficient and shrinkage strain.

Temperature (°C)	Concrete creep coefficient, φ_c		Experimental shrinkage strain, ε_{sh} ($\mu\varepsilon$)
	Experimental	*fib* Model Code 2010 [83]	
20	0.80	0.60	563
50	-[1]	2.64	759

[1] Not available due to failure in setup.

Steel reinforcement

Mechanical properties of steel bars were obtained from tension tests based on UNE-EN ISO 15630-1 [141]. The yielding strength (f_y), the ultimate strength (f_u) and the modulus of elasticity (E_s) were 586.4 MPa (CoV=2.3%), 707.7 MPa (CoV=1.7%) and 205.1 GPa (CoV=1.0%) respectively.

CFRP strips

CFRP strips, consisting of unidirectional carbon fibers (with a volume content fiber higher than 68%) held together by an epoxy vinyl ester resin matrix, were used for strengthening the specimens [20]. The mechanical properties of the CFRP strips were obtained according to ISO 527-5 [142] recommendations. An ultimate tensile strength ($f_{u,FRP}$) of 2251.4 MPa (CoV = 3.2%), an ultimate tensile strain ($\varepsilon_{u,FRP}$) of 0.0133 (CoV = 7.2%), and a modulus of elasticity (E_{FRP}) of 169.5 GPa (CoV = 6.3%) were obtained [191].

Epoxy adhesive

The adhesive used in this study is a high performance, solvent-free, thixotropic, and grey two-component epoxy adhesive specially developed for bonding CFRP to concrete under the commercial name of *S&P 220 HP*. According to the manufacturer's product data sheet [143], the components A (resin) and B (hardener) should be mixed at a ratio of 2:1 by weight, and the suggested curing duration is 7 days. Tensile properties of the epoxy adhesive were determined by ISO-527-1 [144] specifications (see Table 6.4) [207]. To evaluate the effect of temperature on mechanical properties of the epoxy, the specimens were tested under 20 °C and 50 °C. The tensile strength ($f_{u,epoxy}$) and elastic modulus (E_{epoxy}) at 50 °C decreased by 30% and 47%, respectively, when testing temperature changed from 20 °C to 50 °C. Moreover, the glass transition temperature (T_g) of epoxy was also determined with differential scanning calorimetry

(DSC) [145] and dynamic mechanical analysis (DMA) [146]. According to test results, the T_g of epoxy was in the range of 53.9 °C – 65.3 °C [191].

Table 6.4. Mechanical properties of epoxy adhesive [207].

Testing temperature (°C)	$f_{u,epoxy}$ (MPa)	$f_{u,epoxy-50}$ / $f_{u,epoxy-20}$	E_{epoxy} (MPa)	$E_{epoxy-50}$ / $E_{epoxy-20}$
20	28.0 (0.4%)[a]	-	8102.4 (0.8%)[a]	-
50	19.6 (3.6%)[a]	0.7	4289.6 (2.3%)[a]	0.53

[a] Coefficient of variation (CoV) indicated in brackets.

The creep coefficient of epoxy adhesive (φ_{epoxy}) was also evaluated at 20 and 50 °C (see Figure 6.6). Three levels of long-term load (causing 20%, 40% and 60% of epoxy ultimate strain, 0.0035, obtained from tensile test) were applied to the specimens for a duration of 40 days (1000 h), which is similar to the duration used in the literature [7,101,103,104]. The long-term loading was applied through a gravity loading system with a lever arm with a magnification factor of 4 [7,212]. The temperature and humidity conditions applied during the epoxy tensile creep tests were the same as those of the beams. For each temperature, two specimens were tested, and all specimens included two strain gauges (one at each side). The creep coefficient of epoxy adhesive was obtained according to Eq. (6.2):

$$\varphi_{epoxy}(t, t_0) = \frac{\varepsilon_{epoxy}(t, t_0) - \varepsilon_{epoxy}(t_0)}{\varepsilon_{epoxy}(t_0)} \tag{6.2}$$

where $\varepsilon_{epoxy}\,(t,t_0)$ is the epoxy adhesive strain with time and $\varepsilon_{epoxy}\,(t_0)$ is the epoxy adhesive strain at the loading moment.

According to experimental results, epoxy creep coefficient at 20 °C was affected by the sudden drop in humidity and temperature in the laboratory taking place around 200 hours after loading (see Figure 6.6a). Besides, specimens tested at 50 °C failed after a few hours of loading (see Figure 6.6b).
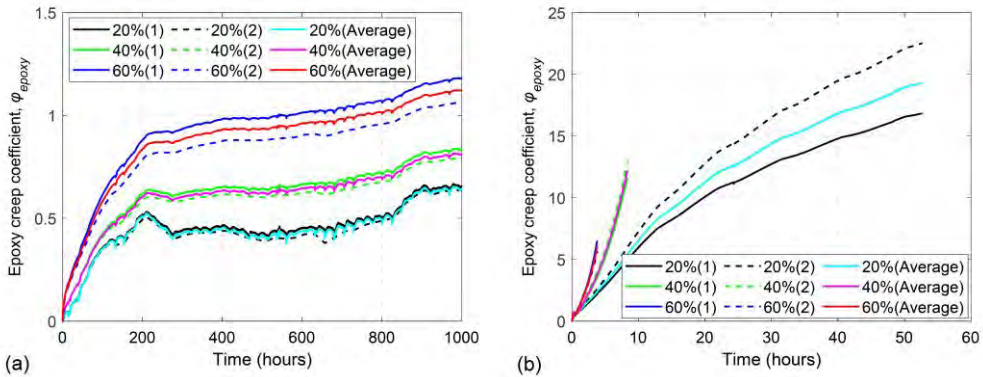
Figure 6.6. Creep coefficient of epoxy adhesive at: (a) 20 °C and (b) 50 °C.

6.2.5 Test procedure

In this experimental program, 4 loading stages were considered. In stage 1, the beams of Series 1 were tested under four-point bending configuration (see Figure 6.1a) to obtain their short-term flexural response. Tests were performed under displacement control mode at a rate of 0.6 mm/min.

In stage 2, prior to long-term test, beams were subjected to pre-loading in order to ensure a level of cracking corresponding to the service load. To this end, beams in Series 2 were subjected to two loading/unloading cycles up to service load level, P_{ser}. The service load was calculated by limiting the stress in compressed concrete ($\sigma_c<0.6f_c$) and steel reinforcement ($\sigma_s<0.8f_y$) [155]. For this pre-loading stage, the same test setup and loading rate as in stage 1 was used.

In stage 3, after the pre-loading, specimens in Series 2 were moved to the long-term loading frames (Figure 6.1b) and the long-term load was applied for a duration of 200 days. The long-term load was chosen to obtain a concrete compressive stress of 0.35 f_c, so that linear creep behavior of concrete was ensured by being under the *fib* Model Code 2010 limitation [83].

Finally, in stage 4, and after the long-term test, specimens in Series 2 were tested up to failure to evaluate their residual flexural strength. Additionally, specimens of Series 3, that were resting in the laboratory for aging, were tested to obtain their short-term flexural response. In this stage, the same test setup and loading rate as in stages 1 and 2 was used.

6.3 Experimental results and discussions

6.3.1 Short-term tests results

Results of short-term flexural tests (Series 1) are presented in Figure 6.7 in terms of load versus midspan deflection curves. In each curve, three phases can be distinguished: i) an initial linear behavior representing the elastic behavior of the uncracked element; ii) a second phase, starting at the cracking load (P_{cr}), where stiffness decreases and load can be increased up to yielding of steel reinforcement; and iii) a post-yielding phase up to failure. For the case of unstrengthened beams (CB), no significant differences between yielding load (P_y) and ultimate load (P_u) exist. For the case of strengthened beams, load can be further increased after steel yielding until the ultimate load. Experimental results of short-term tests (Series 1) are presented in Table 6.5. As a general result, the increase in the CFRP-strengthening ratio produces an increase in stiffness in the post-cracking and post-yielding stages, which results in larger yielding loads, P_y, and ultimate loads, P_u. According to results presented in Table 6.5, larger benefits of the CFRP-strengthening system were obtained in beams with lower steel reinforcement ratio, as expected and depicted by the comparison between the strength increase ratios of specimens in Groups 1 and 2. Finally, no significant effect of temperature is visible in the load-deflection curves. The similarity in short-term responses between specimens tested at 20 °C and 50 °C can be attributed to the fact that 50 °C was below the T_g of the epoxy (53.9 °C < T_g < 65.3 °C) and epoxy adhesive was post-cured and therefore its mechanical properties improved [9,191,207].
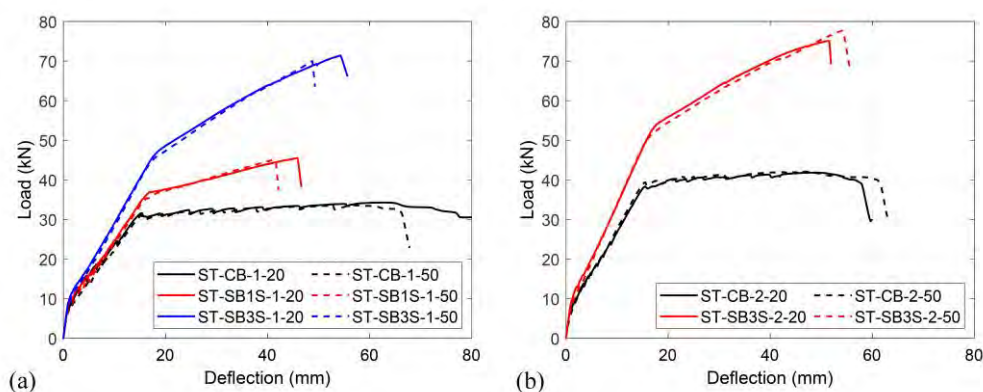
Figure 6.7. Load-deflection curves of specimens in Series 1: (a) Group 1 (ρ_s = 0.79%) and (b) Group 2 (ρ_s = 1.14%).

Table 6.5. Experimental results of specimens in Series 1 under short-term load.

Specimen ID	P_{cr} (kN)	P_y (kN)	P_u (kN)	Strength increase ratio [a]	Failure mode [b]
ST-CB-1-20	7.43	30.75	34.28	-	CC
ST-CB-1-50	7.00	30.00	33.57	-	CC
ST-SB1S-1-20	7.82	36.88	45.50	1.33	FR
ST-SB1S-1-50	6.00	35.36	45.15	1.34	FR
ST-SB3S-1-20	8.85	46.50	71.40	2.08	FR
ST-SB3S-1-50	6.75	45.25	70.00	2.09	FR
ST-CB-2-20	6.70	37.89	41.84	-	CC
ST-CB-2-50	5.95	38.71	42.10	-	CC
ST-SB3S-2-20	9.60	53.36	75.10	1.79	FR
ST-SB3S-2-50	8.20	51.00	77.68	1.85	FR

[a] Ratio of ultimate load of strengthened beam to ultimate load of the control unstrengthened beam of the same group.

[b] CC = concrete crushing after steel yielding; FR = FRP rupture.

Representative images of failure modes are shown in Figure 6.8. Unstrengthened control beams, with and without temperature, failed by concrete crushing (CC) after steel reinforcement yielding. Besides, all strengthened beams failed by FRP rupture, irrespective of the applied temperature and the CFRP-strengthening ratio, and no premature bond failure took place. It should be mentioned that results may change if different test configurations and/or larger temperatures were applied [191].

CC (ST-CB-1-50)   FR (ST-SB3S-1-50)   FR (ST-SB3S-20-20)

Figure 6.8. Representative views of failure modes of specimens in Series 1.

6.3.2   Pre-loading

Before the application of the long-term load, specimens of Series 2 were subjected to a pre-loading stage, consisting in two cycles of loading/unloading. First, the specimens were loaded up to the service load level (P_{ser}); then, two cycles were applied between the minimum load (2 kN) and maximum load (service load). Table 6.6 shows the experimental data from the pre-

loading stage for all of the specimens in Series 2. Finally, the specimens were rested to relax at laboratory conditions for 1 day prior to the application of the long-term load. Deflections were continuously registered, even during the relaxation period, so that the permanent deflection after a one-day relaxation ($\delta_{p,0}$) could be computed. Figure 6.9 presents representative load-deflection curves for the pre-loading process of LT-SB3S-1-20 and LT-SB3S-2-50. In this Figure, P_{LT} stands for level of long-term load to be applied in long-term tests.

(a)   (b)

Figure 6.9. Representative load-deflection curves for pre-loading process for specimens: (a) LT-SB3S-1-20 and (b) LT-SB3S-2-50.

Table 6.6. Experimental results for pre-loading stage in Series 2.

Specimen ID	P_{ser} (kN)	P_{LT} (kN)	$\delta_{p,0}$ (mm)
LT-CB-1-20			2.14
	20.4		
LT-CB-1-50			2.14
LT-SB1S-1-20			2.21
	24.8	13.8	
LT-SB1S-1-50			2.32
LT-SB3S-1-20			1.93
	27.1		
LT-SB3S-1-50			1.93
LT-CB-2-20			2.22
	26.5		
LT-CB-2-50			2.05
		15.8	
LT-SB3S-2-20			1.86
	30.0		
LT-SB3S-2-50			1.67

6.3.3   Time-dependent tests results

Following the pre-loading stage, beams in Series 2 were placed according to the setup shown in Figure 6.1b to be tested under long-term loading. The vertical transducer at midspan section

allowed registering the evolution of deflection due to long-term load. Similarly, the evolution of concrete strains was also recorded.

Deflections

The evolution of the total deflection (δ_{tot}) with time is presented in Figure 6.10. The total deflection results from the addition of the permanent deflection after pre-loading stage ($\delta_{p,0}$), the instantaneous deflection after the application of the long-term load (δ_{ins}) and the time-dependent deflection due to long-term load (δ_{td}). The markers in the vertical axis in Figure 6.10 represent the permanent deflection after pre-loading stage ($\delta_{p,0}$). Additionally, time-dependent deflections (δ_{td}) are presented in Figure 6.11. According to experimental results, summarized in Table 6.7, the increase of the CFRP-strengthening ratio in specimens tested at 20 °C resulted in a decrease in the three components of the total deflection (i.e. $\delta_{p,0}$, δ_{ins} and δ_{td}), irrespective of the steel reinforcement ratio. This is due to the increase in the tensile reinforcement stiffness and due to the same long-term load being applied in all specimens of the same group (i.e. long-term load to be applied was the same for control specimens and specimens with CFRP-strengthening).
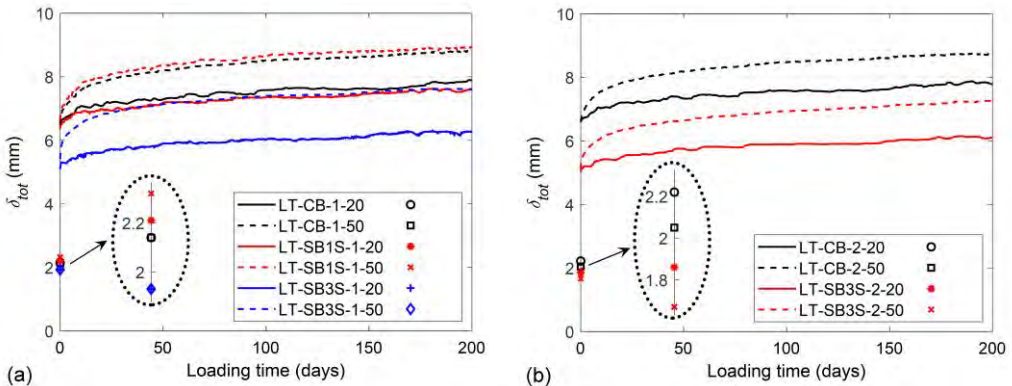
Figure 6.10. Total deflection of beams in Series 2: (a) Group 1 (ρ_s = 0.79%) and (b) Group 2 (ρ_s = 1.14%).
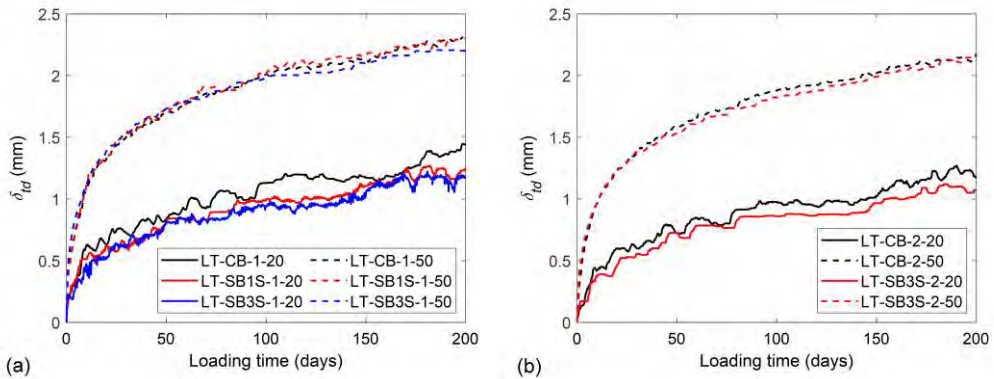
Figure 6.11. Time-dependent deflection of beams in Series 2: (a) Group 1 (ρ_s = 0.79%) and (b) Group 2 (ρ_s = 1.14%).

Experimental results on specimens tested at 50 °C revealed that the application of a high service temperature (50 °C) did not have remarkable effects on the instantaneous deflection after the application of the long-term load (δ_{ins}), when compared to that of specimens at 20 °C. However, the application of high service temperature had a clear effect on time-dependent deflections (δ_{td}), irrespective of the steel reinforcement ratio. In this sense, in Group 1, the time-dependent deflection in unstrengthened control beam (LT-CB-1-50) increased by 60% because of the application of 50 °C, and this percentage increase up to 85% for strengthened beams with either one or three strips (i.e. LT-SB1S-1-50 and LT-SB3S-1-50). Likewise, in Group 2, the time-dependent deflection increased by 86% and 100% in unstrengthened control beam (LT-CB-2-50) and strengthened beam (LT-SB3S-2-50), respectively. It should be mentioned that similar time-dependent deflections were obtained within the same Group of specimens tested at 50 °C, so that the time-dependent response of the strengthened beams approached to the unstrengthened beam.

An initial explanation lies in the larger concrete time-dependent properties (i.e. shrinkage and creep coefficient) at 50 °C. Based on experimental values for concrete shrinkage in prism specimens (see Figure 6.5a), the total shrinkage of the specimens from the day of loading increased from 100 µε at 20 °C to 240 µε at 50 °C. Furthermore, according to analytical predictions presented in Table 6.3, concrete creep coefficient increased from 0.60 to 2.64, showing a 340% difference. A secondary cause can be the detrimental effect of temperature on both instantaneous and time-dependent mechanical properties of the epoxy adhesive. In this sense, short-term values of epoxy tensile strength ($f_{u,epoxy}$) and elastic modulus (E_{epoxy}) decreased

by 30% and 47%, respectively, when epoxy was submitted to 50 °C (see Table 6.4). Additionally, higher creep coefficients were found for epoxy at 50 °C (see Figure 6.6). Nevertheless, it should be mentioned that the effect of higher temperature on the time-dependent behavior of concrete seems to be dominant, as the time-dependent deflections of the unstrengthened control beams in Groups 1 and 2 subjected to temperature (i.e. LT-CB-1-50 and LT-CB-2-50) were increased by 60% and 86%, respectively.

It should be mentioned that the fluctuations observed in the evolution of deflection at 20 °C (Figures 6.10 and 6.11) were probably due to large humidity variations taking place at the structural laboratory (see Figure 6.4a). For the case of heated specimens (submitted to 50 °C), minimum fluctuations in humidity were observed, because of the good performance of the heating and isolation systems (see Figure 6.4b).

The normalized deflections of the specimens ($\delta_{tot} / \delta_{ins,tot}$), where $\delta_{ins,tot} = \delta_{ins} + \delta_{p,0}$, are shown in Figure 6.12. According to experimental results, larger normalized deflections were obtained in specimens strengthened with three strips, and similar normalized deflections were obtained for beams strengthened with one strip and their counterpart unstrengthened beam. This is due to lower instantaneous deflections ($\delta_{ins,tot}$) for beams with three strips and similar time-dependent deflections (δ_{td}) for beams within the same Group. This effect is more clear when deflections of specimens under 50 °C are analyzed.
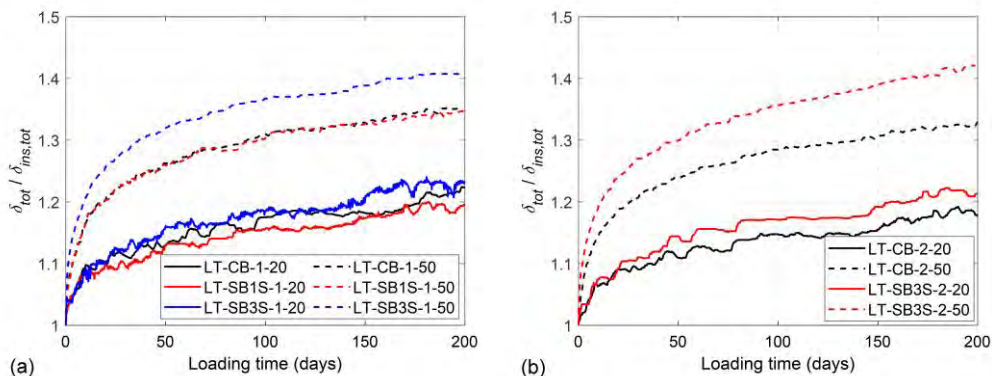
Figure 6.12. Ratio of total to instantaneous deflection of beams in Series 2: (a) Group 1 (ρ_s = 0.79%) and (b) Group 2 (ρ_s = 1.14%).

Table 6.7. Deflections from long-term load.

| Specimen ID | Deflections (mm) | | | | $\delta_{tot} / \delta_{ins,tot}$ |
	δ_{ins}	$\delta_{ins,tot} = \delta_{ins} + \delta_{p,0}$	$\delta_{td,max}{}^{a}$	$\delta_{tot} = \delta_{ins,tot} + \delta_{td,max}$	
LT-CB-1-20	4.31	6.45	1.44	7.89	1.22
LT-CB-1-50	4.36	6.50	2.31	8.81	1.36
LT-SB1S-1-20	4.15	6.36	1.24	7.6	1.19
LT-SB1S-1-50	4.31	6.63	2.30	8.93	1.35
LT-SB3S-1-20	3.16	5.09	1.18	6.27	1.23
LT-SB3S-1-50	3.48	5.41	2.20	7.61	1.41
LT-CB-2-20	4.39	6.61	1.17	7.78	1.18
LT-CB-2-50	4.55	6.60	2.18	8.78	1.33
LT-SB3S-2-20	3.17	5.03	1.07	6.1	1.21
LT-SB3S-2-50	3.44	5.11	2.14	7.25	1.42

[a] Maximum time-dependent deflection from Figure 6.11

Concrete strain

The total and time-dependent strain at the top fiber of concrete at the midspan section (see the position of SG_C in Figure 6.2) is shown in Figures 6.13 and 6.14 respectively. Similar to evolution of total and time-dependent deflections, strengthening with larger amounts of CFRP ratio resulted in a reduction in total and time-dependent concrete strain. In addition, the application of high service temperature produced a sharp increase in the time-dependent concrete strain. For instance, for unstrengthened control beams in Group 1 (LT-CB-1-50) and Group 2 (LT-CB-2-50), the time-dependent concrete strain was increased by 65% and 77%, respectively. For strengthened beams in Group 1 (LT-SB1S-1-50 and LT-SB3S-1-50) the percentage increased up to 79% and 88%, respectively. Furthermore, in strengthened specimens belonging to Group 2 (LT-SB3S-2-50), the time-dependent concrete strain was increased by 136%. According to the results from unstrengthened beams, and similar to the evolution of time-dependent deflections, time-dependent strains in concrete were mostly affected by concrete time-dependent properties and how they depend on service temperature.

Figure 6.13. Top fiber concrete total strain evolution: (a) Group 1 (ρ_s = 0.79%) and (b) Group 2 (ρ_s = 1.14%).
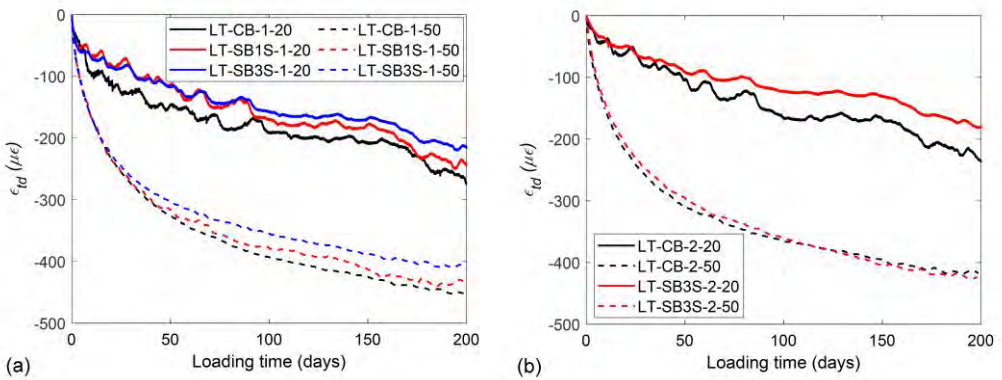
Figure 6.14. Top fiber concrete time-dependent strain evolution: (a) Group 1 (ρ_s = 0.79%) and (b) Group 2 (ρ_s = 1.14%).

6.3.4 Residual flexural strength and aging effect

Following long-term tests, specimens in Series 2 were tested up to failure to evaluate their residual flexural strength. The initial deflection prior to the post long-term tests was obtained by registering the ultimate permanent deflection ($\delta_{p,u}$) after removing the long-term load. In addition, specimens in Series 3 were also tested up to failure to evaluate the aging effect on their instantaneous load-deflection response. Figure 6.15 shows representative load-deflection curves, and detailed results are listed in Table 6.8.

The ultimate permanent deflection ($\delta_{p,u}$) was used to plot the load-deflection curves of specimens in Series 2 during their testing up to failure after long-term loading (see Figure 6.15). According to the results presented in Table 6.8, it is worthy to mention that the ultimate

135

permanent deflection of specimens subjected to 50 °C was larger than that of specimens at 20 °C, which was in agreement with the trend in time-dependent deflections.
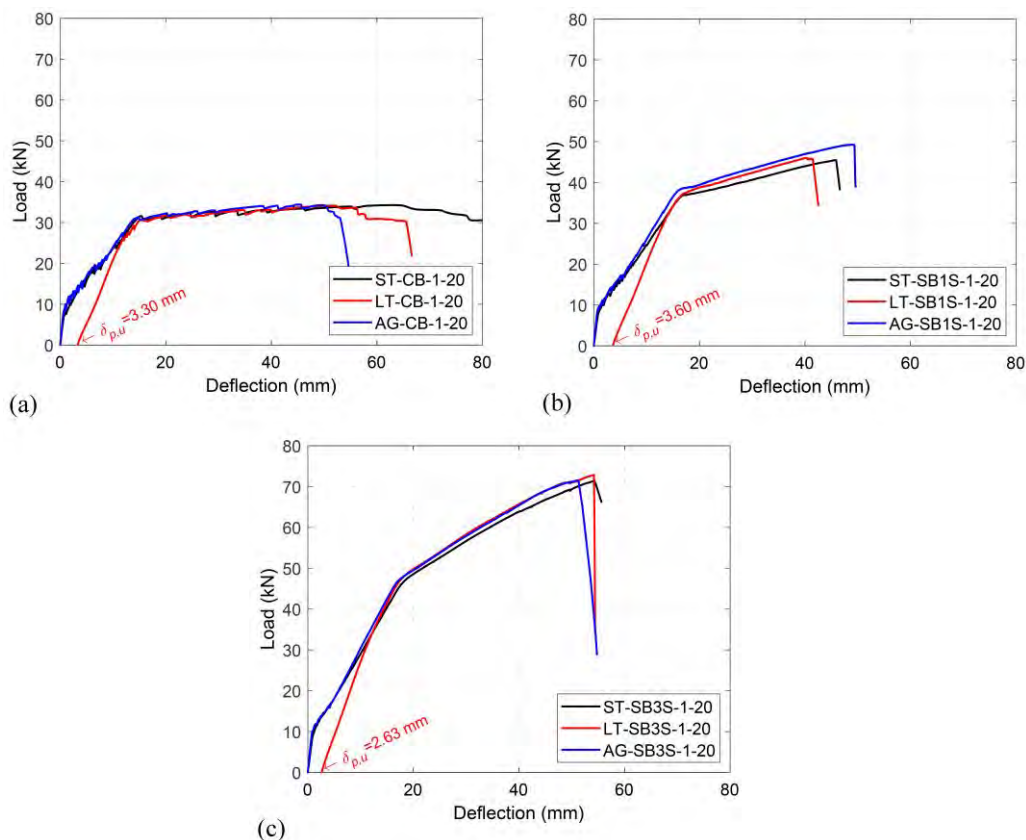
Figure 6.15. Representative load-deflection curves for the analysis of residual flexural strength and aging effect: (a) Unstrengthened control beams in Group 1, (b) Strengthened beams with one strip in Group 1, (c) Strengthened beams with three strips in Group 1.

The comparison between results in Series 1 and Series 2 (black and red lines in Figure 6.15, respectively) allows accounting for the residual strength of the beams after long-term load. For the case of unstrengthened control beams, similar yielding loads and post-yielding behavior were obtained. The differences in their ultimate deflection can be attributed to the failure mode (concrete crushing) and the values for concrete compressive strain at failure. For the case of strengthened beams, in general slightly higher values for yielding load and post-yielding stiffness were found for the case of beams submitted to previous long-term load, irrespective of the temperature applied during the long-term tests. It should be mentioned that failure mode for strengthened beams remained to be FRP rupture, except for the case of beams strengthened

with three strips in Group 2 (LT-SB3S-2-20 and LT-SB3S-2-50). In these latter cases, premature cracking initiated in the compression zone of the specimens and, due to the increase in deflection (and curvature), FRP rupture took place (see Figure 6.16). This change in failure mode from FRP rupture (FR) to concrete crushing followed by FRP rupture (CC-FR) may be the cause of lower ultimate loads.

Table 6.8. Results for the analysis of residual flexural strength and aging effect.

Specimen ID	P_y (kN)	P_u (kN)	Stiffness [a] (kN/mm)	$\delta_{p,u}$ (mm)	Failure mode [b]
LT-CB-1-20	30.43	34.17	3.30	3.30	CC
AG-CB-1-20	30.91	34.42	1.41	-	CC
LT-CB-1-50	29.50	34.05	3.06	5.30	CC
LT-SB1S-1-20	37.25	46.03	3.23	3.60	FR
AG-SB1S-1-20	38.68	49.28	1.75	-	FR
LT-SB1S-1-50	35.72	44.90	2.90	4.48	FR
LT-SB3S-1-20	47.00	72.85	3.64	2.63	FR
AG-SB3S-1-20	47.26	71.56	2.12	-	FR
LT-SB3S-1-50	46.48	69.80	3.46	4.01	FR
LT-CB-2-20	38.00	41.07	3.58	2.48	CC
LT-CB-2-50	38.48	42.73	3.47	4.29	CC
LT-SB3S-2-20	53.57	74.41	4.41	2.80	CC-FR
LT-SB3S-2-50	52.46	73.00	4.20	3.38	CC-FR

[a] Computed as the slope of load-deflection curve between long-term load level and service load level.
[b] CC = concrete crushing after steel yielding; FR = FRP rupture; CC-FR = Concrete crushing followed by FRP rupture.

The effect of long-term loading is also visible in the initial stiffness of the load-deflection curves. Beams in Series 2 being partially cracked derived in the elastic slope lying between the un-cracked and cracked stages. The stiffness presented in Table 6.8 was computed as the ratio between load and deflection corresponding to the long-term load level and the service load level. Initial stiffness of specimens subjected to long-term loading (Series 2) were, by far, the largest ones (see Figure 6.15 and Table 6.8). This behavior is similar to what happened during the pre-loading stage, where two cycles of loading/unloading were applied. Finally, the effect of high service temperature is reflected in the reduction of initial stiffness, when compared to specimens tested at 20 °C. This is again a consequence of larger concrete time-dependent

properties causing larger ultimate permanent deflections after the removal of the long-term load ($\delta_{p,u}$).

For the analysis of the aging effect, results in Series 1 and Series 3 (black and blue lines in Figure 6.15, respectively) should be compared. Similar to what was found in the analysis of the residual strength after long-term load, identical load-deflection curves were obtained for unstrengthened control beams and slightly larger yielding loads and post-yielding stiffness were found for strengthened beams. Failure modes of aged beams did not change when compared to that of Series 1.

CC (AG-CB-1-20) FR (LT-SB3S-1-50) CC-FR (LT-SB3S-2-50)
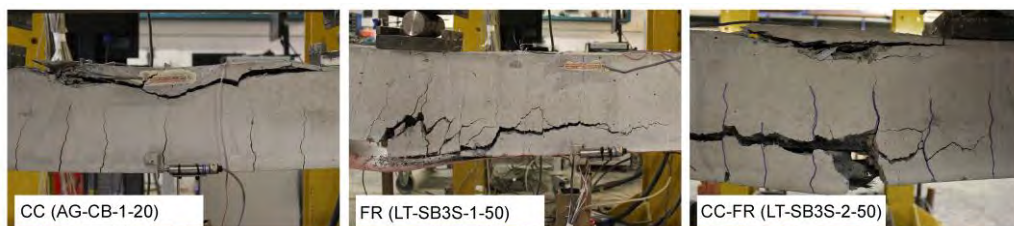
Figure 6.16. Representative view of failure modes of the specimens in Series 2 and 3.

6.4 Analytical predictions on time-dependent deflections

In this section, an analytical procedure based on Gilbert [84] is used to predict time-dependent deflections of CFRP NSM strengthened RC elements. Within the procedure, the age-adjusted effective modulus method (AEMM) is used in the cross-sectional analysis to determine how stresses, strains and curvatures vary with time due to creep and shrinkage of concrete. A schematic view of beam cross-section is shown in Figure 6.17a. Furthermore, in both types of loading (i.e. short-term and long-term), a linear distribution of strains was assumed (see Figure 6.17b).
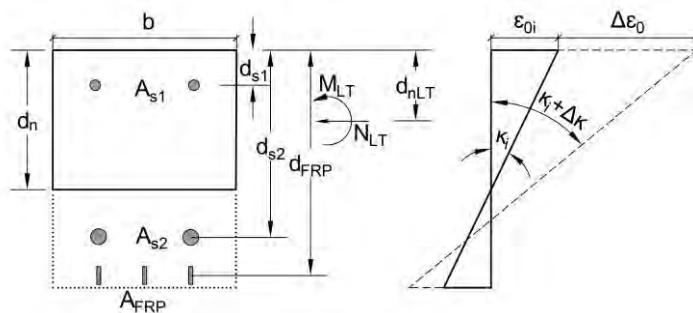
Figure 6.17. Time-dependent analysis: (a) Schematic view of beam cross-section and (b) Instantaneous and long-term strains and curvatures in a cracked section.

Assuming a linear strain distribution (as shown in Figure 6.17b), the instantaneous response of a cracked section, in terms of instantaneous maximum concrete compressive strain (ε_{0i}) and initial section curvature (κ_i), can be calculated as follows:

$$\varepsilon_{0i} = \frac{BM_{LT} + IN_{LT}}{E_c(AI - B^2)} \tag{6.3}$$

$$\kappa_i = \frac{AM_{LT} + BN_{LT}}{E_c(AI - B^2)} \tag{6.4}$$

where M_{LT} and N_{LT} are the moment and axial force applied at the beginning of the long-term loading, respectively ($N_{LT} = 0$ for RC sections under flexural moment only). Moreover, A is the area of the transformed section, and B and I are the first and second moments of inertia of the area of the transformed section, respectively. Furthermore, E_c is the modulus of elasticity of concrete.

Based on Gilbert [84], the variation with time (i.e. time-dependent) of the maximum concrete compressive strain $\Delta\varepsilon_0 (t,t_0)$ and section curvature $\Delta\kappa (t,t_0)$ can be calculated as follows:

$$\Delta\varepsilon_0(t,t_0) = \frac{B_e(t,t_0)\Delta M(t,t_0) + I_e(t,t_0)\Delta N(t,t_0)}{E_e(t,t_0)(A_e(t,t_0)I_e(t,t_0) - B_e^2(t,t_0))} \tag{6.5}$$

$$\Delta\kappa(t,t_0) = \frac{A_e(t,t_0)\Delta M(t,t_0) + B_e(t,t_0)\Delta N(t,t_0)}{E_e(t,t_0)(A_e(t,t_0)I_e(t,t_0) - B_e^2(t,t_0))} \tag{6.6}$$

where t is the age of specimen at the moment considered in days and t_0 is the age of specimen at the beginning of long-term loading in days. In Eqs. 6.5 and 6.6, $A_e (t,t_0)$ is the area of the transformed section, and $B_e (t,t_0)$ and $I_e (t,t_0)$ are the first and second moments of inertia of the area of the transformed section, respectively. Finally, $\Delta M (t,t_0)$ and $\Delta N (t,t_0)$ are the restraining force and moment to prevent free development of creep and shrinkage in concrete, and can be calculated as:

$$\Delta N(t,t_0) = E_e(t,t_0)[\varphi_c(t,t_0)(A_c\varepsilon_{oi} - B_c\kappa_i) + \varepsilon_{sh}(t,t_0)A_c] \tag{6.7}$$

$$\Delta M(t,t_0) = E_e(t,t_0)[\varphi_c(t,t_0)(-B_c\varepsilon_{oi} + I_c\kappa_i) - \varepsilon_{sh}(t,t_0)B_c] \tag{6.8}$$

where A_c is the area of the concrete section, and B_c and I_c are the first and second moments of inertia of the area of the concrete section (without considering the steel reinforcement), respectively. The instantaneous maximum concrete compressive strain (ε_{0i}) and initial section curvature (κ_i) can be computed from Eqs. 6.3 and 6.4, respectively. In addition, $\varphi_c (t,t_0)$ and $\varepsilon_{sh}(t,t_0)$ are the concrete creep coefficient and shrinkage, and $E_e (t,t_0)$ is the effective modulus of elasticity of concrete. In this work, *fib* Model Code 2010 [83] predictions for concrete creep

coefficient and shrinkage were assumed. Besides, in applying the AEMM, the effective modulus of elasticity of concrete can be obtained as bellow:

$$E_e(t, t_0) = \frac{E_c}{1 + \chi(t, t_0)\varphi_c(t, t_0)} \tag{6.9}$$

where χ (t, t_0) is the reduction factor for concrete creep coefficient, which can be taken as 0.8 for normal strength concrete [82,84,106,109].

It should be mentioned that, in addition to the explicit mention of E_e (t, t_0) in Eqs. 6.5-6.8, the effective modulus of concrete should also be taken into account for the calculation of geometrical properties of the transformed section, by updating the time-dependent steel modular ratio, n_s (t, t_0), and time-dependent FRP modular ratio, n_{FRP} (t, t_0), as follows:

$$n_s(t, t_0) = E_s/E_e(t, t_0) \tag{6.10}$$

$$n_{FRP}(t, t_0) = E_{FRP}(t, t_0)/E_e(t, t_0) \tag{6.11}$$

where E_s is the modulus of elasticity of steel reinforcement and E_{FRP} (t, t_0) is the modulus of elasticity of FRP.

6.4.1 Comparison with experimental results

In this section, analytical predictions following the previously presented methodology are compared to experimental results on time-dependent deflections (shown in Figure 6.11). For the analytical predictions, average values for registers on temperature and humidity during the long-term load (see Figure 6.4) were used for determining the concrete creep coefficient and shrinkage following *fib* Model Code 2010 [83]. In addition, the effect of temperature on mechanical properties of concrete was considered according to fib Mode Code 2010 [83]. It should be mentioned that temperature gradient in the height of the section causes an additional curvature/deflection that should be taken into account [84]. In this study, due to uniform heating, the difference in temperature between the bottom and top fibers was about 5 °C, thus causing a negligible extra curvature/deflection.

Comparisons of predicted and experimental time-dependent deflections are shown in Figures 6.18-6.20. According to the results, the analytical predictions at 20 °C underestimate the time-dependent deflection, especially for the unstrengthened control beam with lower steel reinforcement ratio (LT-CB-1-20 with ρ_s = 0.79%). Focusing on the prediction of the time-dependent deflections in specimens under a high service temperature, in general, analytical predictions overestimate the time-dependent deflection especially for those of the unstrengthened control beams (LT-CB-1-70 and LT-CB-2-70). It is worthy to mention that the

140

presented analytical methodology could be also applied to members subjected to cyclic temperatures, as for instance day-night or summer-winter. In that case, the temperature and humidity histories should be considered as an input in the analytical model.

Figure 6.18. Analytical predictions and experimental time-dependent deflections for unstrengthened control beams: (a) Group 1 (LT-CB-1-20 and LT-CB-1-50) and (b) Group 2 (LT-CB-2-20 and LT-CB-2-50).
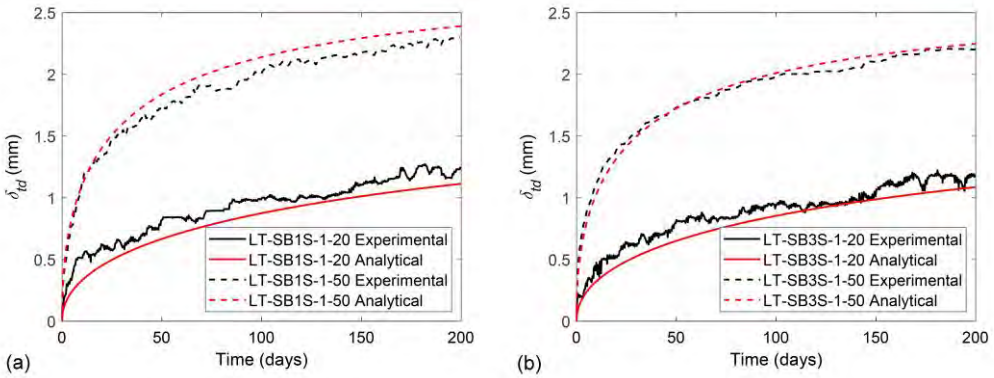
Figure 6.19. Analytical predictions and experimental time-dependent deflections for strengthened beams in Group 1 having: (a) one CFRP strip (LT-SB1S-1-20 and LT-SB1S-1-50) and (b) three CFRP strips (LT-SB3S-1-20 and LT-SB3S-1-50).
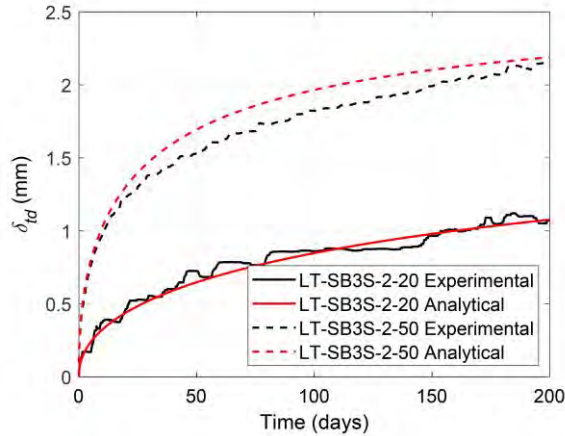
Figure 6.20. Analytical predictions and experimental time-dependent deflections for strengthened beams in Group 2 (LT-SB3S-2-20 and LT-SB3S-2-50).

6.5 Conclusions

The present experimental work aims to study the long-term performance of NSM CFRP-strengthened RC beams under different service temperatures. An experimental campaign consisting of 23 NSM CFRP-strengthened RC beams was performed, where beams with different steel reinforcement ratios and different amounts of CFRP-strengthening ratio were loaded for 200 days. After that, post long-term tests were carried out to analyze the residual flexural strength as well as the ageing effect. Besides, an analytical procedure for the prediction of time-dependent deflections is presented and compared to experimental results.

As a general conclusion, temperature did not affect the instantaneous flexural performance of NSM CFRP-strengthened RC beams, but had a significant effect on their time-dependent behavior and ultimate permanent deflections. More detailed conclusions are presented next.

From the short-term tests, the following conclusions can be drawn:

- The increase in the service temperature up to 50 °C had no significant effect on the load-deflection response of the specimens. This can be attributed to this temperature being below the T_g of epoxy adhesive and to an additional possible post-curing of the epoxy adhesive.

- The application of a high service temperature did not affect failure modes, and unstrengthened beams failed by concrete crushing after yielding of the steel reinforcement whilst strengthened beams failed by FRP rupture.

142

From the long-term tests and analytical predictions, the following conclusions can be drawn:

- The increase in the temperature from 20 °C to 50 °C had an effect on the time-dependent behavior of concrete (larger shrinkage and creep coefficient) and epoxy resin (larger creep coefficient).

- Under 20 °C and the same value of long-term load, lower time-dependent deflections were obtained for beams with larger amounts of FRP-strengthening ratio, as expected. However, for testing temperature equal to 50 °C, the increase in the strengthening ratio did not have a significant effect on the time-dependent deflections and the time-dependent response of the strengthened beams approached that of the unstrengthened beams.

- The effect of temperature on the time-dependent behavior of concrete appeared to be the dominant factor in time-dependent response of RC beams.

- Analytical predictions based on AEMM and *fib* Model Code 2010 were in a good agreement with experimental data.

From the residual flexural strength tests and aging specimens, following conclusions can be drawn:

- Similar to time-dependent deflections, the ultimate permanent deflection of specimens subjected to 50 °C was larger than that of specimens at 20 °C.

- When compared to short-term and aging specimens, no significant change was observed in the residual strength of unstrengthened control beams. On the other hand, for the strengthened beams, a slight increase in yielding load and post-yielding stiffness were found.

- Failure mode of the strengthened specimens with higher reinforcement was changed from FRP rupture to concrete crushing followed by FRP rupture. The rest of the specimens had the same failure mode as in short-term testing.

- The largest initial stiffness was observed for the specimens subjected to long-term load. Furthermore, the specimens subjected to temperature had lower initial stiffness due to larger permanent accumulated deflections.

7 Paper D: Effect of fatigue loading on flexural performance of NSM CFRP-strengthened RC beams under different service temperatures

Younes Jahani[1], Marta Baena[1*], Cristina Barris[1], Lluís Torres[1] and José Sena-Cruz[2]

[1]AMADE, Polytechnic School, University of Girona, 17003, Girona, Spain

[2]University of Minho, ISISE, Department of Civil Engineering, Guimarães, Portugal

[*]Corresponding author

Effect of fatigue loading on flexural performance of NSM CFRP-strengthened RC beams under different service temperatures

Younes Jahani[1], Marta Baena[1*], Cristina Barris[1], Lluís Torres[1] and José Sena-Cruz[2]

[1] AMADE, Polytechnic School, University of Girona, 17003 Girona, Spain

[2] University of Minho, ISISE, Department of Civil Engineering, Guimarães, Portugal

[*] Corresponding author: marta.baena@udg.edu

Abstract

This paper presents an experimental work to investigate the effect of fatigue loading and high service temperature on the flexural performance of near-surface mounted (NSM) carbon fiber-reinforced polymer (CFRP)-strengthened reinforced concrete (RC) beams. The experimental program included 11 beams, where the effect of the strengthening (CFRP) ratio (0.06% and 0.18%), fatigue load level (R1=0.57 and R2=0.38) and applied temperature (20 °C and 70 °C) have been considered. Experimental results on fatigue tests showed that high service temperature resulted in an increase in deflections and reduction in the stiffness of the specimens along the test. Moreover, the application of fatigue cycles with larger amplitude resulted in the failure of the specimens (by steel rupture), whilst specimens submitted to lower fatigue amplitude survived to the fatigue cycles. The NSM CFRP-strengthening helped to postpone the final failure of strengthened RC beams after steel reinforcement rupture during the fatigue test. Besides, damage due to fatigue derived in lower residual yielding and ultimate load in the post-fatigue test.

Keywords: Fatigue, NSM CFRP-strengthening, temperature, experimental

7.1   Introduction

Rehabilitation of civil structures needs attention in order to increase their lifetime and load-carrying capacity. These structures can be degraded by environmental factors and repeated loading (e.g. fatigue) that transfers to the structural members along a certain period and frequency [213-215]. Fatigue failure of a structural element is defined as a progressive cracking/damaging in the materials composing the element up to fracture under repeated loading. Unlike short-term loading, fatigue loading causes a reduction in stiffness of the system due to stress/strain accumulation in the materials that may lead to a failure in the system before reaching its ultimate capacity [116,215,216].

In the last decades, fiber-reinforced polymer (FRP) materials, available in different types and shapes, have been promoted to strengthen distressed structures. Nowadays, different techniques are used in FRP-strengthened structures, namely externally bonded reinforcement (EBR) and near-surface mounted (NSM) techniques [217], being the later the most recent one. In this technique, grooves are cut in the concrete surface and then the FRPs are inserted into these grooves using a proper adhesive. When compared to the EBR system, the NSM technique has several advantages such as: no need for surface treatment, less susceptible to environmental conditions, less prone to vandalism and good finished surface, among others [5,30].

Due to the nature of epoxy adhesives typically used in the NSM FRP-strengthening technique, their mechanical properties can be affected by the application of temperature variations or constant temperature approaching the glass transition temperature (T_g) of the adhesive [8,9,149,207]. Although a significant amount of work on the flexural behavior of NSM FRP-strengthened RC beams under short-term loading exists [5,6,30,43,47,56,218], few studies addressing the effect of high service temperature have been published [36,37,191].

Regarding the fatigue behavior of the FRP-strengthened RC beams, a significant amount of work has been done for the EBR FRP-strengthening system [118,119,123-128,219], whereas less literature exists for the case of NSM FRP-strengthening [67,69,120-122]. The fatigue behavior of RC beams strongly depends on the stress range in steel reinforcement. According to the literature, fatigue life decreases if the fatigue load level or/and the fatigue cycle amplitude are increased [67,118-120], and vice versa [121,122].

Existing studies confirm that fatigue life of EBR CFRP-strengthened beams is higher, when compared to unstrengthened control beams, because of the relief of stresses in internal steel reinforcement [123]. However, the inclusion of EBR CFRP-strengthening has no effect on failure mode, and unstrengthened and strengthened beams fail by steel reinforcement rupture [118,119,123-126], as a result of the stress/strain accumulation in the steel reinforcement. Steel rupture is occasionally followed by a deboning of FRP laminate from concrete surface. Focusing on the effect of environmental conditions on the fatigue performance, fatigue life of EBR CFRP-strengthened specimens is reduced when subjected to the hot-wet environmental conditions [127], and any increase in the corrosion degree (which is more common in old bridge structures) results in a reduction in the fatigue life in both strengthened and unstrengthened beams [128]. Moreover, the effect of temperature was studied in [219], where the application of 50 °C had

no effect on the fatigue behavior of EBR CFRP-strengthened specimens. However, their post fatigue residual strength slightly improved due to possible post-curing in the epoxy adhesive at that temperature [219].

Similarly, results on the fatigue performance of NSM FRP-strengthened RC elements confirm the extension in fatigue life of strengthened specimens and the steel reinforcement rupture failure mode [67,69,120]. However, unlike EBR systems, no debonding occurred after steel rupture [136]. In fact, NSM technique has shown better fatigue performance than EBR technique in those cases where comparative studies have been performed [55,65,136]. Finally, different types of NSM bars and strips [67,69,120] and bonding material [121] have been considered in the evaluation of the fatigue behavior of NSM FRP-strengthened RC elements. In this sense, for a given level of load, sandblasted rods performed better than spirally wound rods [69], and strips performed even better [120]. Besides, a better fatigue performance was observed when cementitious adhesives were used, in comparison to epoxy adhesives, and this was attributed to the better bond and stress transfer between the CFRP strips and concrete [121].

According to the literature, there is a significant amount of work in evaluating the effect of fatigue loading on the performance of EBR FRP-strengthened RC beams, that reduces when we focus on NSM FRP-strengthened RC elements. Besides, to the best of authors knowledge, the analysis on the effect of high service temperature on the fatigue response of NSM carbon FRP (CFRP) strengthened RC beams has not been addressed yet. In this work, an experimental program to investigate the fatigue behavior of NSM CFRP-strengthened RC beams subjected to room temperature (20 °C) and high service temperature (70 °C) is presented. To this end, a total of 11 beams were tested where different parameters were considered: (i) CFRP-strengthening ratio, (ii) testing temperature and (iii) fatigue load range. The fatigue tests were programed up to 2 million cycles if failure does not occur before, with a frequency of 2Hz. Experimental results are presented and discussed in terms of instantaneous load-deflection response of the reference beams, cyclic load-deflection response and evolution of deflection, stiffness, concrete strain and dissipated energy along fatigue cycles. Finally, post-fatigue behavior of the beams and failure modes are also analyzed.

7.2 Experimental program

7.2.1 Materials

Concrete

All the beams were casted using the same batch of ready-mix concrete in laboratory conditions with conventionally vibrating procedure. The cement type was II-42.5R, with a content of 320 kg/m³, the maximum aggregate size was 12 mm, and the water/cement ratio was 0.5. To improve concrete workability, a viscosity modifier was used. The experimental compressive strength (f_c), tensile strength (f_t), and modulus of elasticity (E_c) of concrete were determined at different ages of concrete at room temperature, so that concrete properties were tracked along the whole experimental campaign. To this end, cylinder specimens with 300 mm nominal height and 150 mm nominal diameter were used to determine the f_c, f_t, and E_c according to UNE-EN 12390-3:2003 [137], UNE-EN 12390-6:2010 [138], and ASTM C469-87 [139] standards, respectively. For each test, three specimens were used. Concrete mechanical properties at different ages are shown in Table 7.1.

Table 7.1. Concrete mechanical properties.

Concrete age (days)	Compressive strength, f_c (MPa)	Tensile strength, f_t (MPa)	Modulus of elasticity, E_c (GPa)
31	32.2 (2.2%)[b]	3.1 (1.2%)[b]	37.7 (4.2%)[b]
107[a]	40.7 (2.2%)[b]	3.5 (6.8%)[b]	38.0 (5.6%)[b]
150	41.1 (2.5%)[b]	3.8 (3.6%)[b]	39.9 (3.8%)[b]
204	41.4 (4.8%)[b]	3.7 (8.3%)[b]	39.0 (7.6%)[b]

[a] Age at first fatigue test.

[b] Coefficient of variation (CoV).

Steel reinforcement

In this work, ribbed steel bars with a diameter of 6 mm, 8 mm and 10 mm were used. The tensile mechanical properties of steel bars were obtained from tension tests based on UNE-EN ISO 15630-1 [141]. For each diameter, three samples were tested. Results on the yielding stress (f_y), the ultimate stress (f_u) and the modulus of elasticity (E_s) are reported in Table 7.2.

Table 7.2. Tensile mechanical properties of steel bars.

Bar diameter (mm)	Yielding stress f_y (MPa)	Ultimate stress, f_u (MPa)	Modulus of elasticity, E_s (GPa)
6	553.8 (1.6 %)[a]	703.5 (1.9%)[a]	203.6 (0.8%)[a]
8	536.7 (3.3%)[a]	698.1 (1.9%)[a]	196.4 (3.0%)[a]
10	544.1 (2.9%)[a]	666.0 (1.6%)[a]	202.1 (5.5%)[a]

[a] Coefficient of variation (CoV).

CFRP strips

CFRP strips, consisting of unidirectional carbon fibers (with a volume content fiber higher than 68%) held together by an epoxy vinyl ester resin matrix, were used for strengthening the specimens [20]. The CFRP strips had a cross-section of 1.4 × 10 mm and their tensile mechanical properties were obtained from five CFRP samples, according to ISO 527-5 [142] recommendations. An ultimate tensile strength ($f_{u,FRP}$) of 2251.4 MPa (CoV = 3.2%), an ultimate tensile strain ($\varepsilon_{u,FRP}$) of 0.0133 (CoV = 7.2%), and a modulus of elasticity (E_{FRP}) of 169.5 GPa (CoV = 6.3%) were obtained [191].

Epoxy adhesive

In this study, a high performance, solvent-free, thixotropic, and grey two-component epoxy adhesive specially developed for bonding CFRP to concrete was used. According to the manufacturer's product data sheet [143], the components A (resin) and B (hardener) should be mixed at a ratio of 2:1 by weight. The glass-transition temperature (T_g) of epoxy was determined by differential scanning calorimetry (DSC) [145] and dynamic mechanical analysis (DMA) [146]. The epoxy specimens were tested after a curing time at laboratory conditions of 12 days. According to test results, the T_g of epoxy was in the range of 53.9 °C–65.3 °C [191].

Tensile strength ($f_{u,epoxy}$) and elastic modulus (E_{epoxy}) of the epoxy adhesive were determined by testing dog-bone specimens following ISO-527-1 [144] specifications. Furthermore, in order to evaluate the effect of temperature on mechanical properties of the epoxy adhesive, characterization tests were performed at 20 °C and 70 °C. The mechanical properties of epoxy adhesive are summarized in Table 7.3 [207].

Table 7.3. Mechanical properties of epoxy adhesive tested at different temperatures [207].

Testing temperature (°C)	$f_{u,epoxy}$ (MPa)	$f_{u,epoxy-70}$ / $f_{u,epoxy-20}$[a]	E_{epoxy} (MPa)	$E_{epoxy-70}$ / $E_{epoxy-20}$[a]
20	28.0 (0.4%)[b]	-	8102.4 (0.8%)[b]	-
70	2.7 (3.7%)[b]	0.1	271.5 (4.8%)[b]	0.03

[a] Defined as the ratio between the property value at 70 °C and the reference property value at 20 °C.

[b] Coefficient of variation (CoV).

7.2.2 Test program and configuration

The experimental program included 11 beams divided into two series, where the effect of different parameters was studied, namely: (i) strengthening ratio (i.e. one and three CFRP strips), (ii) temperature (i.e. 20 and 70 °C) and (iii) R ratio (i.e. 0.57 and 0.38). In this sense, R ratio is defined as the ratio between minimum load and maximum load of the fatigue cycle. In Series 1, three beams were considered as reference beams to be tested under short-term loading in order to define the fatigue load level to be applied to beams in Series 2 (see Table 7.4). Among these three reference beams, one beam was unstrengthened and the other two beams were strengthened with one and three CFRP strips, respectively. All beams in Series 1 were tested at 20 °C. In Series 2, eight beams were tested under different fatigue loading levels and temperatures. This series was divided into two groups, according to the temperature applied during the fatigue test (Groups 1 and 2 refer to beams tested at 20 °C and 70 °C, respectively). Each of these two groups included four beams, three of them tested with a R ratio equal to 0.57 and one of them with an R ratio equal to 0.38 (see Table 7.4).

The fatigue load level was defined based on the yielding stress of the reinforcing steel (f_y) of the reference beams under short-term loading (Series 1). In this sense, for the fatigue level R1, the minimum fatigue load (P_{min}) and the maximum fatigue load (P_{max}) were those causing the stress in reinforcing steel to be equal to 40% and 70% of its yielding stress (f_y) at the corresponding reference beam, respectively, which led to a R ratio equal to 0.57. For the fatigue level of R2, this range was between 30% and 80% of f_y of the corresponding reference beam, respectively, which led to a R ratio equal to 0.38. The maximum load was limited to be less than the load causing 80% of steel yielding stress (f_y), according to ACI 440.2R [99].

Specimens' designation reads X-Y-Z, where X denotes the type of beam (CB standing for control beam, and SB1S and SB3S referring to beams strengthened with one and three CFRP strips, respectively). Furthermore, Y stands for the testing temperature. Finally, Z indicates the

loading type (ST standing for short-term loading, and R1 and R2 referring to fatigue loading with different R ratios). For instance, CB-20-ST, refers to the control beam tested at 20 °C under short-term loading. Furthermore, SB3S-70-R1 refers to a beam strengthened with three CFRP strips and tested at 70 °C under fatigue loading with R=0.57.

Table 7.4. Test matrix for fatigue loading.

Series	Group	Beam ID	Age of concrete [a] (days)	No. of CFRP strips	CFRP area (mm²)	Testing Temperature (°C)	R ratio
Series 1	-	CB-20-ST	104	-	-	20	-
		SB1S-20-ST	138	1	14		-
		SB3S-20-ST	170	3	42		-
Series 2	Group 1	CB-20-R1	107	-	-	20	0.57
		SB1S-20-R1	142	1	14		0.57
		SB3S-20-R1	171	3	42		0.57
		SB3S-20-R2	199	3	42		0.38
	Group 2	CB-70-R1	126	-	-	70	0.57
		SB1S-70-R1	158	1	14		0.57
		SB3S-70-R1	184	3	42		0.57
		SB3S-70-R2	206	3	42		0.38

[a] Age of concrete at the beginning of fatigue test.

The beams were tested under a four-point bending test configuration (see Figure 7.1). The beams were 2400 mm long (clear span of 2200 mm), 140 mm wide and 180 mm deep. The loading span and shear span were 700 mm and 750 mm, respectively. Two longitudinal steel bars with 10 mm of diameter (2Φ10) were used in the tension side of the beam, resulting in a reinforcement ratio, ρ_s, of 0.79%. Moreover, 2Φ6 were used in the compression side of the beams. All beams had shear reinforcement consisting of steel stirrups with a diameter of 8 mm placed every 75 mm. In the strengthened beams, CFRP strips with a cross-section of 1.4 × 10 mm and a bonded length of 1950 mm were used. In order to mount the CFRP strips, grooves with dimensions of 6 × 15 mm were cut in the soffit of the beams. In those beams were more than one groove was needed the distance between grooves was set based on *fib* Bulletin 90 [1] recommendations. Finally, during the cutting of the grooves, a notch (5 mm wide and 15 mm deep) was created at midspan in order to act as a crack initiator.
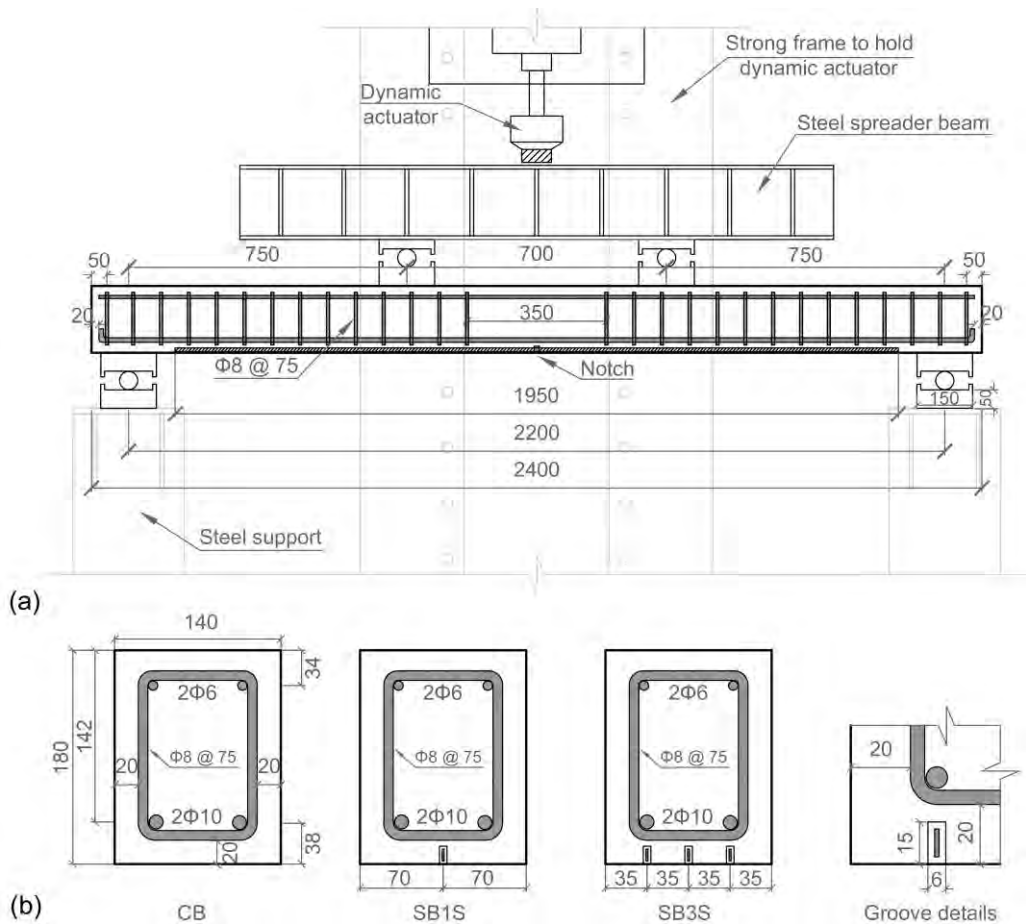
Figure 7.1. Four-point bending test configuration: (a) Test setup and (b) Cross-section details (all dimensions in mm).

7.2.3 Instrumentation

The instrumentation used for the presented experimental work is shown in Figure 7.2. A linear vertical displacement transducer (LVDT) with 100 mm stroke (with linearity error of ±0.10% F.S.) was used in the midspan of the beam to measure the central deflection (LVDT1). Moreover, two LVDTs with 25 mm stroke (with linearity error of ±0.10% F.S.) were used in both support (LVDT2 and LVDT3) in order to measure the possible supports settlement in all of the tests. Furthermore, the strain at the top fiber of concrete was measured with a strain gauge (with a gauge length of 60 mm) that was installed in midspan of the specimens (SG$_C$ in Figure 7.2). Finally, a load-cell of 125 kN was used to register the applied load.
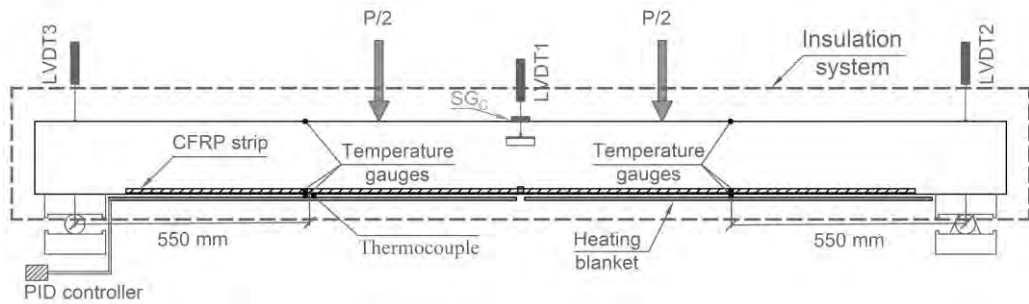
Figure 7.2. Instrumentation adapted in the beams.

Some specimens needed to be conditioned (i.e. heated up to 70 °C) prior to fatigue testing. In those cases, heating blankets installed to the soffit of the beams were used. A proportional integral derivative (PID) controller was utilized for controlling heating process, and Type-T thermocouples, installed between the heating blanket and the soffit of the beam, were used as temperature controller sensor. An isolation system (rock wool with aluminum foil) was used in order to speed up the heating process and reach to a uniform temperature along the beam. Temperature gauges were used to monitor and register temperature at different points: on the concrete surface at the top and bottom of the beam, on the surface of the CFRP and on the surface of epoxy adhesive (see Figure 7.2). The temperature gauges on the surface of the CFRP were installed prior to introducing the strip into the groove, and a thin protection layer was applied in order to protect them from the wet environment during curing of the epoxy adhesive. The heating process started almost 24 hours prior to fatigue testing until the average temperature in the soffit of the beam was stabilized to its target value. During fatigue testing, the PID controller ensured the temperature to be constant along the test. The evolution of the temperature during the heating process and the fatigue test of one of the beams is shown in Figure 7.3. Although there was a small difference between temperature at the concrete top and concrete bottom, the temperature gradient did not affect the outcome of the research carried out. In addition, a general view of test setup for a beam under temperature is shown in Figure 7.4.
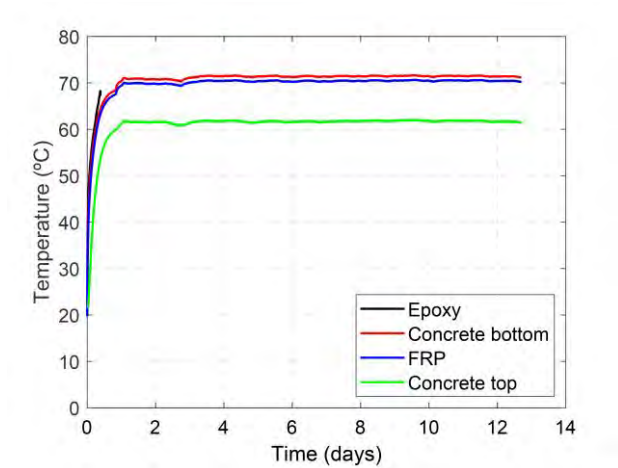
Figure 7.3. Registered temperatures during the heating process and the fatigue test; Note: temperature gauge on epoxy surface failed during the heating phase.
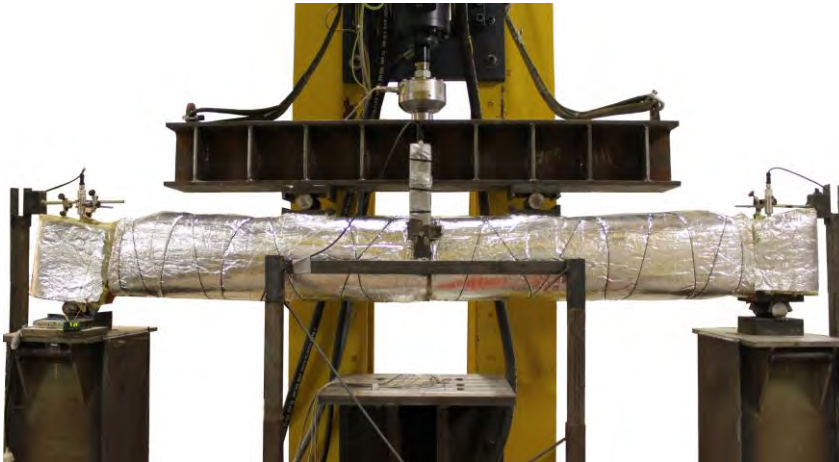
Figure 7.4. General view of test setup.

7.2.4 Loading procedure

Specimens in Series 1 were tested under short-term load under displacement control at a rate of 0.6 mm/min up to failure. As mentioned before, these specimens were used to define the maximum and minimum fatigue loads (P_{max} and P_{min}, respectively) of specimens in Series 2. The fatigue tests were performed in three different steps as below (see Figure 7.5):

- *Step 1:* The beams were loaded up to the maximum fatigue load (P_{max}) under displacement control at a rate of 0.6 mm/min (black line in Figure 7.5).

- *Step 2:* The beams were unloaded up to the average fatigue load ($P_{ave} = (P_{max} + P_{min})/2$) under displacement control at a rate of 0.6 mm/min (red line in Figure 7.5).
- *Step 3:* In this step, the fatigue load was applied through a sinusoidal loading path with a frequency of 2 Hz and a pre-defined amplitude ($P_{amp} = P_{max} - P_{ave}$). This step was conducted under force control. The fatigue test duration was programmed to either 2 million cycles or failure of the beam, whichever occurs first (blue line in Figure 7.5).
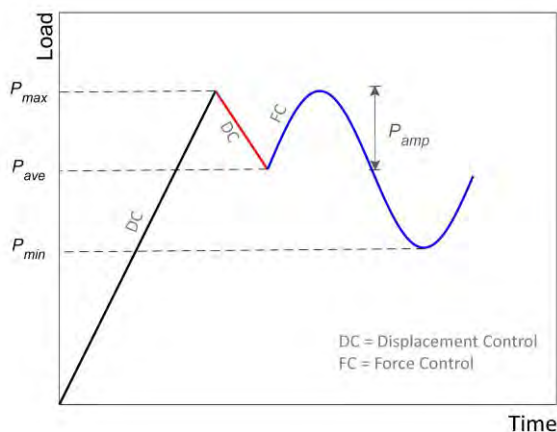
Figure 7.5. Fatigue loading procedure.

7.3 Results and discussions

7.3.1 Short-term tests results

The results of specimens of Series 1 (short-term test) (i) allowed the definition of the fatigue loads (P_{max} and P_{min}) to be applied to specimens in Series 2 and also (ii) were used for comparison purposes with results obtained on the specimens that experienced the post-fatigue stage. Experimental load-midspan deflection curves of specimens in Series 1 are shown in Figure 7.6, where three phases can be observed: (i) uncracked phase, with a linear elastic behavior until cracking load (P_{cr}) is attained; (ii) cracking phase, where stiffness gradually decreases as the load increases up to the yielding of steel reinforcement; and (iii) post-yielding phase up to failure. In this last phase no significant increase in load can be observed for the unstrengthened beam, whilst relevant load increase is observed for strengthened beams. The increase in the strengthening (CFRP) ratio had no significant effect on the cracking load (P_{cr}), whilst larger yielding load (P_y) and ultimate load (P_u) were obtained in the specimen with larger strengthening

ratio, as expected (see Figure 7.6a). In this sense, the yielding and ultimate loads of specimen SB1S-20-ST were 20% and 47% larger than those of specimen CB-20-ST, while for the specimen with three strips (SB3S-20-ST) the percentages rose up to 51% and 108%, respectively. Finally, it should be mentioned that the unstrengthened beam failed by concrete crushing, whilst specimens strengthened with one and three laminates failed by CFRP rupture and intermediate concrete cover separation, respectively. Further discussion about the failure modes is provided in Section 7.3.4.
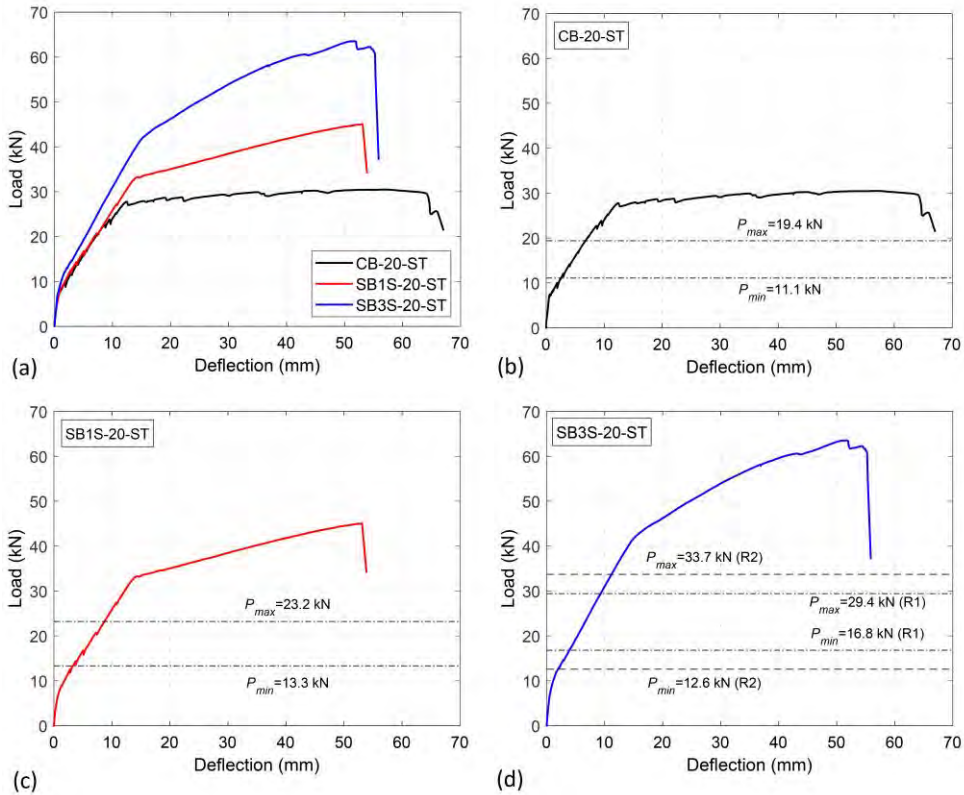
Figure 7.6. Short-term load-deflection curves (Series 1): (a) Effect of strengthening ratio, (b), (c) and (d) definition of P_{max} and P_{min}

7.3.2 Fatigue tests results

Values for P_{min} and P_{max} applied to fatigue tests of specimens in Series 2 are depicted in Figures 7.6b-7.6d and summarized in Table 7.5. It should be mentioned that P_{min} and P_{max} computed from results on short-term tests at 20 °C were applied to fatigue tests at both testing temperatures (20 °C and 70 °C).

Table 7.5. Details on fatigue load levels.

Specimen ID	$P_y{}^a$ (kN)	P_{min} (kN)	P_{max} (kN)	$P_{ave}{}^b$ (kN)	$P_{amp}{}^c$ (kN)	R^d
CB-20-R1	27.7	11.1	19.4	15.3	4.1	0.57
CB-70-R1						
SB1S-20-R1	33.1	13.3	23.2	18.3	4.9	0.57
SB1S-70-R1						
SB3S-20-R1	41.9	16.8	29.4	23.1	6.3	0.57
SB3S-70-R1						
SB3S-20-R2	41.9	12.6	33.7	23.1	10.6	0.38
SB3S-70-R2						

[a] P_y of the reference short-term test in Series 1

[b] Average fatigue load defined as: $P_{ave} = (P_{max} + P_{min})/2$

[c] Amplitude of fatigue cycles defined as: $P_{amp} = P_{max} - P_{ave}$

[d] $R = P_{min} / P_{max}$

Cyclic load-deflection response

Cyclic load-deflection responses of specimens in Series 2 are shown in Figures 7.7-7.10. In every figure, two graphs are presented. Figures 7.7a-7.10a correspond to the initial load-deflection response before cyclic loading (steps 1 and 2 of the fatigue loading procedure presented in section 7.2.4), and Figures 7.7b-7.10b correspond to the cyclic load *versus* normalized deflection (with respect to deflection of first cycle) curves (step 3 of the fatigue loading procedure described in section 7.2.4).

The effect of temperature on the flexural behavior prior to fatigue loading can be assessed in Figures 7.7a-7.10a. In all the cases, the application of a high service temperature (70 °C) resulted in lower cracking loads (P_{cr}) and an increase in the deflection prior to fatigue loading. In this sense, a comparison of the deflections prior to fatigue loading is presented in Figure 7.11, where the greatest effect of temperature corresponds to specimen strengthened with three strips (SB3S-20-R1 vs SB3S-70-R1). On the other hand, unstrengthened control beams (CB-20-R1 and CB-70-R1) show the lowest variation. This behavior could be partially attributed to lower P_{cr} values, and therefore lower M_{cr} (i.e. cracking moment), leading to lower M_{cr}/M ratios which are related to larger deflections. Besides, a possible reduction in the effectiveness of the strengthening system due to the application of a working temperature beyond the T_g of the

epoxy adhesive can also be affecting. This may be related to a reduction in the stiffness of the epoxy adhesive [220].
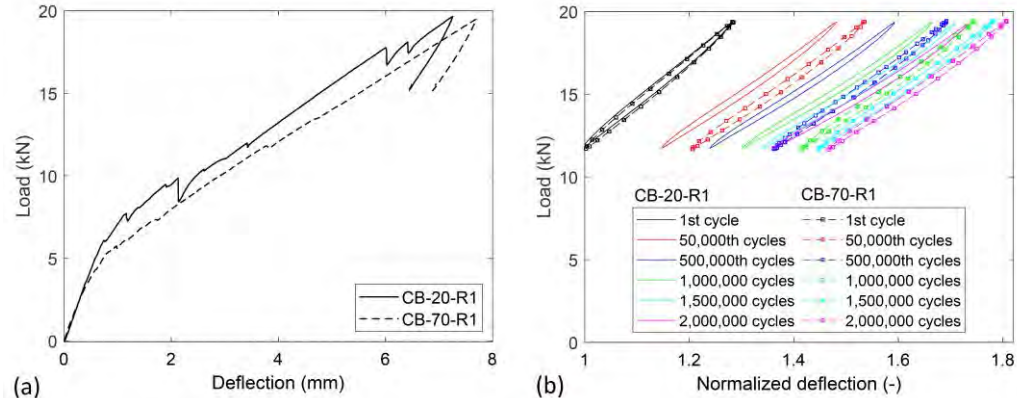
Figure 7.7. Fatigue response of specimens CB-20-R1 and CB-70-R1: (a) Initial load-deflection response prior to cyclic loading and (b) load versus normalized deflection curves during cyclic loading.
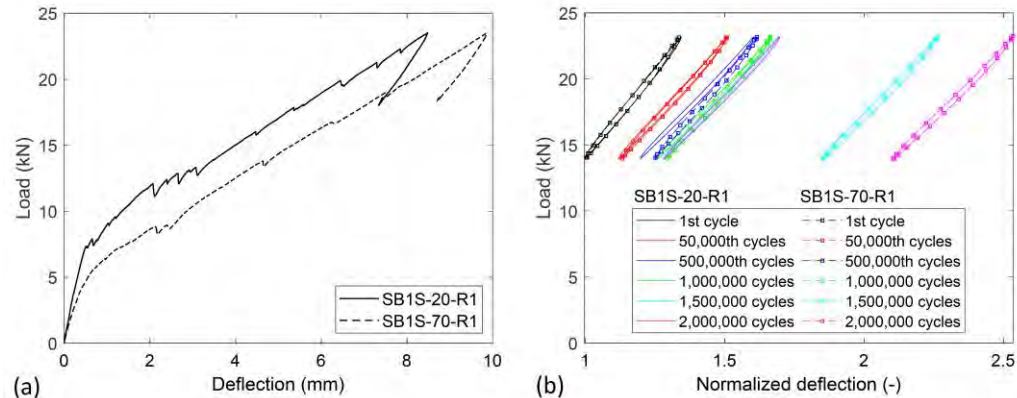
Figure 7.8. Fatigue response of specimens SB1S-20-R1 and SB1S-70-R1: (a) Initial load-deflection response prior to cyclic loading and (b) load versus normalized deflection curves during cyclic loading.
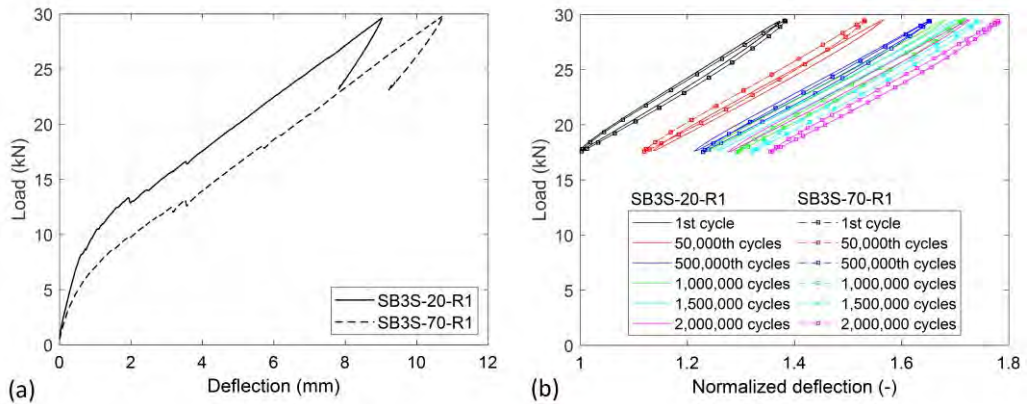
Figure 7.9. Fatigue response of specimens SB3S-20-R1 and SB3S-70-R1: (a) Initial load-deflection response prior to cyclic loading and (b) load versus normalized deflection curves during cyclic loading.
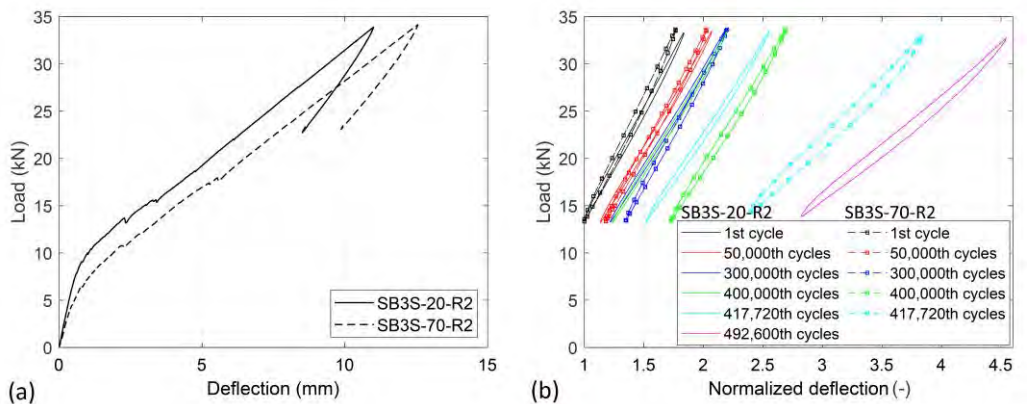
Figure 7.10. Fatigue response of specimens SB3S-20-R2 and SB3S-70-R2: (a) Initial load-deflection response prior to cyclic loading and (b) load versus normalized deflection curves during cyclic loading.
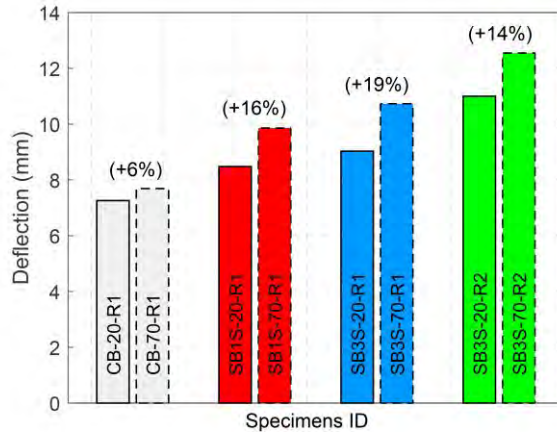
Figure 7.11. Initial deflections prior to cyclic loading; Note: percentages refer to the variation in the deflection due to the effect of temperature.

The effect of cyclic loading and temperature on the flexural response of specimens in Series 2 can be assessed in Figures 7.7b-7.10b, where the cyclic load *versus* normalized deflection curves are plotted. In these subfigures, solid lines correspond to specimens tested at 20 °C while dashed lines refer to specimens tested at 70 °C. In all the cases, normalized deflections increased gradually as the fatigue loading progressed, and larger increments were found in specimens tested at 70 °C, which is in line with results presented in [127]. It is worth to mention that a large portion of fatigue deflections occurred at first 50,000 cycles and after that, the rate of deflection increase slowed down, as observed in [121,122,125,126,213,214].

Moreover, specimens tested under an *R* ratio equal to 0.57 (i.e. R1) did not fail during the application of 2 million cycles. However, special attention should be given to specimen SB1S-70-R1, which experienced a large jump in the normalized deflection at about 1.5 million cycles (see Figure 7.8b). This jump was attributed to a reduction in the effectiveness of the strengthening system that may be due to the reduction in mechanical properties of epoxy adhesive at higher temperature. In this scenario, the value of P_{max} applied to SB1S-70-R1 (P_{max} = 23.2 kN) was larger than the load causing 80% of steel yielding stress (f_y) of the control beam CB-20-ST, thus exceeding the limitation proposed by ACI 440.2R [99]. As a consequence, a possible accumulation of damage in steel reinforcement may have occurred.

On the other hand, specimens tested under an *R* ratio equal to 0.38 (i.e. R2) did not survive the programmed 2 million cycles and failed by steel reinforcement rupture. It should be mentioned that once rupture of the steel reinforcement took place, the integrity of the system

160

was provided by the NSM CFRP-strengthening strips. In this sense, for specimen SB3S-20-R2 the steel reinforcement rupture took place at 411,220 cycles, and after that the NSM CFRP-strengthening was involved alone in order to resist the fatigue loading; from this point on, large increases in the curvature (deflection) occurred and the beam failed at 492,600 cycles. In the case of specimen under temperature (i.e. SB3S-70-R2), rupture of steel reinforcement took place at 340,890 cycles and the beam failed at 417,720 cycles. Therefore, NSM CFRP-strengthening improved the fatigue life of the system by 20% and 22.5% for SB3S-20-R2 and SB3S-70-R2, respectively. Besides, the application of temperature (70 °C) shortened the fatigue life of the specimen by 15% (compare the fatigue life of SB3S-20-R2 and SB3S-70-R2).

Results on fatigue tests at specific number of cycles are reported in Table 7.6.

Table 7.6. Fatigue tests results.

Specimens ID	Fatigue life (cycles)	Failure mode [a]	$E_{tot,acc,diss}$[b] (kN·m)	Cycle	δ_{ave}[c] (mm)	K[d] (kN/mm)	ε_{ave}[e] (µε)
CB-20-R1	>2,000,000	Not failed	1432	1	6.5	4.6	-718
				50,000	7.5	4.0	-778
				500,000	8.1	3.7	-867
				1,000,000	8.5	3.7	-907
				1,500,000	8.7	3.6	-937
				2,000,000	8.8	3.5	-968
CB-70-R1	>2,000,000	Not failed	1462	1	7.0	4.4	-775
				50,000	8.5	3.8	-887
				500,000	9.4	3.8	-1051
				1,000,000	9.7	3.8	-1152
				1,500,000	9.9	3.8	-1200
				2,000,000	10.1	3.7	-1229
SB1S-20-R1	>2,000,000	Not failed	1991	1	7.3	4.2	-646
				50,000	8.2	3.8	-691
				500,000	8.7	3.6	-751
				1,000,000	9.1	3.6	-803
				1,500,000	9.3	3.6	-829
				2,000,000	9.3	3.6	-864
SB1S-70-R1	>2,000,000	Not failed	2394	1	8.5	3.8	-741
				50,000	9.6	3.4	-838
				500,000	10.4	3.4	-982
				1,000,000	10.7	3.4	-1061
				1,500,000	14.9	3.1	-1113
				2,000,000	16.8	3.0	-1164
SB3S-20-R1	>2,000,000	Not failed	2845	1	7.9	4.7	-700

Specimen	Fatigue life	Failure mode[a]	Energy[b]	Cycles	Deflection[c]	Stiffness[d]	Concrete strain[e]
				50,000	9.1	4.1	-771
				500,000	9.6	4.0	-858
				1,000,000	9.8	4.0	-888
				1,500,000	9.9	4.0	-905
				2,000,000	10.1	4.0	-931
SB3S-70-R1	>2,000,000	Not failed	3375	1	9.1	4.1	-887
				50,000	10.1	3.8	-1030
				500,000	11.1	3.7	-1204
				1,000,000	11.5	3.7	-1295
				1,500,000	11.7	3.7	-1369
				2,000,000	12.0	3.6	-1405
SB3S-20-R2	492,600	SR	1933	1	8.4	4.0	-657
				50,000	9.5	3.6	-708
				300,000	10.1	3.5	-753
				400,000	10.2	3.5	-761
				417,720	12.1	3.3	-798
				492,600	21.9	1.6	-1127
SB3S-70-R2	417,720	SR	2266	1	9.9	3.7	-898
				50,000	11.5	3.3	-1027
				300,000	12.7	3.3	-1216
				400,000	15.8	2.9	-2178
				417,720	22.2	1.6	-2548

[a] SR=Steel reinforcement rupture

[b] Total accumulated dissipated energy at the end of the fatigue test

[c] Average deflection

[d] Stiffness

[e] Average concrete strain

163

Average normalized deflection

With the aim at analyzing the evolution of deflection due to fatigue, the average normalized deflection, $\delta_{ave,n}$, has been defined as the average value of deflections corresponding to P_{min} and P_{max} in each cycle normalized with respect to the value at first cycle (i.e. the value of δ_{ave} for first cycle reported in Table 7.6). The evolution of $\delta_{ave,n}$ along fatigue loading is shown in Figure 7.12. According to results presented in Figure 7.12a, the presence of NSM CFRP-strengthening helped to reduce the detrimental effects of fatigue loading and, thus, lower values of $\delta_{ave,n}$ were obtained. Furthermore, the application of a high service temperature (70 °C) negatively affected the fatigue performance of both unstrengthened and strengthened specimens. Besides, the large jump in deflection taking place in specimen SB1S-70-R1 at around 1.5 million cycles is clearly visible in Figure 7.12a (see red dash line in Figure 7.12a). The effect of R ratio on $\delta_{ave,n}$ can be analyzed from results presented in Figure 7.12b. In this case, although similar patterns were obtained during the initial cycles of the fatigue tests, specimens under lower R ratios failed by steel rupture and experienced a sudden increase in $\delta_{ave,n}$ prior to final failure (see green lines in Figure 7.12b). The failure in these specimens can be explained by the combination of having a lower R ratio and a larger maximum fatigue load, P_{max}, that in this case was equal to the upper limit stated in ACI 440.2R [99]. This is in accordance with [67,118-120], who observed that the increase in P_{max} and/or the decrease in R ratio results in a reduction of fatigue life with specimens failing by steel rupture.
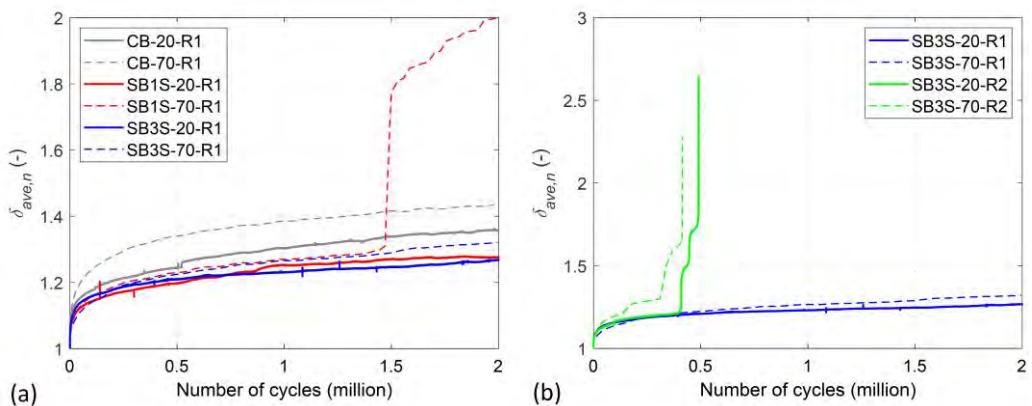
Figure 7.12. Evolution of average normalized deflection ($\delta_{ave,n}$): (a) Effect of strengthening ratio and temperature and (b) Effect of R ratio and temperature in beams with same NSM CFRP-strengthening ratio.

In order to clearly compare the effect of NSM CFRP-strengthening ratio, temperature and R ratio on the average normalized deflection ($\delta_{ave,n}$), a bar diagram is presented in Figure 7.13, where $\delta_{ave,n}$ is compared at three different cycles: i) at 417,720th cycle, where SB3S-70-R2 failed; ii) at 492,600th cycle, where SB3S-20-R2 failed and iii) at 2 million cycle, corresponding to the end of the fatigue test. The comparison of the first set of data (deflections at 417,720th cycle) shows that higher service temperature, applied individually to specimens having an R ratio of 0.57, had no significant effect at that number of cycles (specimen SB3S-20-R1 vs SB3S-70-R1), whereas the change to lower R ratios in specimens at 20 °C had a larger impact on the fatigue performance (specimen SB3S-20-R1 vs SB3S-20-R2). In fact, specimen SB3S-20-R2 had already experienced steel rupture at that cycle as a consequence of the high damage produced by P_{max}. Finally, the application of temperature and lower R ratios in a combined manner had catastrophic consequences, causing the failure of the beam (specimen SB3S-20-R1 vs SB3S-70-R2). Results of the second set of data (deflections at 492,600th cycle) confirm that R ratio had the major effect. Finally, the third set of data confirms that, for an R ratio equal to 0.57, the application of a high service temperature was affecting the fatigue performance of control and strengthened beams in a controlled manner. Special attention should be given to specimen SB1S-70-R1, which experienced and unexpected jump in deflections at 1.5 million cycles, as explained before.
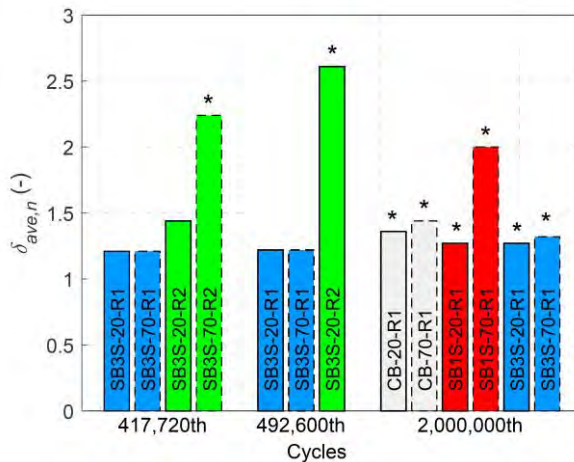
Figure 7.13. Comparison of average normalized deflections ($\delta_{ave,n}$). *The value of average normalized deflection corresponds to the ultimate one ($\delta_{u,ave,n}$).

Stiffness

Fatigue loading has an effect on the stiffness on any structural member, as it consists on a cyclic load being repeated for a long period of time. Thus, evaluation of the stiffness variation during a fatigue test is of paramount importance as the degradation in the stiffness may influence the serviceability of the strengthened system [213]. In this section, the evolution of stiffness along the fatigue loading is analyzed. To this end, the stiffness (K) is calculated based on the behavior of the member within the loading and unloading paths of a cycle [121,122,126], as follows:

$$K_i = \frac{P_{max,i} - P_{min,i}}{\delta_{max,i} - \delta_{min,i}} \tag{7.1}$$

where $\delta_{max,i}$ and $\delta_{min,i}$ are the deflections corresponding to $P_{max,i}$ and $P_{min,i}$ at the ith cycle. A schematic view of this procedure is shown in red lines in Figure 7.14.
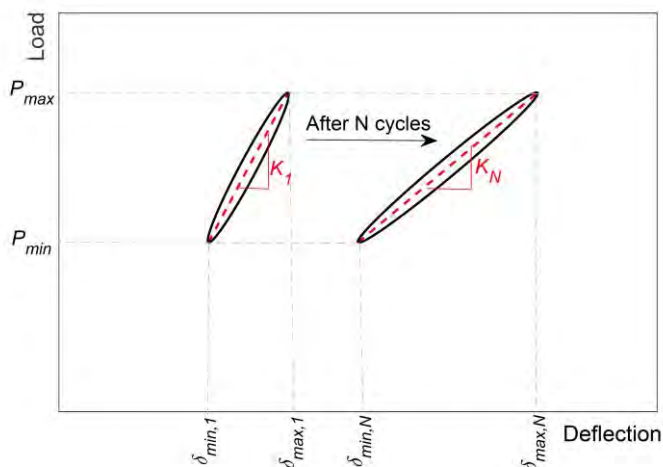
Figure 7.14. Schematic view of stiffness calculation.

The evolution of the stiffness (K) along the fatigue tests is shown in Figure 7.15 and also reported in Table 7.6. According to experimental results, a big drop in stiffness happened during the first cycles, which corresponded to the increase in deflections shown in Figure 7.12. Afterwards, stiffness tends to stabilize, with specimens tested at 20 °C showing larger stiffness than those tested at 70 °C. The same stiffness reduction tendency was observed in [127]. Besides, specimens under a larger R ratio showed larger stiffness (both unstrengthened and strengthened specimens), irrespective of the applied temperature. Furthermore, the increase

in the strengthening ratio resulted in a higher stiffness in the specimens in comparison to unstrengthened control beams. The big drop in stiffness of specimen SB1S-70-R1 around the 1.5 million cycles corresponds to the big jump in deflection shown in Figure 7.12a. Similarly, failure of specimens with low *R* ratio (i.e. R2=0.38) is visible in Figure 7.15b.

(a)

(b)
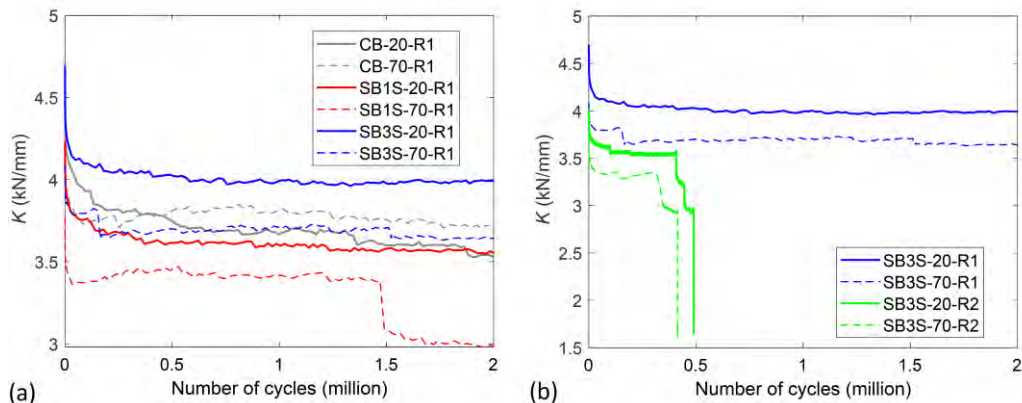
Figure 7.15. Evolution of stiffness (*K*): (a) Effect of strengthening ratio and temperature and (b) Effect of *R* ratio and temperature in beams with same NSM CFRP-strengthening ratio.

Average normalized concrete strain

Measurements from the strain gauge on the top fiber of concrete (see Figure 7.2) allow plotting the evolution of average normalized concrete strain ($\varepsilon_{ave,n}$), as presented in Figure 7.16. Similar to the case of deflections, the average normalized concrete strain has been defined as the average value of concrete strain corresponding to P_{min} and P_{max} in each cycle normalized with respect to the value at first cycle (i.e. the value of ε_{ave} for first cycle reported in Table 7.6). According to experimental results, strengthening ratio did not have a considerable effect on the evolution of the normalized concrete strain along fatigue test. On the other hand, for the specimens under fatigue load level of R1, the increase in the testing temperature resulted in an increase of 20% in the $\varepsilon_{u,ave,n}$ (see Figure 7.16a). Finally, no significant differences can be found in the earlier stage of the evolution of average normalized concrete strain ($\varepsilon_{ave,n}$) whatever the *R* ratio is. However, specimens under low *R* ratio (i.e. R2=0.38) experienced a sudden increase in $\varepsilon_{ave,n}$ prior to the final failure (see Figure 7.16b).
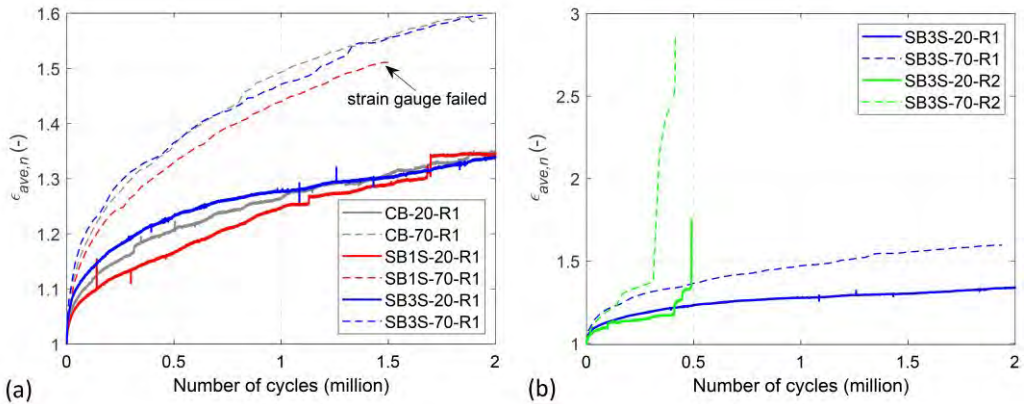
Figure 7.16. Evolution of average normalized concrete strain ($\varepsilon_{ave,n}$): (a) Effect of strengthening ratio and temperature and (b) Effect of R ratio and temperature in beams with same NSM CFRP-strengthening ratio.

Accumulated dissipated energy

One of the most important aspects of structural performance under fatigue loading is the ability of a member to adequately dissipate energy [221]. Dissipated energy (E_{diss}) within a fatigue cycle is calculated as the area of the hysteric load-deflection curve at that cycle. Therefore, the accumulation/addition of the individual dissipated energies of each cycle will result in the total dissipated energy in the fatigue test. The evolution of accumulated dissipated energy ($E_{acc,diss}$) along the fatigue loading is shown in Figure 7.17, in order to evaluate the effect of strengthening ratio, temperature and fatigue load level. Furthermore, the total accumulated dissipated energy at the end of fatigue test ($E_{tot,acc,diss}$) is reported in Table 7.6. According to experimental results, an increase in the CFRP-strengthening ratio derived in larger total accumulated dissipated energy, as expected. In this regard, taking results for specimen CB-20-R1 as the reference value, the $E_{tot,acc,diss}$ was increased by 39% and 99% for SB1S-20-R1 and SB3S-20-R1, respectively. Similarly, the application of a high service temperature (i.e. 70 °C) and larger amplitudes in the fatigue loading (i.e. lower values of R ratio) corresponded also to larger amounts of total accumulated dissipated energy. It should be mentioned that the effect of temperature was more pronounced in strengthened RC beams. This is a sign of temperature affecting the efficiency of the strengthening system.
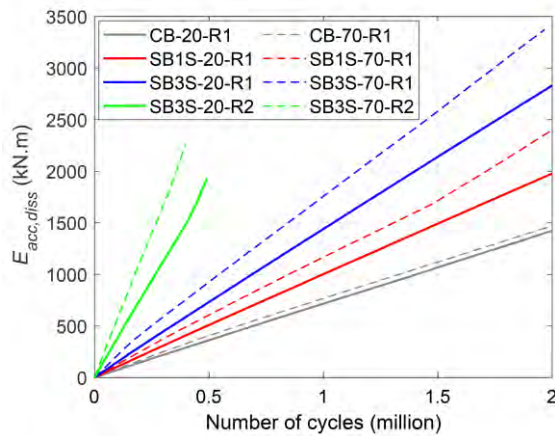
Figure 7.17. Accumulated dissipated energy ($E_{acc,diss}$) versus number of cycles.

7.3.3 Post-fatigue residual strength

After finishing the fatigue loading, the surviving specimens from Series 2 were unloaded and then tested up to failure in order to evaluate their residual strength. A comparison of load-deflection responses of specimens from Series 1 and 2 is shown in Figure 7.18. Furthermore, the detailed results are shown in Table 7.7, where P_{cr} and δ_{cr} are the cracking load and the corresponding deflection; P_y and δ_y are the yielding load and the corresponding deflection; P_u and δ_u are the ultimate load and the corresponding deflection and δ_p is the plastic deflection, which was registered immediately after the unloading process of the fatigue test.

The value of δ_p defines the origin of the post-fatigue load-deflection response and it has been measured after unloading the beams (residual plastic deflection after the fatigue cycles). According to experimental results, plastic deflections, δ_p, generally increased when the temperature changed from 20 °C to 70 °C. It should be mentioned that the largest value of δ_p was registered in specimen SB1S-70-R1 (δ_p=11.3 mm) as a result of steel having worked at high levels of strains during the fatigue cycles, as explained in previous sections. The residual flexural strength depended on the level of accumulated fatigue damage in the beams. In this sense, similar values of P_y were found for short-term specimens (Series 1) and corresponding specimens in Series 2 under 20 °C. This is a sign of low damage in steel due to fatigue loading. On the contrary, larger differences between P_y in short-term specimens (Series 1) and specimens in Series 2 under 70 °C depict that steel reinforcement was damaged at the end of fatigue tests (i.e. at the beginning of post-fatigue tests). The largest reduction in P_y was observed in specimen SB1S-70-R1, and read 25%. This is in accordance with the largest deflection and

reduction in stiffness due to fatigue testing experienced by this same specimen (see Figures 7.12a and 7.15a). An additional evidence of the damage accumulated in the steel reinforcement of specimen SB1S-70-R1 can be found in the value of P_u, which was much lower than P_y of the reference short-term specimen in Series 1 (SB1S-20-ST). To conclude, fatigue loading under large R ratio (R1) and 20 °C did not have significant effect on the residual strength of the specimens. However, the residual strength was affected by the application of 70 °C during the fatigue tests.
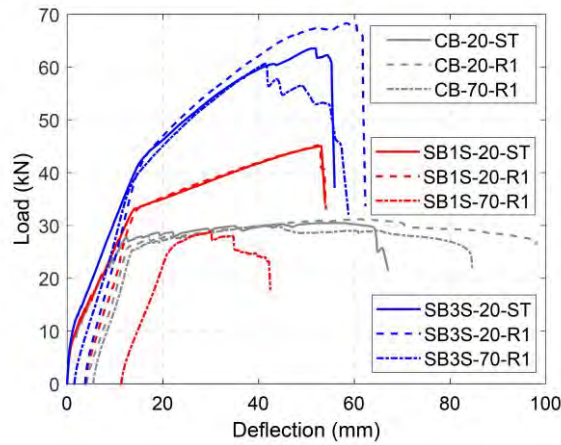
Figure 7.18. Short-term and post-fatigue load-deflection curves.

Table 7.7. Short-term and post-fatigue test results.

Specimen ID	Fatigue life (cycles)	Load (kN)			Deflections (mm)				Failure mode [b]
		P_{cr}	P_y	P_u	δ_{cr}	δ_y	δ_u	δ_p	
CB-20-ST	-	7.4	27.7	30.5	1.0	12.5	56.8	-	CC
CB-20-R1	>2,000,000	7.4[a]	26.1	31.1	1.2[a]	13.2	61.0	4.2	CC
CB-70-R1	>2,000,000	5.7[a]	25.4	30.0	1.0[a]	13.9	41.4	5.4	CC
SB1S-20-ST	-	7.4	33.1	45.0	0.9	14.6	53.0	-	FR
SB1S-20-R1	>2,000,000	7.8[a]	33.1	45.1	0.7[a]	14.7	52.4	3.8	FR
SB1S-70-R1	>2,000,000	5.9[a]	25.0	28.8	0.8[a]	21.2	30.0	11.3	SR
SB3S-20-ST	-	8.6	41.9	63.5	0.8	15.1	51.7	-	ICCS
SB3S-20-R1	>2,000,000	8.6[a]	42.4	68.3	0.7[a]	15.9	58.4	3.8	ICCS
SB3S-70-R1	>2,000,000	6.2[a]	38.3	60.6	0.8[a]	13.8	41.4	1.5	CC
SB3S-20-R2	492,600	9.1[a]	-	-	0.8[a]	-	-	-	SR
SB3S-70-R2	417,720	6.6[a]	-	-	0.8[a]	-	-	-	SR

[a] P_{cr} and δ_{cr} were calculated based on initial branch of the load-deflection curve prior to fatigue loading in Figures 7.7a-7.10a.

[b] CC=concrete crushing; FR=FRP rupture; SR=steel reinforcement rupture; ICCS=intermediate concrete cover separation.

7.3.4 Failure modes

Failure modes of specimens in Series 1 (short-term loading) and Series 2 (instantaneous post-fatigue loading in those specimens that survived fatigue loading) are detailed in Table 7.7, and representative images are shown in Figure 7.19. According to experimental results, failure mode for unstrengthened beams did not change due to the application of a fatigue loading; therefore, the unstrengthened beams in Series 1 and 2 failed by concrete crushing (CC) after steel yielding. It should be mentioned, however, that a large strain was observed in specimens CB-20-R1 and CB-70-R1 (see zoom view regarding to specimen CB-70-R1 in Figure 7.19). Regarding the specimens strengthened with one CFRP strip, experimental results confirm that fatigue loading at 20 °C did not cause significant damage, so that specimens SB1S-20-ST and SB1S-20-R1 experienced same failure mode, i.e. FRP rupture (FR). Similar behavior was observed in [55]. However, the application of a higher temperature during the fatigue tests caused a change in failure mode, and specimen SB1S-70-R1 failed by steel reinforcement rupture (SR). This is an evidence of a highly demanded steel reinforcement, due to bond deterioration, during fatigue

loading. This bond deterioration in the beam was also clear from load-deflection response in Figure 7.18, where the ultimate load of this strengthened beam was smaller than corresponding unstrengthened control beam. Finally, the negligible damage caused in steel due to fatigue loading under 20 °C was also confirmed in failure modes of specimens strengthened with three strips, so that specimens SB3S-20-ST and SB3S-20-R1 failed by intermediate concrete cover separation (ICCS), which was due to unstable diagonal crack that propagated along the height of the section. It should be mentioned that specimens subjected to a lower *R* ratio (R2) did not survive the programmed fatigue test (i.e. failed by SR during the fatigue loading) and, therefore, they cannot be included in the analysis of the post-fatigue failure mode. However, for illustrative purposes, a representative image has been included in Figure 7.19.
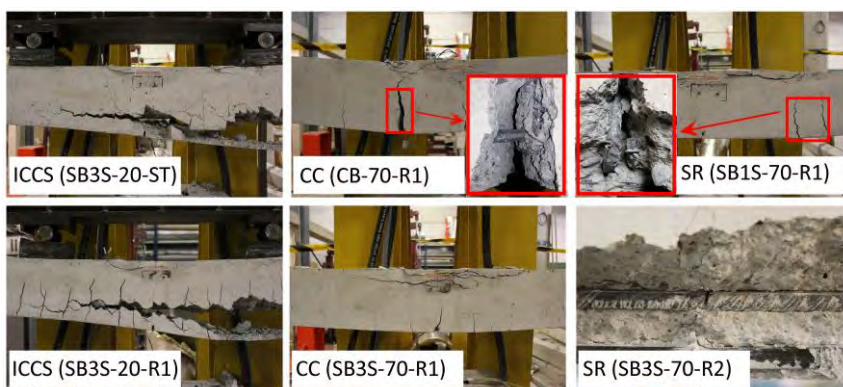
Figure 7.19. Representative failure modes of the tested specimens.

7.4 Conclusions

The present experimental work aimed to study the effect of fatigue loading on the flexural performance of NSM CFRP-strengthened RC beams under two different service temperatures. An experimental campaign consisting of 11 specimens (3 beams tested under short-term loading as reference specimens and 8 beams tested under fatigue loading) was performed, where beams with different amounts of CFRP-strengthening ratio, different fatigue load level and different temperature were loaded for 2 million cycles or failure, whichever happens first, at a frequency of 2 Hz. After that, post fatigue tests were carried out to analyze the residual flexural strength.

As a general conclusion, the increase in the testing temperature resulted in a decrease in the stiffness and the residual strength. Besides, due to bigger hysteric loops, specimens under 70 °C showed a larger amount of accumulated dissipated energy. Based on the test configuration and

setup adopted, the NSM strengthening system showed a good fatigue flexural performance when subjected to testing temperature beyond the T_g of the epoxy adhesive.

A list of detailed conclusions from the experimental tests is presented next:

- Specimens tested under a large *R* ratio (R1=0.57) could withstand the whole fatigue test (i.e. 2 million cycles), whilst rupture of steel reinforcement during fatigue loading took place for low *R* ratios (R2=0.38).

- As the fatigue test progressed, the deflection and concrete strain increased and the stiffness decreased, with the larger rates of variation corresponding to the initial stages of cyclic loading. Besides, in general, the NSM CFRP-strengthened RC beams showed a better fatigue performance when compared to unstrengthened control beams.

- The effect of temperature was more pronounced when combined with low *R* ratio. Therefore, the combined effect of both parameters should be considered in evaluating the fatigue life of the members.

- NSM CFRP-strengthening helped to postpone the failure of the beam during fatigue loading after steel reinforcement rupture. In this sense, fatigue life was extended in about 22%.

- Larger CFRP-strengthening ratios and higher testing temperature resulted in larger dissipated energy, whereas R ratio had the opposite effect.

- The residual strength of the specimens depended on the level of fatigue damage. In this sense, residual strength decreased for NSM CFRP-strengthened specimens under 70 °C, especially for the strengthened beam with low CFRP ratio.

- Fatigue testing did not affect post-fatigue failure mode of unstrengthened beams. For the case of strengthened beams under R1, the application of 70 °C during the fatigue loading caused the change in post-fatigue failure mode.

8 Discussion

This chapter presents the discussion of the main results obtained from the thesis. The discussion is presented in four sections, according to the four journal papers presented in the thesis.

8.1 Instantaneous flexural behavior of NSM CFRP-strengthened RC beams under service temperature

The instantaneous behavior of NSM FRP-strengthened members may be affected by high service temperature when epoxy adhesives are used as bonding material. Paper A was focused on experimentally studying the effect of different service temperatures (20 °C, 40 °C, 60 °C, 70 °C and 85 °C), CFRP strengthening ratios (0.06%, 0.12% and 0.18%) and compressive strengths of concrete (31.8 MPa and 40.8 MPa) on the instantaneous flexural behavior of NSM CFRP-strengthened RC beams. According to experimental characterization, the T_g of the epoxy adhesive used in the experimental program ranged between 53.9 °C and 65.3 °C, with a mean value equal to 59.6 °C. If *fib* Bulletin 90 [1] recommendations on EBR-strengthening are followed (no recommendations are given for NSM), this means that temperature should be limited to 40 °C to avoid premature debonding of the strengthening system. In this sense, results of the present experimental program on NSM CFRP-strengthened RC beams under 40 °C have shown that temperature had no significant effect on neither the load-deflection responses of the specimens nor their failure mode (which remained to be FRP rupture as for the tests at 20 °C), whatever the CFRP-strengthening ratio is (see Figure 8.1). This is attributed to possible post-curing of the epoxy adhesive that can improve its mechanical and physical properties. The opposite behavior was found for strengthened beam tested at 70 °C. Furthermore, unstrengthened (reference) beam tested at 70 °C (i.e. specimen CB-2-70) experienced a reduction in cracking load and stiffness in comparison to the corresponding beam at 20 °C (i.e. specimen CB-2-R), as shown in Figure 8.2. However, the application of 70 °C in the CFRP-strengthened RC beam (i.e. specimen SB2S-2-70) resulted in a decrease in the ultimate load when compared to SB2S-2-R (see Figure 8.2) and failure mode changing from FRP rupture to FRP end debonding (when compared to SB2S-2-R). The reason for premature debonding is related to a decrease in mechanical properties of the adhesive (70 °C is beyond the T_g of the

epoxy adhesive), which ended affecting the bond performance of the strengthening system. With all this, results from this experimental program revealed that service temperature for NSM CFRP-strengthened RC beams under instantaneous loading should be limited according to the T_g of the epoxy adhesive.
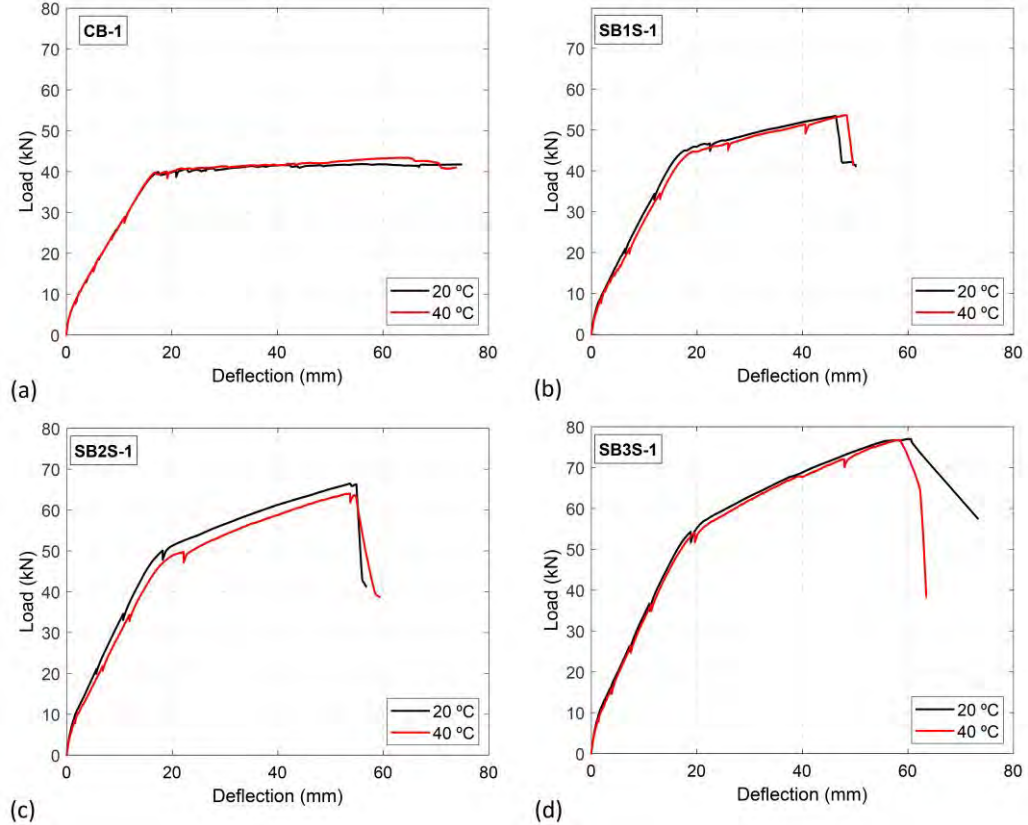
Figure 8.1. Effect of lower temperature (40 °C) on the experimental load-deflection curves of specimens: (a) CB-1, (b) SB1S-1, (c) SB2S-1 and (d) SB3S-1.
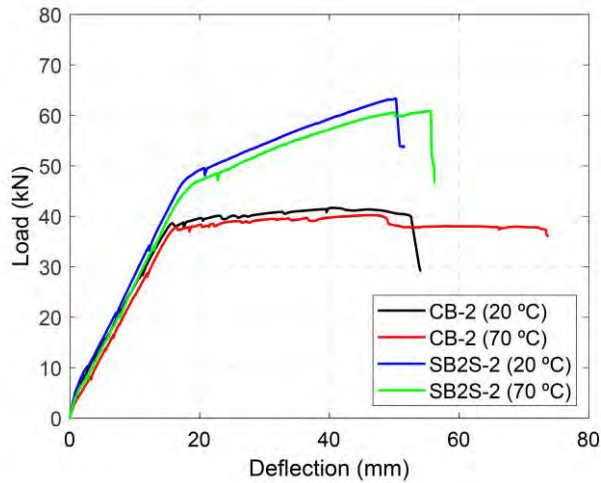
Figure 8.2. Effect of higher temperature (70 °C) on the experimental load-deflection curves of specimens.

In addition to experimental work, a systematic procedure was conducted to consider the effect of concrete shrinkage on the analytical prediction of the instantaneous behavior of FRP-strengthened RC beams. In this sense, analytical predictions demonstrate that concrete shrinkage has a significant influence on the instantaneous response of RC beams. The representative specimens are shown in Figure 4.8. According to the predictions, a considerable shift in the load-deflection response takes place in the case of specimens with larger shrinkage. Besides, good agreement between analytical predictions and experimental results was also observed (see Figure 4.11).

8.2 Effect of curing, post-curing and testing temperatures on mechanical properties of epoxy adhesive

Due to the nature of epoxy adhesives, their mechanical and physical properties are affected by temperature history, from the first moment of casting till the moment of being used. In this sense, epoxies used in NSM CFRP-strengthened structures are usually exposed to temperature variations along their service life, so that their mechanical properties can be modified, thus affecting the effectiveness of the strengthening system. For this reason, Paper B aimed to study the effect of curing, post-curing and testing temperatures on mechanical properties of an epoxy adhesive. The range of temperatures chosen for the study was in line with temperatures applied

in the experimental program presented in Paper A in order to deeply understand the effect of temperature on the instantaneous response of the tested specimens. Besides, the effect of curing and post-curing temperature on T_g of the epoxy was also evaluated.

DSC tests were performed to determine the T_g of different samples of epoxy adhesive that had different curing and post-curing temperatures (20 °C, 50 °C and 70 °C). According to experimental results, presented in Figure 8.3, the T_g value of the epoxy cured at room temperature (20 °C) was 54.9 °C (mid-point temperature, T_m, in DSC test). Besides, T_g increased when the curing or post-curing temperature raised to 50 °C, whilst the application of 70 °C during the curing or post-curing process derived in a reduction in the T_g of the epoxy adhesive. These results confirm the existence of an upper bound value for the T_g, that corresponds to $T_{g\infty}$. In this sense, T_g has been acknowledged to increase as the conditioning (i.e. curing or post-curing) temperature increases, arriving at its maximum value when the conditioning temperature equals $T_{g\infty}$. From that point on, the increase in the conditioning temperature results in a decrease in the T_g [195,197,199]. According to results presented in Figure 8.3, the $T_{g\infty}$ of the epoxy resin used in this experimental program is in the range of 50 °C to 70 °C.
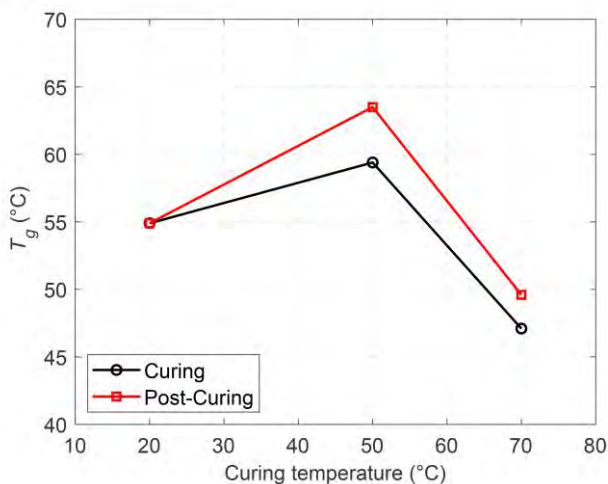
Figure 8.3. Effect of curing and post-curing temperature on the T_g of the epoxy adhesive.

In what follows, results on the study of the effect of testing temperature on the mechanical properties of the epoxy adhesive are presented. Experimental results, presented in Figure 8.4, show that the progressive increase in testing temperature from 20 °C to 85 °C was followed by

a decrease in epoxy mechanical properties. It should be highlighted that a dramatic decrease in mechanical properties was observed for testing temperature near the T_g of the epoxy adhesive (See Figure 8.4), and tensile and compressive strengths tested at 85 °C reduced to around 7% and 12%, respectively, of their reference value at 20 °C.
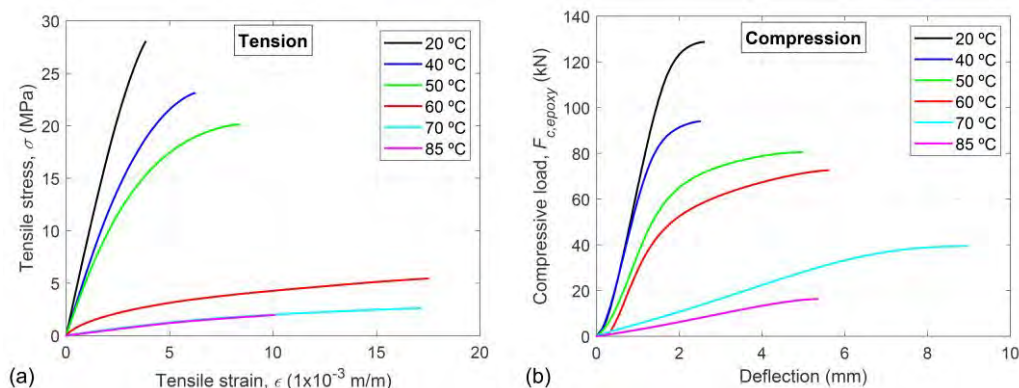
Figure 8.4. Effect of temperature on mechanical properties of epoxy adhesive: (a) Tensile behavior and (b) Compressive behavior.

The improvement or reduction in the performance of a NSM joint submitted to temperature has been traditionally attributed to the effect of the heating process of the NSM joint to the target testing temperature, being this heating process understood to act as a post-curing process for the epoxy resin. Therefore, understanding the effect of curing and post-curing temperatures on mechanical properties of the epoxy resin is of importance.

In this sense, tension and compression tests were performed on epoxy resin samples that were cured at different temperatures (-15 °C, 20 °C, 50 °C and 70 °C). Experimental results, presented in Figure 8.5, showed that mechanical properties (tensile strength, $f_{u,epoxy}$, and compressive strength, $\sigma_{cu,epoxy}$) progressively increased as curing temperature increased below $T_{g\infty}$. On the contrary, curing the epoxy at temperature beyond the $T_{g\infty}$ resulted in a reduction in mechanical properties, which was due to possible thermal degradation on the epoxy adhesive. Similar results have been found in the literature [197]. It should be mentioned that curing at −15 °C had some detrimental effects on the mechanical properties of epoxy adhesive. In fact, at this temperature, the curing process could not be initiated and after 7 days of curing, the epoxy was still soft. As a result, the curing time was shortened, when compared to that of other

specimens, probably leading to an un-complete cure in the epoxy resin. Therefore, in cold regions, a special preparation might be required to cure the epoxy adhesives.
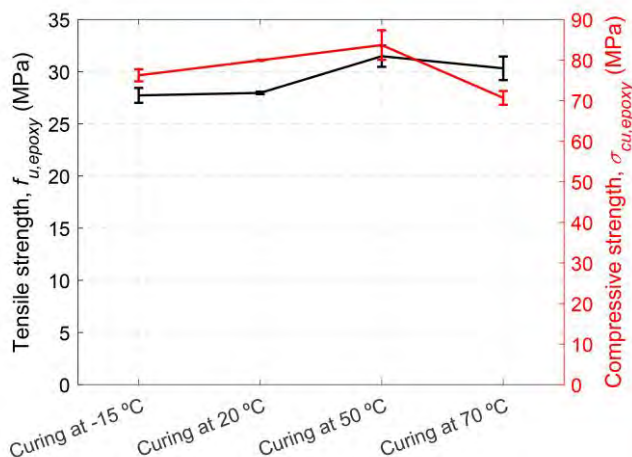
Figure 8.5. Effect of curing temperature on mechanical properties of epoxy adhesive.

As deduced from previous analysis, and also highlighted in the literature, epoxy adhesives cured at ambient temperature may suffer from a not complete cross-linking, that can be reactivated with a post-curing process [189,200,201,205]. Therefore, the fourth part of the experimental program was aimed at analyzing the effect of post-curing temperature on mechanical properties of the epoxy adhesive.

According to experimental results, presented in Figure 8.6, the application of a post-curing process at a temperature up to 60 °C was beneficial for tensile properties ($f_{u,epoxy}$), due to an increase in the cross-linking degree. However, for temperatures higher than 60 °C, a reduction in tensile strength was observed. In the case of compressive loading, the increase in the post-curing temperature from 20 °C to 40 °C resulted in an increase in the compressive strength ($\sigma_{cu,epoxy}$). On the other hand, for post-curing temperatures beyond 40 °C, a decrease in the compressive mechanical properties took place.
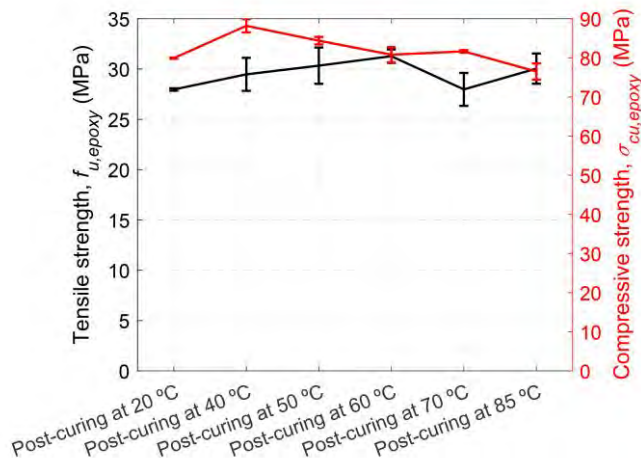
Figure 8.6. Effect of post-curing temperature on mechanical properties of epoxy adhesive.

Experimental data from the study of the effect of curing, post-curing and testing temperature on the epoxy resin (Paper B) supports results obtained from instantaneous flexural tests of NSM CFRP-strengthened RC beams under different temperatures (presented in Paper A). In this sense, no considerable differences in the load-deflection curves for beams subjected up to 60 °C were obtained, and no premature debonding was observed in their failure modes. However, the application of temperatures beyond 60 °C, resulted in a change in failure mode (premature end debonding) and a reduction in their ultimate load capacity. It is worthy to remind that $T_{g\infty}$ of the epoxy used in this experimental program was in the range of 50 °C to 70 °C. Therefore, based on experimental results presented in Papers A and B, it is confirmed that epoxy has a very important role in the load carrying capacity of NSM CFRP-strengthened RC elements, especially when temperature approaches its T_g.

8.3 Long-term flexural behavior of NSM CFRP-strengthened RC beams under service temperature

Although FRP-strengthening methodology has been implemented in a large number of practical projects worldwide, uncertainty about its long-term performance under the effect of long-term loading may pose an obstacle for their more widespread use. Long-term effects on NSM CFRP-strengthened RC elements are not only related to creep and shrinkage of concrete, but there is also a potential creep of the strengthening system (mainly in the epoxy adhesive).

180

Besides, creep and shrinkage of concrete are dependent on environmental conditions, which at the same time affect the mechanical properties of the epoxy adhesive. For all these reasons, Paper C aimed to evaluate the flexural time-dependent behavior of NSM CFRP-strengthened RC beams under different temperatures (20 °C and 50 °C). A total of 23 beams were cast, where the effect of different CFRP-strengthening ratios (ρ_{FRP} = 0.06% and 0.18%) and steel reinforcement ratios (ρ_s = 0.79% and 1.14%) was also considered.

Instantaneous flexural tests on beams serving as reference specimens confirmed that if applied temperature is below T_g of the epoxy adhesive, negligible effects on the load-deflection curve and failure mode are expected. In this sense, failure by concrete crushing was observed for unstrengthened beams, whilst FRP rupture occurred in CFRP-strengthened beams (irrespective of the CFRP ratio, the steel reinforcement ratio and the applied temperature). These results are in line with results presented in Papers A and B.

The study of long-term effects on NSM CFRP-strengthened RC beams was preceded by the characterization of the time-dependent behavior of involved materials at the two target temperatures (20 °C and 50 °C). According to measurements on concrete free shrinkage strains, shrinkage corresponding to the heated specimen (50 °C) was 35% larger than that of specimen at 20 °C. Moreover, the application of 50 °C resulted in an increase by 340% of the creep coefficient of concrete (based on analytical calculation) and a dramatic increase in the creep coefficient of epoxy adhesive (that resulted in failure of epoxy specimens tested at 50 °C before the end of the programmed time-dependent loading).

The characterization of the long-term performance of materials was followed by the study of the flexural long-term performance of NSM CFRP-strengthened elements. In this regard, Figure 6.11 shows the time-dependent deflections of the specimens during 200 days (i.e. duration of the long-term loading). According to these results, the largest rate of increase in time-dependent deflections took place at the beginning of the long-term loading, irrespective of the CFRP-strengthening ratio, the steel reinforcement ratio and the applied temperature. Focusing on specimens tested at room temperature (20 °C), larger time-dependent deflections were obtained for specimens with lower CFRP-strengthening ratio (irrespective of the steel reinforcement ratio), as expected. Moreover, the application of 50 °C resulted in a significant increase in the time-dependent deflections, as a consequence of the combination of larger concrete shrinkage and creep, larger creep of epoxy and lower epoxy mechanical properties. To

be more precise, long-term deflections of unstrengthened specimens increased by 60% and 86% for ρ_s equal to 0.79% and 1,14%, respectively. For the case of specimens with ρ_s equal to 0.79%, the percentage increased to 85% whatever the value of ρ_{FRP} is. Finally, specimens strengthened with ρ_s equal to 1,14% and ρ_{FRP} equal to 0.18% withstood 100% larger time-dependent deflections as a consequence of the application of 50 °C.

It should be highlighted that the application of 50 °C during the long-term test resulted in similar time-dependent deflections for specimens with same steel reinforcement ratios, irrespective of the presence or not of CFRP-strengthening and the number of CFRP strips. This may be a sign of time-dependent behavior of concrete being the dominant factor.

The evolution of time-dependent strain at the top fiber of concrete at the midspan section (shown in Figure 6.14) behaves in a manner similar to that of time-dependent deflections, thus confirming results from instrumentation being coherent.

According to the results from both instantaneous and long-term loading, the CFRP-strengthening ratio had a significant effect on the instantaneous responses of the RC beams, while it had a minor effect on the time-dependent deflections of the specimens. On the other hand, the application of temperature (50 °C) had no considerable effect on the instantaneous load-deflection responses of the specimens, while the same level of temperature resulted in large time-dependent deflections in the specimens. Considering that in real-life civil structures, the members are normally subjected to the long-term loads and higher temperature, their effects on the structural response of the members should be considered.

With the aim at analyzing the effect of long-term loading on the residual strength of the beams, the beams were loaded up-to-failure after long-term tests. In this sense, no considerable change was observed in the residual strength of the unstrengthened beams, whilst a slight increase was found in the yielding load and post-fatigue stiffness of the NSM CFRP-strengthened beams. Furthermore, in the case of strengthened beam with ρ_s equal to 1,14% and ρ_{FRP} equal to 0.18%, the failure mode was changed from FRP rupture to concrete crushing followed by FRP rupture.

To complement the experimental work, an analytical model was implemented to predict the long-term flexural behavior of NSM CFRP-strengthened RC beams. The model is based on AEMM and includes the effect of temperature on the time-dependent properties of materials. For

illustrative purposes, comparison of experimental data and analytical predictions for specimens strengthened with three strips are presented in Figure 8.7, where good agreement is observed.
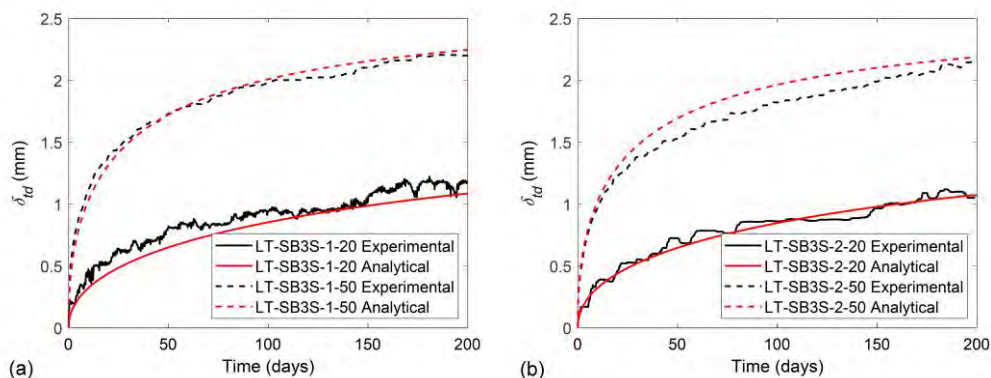
Figure 8.7. Comparison between analytical predictions and experimental time-dependent deflections for strengthened beams with three strips: (a) ρ_s = 0.79% and (b) ρ_s = 1.14%.

8.4   Fatigue behavior of NSM CFRP-strengthened RC beams under service temperature

Proper design of RC structures should not only account for their instantaneous and long-term performance, but also for the effects of fatigue loading. In this sense, a significant amount of work exists in the literature on the fatigue performance of NSM FRP-strengthened RC beams, but to the best of author knowledge, none of the published research accounted for the effect of high service temperature. Therefore, Paper D aimed to expand the experimental database on the flexural behavior of NSM CFRP-strengthened RC beams under fatigue loading and to present the first study on the effect of high service temperature on their fatigue performance. To meet the first objective, an experimental program was performed that considered different CFRP-strengthening ratios (ρ_{FRP} = 0.06% and 0.18%) and different R ratios (R1= 0.57 and R2=0.38). For the second objective, the aforementioned experimental program was expanded to include the analysis of the effect of applied temperature (20 °C and 70 °C). As a result, the experimental program included a total of 11 beams.

Flexural instantaneous tests performed to three specimens (one unstrengthened beam (CB) and two beams strengthened with one (SB1S) and three (SB3S) CFRP strips) allowed to

determine the maximum and minimum loads to be applied in the fatigue tests (P_{max} and P_{min}, respectively). It should be mentioned that values of P_{max} and P_{min}, presented in Table 8.1, did not change for the different testing temperatures (20 °C and 70 °C).

Table 8.1. Fatigue load levels.

Specimen ID	P_{min} (kN)	P_{max} (kN)	R^a
CB-R1	11.1	19.4	0.57
SB1S-R1	13.3	23.2	0.57
SB3S-R1	16.8	29.4	0.57
SB3S-R2	12.6	33.7	0.38

^{a} $R = P_{min} / P_{max}$

Experimental results on fatigue tests showed that specimens submitted to the large R ratio (R1=0.57) withstood the programed fatigue test (2 million cycles at a frequency of 2 Hz), whilst the application of a low R ratio (R2=0.38) resulted in fatigue life reducing to almost 500 thousand cycles. These results on fatigue life are applicable to both applied temperatures (20 °C and 70 °C).

For a better comparison of experimental results, deflections during the fatigue tests are presented as normalized values ($\delta_{ave,n}$) with respect to their value at the first fatigue cycle (see Figure 8.8). In addition, experimental results on evolution of stiffness (K) along the fatigue test are presented in Figure 8.9. To better check the differences in fatigue behavior, plots of normalized deflections have been limited to a maximum value of 2 and plots of stiffness have been limited to a minimum value of 2.5 kN/mm. Plots without these limitations can be found in Figures 7.12 and 7.15.

According to results of specimens tested under the large R ratio (R1=0.57) and submitted to 20 °C, the existence of larger CFRP-strengthening ratio resulted in lower normalized deflections and larger stiffness (see results on R1 specimens in Figures 8.8a and 8.9a). Besides, the application of a high service temperature (70 °C) negatively affected the fatigue performance of both unstrengthened and strengthened specimens, thus resulting in larger normalized deflections and lower stiffness (see results on R1 specimens in Figures 8.8b and 8.9b). Special attention should be given to the specimen strengthened with one CFRP strip, which experienced a big jump in deflection and stiffness at around 1.5 million cycles.
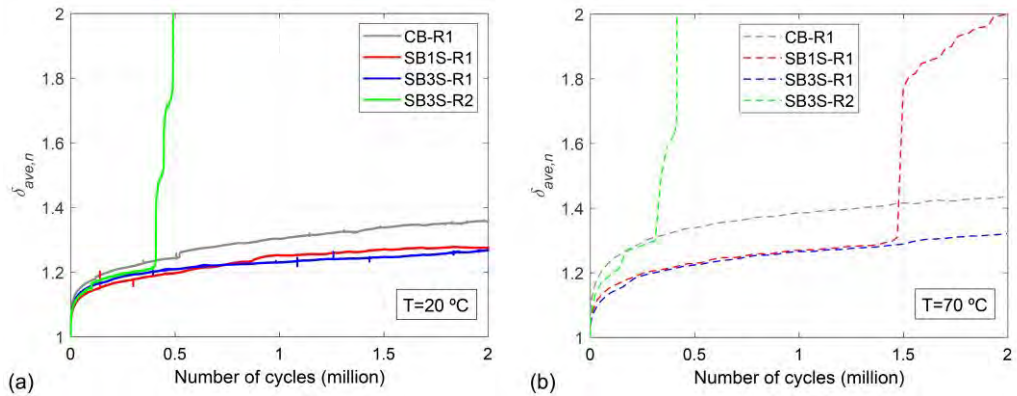
Figure 8.8. Evolution of normalized deflection ($\delta_{ave,n}$) for specimens tested at: (a) 20 °C and (b) 70 °C.

Finally, experimental results on specimens under the low R ratio (R2=0.38) confirm the dramatic reduction in fatigue life, thus observing a rapid increase in deflections and decrease in stiffness as a consequence of failure by steel reinforcement rupture (see results on R2 specimens in Figures 8.8 and 8.9). The failure in these specimens can be explained by the combined effect of low R ratio and a larger maximum fatigue load, P_{max}. Besides, the application of 70 °C speeded the damage of the specimen, which is reflected as the shortest fatigue life.
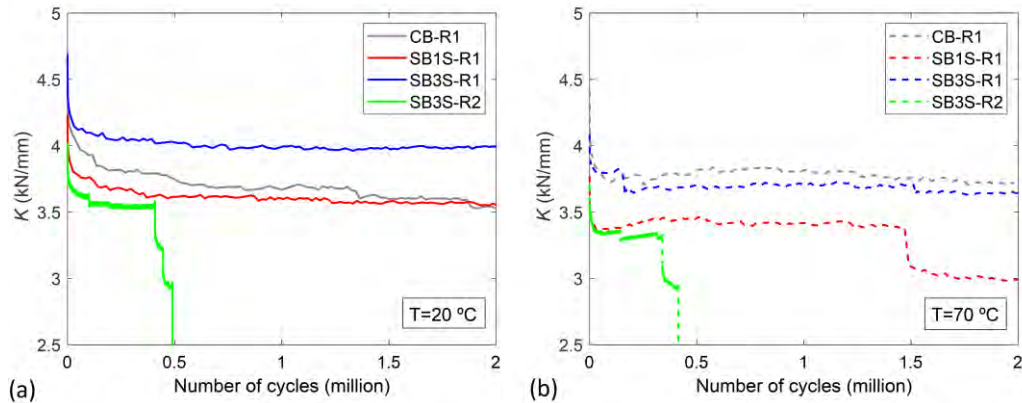
Figure 8.9. Evolution of stiffness (K) for specimens tested at: (a) 20 °C and (b) 70 °C.

To conclude the analysis of results on fatigue testing, the ability of specimens to adequately dissipate energy is analyzed. According to experimental results, the increase in the CFRP-strengthening ratio, the application of high service temperature (70 °C) and the application of

the low *R* ratio (R2=0.38) resulted in larger amounts of total accumulated dissipated energy (see results in Figure 7.17). It should be mentioned that the effect of temperature was more pronounced in strengthened RC beams, which is a sign of temperature affecting the efficiency of the strengthening system.

Finally, the residual strength of the specimens that survived the fatigue loading was analyzed, and those specimens were immediately tested up to failure after the end of the fatigue test. Results on these up-to-failure tests are compared in Figure 8.10 to instantaneous flexural performance of reference beams (i.e. those beams whose results were used to define P_{max} and P_{min} for the fatigue tests). The initial point in the load-deflection curves of specimens that underwent fatigue test corresponds to the plastic deflection (δ_p) after unloading the beams. As it can be seen, no considerable change was observed in the load-deflection response of the control unstrengthened beams (CB), except of larger ultimate deflection (see Figure 8.10a), and failure mode consisted on concrete crushing after steel reinforcement yielding in all cases. For NSM CFRP-strengthened beams with one CFRP strip tested at 20 °C, the fatigue test did not have any relevant effect on the post-yielding load-deflection curve (see Figure 8.10b). However, the application of 70 °C during fatigue tests resulted in much lower values for yielding and ultimate loads. This was due to the fact that this specimen experienced a big jump during the fatigue loading and, therefore, more damage was accumulated in steel reinforcement. In this sense, this specimen experienced the largest value of δ_p. In the cases of short-term and post long-term loading at 20 °C, failure mode consisted on FRP rupture after yielding of steel reinforcement, whilst for the beam tested at 70 °C, failure mode was steel rupture due to the accumulated damage during the fatigue loading. Finally, results on NSM CFRP-strengthened RC beams with three CFRP strips are presented in Figure 8.10c. In this case, specimen submitted to fatigue loading at 20 °C experienced a slight increase in ultimate load, and had the same failure mode as the instantaneous reference specimen (intermediate concrete cover separation). Specimen submitted to fatigue loading at 70 °C experienced a reduction in the ultimate load and a change in failure mode from intermediate concrete cover separation to concrete crushing.
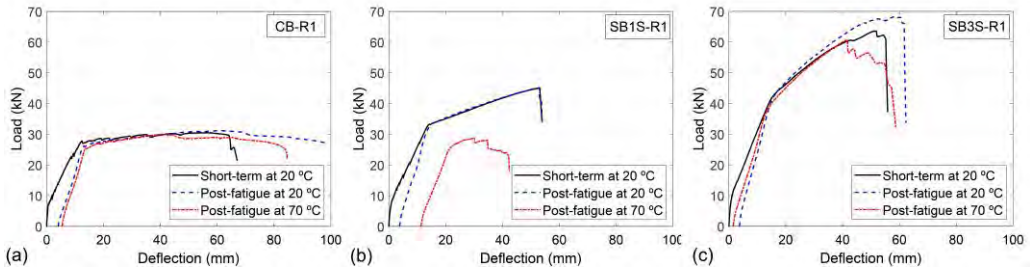
Figure 8.10. Residual strength of specimens: (a) CB-R1, (b) SB1S-R1 and (c) SB3S-R1.

8.5 Concluding remarks

The aim of this PhD thesis is to evaluate the effect of temperature on the instantaneous, time-dependent and fatigue flexural response of NSM CFRP-strengthened RC beams. To this end, a first experimental program was designed to evaluate the effect of different temperatures (i.e. 20 °C to 85 °C), below and beyond the T_g of the epoxy adhesive, on the instantaneous behavior of the strengthened flexural elements. According to the experimental results, no considerable change was observed in the load-deflection response of specimens tested up to 60 °C, with specimens failing by FRP rupture. However, increasing the temperature to 70 °C resulted in a slight reduction in the ultimate load and a change in failure mode to end debonding. It should be highlighted that values for temperature that mark the line between the two different failure modes fall within the range of values of the T_g of the epoxy adhesive (T_g was tested to be in the range of 53.9 °C - 65.3 °C). Furthermore, analytical predictions that considered the effect of concrete shrinkage on the short-term response of RC beams were performed. In this sense, the results showed that large concrete shrinkage had a detrimental significant influence on the response of the specimens, which was in agreement with experimental results.

In light of the effect of testing temperature on the instantaneous flexural performance of NSM CFRP-strengthened RC beams, and being this effect attributed to the temperature-dependent performance of the epoxy resin, a second experimental program was designed to evaluate the effect of curing, post-curing and testing temperatures on the mechanical properties and T_g of the epoxy adhesive. Experimental results showed that $T_{g\infty}$ was in the range of 50 °C to 70 °C. As a result, curing or post-curing the epoxy at temperatures below $T_{g\infty}$ resulted in an increase in the T_g of epoxy, whilst the application of curing or post-curing temperatures

larger than $T_{g\infty}$ derived in smaller values of T_g. Furthermore, a clear effect of testing temperature was observed, where the mechanical properties of epoxy progressively decreased when testing temperature was increased, especially when testing temperature was near or beyond the T_g of the epoxy adhesive. Finally, results on the effect of curing and post-curing temperatures demonstrated that conditioning up to $T_{g\infty}$ improved the mechanical properties of the epoxy adhesive, whilst conditioning beyond this temperature had the opposite behavior. These results are related to the achievement of a complete cross-linking between the molecules of the epoxy (for curing and post-curing temperatures below $T_{g\infty}$) and a possible thermal degradation (for curing and post-curing temperatures beyond $T_{g\infty}$). Results from this experimental program fully support results from the instantaneous flexural tests.

Based on results obtained in the first and second experimental program, a third experimental program was designed to analyze the effect of temperature (50 °C) on the time-dependent behavior of NSM CFRP-strengthened RC beams. Experimental results confirmed that high service temperature had a significant influence on the time-dependent deflections of the specimens, due to different reasons such as: (i) large shrinkage strain and creep coefficient of concrete at 50 °C; (ii) reduction in the mechanical properties (tensile strength and modulus of elasticity) of the epoxy adhesive at 50 °C and (iii) large creep coefficient of epoxy adhesive at 50 °C. However, although mechanical performance of the epoxy adhesive under high service temperature and long-term loading contributes to the larger time-dependent deflections, the effect of temperature on time-dependent properties of concrete (concrete shrinkage and creep) seemed to be dominant. Finally, time-dependent deflections were analytically predicted with a methodology based on AEMM. The registers of temperature and humidity were used to determine concrete creep coefficient and concrete shrinkage, following *fib* Model Code 2010 [83]. Analytical results were in good agreement with experimental time-dependent deflections, thus confirming the accuracy of the developed method.

Finally, the effect of a high service temperature (70 °C) on the fatigue performance of NSM CFRP-strengthened RC beam was also investigated. Experimental results showed that the application of 70 °C resulted in larger deflections and lower stiffness during the fatigue loading. Furthermore, it was also observed that increasing the applied temperature resulted in a reduction of the effectiveness of the strengthening system, which led to damage accumulation in the steel reinforcement. However, the reduction in the effectiveness of the strengthening

system depended on the CFRP-strengthening ratio. Moreover, the application of fatigue cycles with larger amplitudes (i.e. the application of lower R ratios) was the responsible of specimens notwithstanding the programmed fatigue test and failing by steel reinforcement rupture. It should be mentioned that the combined effect of higher fatigue load and higher temperature resulted in the most premature failure of the strengthened beams.

PART IV: Concluding remarks and future works

9 Conclusions

During the last decades, the tendency toward using FRP materials to strengthen RC structures and enhance their structural capacity has widely increased. In this sense, due to its stunning performance, the NSM strengthening technique has been promoted to be one of the most efficient ones. Even though this technique has several advantages when compared to other existing strengthening systems, premature debonding is still a matter of concern, especially when epoxy adhesives (being viscoelastic in nature) are used. In this sense, the mechanical properties of the bonding material may be affected by different loading types (long-term and fatigue) and environmental conditions (high service temperature), which can result in a reduction in the efficiency of the strengthening system.

The main objectives of this PhD thesis were to study the instantaneous, time-dependent and fatigue flexural performance of NSM CFRP-strengthened RC beams under high service temperature. To this end, instantaneous flexural tests on NSM CFRP-strengthened RC beams were performed to evaluate the effect of different temperatures, different CFRP ratios and different concrete compressive strengths on the load-deflection response and failure modes. Besides, analytical predictions on the instantaneous load-deflection curves were also presented, where the effect of shrinkage and temperature were accounted for. The time-dependent flexural performance of NSM CFRP-strengthened RC beams under high service temperature was evaluated in a second experimental program, where the effect of high service temperature, steel reinforcement ratio and CFRP strengthening ratio was analyzed. In this experimental work, the time-dependent behavior of the involved materials was also studied. Furthermore, an analytical work, based on AEMM, was also presented to predict the time-dependent deflections of the tested beams. To continue, a third experimental program was performed to evaluate the fatigue flexural behavior of NSM CFRP-strengthened RC beams. The parameters of the experimental program were the service temperature, the CFRP strengthening ratio and the cyclic loading level. To conclude the experimental work carried out in this thesis, resin specimens were also tested in tension and compression to study the effect of curing, post-curing and testing temperature on its mechanical and physical (T_g) properties.

In the following, the main conclusions of the thesis are presented. It should be highlighted that conclusions are presented in chronological order.

9.1 Effect of temperature variation on the instantaneous flexural behavior of NSM CFRP-strengthened RC beams

The influence of high service temperature on the instantaneous flexural performance of NSM CFRP-strengthened RC beams was presented in Paper A. Based on the data presented, the following conclusions can be drawn:

- For the given test configuration, the NSM system showed excellent behavior as no end debonding took place up to 60 °C (53.9< T_g <65.3).

- The application of temperature up to 60 °C did not have a considerable effect on the load-deflection curves of the specimens. This was due to possible post-curing of epoxy adhesive.

- The application of a temperature beyond the T_g of the epoxy adhesive resulted in a reduction of the stiffness and the ultimate load capacity of the beams. In this sense, the bond capacity of the strengthening system appears to be affected by the reduction of epoxy mechanical properties, thus affecting the efficiency of the strengthening system.

- The application of temperature up to 60 °C did not have an effect on the failure modes of unstrengthened and strengthened beams, and all strengthened specimens failed by FRP rupture. On the contrary, specimens tested at 70 °C failed by premature end debonding, which was evidence of the detrimental effect of temperature on the capacity of the joint.

- Analytical predictions on the short-term load-deflection response of NSM CFRP-strengthened RC beams were obtained, which included the effect of shrinkage. According to analytical predictions, higher concrete shrinkage affects the instantaneous performance of the flexural element leading to lower cracking moment and flexural stiffness. Comparison between analytical predictions on the load-deflection curves and experimental results confirmed the accuracy of the model.

9.2 Effect of temperature on mechanical properties and T_g of epoxy adhesive

The effect of curing, post-curing and testing temperatures on mechanical properties and T_g of the epoxy adhesive was presented in Paper B.

Curing and post-curing affected T_g differently depending on the value of the curing and post-curing temperature. In this sense, when curing and post-curing of an epoxy adhesive takes place at a temperature below $T_{g∞}$, T_g increases as the curing (or post-curing) temperature increases.

On the contrary, when curing (or post-curing) takes place at a temperature beyond $T_{g\infty}$, T_g decreases as the curing (or post-curing) temperature increases.

From the analysis of the effect of testing temperature on mechanical properties of the epoxy adhesive, the following conclusions can be drawn:

- Tensile mechanical properties of the epoxy adhesive progressively decreased for larger values of testing temperature. In this sense, a sharp reduction was observed at temperature near or beyond the T_g of the epoxy adhesive and, due to the complete rubbery state of the epoxy, the elastic modulus was almost negligible.

- The inclusion of an extra cycle of post-curing barely affected the mechanical properties of epoxy specimens.

From the analysis of the effect of curing temperature on mechanical properties of the epoxy adhesive, the following conclusions can be drawn:

- Curing temperatures below $T_{g\infty}$ improved the epoxy mechanical properties because of the cross-linking promotion. On the other hand, curing temperatures beyond $T_{g\infty}$ resulted in a reduction in epoxy mechanical properties due to a possible thermal degradation on the adhesive.

- No considerable effect of an extra post-curing process was observed, which was due to stabilization of epoxy because of post-curing taking place at the same temperature as the curing process.

From the analysis of the effect of post-curing temperature on mechanical properties of the epoxy adhesive, the following conclusions can be drawn:

- Similar to curing temperature, post-curing the epoxy at a temperature below the $T_{g\infty}$, enhanced the mechanical properties because of the reactivation of cross-linking of the non-complete cured epoxy adhesive.

- The largest benefit of post-curing on epoxy tensile strength took place for post-curing temperature equal to 60 °C, whilst for epoxy compressive strength it happened at 40 °C.

9.3 Time-dependent behavior of NSM CFRP-strengthened RC beams under high service temperature

The long-term performance of NSM CFRP-strengthened RC beams under different service temperatures was studied in Paper C.

From the short-term tests, the following conclusion can be drawn:

- Similar to the short-term test results presented in Paper A, the application of 50 °C did not have a significant effect on the load-deflection responses of the specimens and had no effect on the failure mode, as unstrengthened control beams failed by concrete crushing and NSM CFRP-strengthened RC beams failed by FRP rupture, irrespective of applied temperature being equal to 20 °C or 50 °C. This can be attributed to possible post-curing of the epoxy during the loading time, as applied temperature was below the T_g of the epoxy adhesive.

From the long-term tests and analytical predictions, the following conclusions can be drawn:

- The increase in the temperature to 50 °C resulted in larger concrete shrinkage, concrete creep coefficient and epoxy creep coefficient.

- The increase in the CFRP-strengthening ratio produced lower time-dependent deflections in specimens tested at 20 °C submitted to the same long-term load. However, CFRP-strengthening was not significantly affecting time-dependent deflections for testing temperature equal to 50 °C, so that the time-dependent response of the strengthened beams approached that of the unstrengthened ones.

- The effect of temperature on the time-dependent behavior of concrete appeared to be the dominant factor in the time-dependent response of RC elements.

- Analytical predictions on the time-dependent deflections obtained from an analysis based on the AEMM and *fib* Model Code 2010 were in a good agreement with experimental data.

From the residual flexural strength tests and aging specimens, the following conclusions can be drawn:

- Permanent deflections were registered after the removal of the long-term loads. In this regard, and similar to time-dependent deflections, larger permanent deflections were obtained in those beams that withstood a temperature of 50 °C during their long-term loading.

- The residual strength of unstrengthened control beams was similar to that of short-term specimens and aging specimens. For the case of strengthened beams, however, the trend change and a slight increase in the yielding load and the post-yielding stiffness was observed.

9.4 Fatigue performance of NSM CFRP-strengthened RC beam under high service temperature

The effect of fatigue loading on the flexural performance of NSM CFRP-strengthened RC beams under different service temperatures was investigated in Paper D. From the experimental tests, the following conclusions can be drawn:

- For a large R ratio (R1=0.57) no failure was observed during fatigue loading (i.e. 2 million cycles), whilst for a low R ratio (R2=0.38), the specimens failed by steel reinforcement rupture during the fatigue loading.

- A progressive increase in deflections and concrete strain, and decrease in stiffness took place along the application of the fatigue cycles. It should be mentioned, however, that the largest rates of variation were observed at the initial stages of the fatigue loading.

- In general, the NSM CFRP-strengthened RC beams showed a better fatigue performance when compared to unstrengthened control beams.

- The combined effect of temperature and low R ratio was found to be catastrophic for NSM CFRP-strengthened RC members' fatigue life.

- NSM CFRP-strengthening helped to postpone the failure of the beam during fatigue loading after steel reinforcement rupture.

- Larger CFRP-strengthening ratios and testing temperature resulted in larger dissipated energy.

- The residual strength of the specimens was inversely proportional to the level of fatigue damage. In this sense, the residual strength decreased for specimens submitted to fatigue loads at 70 °C.

- Post-fatigue failure mode of unstrengthened beams was not affected by fatigue testing. For strengthened beams, post-fatigue failure mode changed from FRP rupture to steel rupture in the case of the application of 70 °C and a high R ratio (R1=0.57).

10 Future works

Based on the work carried out in this thesis, the following suggestions for future work are drawn:

- To study the effect of cyclic temperature (day/night) on time-dependent behavior of NSM FRP-strengthened RC beams.
- To study the effect of temperature on the time-dependent behavior of NSM FRP-strengthened RC beams where different bonded joints have been assigned (i.e. groove dimensions, bars/strips size).
- To evaluate the effect of higher levels of long-term load, combined with temperature, on the time-dependent behavior of NSM FRP-strengthened RC beams, to examine the influence of nonlinear creep of materials.
- To develop a numerical model to simulate the time-dependent behavior of NSM FRP-strengthened RC beams under different service temperatures.
- To expand the fatigue experimental program in order to consider the influence of groove dimensions and bars/strips size.
- To develop a numerical model that includes the temperature effects on the fatigue performance of NSM FRP-strengthened RC beams.
- To investigate whether the inclusion of anchorages may help to postpone the fatigue failure of NSM FRP-strengthened RC beams.

11 References

[1] fib bulletin 90. Externally applied FRP reinforcement for concrete structures. International Federation for Structural Concrete; 2019.

[2] GangaRao HV, Taly N, Vijay P. Reinforced concrete design with FRP composites. CRC press, 2006. https://doi.org/10.1201/9781420020199

[3] Nanni A. Fiber-Reinforced-Plastic (FRP) Reinforcement for Concrete Structures: Properties and Application, Elsevier Science, Amsterdam, 1993. https://doi.org/10.1016/C2009-0-09136-3

[4] Bisby LA. ISIS Educational Module 2: An Introduction to FRP Composites for Construction. ISIS Canada Educ Modul 2006.

[5] De Lorenzis L, Teng JG. Near-surface mounted FRP reinforcement: An emerging technique for strengthening structures. Compos B Eng 2007; 38 (2): 119-143. https://doi.org/10.1016/j.compositesb.2006.08.003

[6] Parretti R, Nanni A. Strengthening of RC members using near-surface mounted FRP composites: Design overview. Adv Struct Eng 2004; 7(6): 469-483. https://doi.org/10.1260/1369433042863198

[7] Emara M, Torres L, Baena M, Barris C, Moawad M. Effect of sustained loading and environmental conditions on the creep behavior of an epoxy adhesive for concrete structures strengthened with CFRP laminates Compos B Eng 2017; 129: 88-96. https://doi.org/10.1016/j.compositesb.2017.07.026

[8] Firmo JP, Roquette MG, Correia JR, Azevedo AS. Influence of elevated temperatures on epoxy adhesive used in CFRP strengthening systems for civil engineering applications. Int J Adhes Adhes 2019; 93: 102333. https://doi.org/10.1016/j.ijadhadh.2019.01.027

[9] Silva P, Fernandes P, Sena-Cruz J, Xavier J, Castro F, Soares D, Carneiro V. Effects of different environmental conditions on the mechanical characteristics of a structural epoxy. Compos B Eng 2016; 88: 55–63. https://doi.org/10.1016/j.compositesb.2015.10.036

[10] Neville AM. Properties of concrete. Fourth edition, Longman London, 1995.

[11] Gilbert RI, Ranzi G. Time-dependent behaviour of concrete structures. CRC Press, 2010.

[12] Sheikh-Ahmad JY. Machining of polymer composites. Springer, 2009. https://doi.org/10.1007/978-0-387-68619-6

[13] Szabó ZK. Bond characteristics of NSM reinforcements based on advanced test method. PhD thesis. Budapest, Hungary: Budapest University of Technology and Economics, 2013.

[14] Pilakoutas K, Achillides Z, Waldron P. Non-ferrous reinforcement in concrete structures. In: Topping, E.M.L.&.B., Centenary Conference on Innovation in Civil and Structural Engineering. Civil-Comp Ltd. Topping, E.M.L.&.B., Centenary Conference on Innovation in Civil and Structural Engineering. Civil-Comp Ltd. 1997.

[15] Balaguru P, Nanni A, Giancaspro J. FRP composites for reinforced and prestressed concrete structures: a guide to fundamentals and design for repair and retrofit. CRC Press 2008. https://doi.org/10.1201/9781482288537

[16] Carolin A. Carbon fibre reinforced polymers for strengthening of structural elements. PhD thesis. Luleå tekniska universitet, 2003.

[17] Jassal M, Ghosh S. Aramid fibres - An overview. Indian J Fibre Text Res 2002; 27: 290–306.

[18] Mallick P. Fiber-Reinforced Composites. Materials, Manufacturing, and Design. Third Edition, CRC Press 2007. https://doi.org/10.1201/9781420005981

[19] Baena M, Torres L, Turon A, Barris C. Experimental study of bond behaviour between concrete and FRP bars using a pull-out test. Compos B Eng 2009; 40: 784–97. doi:10.1016/j.compositesb.2009.07.003.

[20] S&P. S&P Cfrp Laminate, Technical Datasheet; S&P: Seewen, Switzerland, 2017.

[21] El-Hacha R, Soudki, K. Prestressed near-surface mounted fibre reinforced polymer reinforcement for concrete structures—A review. Can J Civ Eng 2013; 40(11): 1127-1139. https://doi.org/10.1139/cjce-2013-0063

[22] Sonnenschein R, Gajdosova K, Holly I. FRP Composites and their Using in the Construction of Bridges. Procedia Eng 2016; 161: 477–82. doi:10.1016/j.proeng.2016.08.665.

[23] FIB bulletin 14. Externally bonded FRP reinforcement for RC structures. vol. 14. International Federation for Structural Concrete; 2001. doi:10.1016/0262-5075(85)90032-6.

[24] Yao J, Teng JG, Chen JF. Experimental study on FRP-to-concrete bonded joints. Compos B Eng 2005; 36: 99–113. doi:10.1016/j.compositesb.2004.06.001.

[25] Konrad Zilch KB. A general bond stress slip relationship for NSM FRP strips. Proc. of FRPRCS-8, Patras, Greece 2007.

[26] Tumialan JG, Vatovec M, Kelley PL. Case study: strengthening of parking garage decks with near surface-mounted CFRP bars. J Compos Constr 2007; 11: 523–30. doi:10.1061/(ASCE)1090-0268(2007)11:5(523).

[27] Kishi N, Mikami H, Kurihashi Y, Sawada S. Flexural behaviour of RC beams reinforced with NSM AFRP rods. In Proceedings of the International Symposium on Bond Behaviour of FRP in structures 2005.

[28] Sharaky IA, Torres L, Baena M, Miàs C. An experimental study of different factors affecting the bond of NSM FRP bars in concrete. Compos Struct 2013; 99: 350–65. doi:10.1016/j.compstruct.2012.12.014.

[29] Sharaky IA, Torres L, Baena M, Vilanova I. Effect of different material and construction details on the bond behaviour of NSM FRP bars in concrete. Constr Build Mater 2013; 38: 890–902. doi:10.1016/j.conbuildmat.2012.09.015.

[30] Pellegrino C, Sena-Cruz J. Design Procedures for the Use of Composites in Strengthening of Reinforced Concrete Structures: State-of-the-Art Report of the Rilem Technical Committee 234-Duc; Springer: Dordrecht, The Netherlands, 2016; p. 392. doi:10.1007/978-94-017-7336-2

[31] Sena Cruz JM, Barros JAO, Gettu R, Azevedo ÁFM. Bond Behavior of Near-Surface Mounted CFRP Laminate Strips under Monotonic and Cyclic Loading. J Compos Constr 2006; 10: 295–303. doi:10.1061/(ASCE)1090-0268(2006)10:4(295).

[32] Seracino R, Jones NM, Ali MS, Page MW, Oehlers DJ. Bond Strength of Near-Surface Mounted FRP Strip-to-Concrete Joints. J Compos Constr 2007; 11: 401–9. doi:10.1061/(ASCE)1090-0268(2007)11:4(401).

[33] Zhang SS, Teng JG, Yu T. Bond-Slip Model for Interfaces between Near-Surface Mounted CFRP Strips and Concrete. In 11th International Symposium on Fiber Reinforced Polymers for Reinforced Concrete Structures (FRPRCS-11), 2013.

[34] Täljsten B. The importance of bonding—A historic overview and future possibilities. Adv Struct Eng 2006; 9(6): 721-736. https://doi.org/10.1260/136943306779369509

[35] De Lorenzis L, Rizzo A, La Tegola A. A modified pull-out test for bond of near-surface mounted FRP rods in concrete. Compos B Eng 2002; 33(8): 589-603. https://doi.org/10.1016/S1359-8368(02)00052-5

[36] Silva P, Escusa GG, Sena-Cruz J, Azenha M. Experimental investigation of RC slabs strengthened with NSM CFRP system subjected to elevated temperatures up to 80 °C. In

Proceeding of 8th International Conference on Fibre-Reinforced Polymer (FRP) Composites in Civil Engineering, CICE, Hong Kong, China, 2016. http://hdl.handle.net/1822/43902

[37] Azevedo AS, Firmo JP, Correia JR, Tiago C. Influence of elevated temperatures on the bond behaviour between concrete and NSM-CFRP strips. Cem Concr Compos 2020; 111: 103603. https://doi.org/10.1016/j.cemconcomp.2020.103603

[38] Al-Jaberi Z, Myers JJ, Chandrashekhara K. Effect of direct service temperature exposure on the bond behavior between advanced composites and CMU using NSM and EB techniques. Compos Struct 2019; 211: 63-75. https://doi.org/10.1016/j.compstruct.2018.11.085

[39] De Lorenzis L, Nanni A, La Tegola A. Strengthening of reinforced concrete structures with near surface mounted FRP rods. In International meeting on composite materials, PLAST 2000.

[40] Sharaky IA, Reda RM, Ghanem M, Seleem MH, Sallam HEM. Experimental and numerical study of RC beams strengthened with bottom and side NSM GFRP bars having different end conditions. Constr Build Mater 2017; 149: 882-903. https://doi.org/10.1016/j.conbuildmat.2017.05.192

[41] Sena-Cruz J, Barros J, Bianco V, Bilotta A, Bournas D, Ceroni F, Dalfré G, Kotynia R, Monti G, Nigro E, Triantafillou T. NSM systems. In Design procedures for the use of composites in strengthening of reinforced concrete structures, Springer, Dordrecht 2016. https://doi.org/10.1007/978-94-017-7336-2_8

[42] Hassan T, Rizkalla S. Investigation of bond in concrete structures strengthened with near surface mounted carbon fiber reinforced polymer strips. J Compos Constr 2003; 7(3): 248-257. https://doi.org/10.1061/(ASCE)1090-0268(2003)7:3(248)

[43] El-Hacha R, Rizkalla SH. Near-surface-mounted fiber-reinforced polymer reinforcements for flexural strengthening of concrete structures. ACI Struct J 2004; 101(5): 717-726. https://doi.org/10.14359/13394

[44] Barros JA., Fortes AS. Flexural strengthening of concrete beams with CFRP laminates bonded into slits. Cem Concr Compos 2005; 27(4): 471-480. https://doi.org/10.1016/j.cemconcomp.2004.07.004

[45] Barros JA., Dias SJ., Lima JL. Efficacy of CFRP-based techniques for the flexural and shear strengthening of concrete beams. Cem Concr Compos 2007; 29(3): 203-217. https://doi.org/10.1016/j.cemconcomp.2006.09.001

[46] Teng JG, De Lorenzis L, Wang B, Li R, Wong TN, Lam L. Debonding failures of RC beams strengthened with near surface mounted CFRP strips. J Compos Constr 2006; 10(2): 92-105. https://doi.org/10.1061/(ASCE)1090-0268(2006)10:2(92)

[47] Dias SJ, Barros JA, Janwaen W. Behavior of RC beams flexurally strengthened with NSM CFRP laminates. Compos Struct 2018; 201: 363-376. https://doi.org/10.1016/j.compstruct.2018.05.126

[48] Al-Saadi NTK, Mohammed A, Al-Mahaidi R, Sanjayan J. A state-of-the-art review: Near-surface mounted FRP composites for reinforced concrete structures. Constr Build Mater 2019; 209: 748-769. https://doi.org/10.1016/j.conbuildmat.2019.03.121

[49] Sena-Cruz JM, Barros J. Bond between near surface mounted carbon-fiber-reinforced polymer laminate strips and concrete. J Compos Constr 2004; 8: 519–527. https://doi.org/10.1061/(ASCE)1090-0268(2004)8:6(519)

[50] Täljsten B, Carolin A, Nordin H. Concrete structures strengthened with near surface mounted reinforcement of CFRP. Adv Struct Eng 2003; 6(3): 201-213. https://doi.org/10.1260/136943303322419223

[51] Kalayci AS. Development of surface flaw thresholds for pre-cured fiber reinforced polymer and groove size tolerance for near surface mounted fiber reinforced polymer retrofit systems. Florida International University, 2008.

[52] Sharaky IA, Selmy SAI, El-Attar MM, Sallam HEM. The influence of interaction between NSM and internal reinforcements on the structural behavior of upgrading RC beams. Compos Struct 2020; 234, 111751. https://doi.org/10.1016/j.compstruct.2019.111751

[53] Sharaky IA, Baena M, Barris C, Sallam HEM, Torres L. Effect of axial stiffness of NSM FRP reinforcement and concrete cover confinement on flexural behaviour of strengthened RC beams: Experimental and numerical study. Eng Struct 2018; 173: 987-1001. https://doi.org/10.1016/j.engstruct.2018.07.062

[54] Obaidat YT, Barham WS, Aljarah AH. New anchorage technique for NSM-CFRP flexural strengthened RC beam using steel clamped end plate. Constr Build Mater 2020; 263: 20246. https://doi.org/10.1016/j.conbuildmat.2020.120246

[55] Sena-Cruz JM, Barros JA, Coelho MR, Silva LF. Efficiency of different techniques in flexural strengthening of RC beams under monotonic and fatigue loading. Constr Build Mater 2012; 29: 175–182. https://doi.org/10.1016/j.conbuildmat.2011.10.044

[56] Barris B, Sala P, Gómez J, Torres L. Flexural behaviour of FRP reinforced concrete beams strengthened with NSM CFRP strips. Compos Struct 2020; 241: 112059. https://doi.org/10.1016/j.compstruct.2020.112059

[57] Klamer EL, Dick AH, Michael CJH. The influence of temperature on RC beams strengthened with externally bonded CFRP reinforcement. Heron 2008; 53: 157–185.

[58] Krzywoń R. Behavior of EBR FRP strengthened beams exposed to elevated temperature. Procedia Eng 2017; 193: 297–304. https://doi.org/10.1016/j.proeng.2017.06.217

[59] Coelho MR, Sena-Cruz JM, Neves LA. A review on the bond behavior of FRP NSM systems in concrete. Constr Build Mater 2015; 93: 1157-1169. https://doi.org/10.1016/j.conbuildmat.2015.05.010

[60] Yost JR, Gross SP, Deitch MJ. Fatigue behavior of concrete beams strengthened in flexure with near surface mounted CFRP. In Proceedings of the 8th International Symposium on Fiber Reinforced Polymer Reinforcement for Reinforced Concrete Structures (FRPRCS8), University of Patras, Patras, Greece 2007.

[61] Hassan T, Rizkalla S. Bond mechanism of NSM FRP bars for flexural strengthening of concrete structures. ACI Struct J 2004; 101(6): 830-839. https://doi.org/10.14359/13458

[62] Tang WC, Balendran, RV, Nadeem A, Leung HY. Flexural strengthening of reinforced lightweight polystyrene aggregate concrete beams with near-surface mounted GFRP bars. Build environ 2006; 41(10): 1381-1393. https://doi.org/10.1016/j.buildenv.2005.05.029

[63] Choi HT, West JS, Soudki KA. Partially bonded near-surface-mounted CFRP bars for strengthened concrete T-beams. Constr Build Mater 2011; 25(5): 2441-2449. https://doi.org/10.1016/j.conbuildmat.2010.11.056

[64] Sharaky IA, Torres L, Comas J, Barris C. Flexural response of reinforced concrete (RC) beams strengthened with near surface mounted (NSM) fibre reinforced polymer (FRP) bars. Compos Struct 2014; 109: 8-22. https://doi.org/10.1016/j.compstruct.2013.10.051

[65] Quattlebaum JB, Harries KA, Petrou MF. Comparison of three flexural retrofit systems under monotonic and fatigue loads. J Bridge Eng 2005; 10(6): 731-740. https://doi.org/10.1061/(ASCE)1084-0702(2005)10:6(731)

[66] Rosenboom O, Rizkalla S. Behavior of prestressed concrete strengthened with various CFRP systems subjected to fatigue loading. J Compos Constr 2006; 10 (6): 492–502. https://doi.org/10.1061/(ASCE)1090-0268(2006)10:6(492)

[67] Badawi M, Soudki K. Fatigue behavior of RC beams strengthened with NSM CFRP rods. J Compos Constr 2009; 13(5): 415-421. https://doi.org/10.1061/(ASCE)1090-0268(2009)13:5(415)

[68] Blaschko M, Zilch K. Rehabilitation of concrete structures with CFRP strips glued into slits. In Proceedings of the Twelfth International Conference of Composite Materials, ICCM, 1999.

[69] Wahab N, Soudki KA, Topper T. Mechanics of bond fatigue behavior of concrete beams strengthened with NSM CFRP rods. J Compos Constr 2011; 15(6): 934-942. https://doi.org/10.1061/(ASCE)CC.1943-5614.0000228

[70] Wahab N., Soudki KA, Topper T. Experimental investigation of bond fatigue behavior of concrete beams strengthened with NSM prestressed CFRP rods. J Compos Constr 2012; 16(6): 684-692. https://doi.org/10.1061/(ASCE)CC.1943-5614.0000298

[71] Carolin A, Nordin H, Täljsten B. Concrete beams strengthened with near surface mounted reinforcement of CFRP. In International Conference on FRP Composites in Civil Engineering, Elsevier 2001.

[72] De Lorenzis L, Nanni A, La Tegola A. Flexural and shear strengthening of reinforced concrete structures with near surface mounted FRP rods. in Proceedings of 3rd International Conference on Advanced Composite Materials in Bridges and Structures, Ottawa, Canada, 521–528, 2000.

[73] De Lorenzis L, Nanni A. Characterization of FRP rods as near-surface mounted reinforcement. J Compos Constr 2001; 5(2): 114-121. https://doi.org/10.1061/(ASCE)1090-0268(2001)5:2(114)

[74] De Lorenzis L, Nanni A. Bond between near-surface mounted fiber-reinforced polymer rods and concrete in structural strengthening. ACI Struct J 2002; 99(2): 123-132.

[75] Al-Mahmoud F, Castel A, François R, Tourneur C. Strengthening of RC members with near-surface mounted CFRP rods. Compos Struct 2009; 91(2): 138-147. https://doi.org/10.1016/j.compstruct.2009.04.040

[76] Al-Mahmoud F, Castel A, François R, Tourneur C. RC beams strengthened with NSM CFRP rods and modeling of peeling-off failure. Compos Struct 2010; 92(8): 1920-1930. https://doi.org/10.1016/j.compstruct.2010.01.002

[77] Kotynia R. Analysis of the flexural response of NSM FRP-strengthened concrete beams, in: In Proceedings of the eight international conference on fibre-reinforced plastics for reinforced concrete structures (FRPRSCS-8), Patras, Greece, 2007.

[78] Bonaldo E, Barros JAO, Loureņo PB. Efficient strengthening technique to increase the flexural resistance of existing RC slabs. J Compos Constr 2008; 12(2): 149-159. https://doi.org/10.1061/(ASCE)1090-0268(2008)12:2(149)

[79] Costa IG, Barros JA. Flexural and shear strengthening of RC beams with composite materials–The influence of cutting steel stirrups to install CFRP strips. Cem Concr Compos 2010; 32(7): 544-553. https://doi.org/10.1016/j.cemconcomp.2010.03.003

[80] Daud SA, Forth JP, Nikitas N. Time-dependent behaviour of cracked, partially bonded reinforced concrete beams under repeated and sustained loads. Eng Struct 2018; 163: 267-280. https://doi.org/10.1016/j.engstruct.2018.02.054

[81] Mias C, Torres L, Turon A, Sharaky I.A. Effect of material properties on long-term deflections of GFRP reinforced concrete beams. Constr Build Mater 2013; 41: 99-108. https://doi.org/10.1016/j.conbuildmat.2012.11.055

[82] Kim SH, Han KB, Kim KS, Park SK. Stress–strain and deflection relationships of RC beam bonded with FRPs under sustained load. Compos B Eng 2009; 40(4): 292-304. https://doi.org/10.1016/j.compositesb.2008.12.003

[83] International Federation for Structural Concrete (fib). Fib Model Code for Concrete Structures 2010. John Wiley & Sons, New York, USA, 2013.

[84] GILBERT RI. Time effects in concrete structures. Elsevier, Amsterdam, 1988.

[85] Naumenko K, Altenbach H. Modeling of Creep for Structural Analysis, Foundations of Engineering Mechanics, Springer Berlin, Heidelberg 2007. https://doi.org/10.1007/978-3-540-70839-1

[86] Emara MRAE. Bond behavior of NSM FRP strips in concrete under sustained loading. Universitat de Girona, Spain, 2018.

[87] Bazant ZP. Mathematical Modelling of Creep and Shrinkage of Concrete. Wiley, Chichester, New York, 1988.

[88] Chong K.T, Foster SJ, Gilbert RI. Time-dependent modelling of RC structures using the cracked membrane model and solidification theory. Comput Struct 2008; 86(11-12): 1305-1317 https://doi.org/10.1016/j.compstruc.2007.08.005

[89] Gribniak V, Torres L, Kaklauskas G, Daniunas A, Kacianauskas R, Jakubovskis R. Prediction of concrete shrinkage occurring prior to external loading and effect on short-term constitutive modeling and design. Adv Struct Eng 2013; 16: 1061–1080. https://doi.org/10.1260/1369-4332.16.6.1061

[90] ACI committee 318, Building Code Requirements for Structural Concrete and Commentary (ACI 318M-11), 2011.

[91] ACI Committee 209, 209R-92: Prediction of Creep, Shrinkage, and Temperature Effects in Concrete Structures, 2008.

[92] Tan KH, Saha MK. Long-term deflections of reinforced concrete beams externally bonded with FRP system. J Compos Constr 2006; 10(6): 474-482. https://doi.org/10.1061/(ASCE)1090-0268(2006)10:6(474)

[93] Malvar LJ. Durability of Composites in Reinforced Concrete, in: First International Conference on Durability of Composites for Construction, First International Conference on Durability of Composites for Construction, Sherbrooke (Québec), Canada, 1998.

[94] Goertzen WK, Kessler MR. Creep behavior of carbon fiber/epoxy matrix composites. Mater Sci Eng A 2006; 421: 217–25. https://doi.org/10.1016/j.msea.2006.01.063.

[95] Ascione F, Berardi VP, Feo L, Giordano A. An experimental study on the long-term behavior of CFRP pultruded laminates suitable to concrete structures rehabilitation. Compos B Eng 2008; 39: 1147–50. https://doi.org/10.1016/j.compositesb.2008.03.008.

[96] Mazzotti C, Savoia M. Stress redistribution along the interface between concrete and FRP subject to long-term loading. Adv Struct Eng 2009; 12: 651–62. https://doi.org/10.1260/136943309789867926.

[97] Yamaguchi T, Kato Y, Nishimura T, Uomoto T. Creep Rupture of FRP Rods Made of Aramid, Carbon and Glass Fibers. Non-metallic Reinf Concr Struct Sapporo (Japan): Japan Concrete Institute 1997; 179–186.

[98] ACI 440R-07, Report on Fiber-Reinforced Polymer (FRP) Reinforcement for Concrete Structures, ACI 440R-07, 2007.

[99] ACI 440.2R-17. Guide for the Design and Construction of Externally Bonded FRP Systems for Strengthened Concrete Structure. American concrete Institute, ACI, Farmington Hills, MI, USA, 2017.

[100] Feng CW, Keong CW, Hsueh Y.P, Wang YY, Sue H.J. Modeling of long-term creep behavior of structural epoxy adhesives, Int J Adhes Adhes 2005; 25(5): 427-436. https://doi.org/10.1016/j.ijadhadh.2004.11.009

[101] Majda P, Skrodzewicz J. A modified creep model of epoxy adhesive at ambient temperature. Int J Adhes Adhes 2009; 29: 396–404. https://doi.org/10.1016/j.ijadhadh.2008.07.010

[102] Meshgin P, Choi KK, Reda Taha MM. Experimental and analytical investigations of creep of epoxy adhesive at the concrete-FRP interfaces. Int J Adhes Adhes 2009; 29: 56–66. doi:10.1016/j.ijadhadh.2008.01.003.

[103] Costa I, Barros J. Tensile creep of a structural epoxy adhesive: experimental and analytical characterization. Int J Adhes Adhes 2015; 59: 115-124. https://doi.org/10.1016/j.ijadhadh.2015.02.006

[104] Silva P, Valente T, Azenha M, Sena-Cruz J, Barros J. Viscoelastic response of an epoxy adhesive for construction since its early ages: experiments and modelling. Compos B Eng 2016; 116: 266-277. https://doi.org/10.1016/j.compositesb.2016.10.047

[105] Sobuz HR, Ahmed E, Sutan NM, Hasan NMS, Uddin MA, Uddin MJ. Bending and time-dependent responses of RC beams strengthened with bonded carbon fiber composite laminates. Constr Build Mater 2012; 29: 597-611. https://doi.org/10.1016/j.conbuildmat.2011.11.006

[106] Hong S, Park SK. Long-term behavior of fiber-reinforced-polymer-plated concrete beams under sustained loading: Analytical and experimental study. Compos Struct 2016; 152: 140-157. https://doi.org/10.1016/j.compstruct.2016.05.031

[107] Al Chami G, Theriault M, Neale KW. Creep behaviour of CFRP-strengthened reinforced concrete beams. Constr Build Mater 2009; 23(4): 1640-1652. https://doi.org/10.1016/j.conbuildmat.2007.09.006

[108] Li X, Gu X, Ouyang Y, Song X. Long-term behavior of existing low-strength reinforced concrete beams strengthened with carbon fiber composite sheets. Compos B Eng 2012; 43(3): 1637-1644. https://doi.org/10.1016/j.compositesb.2012.01.016

[109] El-Sayed AK, Al-Zaid RA, Al-Negheimish AI, Shuraim AB, Alhozaimy A.M. Long-term behavior of wide shallow RC beams strengthened with externally bonded CFRP plates Constr Build Mater 2014; 51: 473-483. https://doi.org/10.1016/j.conbuildmat.2013.10.055

[110] Jiang S, Yao W, Chen J, Tao S. Time dependent behavior of FRP-strengthened RC beams subjected to preload: experimental study and finite element modeling Compos Struct 2018; 200: 599-613. https://doi.org/10.1016/j.compstruct.2018.05.110

[111] Sena-Cruz J, Silva P, Fernandes P, Azenha M, Barros J, Sousa CF, Castro F, Teixeira TAN. Creep behavior of concrete elements strengthened with NSM CFRP laminate strips under different environmental conditions. FRPRCS-11: 11th International Symposium on Fiber Reinforced Polymer for Reinforced Concrete Structures. Universidade do Minho, 2013.

[112] Kim YJ, Khan F. Creep-Induced Distress on Flexural Behavior of Reinforced Concrete Beams Retrofitted with Near-Surface-Mounted Carbon Fiber-Reinforced Polymer. ACI Struct J 2015; 112(4): 493-504. https://doi.org/10.14359/51687705

[113] Kim YJ. Modeling of near-surface-mounted carbon fiber-reinforced polymer for strengthening reinforced concrete beams in sustained load. ACI Struct J 2015; 112(6): 805-813. https://doi.org/10.14359/51687659

[114] Moawad M, Baena M, Barris C, Torres L, Sallam HEM. Time-dependent behavior of NSM strengthened RC beams under sustained loading. Eng Struct 2021; 247: 113210. https://doi.org/10.1016/j.engstruct.2021.113210

[115] Tavakoli HR, Mahmoudi S, Goltabar AR, Jalali P. Experimental evaluation of the effects of reverse cyclic loading rate on the mechanical behavior of reinforced SCC beams. Constr Build Mater 2017; 131: 254-266. https://doi.org/10.1016/j.conbuildmat.2016.11.043

[116] Dineshkumar R, Ramkumar S. Review paper on fatigue behavior of reinforced concrete beams. Mater Today: Proc 2020; 21: 19-23. https://doi.org/10.1016/j.matpr.2019.05.353

[117] GHEORGHIU Catalin, LABOSSIERE Pierre, PROULX Jean. Response of CFRP-strengthened beams under fatigue with different load amplitudes. Constr Build Mater 2007; 21(4): 756-763. https://doi.org/10.1016/j.conbuildmat.2006.06.019

[118] Dong Y, Ansari F, Karbhari VM. Fatigue performance of reinforced concrete beams with externally bonded CFRP reinforcement. Struct Infrastruct Eng 2011; 7(3): 229-241. https://doi.org/10.1080/15732470802383669

[119] Toutanji H, Zhao L, Deng Y, Zhang Y, Balaguru P. Cyclic behavior of RC beams strengthened with carbon fiber sheets bonded by inorganic matrix. J Mater Civ Eng 2006; 18(1): 28-35. https://doi.org/10.1061/(ASCE)0899-1561(2006)18:1(28)

[120] Chen C, Cheng L. Fatigue behavior and prediction of NSM CFRP-strengthened reinforced concrete beams. J Compos Constr 2016; 20(5): 04016033. https://doi.org/10.1061/(ASCE)CC.1943-5614.0000691

[121] Al-Saadi NTK, Mohammed A, Al-Mahaidi R. Fatigue performance of near-surface mounted CFRP strips embedded in concrete girders using cementitious adhesive made with graphene oxide. Constr Build Mater 2017; 148: 632-647. https://doi.org/10.1016/j.conbuildmat.2017.05.103

[122] Fernandes PM, Silva PM, Sena-Cruz J. Bond and flexural behavior of concrete elements strengthened with NSM CFRP laminate strips under fatigue loading. Eng Struct 2018; 84: 350-361. https://doi.org/10.1016/j.engstruct.2014.11.039

[123] Aidoo J, Harries KA, Petrou MF. Fatigue behavior of carbon fiber reinforced polymer-strengthened reinforced concrete bridge girders. J Compos Constr 2004; 8(6): 501-509. https://doi.org/10.1061/(ASCE)1090-0268(2004)8:6(501)

[124] Barnes RA, Mays GC. Fatigue performance of concrete beams strengthened with CFRP plates. J Compos Constr 1999; (2): 63-72. https://doi.org/10.1061/(ASCE)1090-0268(1999)3:2(63)

[125] Heffernan PJ, Erki MA. Fatigue behavior of reinforced concrete beams strengthened with carbon fiber reinforced plastic laminates. J Compos Constr 2004; 8(2): 132-140. https://doi.org/10.1061/(ASCE)1090-0268(2004)8:2(132)

[126] Ekenel M, Rizzo A, Myers JJ, Nanni A. Flexural fatigue behavior of reinforced concrete beams strengthened with FRP fabric and precured laminate systems. J Compos Constr 2006; 10(5): 433-442. https://doi.org/10.1061/(ASCE)1090-0268(2006)10:5(433)

[127] Lin JX, Huang PY, Guo YC, Guo XY, Zeng JJ, Zhao C, Chen ZB. Fatigue behavior of RC beams strengthened with CFRP laminate under hot-wet environments and vehicle random loads coupling. Int J Fatigue 2020; 131: 105329. https://doi.org/10.1016/j.ijfatigue.2019.105329

[128] Song L, Yu Z. Fatigue performance of corroded reinforced concrete beams strengthened with CFRP sheets. Constr Build Mater 2015; 90: 99-109. https://doi.org/10.1016/j.conbuildmat.2015.05.024

[129] Papakonstantinou CG, Petrou MF, Harries KA. Fatigue behavior of RC beams strengthened with GFRP sheets. J Compos Constr2001; 5(4): 246-253. https://doi.org/10.1061/(ASCE)1090-0268(2001)5:4(246)

[130] Shahawy M; Beitelman TE. Static and fatigue performance of RC beams strengthened with CFRP laminates. J Struct Eng 1999; 125(6): 613-621. https://doi.org/10.1061/(ASCE)0733-9445(1999)125:6(613)

[131] Masoud S, Soudki K, Topper T. CFRP-strengthened and corroded RC beams under monotonic and fatigue loads. J Compos Constr 2001; 5(4): 228-236. https://doi.org/10.1061/(ASCE)1090-0268(2001)5:4(228)

[132] Huang H, Wang WW, Dai JG, Brigham JC. Fatigue behavior of reinforced concrete beams strengthened with externally bonded prestressed CFRP sheets. J Compos Constr 2017; 21(3): 04016108. https://doi.org/10.1061/(ASCE)1090-0268(2004)8:2(132)

[133] Xie JH, Huang PY, Guo YC. Fatigue behavior of reinforced concrete beams strengthened with prestressed fiber reinforced polymer. Constr Build Mater 2012; 27(1): 149-157. https://doi.org/10.1016/j.conbuildmat.2011.08.002

[134] Eljufout T, Toutanji H. Fatigue behavior of prefatigued reinforced concrete beams rehabilitated with near surface mounted carbon fiber reinforced polymer reinforcement. Struct Concr 2020; 21(2): 533-547. https://doi.org/10.1002/suco.201900131

[135] Oudah F, El-Hacha R. Fatigue behavior of RC beams strengthened with prestressed NSM CFRP rods. Compos Struct 2012; 94(4): 1333-1342. https://doi.org/10.1016/j.compstruct.2011.11.025

[136] Charalambidi BG, Rousakis TC, Karabinis AI. Fatigue behavior of large-scale reinforced concrete beams strengthened in flexure with fiber-reinforced polymer laminates. J Compos Constr 2016; 20(5): 04016035. https://doi.org/10.1061/(ASCE)CC.1943-5614.0000689

[137] UNE-EN 12390-3. Testing Hardened Concrete—Part 3: Compressive Strength of Test Specimens; AENOR: Madrid, Spain, 2003.

[138] UNE-EN 12390-6. Testing Hardened Concrete—Part 6: Tensile Splitting Strength of Test Specimens; AENOR: Madrid, Spain, 2010.

[139] ASTM C469/C469M-14. Standard Test Method for Static Modulus of Elasticity and Poisson's Ratio of Concrete in Compression; ASTM International: West Conshohocken, PA, USA, 2014.

[140] ASTM, ASTM C512 - Standard Test Method for Creep of Concrete in Compression, ASTM International, West Conshohocken, 2010.

[141] UNE-EN ISO 15630-1. Steel for the Reinforcement and Prestressing of Concrete-Test Methods—Part 1: Reinforcing Bars, Wire Rod and Wire; AENOR: Madrid, Spain, 2011.

[142] ISO 527-5. Plastics-Determination of Tensile Properties—Part 5: Test Conditions FOR Unidirectional Fibre-Reinforced Plastic Composites; ISO: Geneva, Switzerland, 2009.

[143] S&P. S&P Resin 220 HP Epoxy Adhesive, Technical Data Sheet; S&P: Seewen, Switzerland, 2019.

[144] ISO 527-1. Plastics-Determination of Tensile Properties—Part 1: General Principles; ISO: Geneva, Switzerland, 2012.

[145] ASTM E1356-08. Standard Test Method for Assignment of the Glass Transition Temperatures by Differential Scanning Calorimetry; ASTM International: West Conshohocken, PA, USA, 2008.

[146] ASTM D5023-15. Standard Test Method for Plastics: Dynamic Mechanical Properties: In Flexure (Three-Point Bending); ASTM International: West Conshohocken, PA, USA, 2015.

[147] Michels J, Widmann R, Czaderski C, Allahvirdizade R, Motavalli M. Glass transition evaluation of commercially available epoxy resins used for civil engineering applications. Compos B Eng 2015; 77: 484–493. https://doi.org/10.1016/j.compositesb.2015.03.053

[148] EN 196-1. Methods of Testing Cement – Part 1: Determination of Strength.

[149] Michel M, Ferrier E. Effect of curing temperature conditions on glass transition temperature values of epoxy polymer used for wet lay-up applications. Constr Build Mater 2020; 231: 117206. https://doi.org/10.1016/j.conbuildmat.2019.117206

[150] Michels J, Sena-Cruz J, Christen R, Czaderski C, Motavalli M. Mechanical performance of cold-curing epoxy adhesives after different mixing and curing procedures. Compos B Eng 2016; 98: 434–443. https://doi.org/10.1016/j.compositesb.2016.05.054

[151] Klamer EL. Influence of Temperature on Concrete Beams Strengthened in Flexure with CFRP. Ph.D. Thesis, TU Eindhoven, Eindhoven, The Netherlands, 2009.

[152] Ferrier E, Michel L, Jurkiewiez B, Hamelin P. Creep behavior of adhesives used for external FRP strengthening of RC structures. Constr Build Mater 2011; 25: 461–467. https://doi.org/10.1016/j.conbuildmat.2010.01.002

[153] Bisby LA, Green MF. Resistance to freezing and thawing of fiber–reinforced polymer–concrete bond. ACI Struct J 2002; 99: 215–223. https://doi.org/10.14359/11547

[154] Leone M, Aiello MA, Matthys S. Effect of elevated service temperature on bond between FRP EBR systems and concrete. Compos B Eng 2009; 40: 85–93. https://doi.org/10.1016/j.compositesb.2008.06.004

[155] EN 1992-1-1. Eurocode 2. Design of Concrete Structures—Part 1-1: General Rules and Rules for Buildings; British Standard Institution: London, UK, 2004.

[156] Comité Euro-International du Béton (CEB). CEB-FIP Model Code 1990 (MC-90); Thomas Telford: London, UK, 1993.

[157] Bischoff PH, Darabi M. Unified Approach for Computing Deflection of Steel and FRP Reinforced Concrete. In Andy Scanlon Symposium on Serviceability and Safety of Concrete Structures: From Research to Practice; American Concrete Institute: Michigan, MI, USA, 2012; pp. 1–20. https://doi.org/ 10.14359/51683811

[158] Scanlon A, Bischoff PH. Shrinkage restraint and loading history effects on deflections of flexural members. ACI Struct J 2008; 105: 498. https://doi.org/10.14359/19864

[159] Gribniak V, Kaklauskas G, Kliukas R, Jakubovskis R. Shrinkage effect on short-term deformation behavior of reinforced concrete—When it should not be neglected. Mater Des 2013; 5: 1060–1070. https://doi.org/10.1016/j.matdes.2013.05.028

[160] Yu B, Kodur VKR. Fire behavior of concrete T-beams strengthened with near-surface mounted FRP reinforcement. Eng Struct 2014; 80: 350–361. https://doi.org/10.1016/j.engstruct.2014.09.003

[161] Palmieri A, Matthys S, Taerwe L. Fire endurance and residual strength of insulated concrete beams strengthened with near-surface mounted reinforcement. J Compos Constr 2012; 17: 454–462. http://hdl.handle.net/1854/LU-3238162

[162] Palmieri A, Matthys S, Taerwe L. Strengthening with near surface mounted reinforcement: Structural and fire behavior. In Proceedings of the 3th International Congress and Exhibition Fib "Think Globally, Build Locally", Washington, DC, USA, 29 May–2 June 2010; pp. 1–10. http://hdl.handle.net/1854/LU-1843188

[163] Palmieri A, Matthys S, Taerwe L. Experimental investigation on fire endurance of insulated concrete beams strengthened with near surface mounted FRP bar reinforcement. Compos B Eng 2012; 43: 885–895. https://doi.org/10.1016/j.compositesb.2011.11.061

[164] Firmo JP, Correia JR. Fire behaviour of thermally insulated RC beams strengthened with EBR-CFRP strips: Experimental study. Compos Struct 2015; 122: 144–154. https://doi.org/10.1016/j.compstruct.2014.11.063

[165] Firmo JP, Correia JR. Fire behaviour of thermally insulated RC beams strengthened with NSM-CFRP strips: Experimental study. Compos B Eng 2015; 76: 112–121. https://doi.org/10.1016/j.compositesb.2015.02.018

[166] Carlos TB, Rodrigues JPC, de Lima RC, Dhima D. Experimental analysis on flexural behaviour of RC beams strengthened with CFRP laminates and under fire conditions. Compos Struct 2018; 189: 516–528. https://doi.org/10.1016/j.compstruct.2018.01.094

[167] Jadooe A, Al-Mahaidi R, Abdouka K. Experimental and numerical study of strengthening of heat-damaged RC beams using NSM CFRP strips. Constr Build Mater 2017; 154: 899–913. https://doi.org/10.1016/j.conbuildmat.2017.07.202

[168] Haddad RH, Almomani OA. Recovering flexural performance of thermally damaged concrete beams using NSM CFRP strips. Constr Build Mater 2017; 154: 632–643. https://doi.org/10.1016/j.conbuildmat.2017.07.211

[169] Burke PJ, Luke AB, Mark FG. Effects of elevated temperature on near surface mounted and externally bonded FRP strengthening systems for concrete. Cem Concr Compos 2013; 35: 190–199. https://doi.org/10.1016/j.cemconcomp.2012.10.003

[170] Firmo JP, Correia JR, Bisby LA. Fire behaviour of FRP-strengthened reinforced concrete structural elements: A state-of-the-art review. Compos B Eng 2015; 80: 198–216. https://doi.org/10.1016/j.compositesb.2015.05.045

[171] Ferrier E, Rabinovitch O, Michel L. Mechanical behavior of concrete–resin/adhesive–FRP structural assemblies under low and high temperatures. Constr Build Mater 2016; 127: 1017–1028. https://doi.org/10.1016/j.conbuildmat.2015.12.127

[172] Abed F, Oucif C, Awera Y, Mhanna HH, Alkhraisha H. FE modeling of concrete beams and columns reinforced with FRP composites. Def Technol 2021; 7: 1–14. https://doi.org/10.1016/j.dt.2020.02.015

[173] Al-Rahmani A, Abed FH. Numerical investigation of hybrid FRP reinforced beams. In Proceedings of the 5th International Conference on Modeling, Simulation and Applied Optimization (ICMSAO), Hammamet, Tunisia, 28–30 April 2013. 10.1109/ICMSAO.2013.6552565

[174] Alkhraisha H, Mhanna H, Abed F. FE Modeling of RC Beams Reinforced in Flexure with BFRP Bars Exposed to Harsh Conditions. In Sustainable Issues in Infrastructure Engineering Springer: Cham, Switzerland, 2021; pp. 3–13. DOI: 10.1007/978-3-030-62586-3_1

[175] Abed FH, Al-Rahmani A, Al-Rahmani AH. Finite element simulations of the shear capacity of GFRP-reinforced concrete short beams. In Proceedings of the 5th International Conference on Modeling, Simulation and Applied Optimization (ICMSAO), Hammamet, Tunisia, 28–30 April 2013. 10.1109/ICMSAO.2013.6552566

[176] Abed F, El Refai A, Abdalla S. Experimental and finite element investigation of the shear performance of BFRP-RC short beams. Struct 2019; 20: 689–701. https://doi.org/10.1016/j.istruc.2019.06.019

[177] Hawileh RA, Naser M, Zaidan W, Rasheed HA. Modeling of insulated CFRP strengthened reinforced concrete T-beam exposed to fire. Eng Struct 2009; 31: 3072–3079. https://doi.org/10.1016/j.engstruct.2009.08.008

[178] Dai JG, Gao WY, Teng JG. Finite element modeling of insulated FRP-strengthened RC beams exposed to fire. J Compos Construct 2015; 19: 04014046. https://doi.org/10.1007/978-3-642-17487-2_93

[179] Firmo JP, Arruda MRT, Correia JR, Rosa IC. Three-dimensional finite element modelling of the fire behaviour of insulated RC beams strengthened with EBR and NSM CFRP strips. Compos Struct 2018; 183: 124–136. https://doi.org/10.1016/j.compstruct.2017.01.082

[180] Fernandes P, Sena-Cruz J, Xavier J, Silva P, Pereira E, Cruz J. Durability of bond in NSM CFRP-concrete systems under different environmental conditions. Compos B Eng 2018; 138: 19–34. https://doi.org/10.1016/j.compositesb.2017.11.022

[181] Abaqus, Version 6.16; Documentation, Abaqus v6.16. Available online: http://130.149.89.49:2080/v2016/index.html (accessed on 21 August 2016).

[182] Torres L, Lopez-Almansa F, Bozzo LM. Tension-stiffening model for cracked flexural concrete members. J Struct Eng 2004; 130: 1242–1251. https://doi.org/10.1061/(ASCE)0733-9445(2004)130:8(1242)

[183] Emara M, Torres L, Baena M, Barris C, Cahís X. Bond response of NSM CFRP strips in concrete under sustained loading and different temperature and humidity conditions. Compos Struct 2018; 192: 1-7. https://doi.org/10.1016/j.compstruct.2018.02.048

[184] Gil L, Cruz JJ, Perez MAA. pull-shear test for debonding of FRP-laminates for concrete structures. KEM 2009; 399: 141-151. https://doi.org/10.4028/www.scientific.net/KEM.399.141

[185] Wang S, Stratford T, Reynolds TPS. Linear creep of bonded FRP-strengthened metallic structures at warm service temperatures. Constr Build Mater 2021; 283: 122699. https://doi.org/10.1016/j.conbuildmat.2021.122699

[186] Marques EAS, Da Silva LFM, Banea MD, Carbas RJC. Adhesive joints for low-and high-temperature use: an overview. J Adhes 2015; 91(7): 556-585. https://doi.org/10.1080/00218464.2014.943395

[187] Banea MD, Da Silva LFM, Campilho RDSG. Effect of temperature on tensile strength and mode I fracture toughness of a high temperature epoxy adhesive. J Adhes Sci Technol 2012; 26(7): 939-53. https://doi.org/10.1163/156856111X593649

[188] Banea MD, De Sousa FSM, Da Silva LFM, Campilho RDSG, Bastos de Pereira AM. Effects of temperature and loading rate on the mechanical properties of a high temperature epoxy adhesive. J Adhes Sci Technol 2011; 25(18): 2461-74. https://doi.org/10.1163/016942411X580144

[189] Wu CS. Influence of post-curing and temperature effects on bulk density, glass transition and stress-strain behaviour of imidazole-cured epoxy network. J Mater Sci 1992; 27(11): 2952-9. https://doi.org/10.1007/BF01154105

[190] Reis JMLD. Effect of temperature on the mechanical properties of polymer mortars. Mater Res 2012; 15(4): 645-649. https://doi.org/10.1590/S1516-14392012005000091

[191] Jahani Y, Baena M, Gómez J, Barris C, Torres L. Experimental Study of the Effect of High Service Temperature on the Flexural Performance of Near-Surface Mounted (NSM) Carbon Fiber-Reinforced Polymer (CFRP)-Strengthened Concrete Beams. Polymers 2021; 13(6): 920. https://doi.org/10.3390/polym13060920

[192] Moussa O, Vassilopoulos AP, de Castro J, Keller T. Time–temperature dependence of thermomechanical recovery of cold-curing structural adhesives. Int J Adhes Adhes 2012; 35: 94-101. https://doi.org/10.1016/j.ijadhadh.2012.02.005

[193] Cruz R, Correia L, Cabral-Fonseca S, Sena-Cruz JM. Effects of the preparation, curing and hygrothermal conditions on the viscoelastic response of a structural epoxy adhesive. Int J Adhes Adhes 2021; 110: 102961. https://doi.org/10.1016/j.ijadhadh.2021.102961

[194] Lapique F, Redford K. Curing effects on viscosity and mechanical properties of a commercial epoxy resin adhesive. Int J Adhes Adhes 2002; 22(4): 337-46. https://doi.org/10.1016/S0143-7496(02)00013-1

[195] Moussa O, Vassilopoulos AP, Keller T. Effects of low-temperature curing on physical behavior of cold-curing epoxy adhesives in bridge construction. Int J Adhes Adhes 2012; 32: 15-22. https://doi.org/10.1016/j.ijadhadh.2011.09.001

[196] Lahouar MA, Caron JF, Pinoteau N, Forêt G, Benzarti K. Mechanical behavior of adhesive anchors under high temperature exposure: Experimental investigation. Int J Adhes Adhes 2017; 78: 200-11. https://doi.org/10.1016/j.ijadhadh.2017.07.004

[197] Carbas RJC, Marques EAS, Da Silva LFM, Lopes AM. Effect of cure temperature on the glass transition temperature and mechanical properties of epoxy adhesives. J Adhes 2014; 90(1): 104-19. https://doi.org/10.1080/00218464.2013.779559

[198] Varley RJ, Hodgkin JH, Simon GP. Toughening of trifunctional epoxy system. V. Structure–property relationships of neat resin. J Appl Polym Sci 2000; 77(2): 237-248. https://doi.org/10.1002/(SICI)1097-4628(20000711)77:2<237::AID-APP1>3.0.CO;2-5

[199] Enns JB, Gillham JK. Effect of the extent of cure on the modulus, glass transition, water absorptio, and density of an amine-cured epoxy. J Appl Polym Sci 1983; 28(9): 2831-2846. https://doi.org/10.1002/app.1983.070280914

[200] Ziaee S, Palmese GR. Effects of temperature on cure kinetics and mechanical properties of vinyl–ester resins. J Polym Sci B Polym Phys 1999; 37(7): 725-744. https://doi.org/10.1002/(SICI)1099-0488(19990401)37:7<725::AID-POLB23>3.0.CO;2-E

[201] Carbas RJC, Da Silva LFM, Marques EAS, Lopes AM. Effect of post-cure on the glass transition temperature and mechanical properties of epoxy adhesives. J Adhes Sci Technol 2013; 27(23): 2542-57. https://doi.org/10.1080/01694243.2013.790294

[202] Benedetti A, Fernandes P, Granja JL, Sena-Cruz, JM, Azenha M. Influence of temperature on the curing of an epoxy adhesive and its influence on bond behaviour of NSM-CFRP systems. Compos B Eng 2016; 89: 219-229. https://doi.org/10.1016/j.compositesb.2015.11.034

[203] Savvilotidou M, Vassilopoulos AP, Frigione M, Keller T. Effects of aging in dry environment on physical and mechanical properties of a cold-curing structural epoxy adhesive for bridge construction. Constr Build Mater 2017; 140: 552-561. https://doi.org/10.1016/j.conbuildmat.2017.02.063

[204] Moussa O, Vassilopoulos AP, De Castro J, Keller T. Early-age tensile properties of structural epoxy adhesives subjected to low-temperature curing. Int J Adhes Adhes 2012; 35: 9-16. https://doi.org/10.1016/j.ijadhadh.2012.01.023

[205] Stewart I, Chambers A, Gordon T. The cohesive mechanical properties of a toughened epoxy adhesive as a function of cure level. Int J Adhes Adhes 2007; 27(4): 277-287. https://doi.org/10.1016/j.ijadhadh.2006.05.003

[206] Malumbela G, Moyo P, Alexander M. Behaviour of RC beams corroded under sustained service loads. Constr Build Mater 2009; 23(11): 3346-3351. https://doi.org/10.1016/j.conbuildmat.2009.06.005

[207] Jahani Y, Baena M, Barris C, Perera R, Torres L. Influence of curing, post-curing and testing temperatures on mechanical properties of a structural adhesive. Constr Build Mater 2022; 324: 126698. https://doi.org/10.1016/j.conbuildmat.2022.126698

[208] Capozucca R. Static and dynamic response of damaged RC beams strengthened with NSM CFRP rods. Compos Struct 2009; 91(3): 237-248. https://doi.org/10.1016/j.compstruct.2009.05.003

[209] Reda RM, Sharaky IA, Ghanem M, Seleem MH, Sallam HEM. Flexural behavior of RC beams strengthened by NSM GFRP Bars having different end conditions. Compos Struct 2016; 14: 131-142. https://doi.org/10.1016/j.compstruct.2016.03.018

[210] Bilotta A, Ceroni F, Di Ludovico M, Nigro E, Pecce M, Manfredi G. Bond efficiency of EBR and NSM FRP systems for strengthening concrete members. J Compos Constr 2011; 15(5): 757-772. https://doi.org/10.1061/(ASCE)CC.1943-5614.0000204

[211] Triantafyllou G, Rousakis T, Karabinis A. (2019). Corroded RC beams at service load before and after patch repair and strengthening with NSM CFRP strips. Build 2019; 9(3): 67. https://doi.org/10.3390/buildings9030067

[212] Gómez J, Barris C, Jahani Y, Baena M, Torres L. Experimental study and numerical prediction of the bond response of NSM CFRP laminates in RC elements under sustained loading. Constr Build Mater 2021; 288: 123082. https://doi.org/10.1016/j.conbuildmat.2021.123082

[213] Kim YJ, Heffernan PJ. Fatigue behavior of externally strengthened concrete beams with fiber-reinforced polymers: State of the art. J Compos Constr 2008; 12(3): 246-256. https://doi.org/10.1061/(ASCE)1090-0268(2008)12:3(246)

[214] Oudah F, El-Hacha R. Research progress on the fatigue performance of RC beams strengthened in flexure using Fiber Reinforced Polymers. Compos B Eng 2013; 47: 82-95. https://doi.org/10.1016/j.compositesb.2012.09.057

[215] Zhu Z, Zhu E, Ni Y, Li D. Flexural fatigue behavior of large-scale beams strengthened with side near surface mounted (SNSM) CFRP strips. Eng Struct 2019; 180: 134-147. https://doi.org/10.1016/j.engstruct.2018.11.039

[216] Chen C, Cheng L. Fatigue life-based design of RC beams strengthened with NSM FRP. Eng Struct 2017; 140: 256-266. https://doi.org/10.1016/j.engstruct.2017.02.065

[217] Siddika A, Al Mamun MA, Alyousef R, Amran YM. Strengthening of reinforced concrete beams by using fiber-reinforced polymer composites: A review. J Build Eng 2019; 25: 100798. https://doi.org/10.1016/j.jobe.2019.100798

[218] Al-Abdwais AH, Al-Mahaidi RS. Experimental and finite element analysis of flexural performance of RC beams retrofitted using near-surface mounted with CFRP composites and cement adhesive. Eng Struct 2021; 241: 112429. https://doi.org/10.1016/j.engstruct.2021.112429

[219] Gallego JM, Czaderski C, Breveglieri M, Michels J. Fatigue behaviour at elevated temperature of RC slabs strengthened with EB CFRP strips. Compos B Eng 2018; 141: 37-49. https://doi.org/10.1016/j.compositesb.2017.12.026

[220] Breveglieri M, Czaderski C. RC slabs strengthened with externally bonded CFRP strips under long-term environmental exposure and sustained loading. Part 2: Laboratory experiments. JCOMC 2021; 6, 100210. https://doi.org/10.1016/j.jcomc.2021.100210

[221] Darwin D, Nmai CK. Energy dissipation in RC beams under cyclic load. J Struct Eng 1986; 112(8): 1829-1846. https://doi.org/10.1061/(ASCE)0733-9445(1986)112:8(1829)

PART V: Appendix. Published Papers

A.1 Paper A

Experimental study of the effect of high service temperature on the flexural performance of near-surface mounted (NSM) carbon fiber-reinforced polymer (CFRP)-strengthened concrete beams

Younes Jahani[1]*, Marta Baena[1], Javier Gómez[1], Cristina Barris[1] and Lluís Torres[1]

[1]AMADE, Polytechnic School, University of Girona, 17003, Girona, Spain

*Corresponding author

Experimental Study of the Effect of High Service Temperature on the Flexural Performance of Near-Surface Mounted (NSM) Carbon Fiber-Reinforced Polymer (CFRP)-Strengthened Concrete Beams

Younes Jahani * , **Marta Baena** , **Javier Gómez** , **Cristina Barris** and **Lluís Torres**

AMADE, Polytechnic School, University of Girona, 17003 Girona, Spain; marta.baena@udg.edu (M.B.); javier.gomez@udg.edu (J.G.); cristina.barris@udg.edu (C.B.); lluis.torres@udg.edu (L.T.)
* Correspondence: younes.jahani@udg.edu; Tel.: +34-972-418-817

Abstract: This paper presents a study of the effect of high service temperature (near or beyond glass transition temperature (T_g) of structural epoxy adhesive) on the behavior of near-surface mounted (NSM) carbon fiber-reinforced polymer (CFRP)-strengthened reinforced concrete (RC) beams. The study includes experimental work as well as analytical and numerical analysis. To this end, fourteen beams have been tested up to failure in two different series. In series 1, specimens with three different CFRP areas have been tested at two different temperatures (i.e., 20 and 40 °C). In series 2, and with the aim of evaluating the effect of higher temperatures, only one CFRP area was tested under four different temperatures (i.e., 20, 60, 70, and 85 °C). Experimental results are evaluated in terms of load–deflections, failure modes, and bond performance. Furthermore, the experimental load–deflection curves are satisfactorily compared to both analytical predictions and finite element (FE) numerical simulations. In both cases, shrinkage and temperature effects on the short-term response of flexural elements have been accounted for. No significant reduction in stiffness and ultimate load was observed for specimens being tested up to 60 °C (in the range of epoxy T_g), showing FRP rupture failure in all of them. For specimens under 70 and 85 °C, the failure mode changed from FRP rupture to FRP end debonding and concrete crushing, respectively.

Keywords: NSM strengthening; carbon fiber reinforced polymer; epoxy adhesive; temperature; experimental; shrinkage

1. Introduction

In the past decades, fiber-reinforced polymer (FRP) materials have been produced in different configurations and have been widely used for different purposes, such as the strengthening of reinforced concrete (RC) structures. Currently, externally bonded reinforcement (EBR) and near-surface mounted (NSM) are the two most used strengthening techniques in civil structures. In the EBR technique, the FRP is bonded to the previously prepared concrete surface, usually with an epoxy resin, while in the NSM technique, a groove is cut in the concrete cover and the FRP bar or strip is inserted and bonded using groove filler, which is typically an epoxy adhesive or a cement grout. The improvement of the bond performance, along with higher protection against potential aggressive environmental exposure and vandalism actions, are some of the advantages of the NSM technique [1–3].

The performance of the NSM strengthening system relies on the bond capacity of the joint between concrete and FRP material, which in turn depends on the properties of the adhesive (usually epoxy resin), among other parameters. Typically, epoxy adhesives can be affected by temperature, as near or beyond the glass transition temperature (T_g), their mechanical properties may change [4–7]. This may lead to a decrease of its performance and premature debonding and therefore to a not complete exploitation of the strengthening

system. In this sense, some limitations on the working temperature of these strengthening systems exist. According to fib Bulletin 90 [8], to avoid any considerable change in the adhesive properties in the service condition, the maximum temperature should be 20 °C less than T_g. In this same line, Michels et al. [9] summarized the various design codes provisions to define the service temperature in FRP strengthened RC structures to be 10 to 20 °C less than T_g, whilst Klamer et al. [10] suggested the service temperature to be limited to 10 °C less than T_g. Furthermore, Ferrier et al. [11] limited the service temperature to be 15 °C less than T_g for avoiding temperature effects in the creep of epoxies with lower range of T_g ($T_g < 55$ °C). Moreover, other studies [12,13] limited the maximum temperature to 10 °C less than T_g to avoid premature debonding of FRP sheets from concrete surface. These limitations are related to the EBR technique, while for the NSM technique, less information is available, and no specific limitation has been stated.

Focusing on the existing experimental work, the flexural behavior of NSM strengthened concrete beams under room temperature have been widely studied in the literature [14–20], while the structural performance of this technique under elevated temperature and high service temperature is still an open topic that needs detailed research. The fire resistance of FRP-strengthened RC flexural elements has been analyzed in different studies [21–30]. Results from these works showed that the efficiency of the NSM method was better than EBR technique, and the thicker layers of the insulation system helped significantly reduce the temperature in the concrete and the adhesive. As a result, failure in the interface between laminate and concrete was postponed and, therefore, the durability of the system increased. A deep state-of-the-art review on the performance of FRP-strengthened RC elements exposed to fire conditions can be found in [31].

Compared to fire resistance, the performance of FRP-strengthened RC flexural elements exposed to high service temperature has been hardly investigated. The behavior of four different EBR strengthened RC beams under three different temperatures (i.e., 20, 50, and 70 °C), was studied and analyzed in [32]. Results showed that the failure load of the specimens was not significantly affected by temperature. However, a change in the failure interface took place for specimens with shorter anchorage length exposed to higher temperature (70 °C). Similar results were obtained in [33], who applied temperatures in the range of 20 to 80 °C and concluded that the load capacity of EBR-strengthened beams subjected up to 62 °C was slightly decreased, whilst the application of larger temperatures (from 70 °C on) resulted in a reduction in load capacity of approximately 20% of its nominal capacity at room temperature. Moreover, the application of larger temperatures made the failure mode change from cohesive in concrete to adhesive at the concrete–epoxy interface. Moving from beams to slabs, Silva et al. [34] studied the flexural performance of concrete slabs strengthened with the NSM technique under service temperature (up to 80 °C). According to this work, the maximum ultimate load capacity was observed in a slab under 40 °C, which was attributed to possible post-curing in epoxy adhesive, and the increase in the temperature up to 80 °C was followed by a decrease of the ultimate capacity of the slab of about 12%. In addition, the specimens subjected to 80 °C failed by cohesive failure at the epoxy, while in the rest of the specimens, the failure mode was concrete crushing. Focusing on EBR adhesive double lab joints with a wet lay-up system, Ferrier et al. [35] investigated the effect of temperature (ranging from −40 to 120 °C). According to the experimental results, the increase of temperature was followed by an increase of the slip between joint elements that made the specimens failed at lower loads.

In addition to experimental work, finite element methods have been also widely used to simulate the FRP-strengthened beams and columns under different loading and environmental conditions [36–43]. In these studies, different types of FRP material (i.e., carbon, glass, and basalt) have been considered as NSM or EBR reinforcement, and both the flexural and shear performance of the strengthened members have been validated. It should be noted that these studies correspond to specimens under room and fire conditions.

According to the literature, it is seen that there are a limited number of studies related to the flexural performance of NSM FRP-strengthened RC beams under high service

temperature, which justifies the need for further research in this field. The present work aims at studying the effect of relatively high service temperature (near and beyond T_g) on the flexural performance of NSM carbon FRP (CFRP)-strengthened RC beams when different strengthening areas of CFRP are used. For this purpose, an experimental program has been carried out, and results are analyzed in terms of flexural behavior, failure modes, and bond performance along the FRP laminate. Additionally, experimental results are also compared to analytical predictions and numerical simulations with the finite element method. The influence of shrinkage and temperature on the short-term response of the specimens was included in both analytical calculations and numerical predictions.

2. Experimental Program

2.1. Experimental Test Setup

The experimental program included fourteen specimens divided into two series (Table 1). Series 1 included eight beams, which were distributed as follows: two control beams (exposed to 20 and 40 °C) and six NSM CFRP-strengthened beams (exposed to 20 and 40 °C) with three different areas of CFRP. In series 2, unlike series 1, only one CFRP-strengthening ratio was used, and four different temperatures were applied (20, 60, 70, and 85 °C). The beams were tested under a four-point bending configuration (Figure 1). The beams had a rectangular cross-section of 140×180 mm and a total length of 2400 mm. The clear span was 2200 mm and the shear span was 750 mm, thus leading to a flexural span of 700 mm. Two ribbed steel bars with a diameter of 12 mm were utilized as longitudinal reinforcement on the tension side, while two ribbed steel bars with the diameter of 8 mm were used on the compression side. The shear span and some portion of the flexural span were reinforced with ϕ8 mm steel stirrups every 75 mm to avoid shear failure. All beams had a 5 mm wide and 15 mm deep notch at midspan (to act as a crack initiator at this specific position).

Table 1. Details of the tested specimens.

Experimental Campaign	Beam ID	Test Temperature (°C)	Concrete Compressive Strength (MPa)	FRP Dimension $w \times h$ (mm²)	No. of Strips	CFRP Area (mm²)
Series 1	CB-1-R	20	31.8	-	-	-
	CB-1-40	40		-	-	-
	SB1S-1-R	20		1.4×10	1	14
	SB1S-1-40	40		1.4×10	1	14
	SB2S-1-R	20		1.4×10	2	28
	SB2S-1-40	40		1.4×10	2	28
	SB3S-1-R	20		1.4×10	3	42
	SB3S-1-40	40		1.4×10	3	42
Series 2	CB-2-R	20	40.8	-	-	-
	CB-2-70	70		-	-	-
	SB2S-2-R	20		1.4×10	2	28
	SB2S-2-60	60		1.4×10	2	28
	SB2S-2-70	70		1.4×10	2	28
	SB2S-2-85	85		1.4×10	2	28

The same CFRP strip, having a thickness of 1.4 mm and a width of 10 mm, was used in all the strengthened beams, but different configurations of the strengthening system were considered (see Figure 1). The bonded length of the CFRP strips was 1950 mm for all specimens. Grooves of size 6×15 mm were cut using a sawing machine. After cutting them, the grooves were completely cleaned with air pressure to make sure there was no dust inside the grooves.
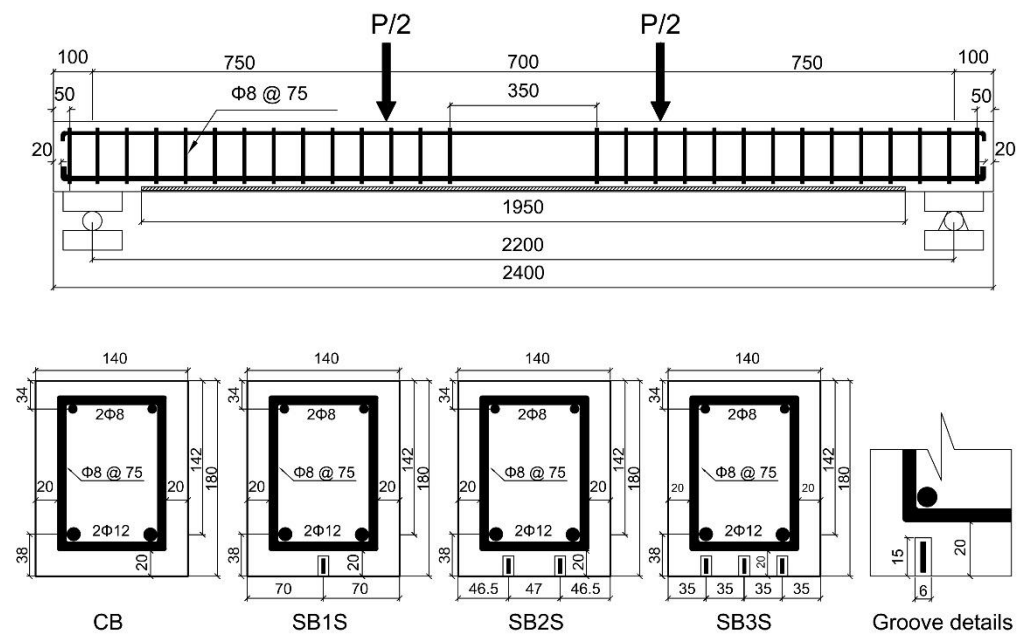
Figure 1. Beam details (dimensions in mm).

The specimens were designated as X-Y-Z, where X denotes the type of beam (CB for control beams with no strengthening system, SB1S for beams strengthened with one CFRP strip, SB2S for beams strengthened with two CFRP strips, and SB3S for beams strengthened with three CFRP strips), Y indicates the series of specimens, and Z is the temperature applied to the beam (where R refers to room temperature equal to 20 °C). For example, SB1S-1-R refers to the strengthened beam with one strip in series 1 of specimens at 20 °C. Details of the specimens are shown in Table 1.

Beams to be tested at high temperature were submitted to a heating process before instantaneous testing. The heating was applied on the tension face of the beam by using silicone rubber fiberglass-reinforced heating blankets. An insulating support was used to hold the heating blankets in contact with the tension face of the beam. A proportional integral derivative (PID) controller was utilized for the heating process, and Type-T thermocouples, located between the heating blankets and the concrete surface, were used as temperature controlling sensors. The evolution of temperature with time at different locations is shown in Figure 2. Tests started after the stabilization of temperature (see Figure 2), which remained constant along the test. Temperature strain gauges located at different points of the beam section allowed the registering of temperature along both the heating process and flexural test.
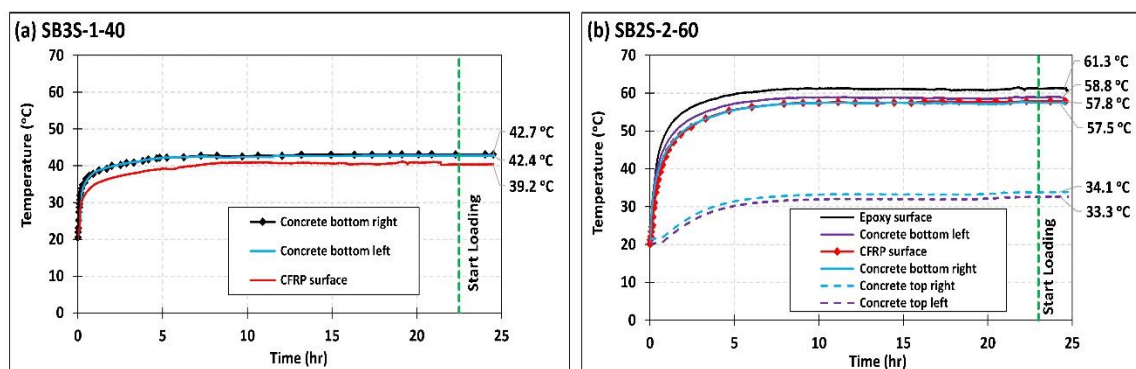
Figure 2. Evolution of temperature with time at different locations of specimens (**a**) SB3S-1-40 and (**b**) SB2S-2-60 (before and during loading).

In all the cases, a hydraulic jack applied the load onto the specimens through a spreader beam. The load was applied under displacement control mode at a rate of 0.6 mm/min.

2.2. Instrumentation

Five linear vertical displacement transducers (LVDTs) were used to record the vertical displacements, and two other LVDTs were utilized to measure the settlement of the supports. Due to the use of heating blankets in the soffit of the beam, two LVDTs were installed to the side faces of the beam under each loading point. Furthermore, end slips of the NSM CFRP strip were measured with two horizontal LVDTs (see Figure 3a). The measurements from horizontal LVDTs were almost negligible in all specimens.
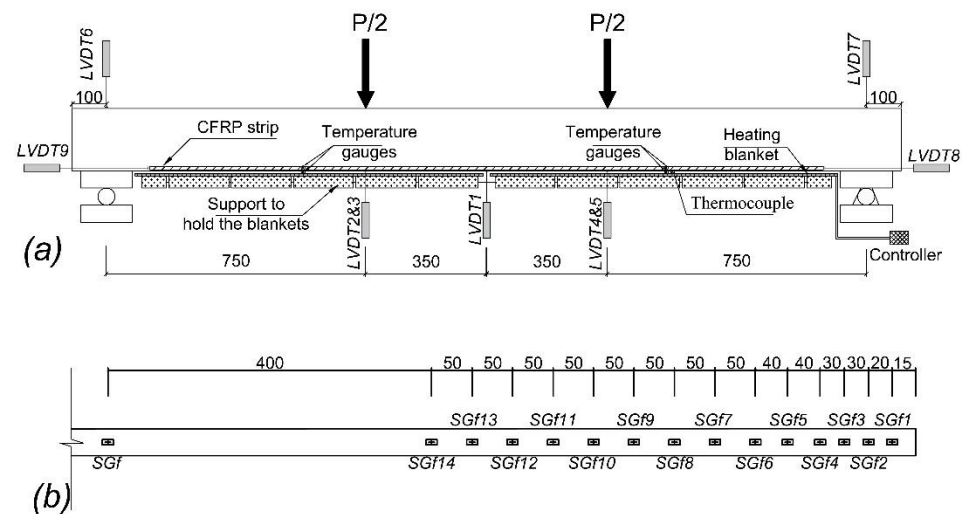
Figure 3. Test configuration: (**a**) position of linear vertical displacement transducers (LVDTs), temperature gauges, thermocouples, and heating system; (**b**) strain gauges along the carbon fiber-reinforced polymer (CFRP) laminate in specimens SB1S-1-R and SB1S-1-40 (dimensions in mm).

A strain gauge was installed at the midspan section of specimens on FRP surface (SGf) to assess strain variation with load. Furthermore, to evaluate the bond behavior between the CFRP strip and concrete, 14 additional strain gauges (SGf1 to SGf14) were installed along the strengthening strip for SB1S-1-R and SB1S-1-40 specimens (see Figure 3b). To avoid reducing the bonded surface, the strain gauges were installed in both sides of the strip (i.e., alternate in front and back of the strip).

Moreover, to record the temperature variation, temperature gauges (thermocouples) were installed in specimens under temperature at the surface of the concrete at the top and soffit of the beam and inside the groove. The temperature variations were recorded during the heating process as well as during the flexural tests. The position of the thermocouples is shown in Figure 3a. A general overview of test scene, along with the elements of the heating system (PID controller and heating blanket) is shown in Figure 4.
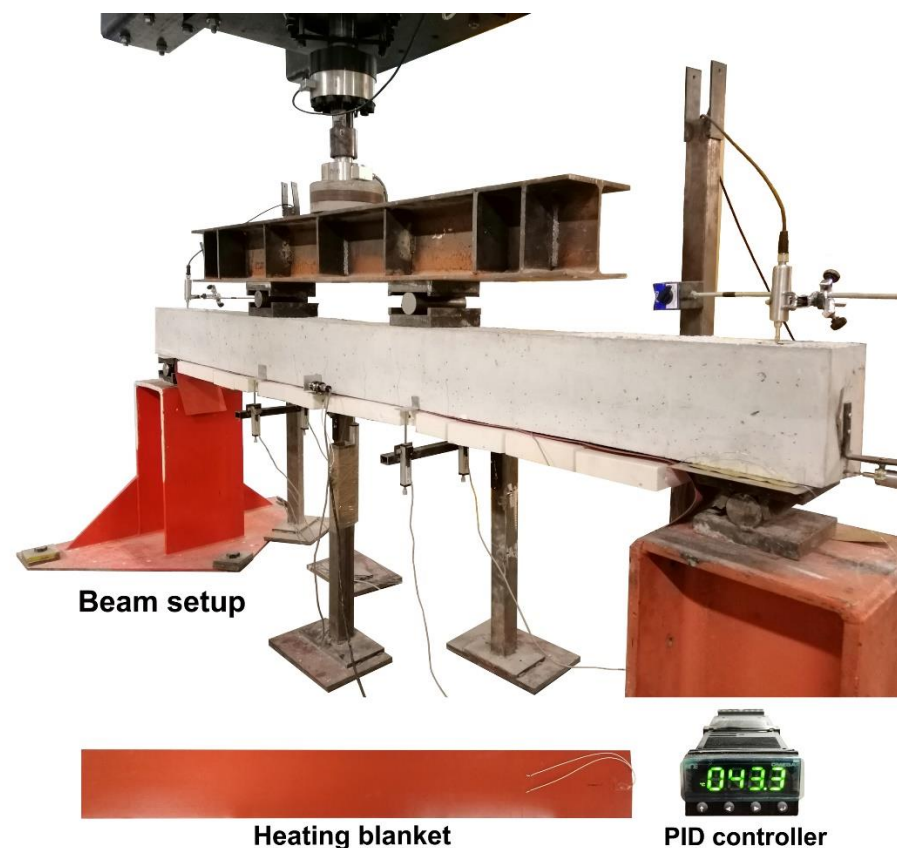
Figure 4. General overview of test scene and elements of the heating system.

2.3. Materials

The specimens were cast in lab conditions with conventionally vibrating procedure. Two different concrete batches were used. For concrete of series 1, the cement type was I-42.5R, with a content of 390 kg/m^3, the maximum aggregate size was 12 mm, and the water/cement relationship was 0.46. For concrete of series 2, the cement type was I-42.5R, with a content of 333 kg/m^3, the maximum aggregate size was 10 mm, and the water/cement relationship was 0.48. In both series, a viscosity modifier and underwater admixture were used to improve workability. The experimental compressive strength, tensile strength, and modulus of elasticity of concrete were determined from three cylinder tests (300 mm high and 150 mm diameter) according to UNE-EN 12390-3:2003 [44], UNE-EN 12390-6:2010 [45], and ASTM C469-87 [46] standards, respectively. According to the test results, for series 1 of specimens, an average compressive strength of 31.8 MPa (CoV = 6.6%), an average tensile strength of 4.2 MPa (CoV = 2.3%), and an average modulus of elasticity of 31.5 GPa (CoV = 7.8%) were obtained. Furthermore, for series 2 of specimens, the compressive strength, tensile strength, and modulus of elasticity were 40.8 MPa (CoV = 2.8%), 5.2 MPa (CoV = 0.5%), and 29.4 GPa (CoV = 0.8%), respectively.

The mechanical properties of steel bars were obtained from tension tests based on UNE-EN ISO 15630-1 [47]. The yielding stress and the modulus of elasticity were 573.2 MPa (CoV = 1.1%) and 200.8 GPa (CoV = 0.7%), respectively.

The CFRP laminates used in the experimental work consisted of unidirectional carbon fibers (with a volume content fiber higher than 68%) held together by an epoxy vinyl ester resin matrix [48]. The mechanical properties were obtained according to ISO 527-5:2009 [49] recommendations. An ultimate tensile strength of 2251.4 MPa (CoV = 3.2%), an ultimate tensile strain of 0.0133 (CoV = 7.2%), and modulus of elasticity of 169.5 GPa (CoV = 6.3%) were obtained.

A two-component epoxy adhesive was used to bond the CFRP strip to a concrete groove. According to the manufacturer's product guide specification [50], the components

A and B should be mixed at a ratio of 2:1 by weight. In addition, the proposed curing time was 7 days. However, in this study, the specimens were tested after 12 days of epoxy curing at room temperature.

Mechanical properties of the epoxy adhesive were assessed according to ISO-527-1 [51]. A modulus of elasticity of 7.1 GPa (CoV = 7.8%) and tensile strength of 30.4 MPa (CoV = 4.3%) were obtained.

As mentioned previously, the aim of this study is to evaluate the effect of high service temperature on the flexural behavior of NSM CFRP-strengthened beams. Therefore, characterization of the glass transition temperature (T_g) of the epoxy adhesive is of interest. According to the literature, there are two different well-known methods to obtain T_g of the adhesive: differential scanning calorimetry (DSC) [52] and dynamic mechanical analysis (DMA) [53]. The DSC technique provides information about changes in physical, chemical, and heat capacity of the adhesive. In this experimental program, isothermal DSC tests were carried out using the DSC Q2000. A heating rate of 10 °C/min was applied using nitrogen as the purge gas at 50 mL/min. The temperature range was between 25 and 80 °C. To determine T_g, three temperatures were measured: the extrapolated onset temperature (T_f), the mid-point temperature (T_m), and the extrapolated end temperature (T_e). The DMA test is an alternative method to determining the T_g and viscoelastic properties of polymeric materials. In this study, a METTLER TOLEDO DMA/SDTA861e analyzer with a 3-point bending test configuration and 45 mm between supports was utilized. The specimens were subjected to a heating rate of 2 °C/min within a temperature range of 30 to 100 °C. A 5 μm, constant displacement amplitude was applied at a frequency of 1 Hz. T_g was obtained by analyzing the storage modulus (E'), the loss modulus (E''), and the loss factor ($tan\delta$) as functions of temperature. In the present work, both methods (DSC and DMA) were utilized to determine the T_g after 12 days of curing time at room temperature. According to the test results, presented in Table 2, T_g cannot be considered as a unique temperature, but rather, it should be considered as a range of temperatures, as stated elsewhere [9]. The results of DSC and DMA tests are plotted in Figures 5 and 6, respectively. According to these results, T_g was in the range of 53.9–65.3 °C.

Table 2. Results of DSC and DMA methods.

Methodology	DSC			DMA		
	T_f	T_m	T_e	Storage Modulus (E')	Loss Modulus (E'')	Loss Factor ($tan\delta$)
T_g (°C)	53.9	55.2	55.9	56.2	57.7	65.3
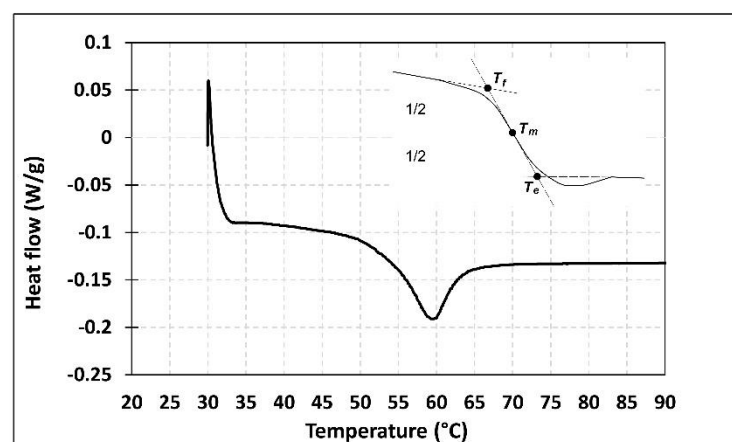
Figure 5. Differential scanning calorimetry (DSC) test results.
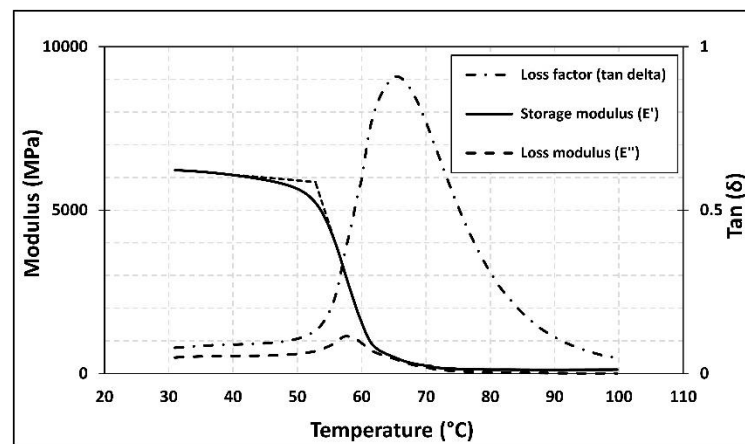
Figure 6. Dynamic mechanical analysis (DMA) test results.

3. Results and Discussion

In this section, experimental results are presented and discussed in terms of load–deflection curve, failure mode, and strain distribution along the CFRP strips. Analytical predictions for the load–deflection relationship are also presented.

In the analytical work, equilibrium of forces and moments is applied, where the following assumptions have been considered: (i) strain compatibility; (ii) Bernoulli's hypothesis; (iii) perfect bond, and (iv) the parabola–rectangle stress–strain curve defined in Eurocode 2 [20]. Based on this, theoretical moment–curvature is determined for uncracked and cracked sections and, finally, the moment–curvature relationship is derived as the interpolation between cracked and uncracked sections, according to CEB-FIP Model Code 1990 [54]. Afterwards, an analytical load–deflection curve is obtained from an integration of curvatures. It should be noted that shrinkage previous to loading has been found to affect the load–deflection behavior of RC members [55–58]. This influence has also been experienced in the NSM FRP-strengthened beams included in this work. Therefore, a systematic procedure is applied to account for this effect in the analytical predictions for their load–deflection relationship.

3.1. Shrinkage Effects on Instantaneous Deflection of Concrete Beams

Concrete shrinkage is a reduction in its volume due to moisture loss. This reduction starts after casting the concrete and depends on the water/cement ratio, ambient humidity, shape of aggregates, mixture properties, curing method and temperature, and geometry of specimens, among other parameters. In plain concrete without reinforcement, this shortening would happen without any restrictions. However, in the case of reinforced concrete, the presence of the embedded reinforcement acts as an impediment to free shrinkage. As a result of the restrain provided by the reinforcement, compressive and tensile loads appear in the reinforcement and the concrete, respectively, therefore causing unsightly cracks in concrete. Additionally to these premature cracks, in those cases where non-uniform distribution of reinforcement in section depth exists, an additional curvature can be observed [58].

Shrinkage is an important parameter in predicting the long-term deflection of RC flexural members, although depending on the amount of shrinkage and reinforcement ratio, it may have a significant influence even in the short-term behavior of RC elements [55–58]. Considerable shrinkage can be developed in concrete elements before testing unless special attention to the curing method and conditions is paid. With increasing the shrinkage at early age of concrete, tensile stresses are developed in concrete due to the restrain caused by internal reinforcement. This causes a reduction in the cracking moment of the flexural element and a shift on the bare bar response and therefore an increase in deflections.

In this work, shrinkage before flexural loading was assessed since shrinkage strain recorded from the day of casting was significantly higher for specimens in series 2 (344 με) when compared to that of series 1 (88 με).

The original uncracked and cracked responses (moment–curvature relationships) of a flexural specimen without considering the shrinkage are shown in Figure 7 (black lines). The corresponding uncracked and cracked additional curvatures due to shrinkage can be calculated according to [59]:

$$\varphi_{ucr} = \frac{A_{ucr}\Delta M_{ucr} + B_{ucr}\Delta N_{ucr}}{E_c(A_{ucr}I_{ucr} - B_{ucr}^2)} \tag{1}$$

$$\varphi_{cr} = \frac{A_{cr}\Delta M_{cr} + B_{cr}\Delta N_{cr}}{E_c(A_{cr}I_{cr} - B_{cr}^2)} \tag{2}$$

where E_c is the modulus of elasticity of concrete, A_{ucr} is the area of uncracked transformed section, and B_{ucr} and I_{ucr} are the first and second moments of inertia of the area of the uncracked transformed section, respectively. Moreover, A_{cr}, B_{cr}, and I_{cr} are the corresponding values for the cracked transformed section. Furthermore, ΔM and ΔN are the restraining moment and axial force against shrinkage.

$$\Delta N_{ucr} = -E_c\varepsilon_{sh}A_{c,ucr} \tag{3}$$

$$\Delta M_{ucr} = E_c\varepsilon_{sh}B_{c,ucr} \tag{4}$$

$$\Delta N_{cr} = -E_c\varepsilon_{sh}A_{c,cr} \tag{5}$$

$$\Delta M_{cr} = E_c\varepsilon_{sh}B_{c,cr} \tag{6}$$

where ε_{sh} is the shrinkage in concrete and A_c and B_c are the area of concrete and the first moment of inertia of the area of concrete (ignoring steel as shrinkage takes place only in concrete).
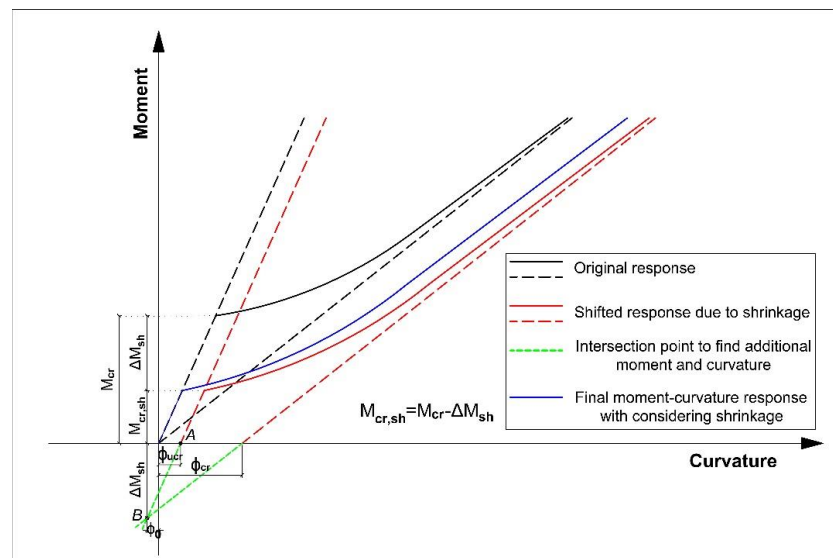
Figure 7. Flexural response of beam with and without shrinkage.

To account for the effect of shrinkage, these uncracked (φ_{ucr}) and cracked (φ_{cr}) additional curvatures are applied, so that the black dash lines in Figure 7 are shifted to the right (red dash lines). To find the additional moment due to shrinkage (ΔM_{sh}), the intersection point between red dash lines is obtained (point B). This means that if shrinkage of the flexural element is accounted for, point B should be the origin of the moment–curvature response. Hence, a reduction in the cracking moment equal to ΔM_{sh} should be applied

(moving from black solid line to red solid line in Figure 7). Then, point A should be shifted to the origin of the absolute coordinate system (moving from the red solid line to the blue solid line in Figure 7). Finally, the blue solid line is the final moment–curvature response of the beam when shrinkage effects are considered. It can be observed that if shrinkage is accounted for, the cracking moment reduces from M_{cr} to $M_{cr,sh}$ and additional deflections appear due to an extra curvature.

Representative comparisons between the analytical predictions of load–deflection curves for beams (both unstrengthened and strengthened) of the present work, with and without considering the effect of shrinkage are presented in Figure 8. A larger difference between the two predictions exists for those beams of series 2, as expected.
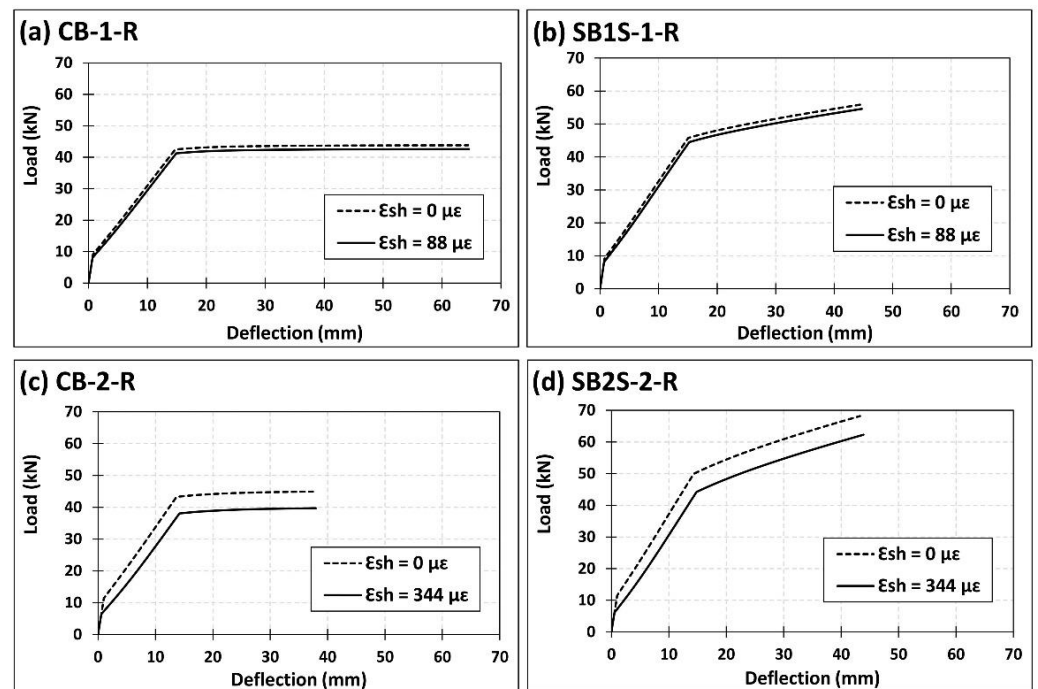
Figure 8. Analytical predictions of load–deflection curves with and without accounting for the shrinkage effect for specimens (**a**) CB-1-R; (**b**) SB1S-1-R; (**c**) CB-2-R; and (**d**) SB2S-2-R.

3.2. Load–Deflection Curves

The experimental load versus midspan deflection of the specimens of the present work is presented in Figure 9. As a general description, an initial linear behavior is observed that represents the elastic behavior of the flexural element. Once the cracking load is attained, the stiffness of the system decreases, and the load can be further increased until the yielding load; after this yielding load, the stiffness drops dramatically. From the yielding point onwards, no considerable increase in the ultimate capacity of control RC beams (unstrengthened) is found, whilst the ultimate capacity of strengthened beams is increased. In this sense, with the increase in the strengthening level (i.e., CFRP area), a slight increase of the cracking load was observed (see Table 3). In the strengthened specimens, the stiffness of load–deflection curves was relatively higher than in the RC beams, as expected. Moreover, the yielding (P_y) and ultimate (P_u) loads of the strengthened specimens were accordingly increased, irrespective of the applied temperature (see Figure 9).
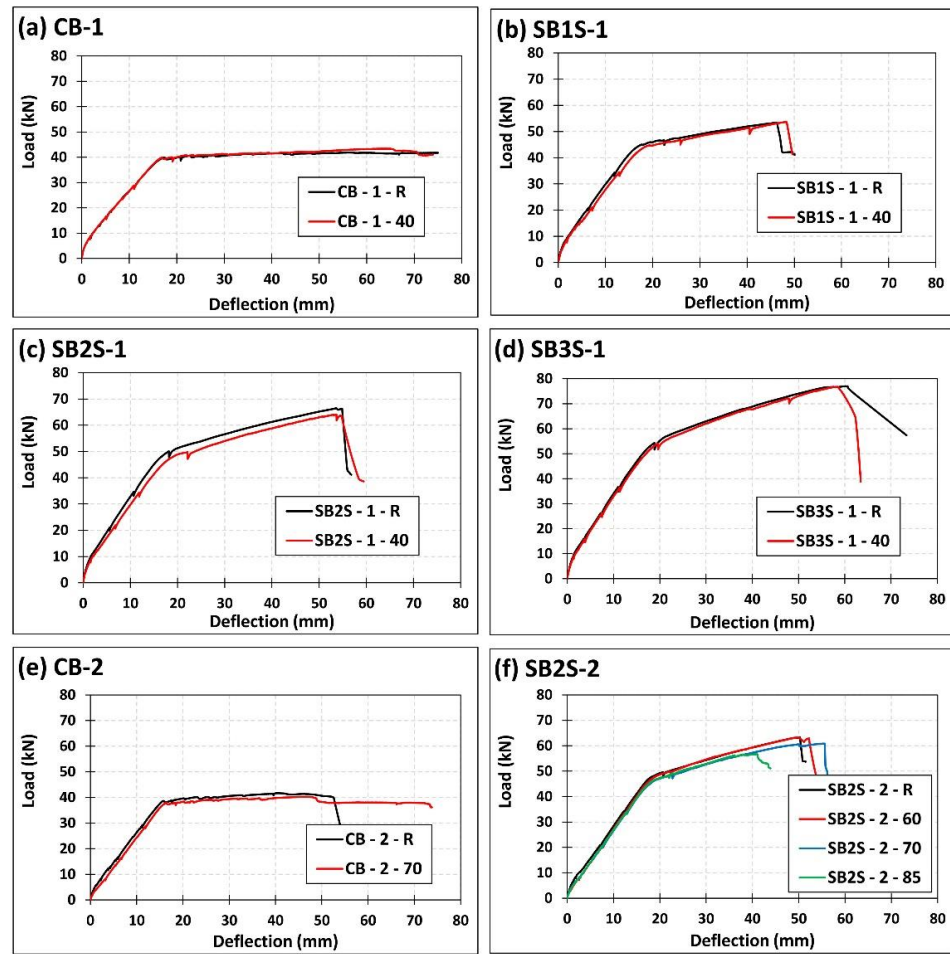
Figure 9. Effect of temperature on the experimental load–deflection curves of specimens (**a**) CB-1; (**b**) SB1S-1; (**c**) SB2S-1; (**d**) SB3S-1; (**e**) CB-2; and (**f**) SB2S-2.

Table 3. Experimental results and analytical predictions.

Beam ID	Cracking Load, P_{cr} (kN)		Yielding Load, P_y (kN)		Ultimate Load, P_u (kN)		Ultimate CFRP Strain, $\varepsilon_{u,\,FRP}$ (mm/mm)	Failure Mode [1]	
	Exp.	Analyt.	Exp.	Analyt.	Exp.	Analyt.	Exp.	Exp.	Analyt.
CB-1-R	6.53	7.98	39.90	41.29	41.87	42.59	-	CC	CC
CB-1-40	5.51	7.48	39.68	41.07	43.39	42.23	-	CC	CC
SB1S-1-R	7.11	7.97	44.90	44.68	53.44	54.57	0.0139	FR	FR
SB1S-1-40	6.07	7.47	44.69	44.36	53.63	54.39	0.0142	FR	FR
SB2S-1-R	7.21	7.96	49.40	47.90	66.50	65.04	0.0132	FR	FR
SB2S-1-40	6.12	7.46	49.27	47.68	64.06	64.19	0.0134	FR	FR
SB3S-1-R	7.56	7.95	56.80	51.29	77.04	74.74	0.0127	FR	FR
SB3S-1-40	6.41	7.45	55.60	51.03	76.77	73.39	0.0124	FR	FR
CB-2-R	3.69	6.17	38.59	38.12	41.71	39.72	-	CC	CC
CB-2-70	2.12	4.66	37.76	37.64	40.26	39.14	-	CC	CC
SB2S-2-R	4.79	5.67	48.21	44.51	63.36	62.27	0.0131	FR	FR
SB2S-2-60	2.09	4.45	47.88	43.99	63.39	59.35	0.0119	FR	FR
SB2S-2-70	1.82	4.15	46.70	43.80	60.86	56.21	0.0103	ED	FR
SB2S-2-85	1.68	3.69	46.47	43.70	56.72	55.24	- [2]	CC	FR

[1] Failure modes. CC: concrete crushing after steel yielding; FR: FRP rupture; ED: end debonding; [2] Strain gauge failed during the loading.

According to Figure 9, small differences can be observed between the load–deflection curves of specimens in series 1 when the temperature was increased from 20 to 40 °C. In this sense, the application of 40 °C derived in a slight reduction of the stiffness in load–deflection curves, which is in accordance with results presented in [32–34]. This reduction in stiffness was followed by a slight decrease in the ultimate capacity of the beams. In series 2, the application of a temperature that is approaching and even exceeding the epoxy T_g (i.e., 60 to 85 °C) generated a small reduction in the stiffness of the specimens. Moreover, the ultimate capacity of the beams in this series decreased by 3.48%, 3.95%, and 10.45% for CB-2-70, SB2S-2-70, and SB2S-2-85, respectively. No change was observed in SB2S-2-60 specimen. In unstrengthened beams, the increase in the temperature derived in a reduction of the cracking load and stiffness of system (see Figure 10). This reduction has been also observed in strengthened beams, where the increase in the temperature (near or beyond T_g) was followed by bond decrease and, subsequently, the efficiency of strengthening system was slightly reduced, thus making beams more susceptible to premature debonding.
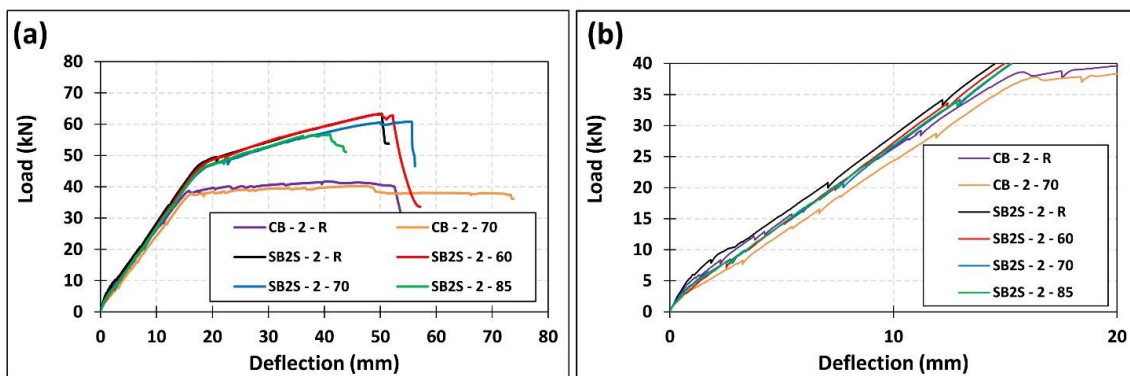
Figure 10. Effect of temperature on the experimental load–deflection curves of series 2 of specimens: (**a**) Total view; (**b**) Zoom in view.

Experimental results in terms of cracking load (P_{cr}), yielding load (P_y), ultimate load (P_u), ultimate CFRP strain ($\varepsilon_{u,FRP}$), and failure modes are presented and compared to analytical predictions in Table 3. For the analytical predictions, the effect of temperature on normal weight concrete properties is considered following the equations proposed in fib Model Code 2010 [60], which is said to be valid for temperatures ranging approximately from 0 to 80 °C:

$$f_{cm}(T) = f_{cm}(1.06 - 0.003T) \tag{7}$$

$$f_{ct,sp}(T) = f_{ct,sp}(1.06 - 0.003T) \tag{8}$$

$$E_c(T) = E_c(1.06 - 0.003T) \tag{9}$$

where $f_{cm}(T)$, $f_{ct,sp}(T)$, and $E_c(T)$ are the compressive strength, the splitting tensile strength, and the modulus of elasticity of concrete at temperature T (in °C), respectively. Moreover, f_{cm}, $f_{ct,sp}$, and E_c are the compressive strength, the splitting tensile strength, and the modulus of elasticity of concrete at T = 20 °C, respectively.

The mechanical properties of steel reinforcement and CFRP strips were not modified to include any effect of temperature because they are not sensitive to this range of temperatures [25,26,31,61]. For CFRP material, the ultimate strain (stress) value obtained from experimental results was used in analytical predictions.

To complement the comparison between experimental results and analytical predictions presented in Table 3, experimental and analytical load–deflection curves are compared in Figure 11. According to the figure, good agreement between experimental results and analytical predictions can be observed in terms of the cracking load, yielding load (and their corresponding deflections), and stiffness of the system before and after cracking load and after yielding load, thus meaning that shrinkage and temperature were correctly

accounted for in the analytical work. However, it should be noted that some differences exist between experimental and analytical ultimate load and deflections.
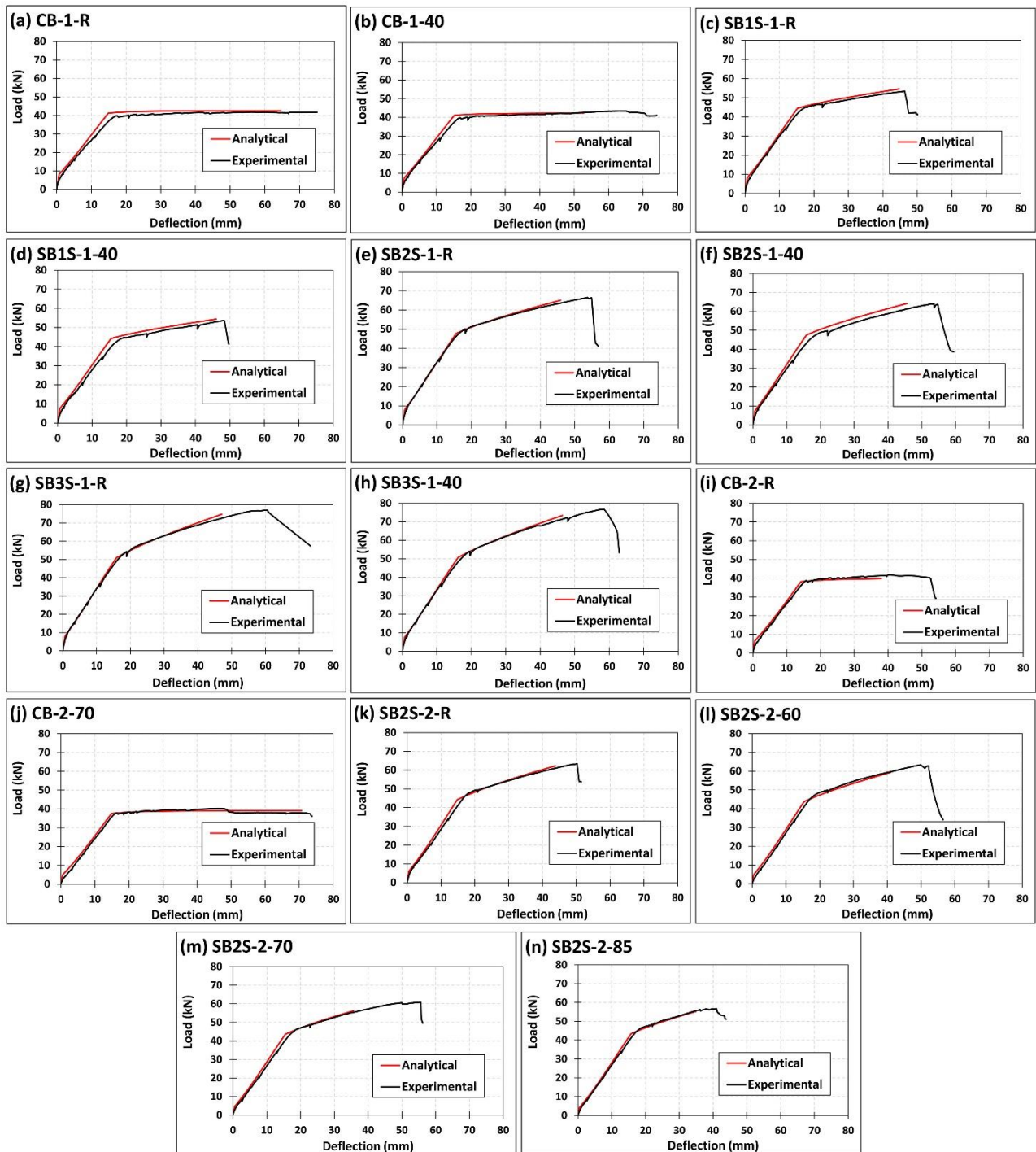
Figure 11. Comparison between experimental and analytical predictions on load–deflection curves of specimens (**a**) CB-1-R; (**b**) CB-1-40; (**c**) SB1S-1-R; (**d**) SB1S-1-40; (**e**) SB2S-1-R; (**f**) SB2S-1-40; (**g**) SB3S-1-R; (**h**) SB3S-1-40; (**i**) CB-2-R; (**j**) CB-2-70; (**k**) SB2S-2-R; (**l**) SB2S-2-60; (**m**) SB2S-2-70; and (**n**) SB2S-2-85.

3.3. Failure Mode

According to Table 3, control unstrengthened beams of both series (i.e., CB-1 and CB-2, at different temperatures) failed by concrete crushing in the compression zone of the beam after steel yielding. On the other hand, FRP rupture (after yielding of steel reinforcement)

was the failure mode of all strengthened beams of series 1. This means that with the application of 40 °C, the anchorage length of the CFRP strips was long enough to avoid FRP debonding failure, and the effect of the application of temperatures within this range is negligible. In series 2 of specimens, the application of 60 °C (i.e., specimen SB2S-2-60) resulted in FRP rupture failure mode, while the application of 70 °C (i.e., specimen SB2S-2-70) lead to failure by CFRP end debonding. To conclude, in specimen SB2S-2-85 (i.e., application of 85 °C), concrete was initially crushed in the compression zone of the section and, as a result, the load suddenly dropped without end debonding. This unexpected behavior can be due to a change in concrete mechanical properties, FRP, and epoxy at high service temperatures. As a general comment regarding the failure mechanism of the specimens, the increase in the temperature may be followed by a reduction of the efficiency of the strengthening system and, subsequently, it can lead to changes in the failure mechanism of the system (changing from FRP rupture to FRP debonding or even concrete crushing). Representative images of experienced failure modes are shown in Figure 12. It should be noted that in those cases where FRP rupture took place, it was subsequently followed by the detachment of the concrete around the FRP laminate.
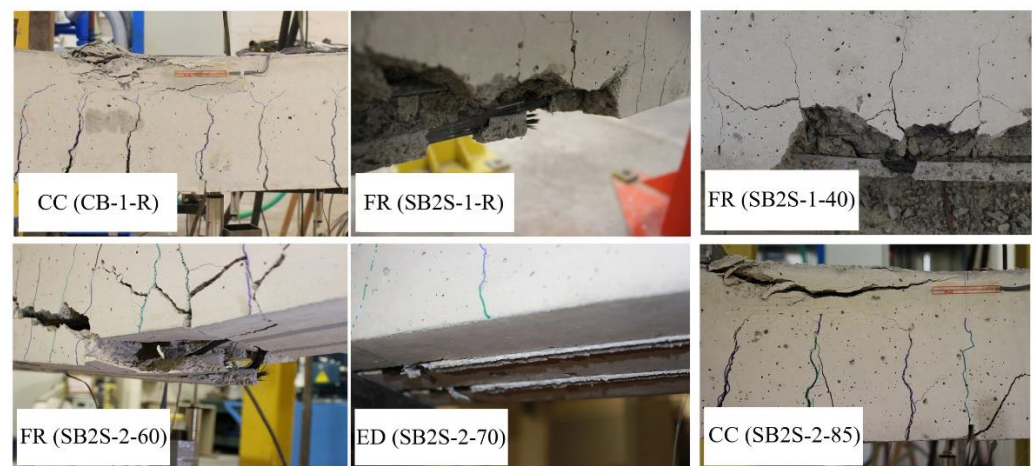
Figure 12. Experimental failure modes.

As previously mentioned, fib Bulletin 90 [8] recommends limiting the maximum temperature to avoid premature failure in EBR-strengthened systems. According to experimental observations, as long as the temperature is sufficiently lower than T_g, no premature failure was observed. On the contrary, the application of a temperature exceeding the T_g resulted in end debonding failure mode (i.e., specimen SB2S-2-70). It should be noted that no premature failure (i.e., end debonding) occurred when temperature in the range of T_g was applied ($T = 60$ °C), thus showing a good performance related to end debonding for the NSM strengthening system. Nevertheless, it must be noted that additional experimental work is needed to confirm the findings of the experimental program presented in this communication.

3.4. Strain Distribution along the CFRP Strip

The distribution of strains along the CFRP strips can give useful information about the bond behavior (i.e., the force distribution between the CFRP and concrete interface) and its influence on cracking phenomena. Instrumentation with strain gauges presented in Figure 3b allowed the register of strains at several sections along the CFRP strip in SB1S-1-R and SB1S-1-40 specimens. Experimental strain distributions along half of the CFRP laminate of these specimens are plotted at different levels of load in Figure 13. Experimental results show that the increase in temperature was followed by an increase of strains in the strip. In addition, in both specimens, the strain in the CFRP strip increased dramatically

after yielding of the longitudinal steel reinforcement. The available fluctuation in the strain distributions may be related to the appearance and opening of new cracks.
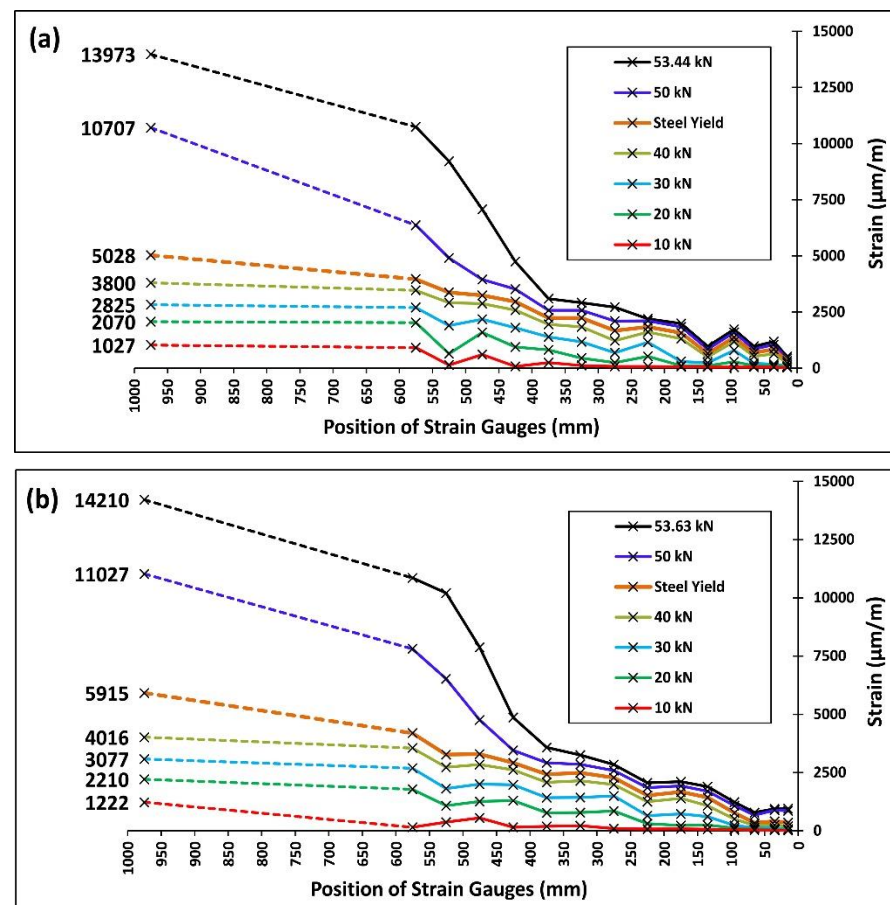
Figure 13. Strain distributions along one half of the CFRP strip at different levels of load for specimens (**a**) SB1S-1-R and (**b**) SB1S-1-40.

4. Finite Element Analysis

Nonlinear finite element (FE) analysis of control and CFRP-strengthened beams subjected to four-pointed loads was carried out to compare with the results obtained from the experimental work. A three dimensional FE model was created using the well-known commercial FE program ABAQUS [62].

4.1. Description of FE Model

FE models include concrete, steel reinforcements (longitudinal and stirrups), CFRP strips, and epoxy. Concrete and epoxy are modeled by an eight-node linear hexahedral solid element with reduced integration (C3D8R), steel reinforcements are modeled by a two-node linear 3D truss element (T3D2), and FRP strips are modeled by a two-node linear beam (B31). A mesh convergence analysis was performed to select the optimum mesh sizes for different parts involved in the FE model. In this study, it was observed that the meshing refinement was not sensitive after having the maximum mesh size of 25 mm for all elements except epoxy that had 10 mm mesh size. By taking advantage of symmetry in two perpendicular planes, only a quarter of the beam was modeled. Boundary conditions of the experimental test set-up were considered. Finite element mesh along with the boundary conditions is shown in Figure 14.

Figure 14. Finite element mesh of simulated beam (one quarter).

Considering perfect bond, steel reinforcements and CFRP strips are embedded inside the concrete and epoxy, respectively. In order to address this condition, the embedded region function of ABAQUS is used. Moreover, the tie constraint function is assumed to simulate the interaction in the interface between epoxy and concrete. The selection of these interfacial behaviors is based on the fact that the bond was good enough and bond failure took place only in one of the beams of the present experimental program (i.e., specimen SB2S-2-70). As a result of this, specimen SB2S-2-70 is not included in the numerical simulations.

Similar to the case of analytical predictions presented in Section 3.1, the effect of shrinkage is also addressed in the numerical simulations. To this end, an initial extra deflection due to shrinkage (calculated following Section 3.1) is applied to the middle of the beam in a separate step. Afterwards, the main flexural load is applied in a displacement control mode through a rigid plate to avoid any extra deformation along the loading.

4.2. Materials Definition

Steel reinforcement is modeled as an isotropic bilinear elasto-plastic material, while epoxy is modeled as isotropic linear elastic material and CFRP is modeled as brittle material (with ultimate strain value obtained from experimental results). Moreover, to simulate the inelastic behavior of concrete, concrete damage plasticity (CDP) is used. This continuum, plasticity-based, damage model for concrete is applicable to different loading conditions and can be utilized for concrete with embedded reinforcement [62]. This model assumes that the two main failure mechanisms are tensile cracking and compressive crushing. Therefore, the evolution of the failure surface is controlled by two hardening variables linked to the failure mechanisms under tension and compression loading. The required material parameters for the definition of the CDP model are dilation angle (ψ), flow potential eccentricity (ϵ), the ratio of the biaxial compressive stress to the uniaxial compressive stress (σ_{b0}/σ_{c0}), the ratio of the second stress invariant on the tensile meridian to that on the compressive meridian (K_c), and viscosity (μ). In this numerical study, these parameters are considered as $\psi = 36°$, $\epsilon = 0.1$, $\sigma_{b0}/\sigma_{c0} = 1.16$, $K_c = 0.67$, and $\mu = 0.0005$.

The concrete stress–strain compression relationship is modeled according to Eurocode 2 [63]. Moreover, the tensile post-cracking behavior of concrete is modeled according to Torres et al. [64], where α_1 and α_2 are two dimensionless coefficients that define the tensile post-cracking stress–strain relationship of concrete (see Figure 15). In this study, based on the loading condition, α_1 was assumed to be equal to 0.4 and based on section properties, α_2 was assumed to be in the range of 13 to 15.

The effect of temperature is applied directly in the definition of materials' properties, following the same strategy as in the analytical work (see Section 3.2). The effect of temperature on epoxy material is considered according to the experimental results presented in [7]. This assumption is based on the fact that the possible effect of the heating process, taking place before the main flexural test, is not included in the experimental load–deflection responses obtained in the laboratory (i.e., the system is zeroed before testing).
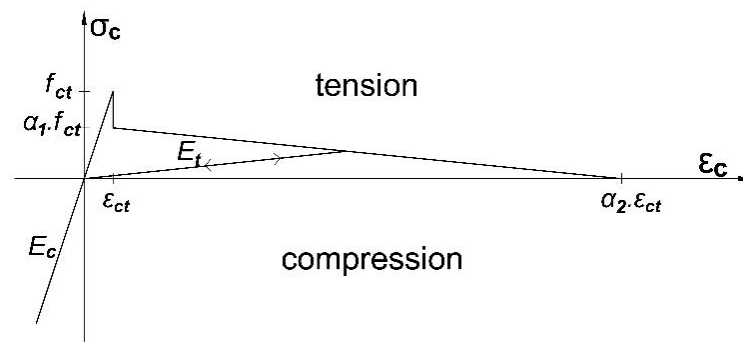
Figure 15. Equivalent stress–strain relationship for tensioned concrete [64].

4.3. FE Results

The comparison between numerical predictions and experimental results is presented in Figure 16 and Table 4. In all cases, the FE model reasonably predicts the experimental behavior of beams under flexural load. Slightly higher initial stiffness is observed in the numerical simulation when compared to experimental curves, with a mean difference in deflections of 7.15% observed at the service load level [8]. In terms of yielding and ultimate loads, differences of only 3% and 2.9% are observed, respectively, with the same failure mode in both experimental work and numerical simulations. In this sense, it should be highlighted that concrete crushing was the predicted failure mode in the numerical simulation of specimen SB2S-2-85, which coincides with experimental observation. This would confirm that the negative effect of temperature on the mechanical properties of concrete and epoxy leads to an unexpected concrete crushing failure mode.

Table 4. Comparison between numerical predictions and experimental results.

Beam ID	Service Load (kN)	Deflection at Service Load, d_s (mm)		Diff. (%)	Yielding Load, P_y (kN)		Diff. (%)	Ultimate Load, P_u (kN)		Diff. (%)	Failure Mode [1]	
		Exp.	Numeric.		Exp.	Numeric.		Exp.	Numeric.		Exp.	Numeric.
CB-1-R	20.57	7.04	5.99	14.91	39.90	39.15	1.88	41.87	41.22	1.55	CC	CC
CB-1-40	19.82	6.65	6.07	8.72	39.68	39.11	1.44	43.39	40.75	6.08	CC	CC
SB1S-1-R	21.37	6.70	5.93	11.49	44.90	43.39	3.36	53.44	55.86	4.53	FR	FR
SB1S-1-40	20.59	7.01	5.94	15.26	44.69	43.18	3.38	53.63	53.73	0.19	FR	FR
SB2S-1-R	22.12	6.10	5.82	4.59	49.40	49.99	1.19	66.50	68.20	2.56	FR	FR
SB2S-1-40	21.32	6.60	5.78	12.42	49.27	48.83	0.89	64.06	66.07	3.14	FR	FR
SB3S-1-R	22.85	6.02	5.67	5.81	56.80	54.11	4.74	77.04	78.77	2.25	FR	FR
SB3S-1-40	22.01	5.97	5.51	7.71	55.60	53.76	3.31	76.77	74.38	3.11	FR	FR
CB-2-R	26.28	9.98	9.99	0.10	38.59	36.95	4.25	41.71	40.78	2.23	CC	CC
CB-2-70	24.64	10.20	10.05	1.47	37.76	36.38	3.65	40.26	39.60	1.64	CC	CC
SB2S-2-R	29.20	10.31	9.55	7.37	48.21	47.49	1.49	63.36	64.24	1.39	FR	FR
SB2S-2-60	27.04	9.94	9.65	2.92	47.88	45.71	4.53	63.39	58.72	7.37	FR	FR
SB2S-2-85	25.63	9.52	9.51	0.11	46.47	44.34	4.58	56.72	55.55	2.06	CC	CC
		Mean diff. (%)		7.15	Mean diff. (%)		2.98	Mean diff. (%)		2.93		

[1] Failure modes. CC: concrete crushing after steel yielding; FR: FRP rupture.

Figure 16. Comparison between experimental and numerical work of specimens (**a**) CB-1-R; (**b**) CB-1-40; (**c**) SB1S-1-R; (**d**) SB1S-1-40; (**e**) SB2S-1-R; (**f**) SB2S-1-40; (**g**) SB3S-1-R; (**h**) SB3S-1-40; (**i**) CB-2-R; (**j**) CB-2-70; (**k**) SB2S-2-R; (**l**) SB2S-2-60; and (**m**) SB2S-2-85.

5. Conclusions

In the present work, an experimental program to study the influence of high service temperature on the flexural performance of NSM CFRP-strengthened RC beams is presented. The experimental results are compared to analytical and numerical predictions. Based on the data presented, the following conclusions can be drawn:

- No considerable differences can be observed in the load–deflection curve when specimens are subjected to 40 °C (i.e., series 1). This behavior can be attributed to 40 °C being far below the T_g of the epoxy resin.

- In series 2, as a result of the increase in temperature near or beyond the T_g, the stiffness and the ultimate load of strengthened and unstrengthened specimens decreased. The interface bond capacity between epoxy and concrete could have been affected, and the efficiency of the strengthening system showed some reduction, thus making the beam to be more prone to experience end debonding failure.
- In both series of specimens, the failure mode of the control unstrengthened beams was concrete crushing after steel yielding. For the strengthened beams under 20, 40, and 60 °C, the failure mode was FRP rupture. With the increase of temperature up to 70 °C, the beam failed by end debonding. Finally, specimens under 85 °C experienced concrete crushing and, as a result, the load suddenly dropped without giving place to end debonding. This failure mode can be attributed to the reduction in mechanical properties of concrete and epoxy when submitted to higher temperature.
- No end debonding or significant reduction in ultimate load occurred for specimens being tested up to 60 °C, thus showing a good performance of the NSM strengthening system.
- The application of temperature exceeding the epoxy T_g generated a small reduction in the stiffness of the specimen and a decrease by 3.48%, 3.95%, and 10.45% in the ultimate capacity of beams CB-2-70, SB2S-2-70, and SB2S-2-85, respectively.
- The effect of temperature on the experimental bond behavior of specimen at 40 °C was studied in one of the strengthened beams (i.e., SB1S-1 specimens). With the increase in the temperature, strains (and stresses) in the CFRP strip increased.
- A systematic procedure was applied to consider the effect of shrinkage in short-term response of the specimens. It was observed that the increase in the concrete shrinkage resulted in a reduction of the elements' stiffness and cracking load. Good agreement was observed between analytical predictions and experimental results.
- A simple but trustable FE model accounting for initial shrinkage and effects of temperature was created to be compared with experimental work. In all cases, numerical models correctly predict the experimental load–deflection responses and failure modes.

References

1. Pellegrino, C.; Sena-Cruz, J. *Design Procedures for the Use of Composites in Strengthening of Reinforced Concrete Structures: State-of-the-Art Report of the Rilem Technical Committee 234-Duc*; Springer: Dordrecht, The Netherlands, 2016; p. 392. [CrossRef]
2. De Lorenzis, L.; Teng, J.G. Near-surface mounted FRP reinforcement: An emerging technique for strengthening structures. *Compos. Part B* **2007**, *38*, 119–143. [CrossRef]
3. Parretti, R.; Nanni, A. Strengthening of RC members using near-surface mounted FRP composites: Design overview. *Adv. Struct. Eng.* **2004**, *7*, 469–483. [CrossRef]

4. Michel, M.; Ferrier, E. Effect of curing temperature conditions on glass transition temperature values of epoxy polymer used for wet lay-up applications. *Constr. Build. Mater.* **2020**, *231*, 117206. [CrossRef]

5. Silva, P.; Fernandes, P.; Sena-Cruz, J.; Xavier, J.; Castro, F.; Soares, D.; Carneiro, V. Effects of different environmental conditions on the mechanical characteristics of a structural epoxy. *Compos. Part B* **2016**, *88*, 55–63. [CrossRef]

6. Michels, J.; Sena-Cruz, J.; Christen, R.; Czaderski, C.; Motavalli, M. Mechanical performance of cold-curing epoxy adhesives after different mixing and curing procedures. *Compos. Part B* **2016**, *98*, 434–443. [CrossRef]

7. Firmo, J.P.; Roquette, M.G.; Correia, J.R.; Azevedo, A.S. Influence of elevated temperatures on epoxy adhesive used in CFRP strengthening systems for civil engineering applications. *Int. J. Adhes. Adhes.* **2019**, *93*, 102333. [CrossRef]

8. Fib Bulletin 90. *Externally Applied FRP Reinforcement for Concrete Structures*; International Federation for Structural Concrete: Lausanne, Switzerland, 2019.

9. Michels, J.; Widmann, R.; Czaderski, C.; Allahvirdizade, R.; Motavalli, M. Glass transition evaluation of commercially available epoxy resins used for civil engineering applications. *Compos. Part B* **2015**, *77*, 484–493. [CrossRef]

10. Klamer, E.L. Influence of Temperature on Concrete Beams Strengthened in Flexure with CFRP. Ph.D. Thesis, TU Eindhoven, Eindhoven, The Netherlands, 2009.

11. Ferrier, E.; Michel, L.; Jurkiewiez, B.; Hamelin, P. Creep behavior of adhesives used for external FRP strengthening of RC structures. *Constr. Build. Mater.* **2011**, *25*, 461–467. [CrossRef]

12. Bisby, L.A.; Green, M.F. Resistance to freezing and thawing of fiber–reinforced polymer–concrete bond. *ACI Struct. J.* **2002**, *99*, 215–223.

13. Leone, M.; Aiello, M.A.; Matthys, S. Effect of elevated service temperature on bond between FRP EBR systems and concrete. *Compos. Part B* **2009**, *40*, 85–93. [CrossRef]

14. El-Hacha, R.; Rizkalla, S.H. Near-surface-mounted fiber-reinforced polymer reinforcements for flexural strengthening of concrete structures. *ACI Struct. J.* **2004**, *101*, 717–726.

15. Sharaky, I.A.; Baena, M.; Barris, C.; Sallam, H.E.M.; Torres, L. Effect of axial stiffness of NSM FRP reinforcement and concrete cover confinement on flexural behaviour of strengthened RC beams: Experimental and numerical study. *Eng. Struct.* **2018**, *173*, 987–1001. [CrossRef]

16. Obaidat, Y.T.; Barham, W.S.; Aljarah, A.H. New anchorage technique for NSM-CFRP flexural strengthened RC beam using steel clamped end plate. *Constr. Build. Mater.* **2020**, *263*, 20246. [CrossRef]

17. Sena-Cruz, J.M.; Barros, J. Bond between near surface mounted carbon-fiber-reinforced polymer laminate strips and concrete. *J. Compos. Constr.* **2004**, *8*, 519–527. [CrossRef]

18. Sena-Cruz, J.M.; Barros, J.A.; Coelho, M.R.; Silva, L.F. Efficiency of different techniques in flexural strengthening of RC beams under monotonic and fatigue loading. *Constr. Build. Mater.* **2012**, *29*, 175–182. [CrossRef]

19. Dias, S.J.; Barros, J.A.; Janwaen, W. Behavior of RC beams flexurally strengthened with NSM CFRP laminates. *Compos. Struct.* **2018**, *201*, 363–376. [CrossRef]

20. Barris, B.; Sala, P.; Gómez, J.; Torres, L. Flexural behaviour of FRP reinforced concrete beams strengthened with NSM CFRP strips. *Compos. Struct.* **2020**, 112059. [CrossRef]

21. Yu, B.; Kodur, V.K.R. Fire behavior of concrete T-beams strengthened with near-surface mounted FRP reinforcement. *Eng. Struct.* **2014**, *80*, 350–361. [CrossRef]

22. Palmieri, A.; Matthys, S.; Taerwe, L. Fire endurance and residual strength of insulated concrete beams strengthened with near-surface mounted reinforcement. *J. Compos. Constr.* **2012**, *17*, 454–462. [CrossRef]

23. Palmieri, A.; Matthys, S.; Taerwe, L. Strengthening with near surface mounted reinforcement: Structural and fire behavior. In Proceedings of the 3th International Congress and Exhibition Fib "Think Globally, Build Locally", Washington, DC, USA, 29 May–2 June 2010; pp. 1–10.

24. Palmieri, A.; Matthys, S.; Taerwe, L. Experimental investigation on fire endurance of insulated concrete beams strengthened with near surface mounted FRP bar reinforcement. *Compos. Part B* **2012**, *43*, 885–895. [CrossRef]

25. Firmo, J.P.; Correia, J.R. Fire behaviour of thermally insulated RC beams strengthened with EBR-CFRP strips: Experimental study. *Compos. Struct.* **2015**, *122*, 144–154. [CrossRef]

26. Firmo, J.P.; Correia, J.R. Fire behaviour of thermally insulated RC beams strengthened with NSM-CFRP strips: Experimental study. *Compos. Part B* **2015**, *76*, 112–121. [CrossRef]

27. Carlos, T.B.; Rodrigues, J.P.C.; de Lima, R.C.; Dhima, D. Experimental analysis on flexural behaviour of RC beams strengthened with CFRP laminates and under fire conditions. *Compos. Struct.* **2018**, *189*, 516–528. [CrossRef]

28. Jadooe, A.; Al-Mahaidi, R.; Abdouka, K. Experimental and numerical study of strengthening of heat-damaged RC beams using NSM CFRP strips. *Constr. Build. Mater.* **2017**, *154*, 899–913. [CrossRef]

29. Haddad, R.H.; Almomani, O.A. Recovering flexural performance of thermally damaged concrete beams using NSM CFRP strips. *Constr. Build. Mater.* **2017**, *154*, 632–643. [CrossRef]

30. Burke, P.J.; Luke, A.B.; Mark, F.G. Effects of elevated temperature on near surface mounted and externally bonded FRP strengthening systems for concrete. *Cem. Concr. Compos.* **2013**, *35*, 190–199. [CrossRef]

31. Firmo, J.P.; Correia, J.R.; Bisby, L.A. Fire behaviour of FRP-strengthened reinforced concrete structural elements: A state-of-the-art review. *Compos. Part B* **2015**, *80*, 198–216. [CrossRef]

32. Klamer, E.L.; Dick, A.H.; Michael, C.J.H. The influence of temperature on RC beams strengthened with externally bonded CFRP reinforcement. *Heron* **2008**, *53*, 157–185.
33. Krzywoń, R. Behavior of EBR FRP strengthened beams exposed to elevated temperature. *Procedia. Eng.* **2017**, *193*, 297–304. [CrossRef]
34. Silva, P.M.; Escusa, G.G.; Sena-Cruz, J.M.; Azenha, M. Experimental investigation of RC slabs strengthened with NSM CFRP system subjected to elevated temperatures up to 80 °C. In Proceedings of the 8th International Conference on Fibre-Reinforced Polymer (FRP) Composites in Civil Engineering, CICE, Hong Kong, China, 14–16 December 2016.
35. Ferrier, E.; Rabinovitch, O.; Michel, L. Mechanical behavior of concrete–resin/adhesive–FRP structural assemblies under low and high temperatures. *Constr. Build. Mater.* **2016**, *127*, 1017–1028. [CrossRef]
36. Abed, F.; Oucif, C.; Awera, Y.; Mhanna, H.H.; Alkhraisha, H. FE modeling of concrete beams and columns reinforced with FRP composites. *Def. Technol.* **2021**, *7*, 1–14. [CrossRef]
37. Al-Rahmani, A.; Abed, F.H. Numerical investigation of hybrid FRP reinforced beams. In Proceedings of the 5th International Conference on Modeling, Simulation and Applied Optimization (ICMSAO), Hammamet, Tunisia, 28–30 April 2013. [CrossRef]
38. Alkhraisha, H.; Mhanna, H.; Abed, F. FE Modeling of RC Beams Reinforced in Flexure with BFRP Bars Exposed to Harsh Conditions. In *Sustainable Issues in Infrastructure Engineering*; Springer: Cham, Switzerland, 2021; pp. 3–13. [CrossRef]
39. Abed, F.H.; Al-Rahmani, A.; Al-Rahmani, A.H. Finite element simulations of the shear capacity of GFRP-reinforced concrete short beams. In Proceedings of the 5th International Conference on Modeling, Simulation and Applied Optimization (ICMSAO), Hammamet, Tunisia, 28–30 April 2013. [CrossRef]
40. Abed, F.; El Refai, A.; Abdalla, S. Experimental and finite element investigation of the shear performance of BFRP-RC short beams. *Structures* **2019**, *20*, 689–701. [CrossRef]
41. Hawileh, R.A.; Naser, M.; Zaidan, W.; Rasheed, H.A. Modeling of insulated CFRP strengthened reinforced concrete T-beam exposed to fire. *Eng. Struct.* **2009**, *31*, 3072–3079. [CrossRef]
42. Dai, J.G.; Gao, W.Y.; Teng, J.G. Finite element modeling of insulated FRP-strengthened RC beams exposed to fire. *J. Compos. Construct.* **2015**, *19*, 04014046. [CrossRef]
43. Firmo, J.P.; Arruda, M.R.T.; Correia, J.R.; Rosa, I.C. Three-dimensional finite element modelling of the fire behaviour of insulated RC beams strengthened with EBR and NSM CFRP strips. *Compos. Struct.* **2018**, *183*, 124–136. [CrossRef]
44. UNE-EN 12390-3. *Testing Hardened Concrete—Part 3: Compressive Strength of Test Specimens*; AENOR: Madrid, Spain, 2003.
45. UNE-EN 12390-6. *Testing Hardened Concrete—Part 6: Tensile Splitting Strength of Test Specimens*; AENOR: Madrid, Spain, 2010.
46. ASTM C469/C469M-14. *Standard Test Method for Static Modulus of Elasticity and Poisson's Ratio of Concrete in Compression*; ASTM International: West Conshohocken, PA, USA, 2014.
47. UNE-EN ISO 15630-1. *Steel for the Reinforcement and Prestressing of Concrete-Test Methods—Part 1: Reinforcing Bars, Wire Rod and Wire*; AENOR: Madrid, Spain, 2011.
48. S&P. *S&P Cfrp Laminate, Technical Datasheet*; S&P: Seewen, Switzerland, 2017.
49. ISO 527-5. *Plastics-Determination of Tensile Properties—Part 5: Test Conditions FOR Unidirectional Fibre-Reinforced Plastic Composites*; ISO: Geneva, Switzerland, 2009; Volume 1.
50. S&P. *S&P Resin 220 HP Epoxy Adhesive, Technical Data Sheet*; S&P: Seewen, Switzerland, 2019.
51. ISO 527-1. *Plastics-Determination of Tensile Properties—Part 1: General Principles*; ISO: Geneva, Switzerland, 2012.
52. ASTM E1356-08. *Standard Test Method for Assignment of the Glass Transition Temperatures by Differential Scanning Calorimetry*; ASTM International: West Conshohocken, PA, USA, 2008.
53. ASTM D5023-15. *Standard Test Method for Plastics: Dynamic Mechanical Properties: In Flexure (Three-Point Bending)*; ASTM International: West Conshohocken, PA, USA, 2015.
54. Comité Euro-International du Béton (CEB). *CEB-FIP Model Code 1990 (MC-90)*; Thomas Telford: London, UK, 1993.
55. Bischoff, P.H.; Darabi, M. Unified Approach for Computing Deflection of Steel and FRP Reinforced Concrete. In *Andy Scanlon Symposium on Serviceability and Safety of Concrete Structures: From Research to Practice*; American Concrete Institute: Michigan, MI, USA, 2012; pp. 1–20.
56. Scanlon, A.; Bischoff, P.H. Shrinkage restraint and loading history effects on deflections of flexural members. *ACI Struct. J.* **2008**, *105*, 498.
57. Gribniak, V.; Kaklauskas, G.; Kliukas, R.; Jakubovskis, R. Shrinkage effect on short-term deformation behavior of reinforced concrete—When it should not be neglected. *Mater. Des.* **2013**, *5*, 1060–1070. [CrossRef]
58. Gribniak, V.; Torres, L.; Kaklauskas, G.; Daniunas, A.; Kacianauskas, R.; Jakubovskis; R. Prediction of concrete shrinkage occurring prior to external loading and effect on short-term constitutive modeling and design. *Adv. Struct. Eng.* **2013**, *16*, 1061–1080. [CrossRef]
59. Gilbert, R.I. *Time Effect in Concrete Structures*; Elsevier: Amsterdam, The Netherland, 1988; p. 321.
60. International Federation for Structural Concrete (fib). *Fib Model Code for Concrete Structures 2010*; fib, John Wiley & Sons: New York, NY, USA, 2013.
61. Fernandes, P.; Sena-Cruz, J.; Xavier, J.; Silva, P.; Pereira, E.; Cruz, J. Durability of bond in NSM CFRP-concrete systems under different environmental conditions. *Compos. Part B* **2018**, *138*, 19–34. [CrossRef]
62. Abaqus, Version 6.16; Documentation, Abaqus v6.16. Available online: http://130.149.89.49:2080/v2016/index.html (accessed on 21 August 2016).

63. EN 1992-1-1. *Eurocode 2. Design of Concrete Structures—Part 1-1: General Rules and Rules for Buildings*; British Standard Institution: London, UK, 2004.
64. Torres, L.; Lopez-Almansa, F.; Bozzo, L.M. Tension-stiffening model for cracked flexural concrete members. *J. Struct. Eng.* **2004**, *130*, 1242–1251. [CrossRef]

A.2 Paper B

Influence of curing, post-curing and testing temperatures on mechanical properties of a structural adhesive

Younes Jahani[1*], Marta Baena[1], Cristina Barris[1], Ricardo Perera[2] and Lluís Torres[1]

[1]AMADE, Polytechnic School, University of Girona, 17003, Girona, Spain

[2]Department of Mechanical Engineering, Technical University of Madrid, 28006 Madrid, Spain

[*]Corresponding author

Influence of curing, post-curing and testing temperatures on mechanical properties of a structural adhesive

Younes Jahani [a],[*], Marta Baena [a], Cristina Barris [a], Ricardo Perera [b], Lluís Torres [a]

[a] *AMADE, Polytechnic School, University of Girona, 17003 Girona, Spain*
[b] *Department of Mechanical Engineering, Technical University of Madrid, 28006 Madrid, Spain*

ARTICLE INFO	ABSTRACT
	Structural cold-curing adhesives are widely used to strengthen Reinforced Concrete (RC) structures with Fibre Reinforced Polymers (FRPs). The performance of these adhesives, and therefore the performance of the strengthening system, may be affected by temperature, as ambient-cured structural adhesives usually have low glass transition temperature (T_g). This paper presents a comprehensive experimental investigation on the influence of temperature on mechanical properties and T_g of a structural epoxy adhesive. The experimental program was divided in four groups of specimens. In Group 1, the effect of curing and post-curing temperature on T_g of the epoxy adhesive was investigated. In Groups 2–4, the effects of testing temperature, curing temperature and post-curing temperature, respectively, on adhesive mechanical properties were studied. Experimental results confirm that curing and post-curing temperature affected T_g differently depending whether the applied temperature was below or beyond the epoxy T_g. Similar behavior was observed in the mechanical properties of the epoxy, as they showed improvements when curing process (curing and post-curing) temperature was below T_g and they were negatively affected when curing process temperature was beyond T_g. Besides, tensile and compressive mechanical properties were negatively affected by testing temperatures beyond 20 °C.

1. Introduction

Structural epoxy adhesives are widely used to bond Fiber Reinforced Polymers (FRPs) to concrete in both Externally Bonded Reinforcement (EBR) and Near-Surface Mounted (NSM) strengthening techniques [1,2]. The performance of the strengthened structure will depend on the bonded joint, whose behavior has been acknowledged to be partially governed by the mechanical properties of the adhesive [3–5].

In civil engineering applications adhesive joint is typically cured at ambient temperature. Accordingly, cold-curing adhesives are the most widely used, as its use is easier and they present good mechanical properties after the required curing time (which depends on the curing agent and temperature). It is a feature of commonly used ambient-cured structural adhesives to have glass transition temperatures (T_g) ranging between 40 °C and 70 °C [6]. Being T_g defined as the temperature range where a thermosetting polymer changes from a glassy to a rubbery state, (i.e. the temperature ranges over which the mobility of the polymer chains increases significantly) [7], these relatively low values of T_g can be a limiting factor because these adhesives can exhibit substantial changes in their mechanical properties if working temperature

approaches its T_g [8–14]. As a consequence of the reduction in the adhesion strength of the epoxy as the T_g range is approached, a reduction in the stiffness and ultimate capacity of the FRP-strengthened element can take place and the failure mode can change [8,15–19].

A reduced number of studies have investigated the influence of testing temperature on the mechanical properties of cold-curing epoxy adhesive typically used in civil engineering [9–20]. Firmo et al. [9] presented an experimental work to assess the mechanical properties of a commercial epoxy adhesive typically used in civil engineering at different temperatures (from 20 °C to 120 °C). The results showed that mechanical properties were significantly affected by testing temperatures larger than T_g ($T_g = 47$ °C), as the shear and the tensile strength of epoxy were reduced to around 30% of their corresponding ambient strengths. Additionally, the shear and the tensile modulus were almost negligible for tests at 50 °C. These results are similar to those obtained in other studies on epoxy adhesives with larger T_g values used in other applications, such as aerospace industry [10–12]. As an example, Banea et al. [10,11] investigated the effect of testing temperature on the mechanical properties of an epoxy adhesive having a T_g value equal to 150 °C. In these studies, four different temperatures were applied during

---

testing (i.e. room temperature, 100, 150 and 200 °C), and experimental results showed a reduction in the tensile strength and an increase in the ductility when testing temperature was increased. The maximum reduction was observed for testing temperatures near to and beyond T_g, where the adhesive was in rubbery state. Similarly, Wu [12] studied the influence of testing temperature on mechanical properties of an epoxy whose T_g equals 177 °C. According to their experimental results, increasing the testing temperature produced a decrease in both the tensile strength and the elastic modulus. It should be noted that the rate of loss of the mechanical properties was sharply increased for testing temperature beyond T_g. Besides, Reis [13] presented a comparative study on the effect of testing temperature (ranging from 23 to 90 °C) on compressive strength of epoxy polymer mortar and unsaturated polyester mortar (mixture of a quartz foundry sand with the thermoset resin binder). Although both materials experienced a decrease in their mechanical properties when testing temperature was increased, epoxy polymer mortars were more sensitive to temperature changes than unsaturated polyester mortars. This temperature dependency was related to the T_g of the resins used.

In addition to testing temperature, curing and post-curing procedures can also affect the structural performance of an epoxy adhesive, in terms of the value of T_g and the epoxy mechanical properties [21–30]. Michels et al. [21] studied the effect of different curing conditions and mixing processes on mechanical properties of three different epoxy adhesives. Specimens exposed to accelerated curing (consisting in exposing the epoxy specimens to an elevated temperature, 90 °C, for a period of 25 min just after casting) showed higher porosity, which appeared to be the cause of their apparent lower tensile properties. The higher porosity can be attributed to a faster development of strength and stiffness, that finally affects to the cross-linking process, thus showing the influence of the cure-kinetics. Mixing the epoxy under vacuum reduced the porosity of both specimens (with and without accelerated curing) leading to higher tensile properties. Similar results were obtained in Cruz et al. [22]. It has been shown in the literature that longer curing times are needed for lower curing temperatures. This effect, which is of high importance in cold-curing epoxy adhesives, is a consequence of the vitrification of the network that takes place when the resin is cured at a temperature below the ultimate glass transition of the completely cross-linked resin. As a result, the resin is in a glassy but uncured state, so that cross-linking reaction has slowed down dramatically and it may take a long time before the ultimate properties of the adhesives are reached. This dependency was confirmed for cold-curing epoxy adhesives in Lapique and Redford [23] and Moussa et al. [24]. For the case of Lapique and Redford [23], they obtained same mechanical properties with 4 h curing at 64 °C and 28 days curing at room temperature. For the case of Moussa et al. [24], epoxy cured at low temperatures of 5 °C to 10 °C required a 3-days curing period for attaining the full curing, whereas few hours (3.7 h to 1.6 h) were needed for curing temperatures in the range of 35 °C to 60 °C. Lahouar et al [25] investigated the evolution of epoxy T_g under four different curing temperatures (i.e. 20, 50, 82 and 108 °C). According to their results on DSC tests, the T_g increased gradually by increasing the curing temperature. However, this increase in T_g had an upper bound value, as curing beyond 82 °C had no effect on T_g. This upper bound value corresponds to the glass transition temperature of the fully cured network ($T_{g\infty}$), at which the resin reaches its maximum degree of cross-linking. The existence of a T_g upper bound value ($T_{g\infty}$) was also confirmed in a study from Carbas et al. [26], who studied the effect of the curing temperature on the mechanical properties and T_g of three different structural epoxy adhesives. For each adhesive, samples of the bulk adhesive were cured at various temperatures and T_g was measured by a dynamic mechanical analysis using an in-house developed apparatus. It should be mentioned that the main concern of the applied method is related to thermodynamics and the existence of a temperature gradient in the adhesive. Therefore, the speed of the test should be a compromise value that ensures a homogeneous temperature distribution in the specimen and

avoids causing a post-curing in the specimen. Once T_g was determined at various curing temperatures, $T_{g\infty}$ could be determined. In addition to the determination of the $T_{g\infty}$ values for the three adhesives, results of their experimental program confirmed that, as far as the curing temperature was below $T_{g\infty}$, any increase in the curing temperature derived in an increase in the mechanical properties and T_g. On the contrary, for curing temperatures above $T_{g\infty}$, the mechanical properties and T_g decreased. Although these findings are in agreement with [27–29], it should be mentioned that T_g is a kinetic parameter that depends on the heating rate and on the measurement conditions [26]. Experimental work presented in [26] was complemented with a second program presented in Carbas et al. [30], where the effect of post-curing was analyzed. Post-curing process can be of high importance for the case of cold-curing epoxy adhesives. It may be the case that an un-complete cure in the epoxy resin exists because of the longer curing time needed, especially if they are cured at ambient temperature. In this case, the reactivation of the cross-linking process of the epoxy can take place if a post-curing process is applied. In this sense, experimental results presented in [30] showed that the effect of post-curing at temperature below $T_{g\infty}$ depended on whether the cross-linking process was complete or not. Finally, post-curing above $T_{g\infty}$ produced thermal degradation that caused a progressive decrease in mechanical properties and T_g. According to the literature [7,21,23,25,26,31,32], cross-linking plays an important role in the mechanical performance of an epoxy. In this sense, results presented in Michel and Ferrier [7] confirmed that cross-linking of an epoxy resin is found to be an irreversible process, so that larger T_g values are obtained when curing at higher temperatures and its value does not change when the polymer is exposed back to a lower temperature. Similar results were obtained in [21].

This paper presents part of a larger experimental program on the flexural behavior of NSM FRP-strengthened Reinforced Concrete (RC) beams tested at different temperatures. Specifically, the main objective of this paper is the assessment of a commercial structural epoxy adhesive commonly used for RC strengthening and retrofitting with FRP materials. To this end, a comprehensive experimental program was performed to evaluate the influence of the temperature on mechanical properties (namely the uniaxial tensile strength (σ_{tu}), the tensile elastic modulus (E), the uniaxial ultimate compressive load (F_{cu}), the uniaxial compressive strength (σ_{cu})) and T_g of a structural epoxy adhesive. Different curing temperatures, post-curing temperatures and testing temperatures have been considered. The experimental program is described and the main results are presented and discussed.

2. Experimental program

2.1. Material

The adhesive used in this study is a high performance, solvent-free, thixotropic, and grey two-component epoxy adhesive specially developed for bonding Carbon Fiber Reinforced Polymers (CFRP) on concrete, that is traded under the commercial name of *S&P 220 HP*. According to the manufacturer's product data sheet [33], the components A (Bisphenol A and Bisphenol F based resin) and component B (hardener, with a mixture of amines) should be mixed at a ratio of 2:1 by weight, and the suggested curing duration is 7 days. Furthermore, the nominal elastic modulus, compressive strength and T_g of epoxy declared by the manufacturer are 7.1 GPa, 81 MPa and 58.2 °C, respectively. The mixture of epoxy adhesive is shown in Fig. 1.

2.2. Specimens curing process and testing configuration

In this experimental program, 4 groups of specimens were considered. Group 1 comprised those specimens used for determining the effect of curing and post-curing temperature on T_g of the epoxy adhesive. Groups 2, 3 and 4 comprised those specimens used for evaluating the effect of testing temperature (Group 2), curing temperature (Group 3)

Fig. 1. Epoxy adhesive mixture.

and post-curing temperature (Group 4) on mechanical properties of the epoxy adhesive. The specimens were designated as X-Y-Z. In this designation X indicates the testing group, so that TG refers to specimens tested to determine the T_g (i.e. Group 1), TT refers to specimens tested to study the influence of testing temperature on epoxy mechanical properties (i.e. Group 2), CT refers to specimens tested to analyze the influence of curing temperature on epoxy mechanical properties (i.e. Group 3) and PT refers to specimens tested to determine the influence of post-curing temperature on epoxy mechanical properties (i.e. Group 4). In the proposed specimens' designation, Y indicates the curing process

Table 1
Details of the experimental program.

Group	Specimen ID	Number of specimens	Curing process	Curing process temperature (°C)	Test	Testing temperature (°C)
Group 1	TG-C-20	1	See Fig. 2a	20	Glass transition temperature of epoxy	According to standard
	TG-C-50	1		50		
	TG-C-70	1		70		
	TG-PC-50	1		50		
	TG-PC-70	1		70		
Group 2	TT-TEN-20	3	See Fig. 2b	20	Tensile strength and elastic modulus	20
	TT-TEN-40	3		20		40
	TT-TEN-50	3		20		50
	TT*-TEN-50	3		50		50
	TT-TEN-60	3		20		60
	TT-TEN-70	3		20		70
	TT*-TEN-70	3		70		70
	TT-TEN-85	3		20		85
	TT-COM-20	3		20	Compressive strength	20
	TT-COM-40	3		20		40
	TT-COM-50	3		20		50
	TT*-COM-50	3		50		50
	TT-COM-60	3		20		60
	TT-COM-70	3		20		70
	TT*-COM-70	3		70		70
	TT-COM-85	3		20		85
Group 3	CT-TEN-(−15)	3	See Fig. 2c	−15	Tensile strength and elastic modulus	20
	CT-TEN-50	3		50		20
	CT*-TEN-50[1]	3		50		20
	CT-TEN-70	3		70		20
	CT*-TEN-70[2]	3		70		20
	CT-COM-(−15)	3		−15	Compressive strength	20
	CT-COM-50	3		50		20
	CT*-COM-50[1]	3		50		20
	CT-COM-70	3		70		20
	CT*-COM-70[2]	3		70		20
Group 4	PT-TEN-40	3	See Fig. 2d	40	Tensile strength and elastic modulus	20
	PT-TEN-50	3		50		20
	PT-TEN-60	3		60		20
	PT-TEN-70	3		70		20
	PT-TEN-85	3		85		20
	PT-COM-40	3		40	Compressive strength	20
	PT-COM-50	3		50		20
	PT-COM-60	3		60		20
	PT-COM-70	3		70		20
	PT-COM-85	3		85		20

[1] Curing at 50 °C for 7 days and later exposed to a one-day post-curing at 50 °C.
[2] Curing at 70 °C for 7 days and later exposed to a one-day post-curing at 70 °C.

type (C for curing and PC for post-curing) for specimens of Group 1 and refers to mechanical test type (TEN for tension test and COM for compression test) for specimens of Groups 2–4. Finally, Z denotes the temperature. For example, TG-C-50, refers to a specimen that was cured at 50 °C and tested in order to determine the value of T_g (Group 1). Similarly, PT-TEN-70 refers to a specimen that was post-cured at 70 °C and tested in order to analyze the effect of post-curing temperature (Group 4) on tensile properties of the epoxy adhesive. It should be mentioned that the asterisk symbol appearing in some specimens' designation shows one extra day of post-curing. All specimens were tested at the age of 12 days. Curing and post-curing periods with target temperature different from 20 °C lasted 7 days and 1 day, respectively. Details on the curing process and testing configuration of each group are presented below and summarized in Table 1:

● *Group 1:* effect of curing and post-curing temperature on T_g

This group includes a total of 5 specimens, whose curing and post-curing temperatures varied with the aim at analyzing its effect on the T_g of the epoxy adhesive. One specimen was cured at room temperature (20 °C) for 12 days as a reference sample (TG-C-20) (see black line in Fig. 2a. Two other specimens were cured for 7 days under the target temperature (50 °C and 70 °C) to be later left 5 more days at 20 °C before testing the T_g (TG-C-50 and TG-C-70) (see blue line in Fig. 2a. To conclude, two specimens were initially cured for 9 days at 20 °C, after which a post-curing process of one-day under the target temperature (50 °C and 70 °C) was applied, that was finally followed by a cooling-down process for 2 days at 20 °C prior to T_g testing (TG-PC-50 and TG-PC-70) (see red line in Fig. 2a.

● *Group 2:* effect of testing temperature on mechanical properties

This group includes a total of 48 specimens whose testing temperatures varied to evaluate its effect on epoxy adhesive mechanical properties. The specimens were cured at 20 °C for 11 days (see black line in Fig. 2b. After this curing process, specimens were heated to the target temperature for one-day (20, 40, 50, 60, 70 and 85 °C) to be finally tested under tension and compression. It should be mentioned that the one-day heating process previous to testing should be considered as a one-day post-curing process. Furthermore, two additional configurations (marked with asterisk symbol) were considered where an additional one-day post-curing at the target temperature (50 and 70 °C) was applied (see red line in Fig. 2b.

● *Group 3:* effect of curing temperature on mechanical properties

This group includes a total of 30 specimens whose curing temperature varied with the aim at evaluating its effects on epoxy adhesive mechanical properties. Immediately after being cast, specimens were moved to the chamber to be cured at different target temperatures (-15, 50 and 70 °C) for a period of 7 days. After this curing phase, specimens were left at 20 °C for 5 days before testing (see black line in Fig. 2c. As in previous group, two additional configurations (marked with asterisk symbol) were exposed to a one-day post-curing at target temperature (50 and 70 °C) and cooled-down again at 20 °C (see red line in Fig. 2c.

● *Group 4:* effect of post-curing temperature on mechanical properties

This group includes a total of 30 specimens that were post-cured at different temperatures to evaluate its effect on epoxy adhesive mechanical properties. In this last group, the specimens were cured at 20 °C for 9 days, to be later exposed to a one-day post-curing at different target temperatures (40, 50, 60, 70 and 85 °C) and a final cooling-down at 20 °C before testing (see Fig. 2d.

2.3. Test procedures

2.3.1. Differential scanning calorimetry test

The differential scanning calorimetry (DSC) technique [34] was used to calculate the T_g of the epoxy adhesive after different curing and post-curing conditions (Group 1 of the experimental campaign). For each curing condition, one specimen was tested. The DSC technique provides information about changes in physical, chemical, and heat capacity of the adhesive which may lead to important information about their
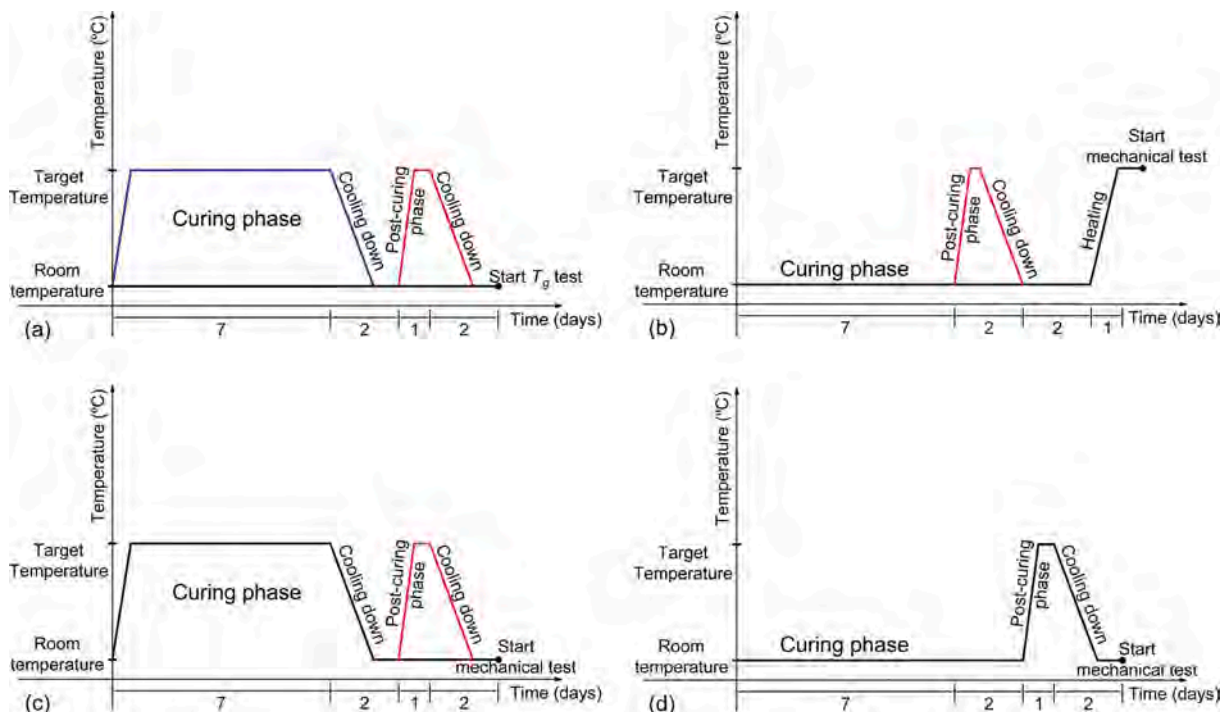

Fig. 2. Diagram of the curing processes. (a) Group 1; (b) Group 2; (c) Group 3; and (d) Group 4.

thermal history (i.e. the temperature that epoxy undergoes), stability, processing conditions, progress of chemical reactions and possible changes in mechanical properties [34]. The dynamic DSC tests were carried out using the DSC Q2000 machine. A heating rate of 10 °C/min was applied using nitrogen as the purge gas at 50 mL/min. The temperature range was between 20 and 80 °C. To determine T_g, and according to ASTM E1356-08 [34], the extrapolated onset temperature (T_f) and the extrapolated end temperature (T_e) were measured. The midpoint temperature (T_m), computed as the mean between T_f and T_e, is the most commonly used as the glass transition temperature [34].

2.3.1.1. Tension test. Tensile properties of the epoxy adhesive were determined following ISO-527–1 [35] specifications. To this end, dog-bone specimens were manufactured following the geometry and dimensions shown in Fig. 3a and tested under displacement-control at a speed of 1 mm/min. For each curing condition, three specimens were tested. The test setup is shown in Fig. 3b. As mentioned in section 2.2, specimens of Group 2 were heated to the target testing temperature for a duration of 24 h prior to testing and, once temperature was stabilized, the test was performed. To allow the curing process, a thermal chamber was mounted on the testing machine (see Fig. 3b). Two strain gauges located at the back and front sides of the specimens and one axial extensometer with a 25 mm gauge length were used to measure the strain during the tension tests. Furthermore, two thermocouples (one to measure the environmental temperature inside the thermal chamber and the other glued on the surface of specimen) were used to measure the temperature before and during the test. In each specimen, registers of loads were transformed to stresses by using the mean cross-section area from three different measurements. The tensile elastic modulus was obtained from the slope of axial stress–strain curve between 0.05% and 0.25% of the maximum tensile strain [35]. Details of the specimens and test setup are shown in Fig. 3.

2.3.1.2. Compression test. The compressive strength of the epoxy adhesive was determined according to EN 196-1 [36], with the aim at following the same standard used by the epoxy manufacturer. According to EN 196–1 [36], 80 mm length prism having a 40x40 mm² cross-section should be used for determining the epoxy compressive strength (see Fig. 4a and 4b. During the compression test, the load should be increased smoothly, under force-control, at a ratio of 2400 ± 200 N/s until fracture. Similar to tension tests, also for compression specimens, three specimens were considered for each curing condition. The test setup is shown in Fig. 4c. Two centralized steel plates, with dimensions of 40x40 mm², were placed at the top and the bottom of the specimen to transfer the load. Moreover, a spherical hinge was located at one loading side to avoid the effect of any possible eccentricity during loading. Similar to tension tests, a thermal chamber was mounted on the testing machine for the curing process (see Fig. 4c. One strain gauge was installed to measure the evolution of specimen's longitudinal strain. However, data obtained from the strain gauge were not reliable due to the earlier detachment and peeling in the surface that took place during the loading. Therefore, only the ultimate compressive strength of specimens was finally evaluated. Similar to tension tests, two thermocouples (one to measure the environmental temperature and the other glued on the surface of the specimen) were used to record the temperature before and during the test. The ultimate compressive strength of epoxy was calculated by dividing the ultimate load by initial contacted surface area. Due to possible unavoidable variations in dimensions of the specimens, measurements of the area were taken for each specimen prior to testing. Details of the specimen and test setup are shown in Fig. 4.
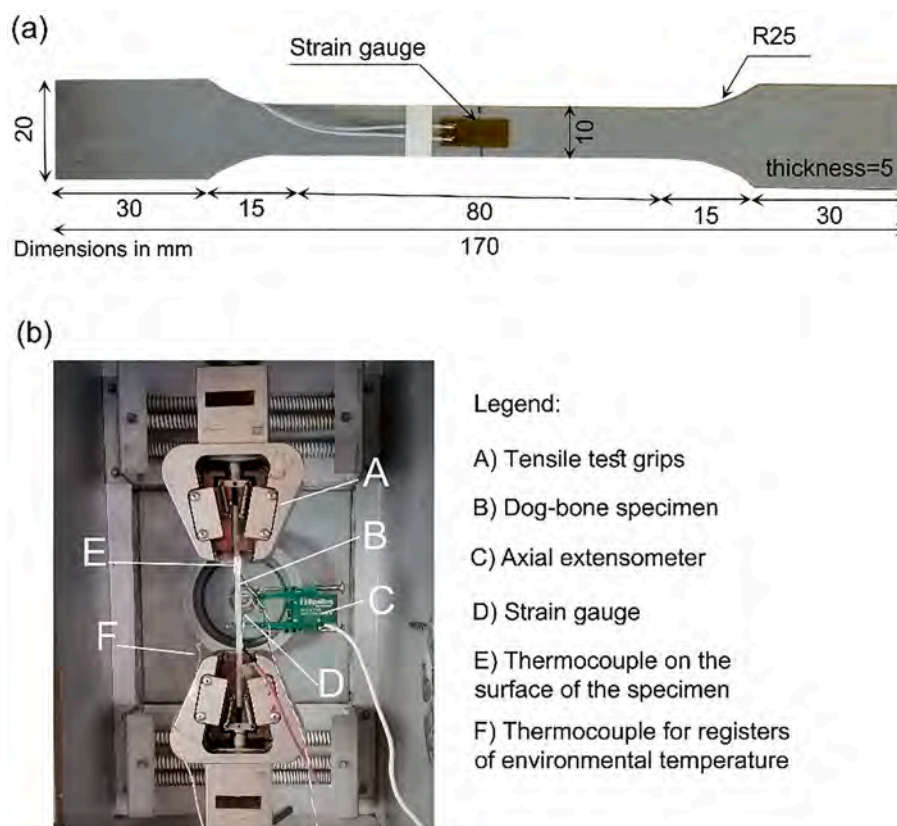
Fig. 3. Details of the tension test. (a) specimen dimensions; (b) Test setup inside the thermal chamber.
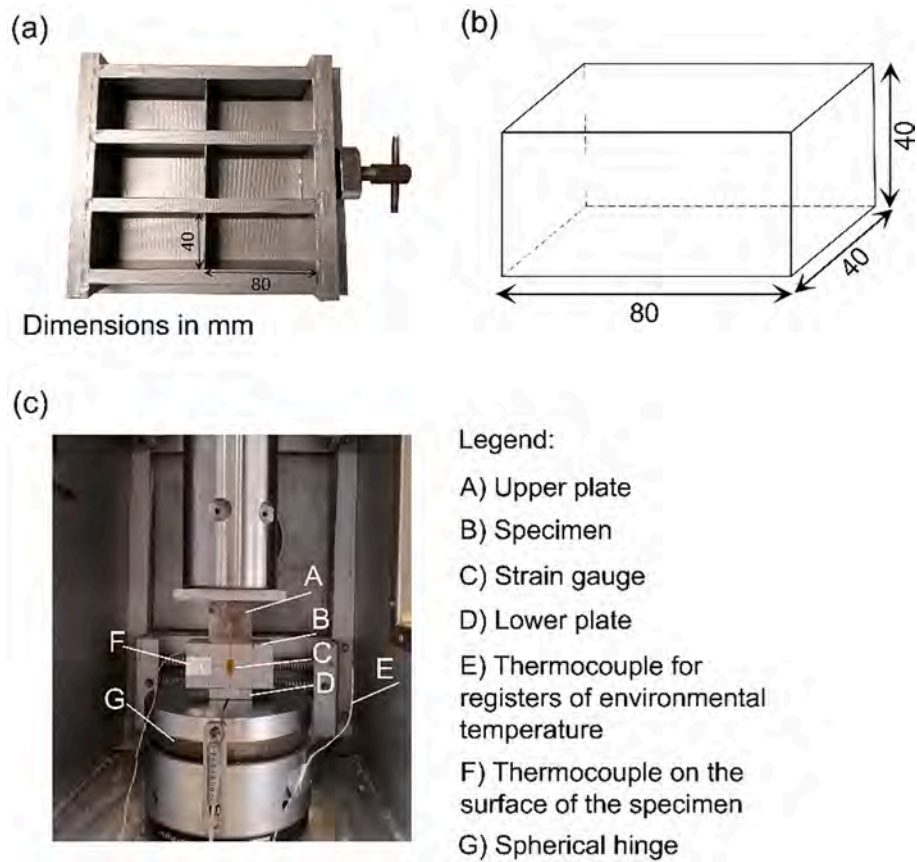
Fig. 4. Details of the compression test. (a) Typical mould; (b) specimen dimensions; and (c) Test setup inside the thermal chamber.

3. Results and discussions

3.1. Effect of curing and post-curing temperature on T_g

Results of the DSC tests performed on specimens of Group 1 are presented in Fig. 5a in the form of curves showing the variation of the heat flow versus temperature. It is acknowledged that the change of the heat flow versus temperature curve is related to an absorption of energy and can, therefore, be an indicator of a possible change in the physical state of the resin. Considering that the T_g is defined as the temperature at which the physical state of the resin changes from the glassy state into the rubbery state, it has been accepted that T_g is in the range of the temperatures limiting the change in the baseline of the curve. It should

be mentioned that in some of the curves presented in Fig. 5a, an enthalpy relaxation peak can be observed immediately after the T_g range. This is an indication that physical aging has occurred [37]. It is worth noting that physical aging occurs in an amorphous polymer held below its T_g.

Table 2
Experimental values of T_g from DSC tests.

Specimens ID	TG-C-20	TG-C-50	TG-C-70	TG-PC-50	TG-PC-70
T_g (°C)	54.9	59.4	47.1	63.5	49.6
Difference with T_g at 20 °C (%)	–	8	−14	16	−10

Fig. 5. (a) Results from DSC tests (b) Evolution of T_g as a function of the curing and post-curing temperatures.

According to experimental results presented in Table 2, the T_g value of the epoxy cured at room temperature (specimen TG-C-20) was 54.9 °C. Based on this, two different behaviors can be observed in Fig. 5a: curing or post-curing the specimens at a temperature below epoxy T_g (i.e. specimens cured (and post-cured) at 50 °C of the present experimental program) resulted in a shift to the right of the peak in the heat flow versus temperature curve; contrarily, curing or post-curing the specimens at a temperature beyond epoxy T_g (i.e. specimens cured (and post-cured) at 70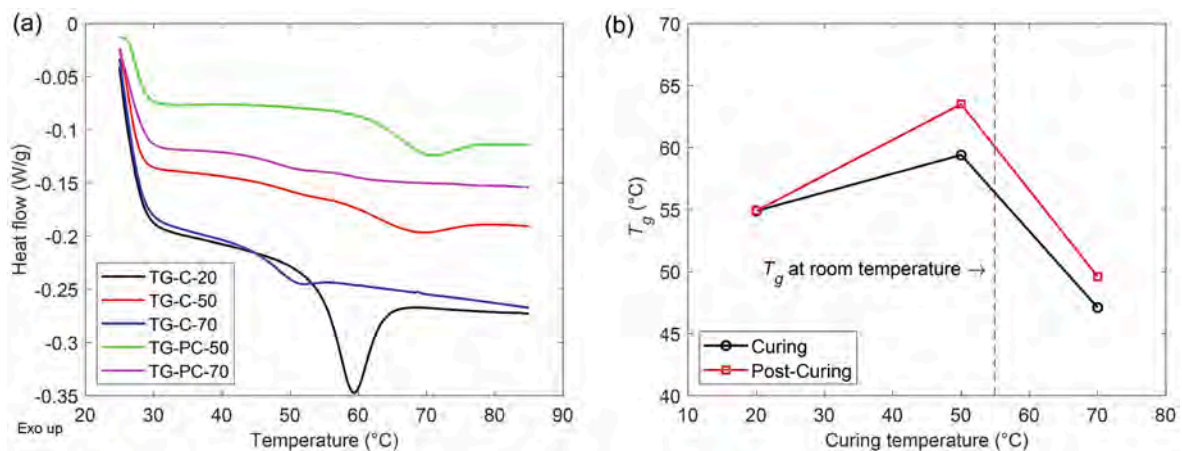 °C of the present experimental program) resulted in a shift to the left of the peak in the heat flow versus temperature curve. This shifts to the right and left are therefore indicating an increase and reduction of the T_g value, respectively. These two different trends can also be observed in Fig. 5b, where the dashed line represents the T_g value of the specimen cured at room temperature (TG-C-20), and the black and red solid lines represent the evolution of T_g for specimens that were cured and post-cured, respectively. When curing or post-curing of an adhesive takes place at a temperature below $T_{g\infty}$, T_g increases as the curing temperature increases. On the contrary, when curing or post-curing of an adhesive takes place at a temperature above $T_{g\infty}$, T_g decreases as the curing temperature increases [24,26,28]. This change in epoxy T_g is due to possible variations in the degree of cross-linking (i.e. possible thermal degradation or oxidative cross-linking) in the epoxy adhesive [7,12,30–32]. Based on this, and according to experimental results, for the epoxy adhesive studied in this paper, the curing temperature that leads to the fully cured network ($T_{g\infty}$) should be between 50 °C and 70 °C. Table 2 summarizes the experimental values of the T_g and its percentages of variation with respect to reference specimen (specimen TG-C-20).

3.2. Effect of testing temperature on mechanical properties

In this section, results from tension and compression tests on specimens of Group 2 are presented and analyzed to study the effect of testing temperature on mechanical properties of the epoxy adhesive.

Regarding to the tension tests, Fig. 6a shows the axial tensile stress versus strain curves, for one representative specimen of each testing temperature. From Fig. 6a it can be observed that specimen tested at room temperature (TT-TEN-20) showed an almost perfect linear behavior up to failure. With the application of higher testing temperature (but still below T_g), the initial linear behavior was followed by a non-linear one before specimen's failure. Lately, when testing temperature was beyond T_g, the stress–strain curves became highly non-linear and properties were greatly affected, as a result of the rubbery behavior of the epoxy. Same behavior was observed in [9–13].

Experimental results in terms of tensile strength and elastic modulus are presented in Table 3 and Fig. 6b. It can be observed that, the increase of the testing temperature was followed by a monotonic decrease in tensile strength and elastic modulus, with the most remarkable reduction taking place when testing temperature changed from 50 °C to 60 °C (epoxy T_g being within this range of temperatures). From this testing temperature on, the elastic modulus was almost negligible. These results are in agreement with previous studies on cold-curing epoxy adhesives [9,20].

According to the test matrix (Table 1, two additional configurations were considered whose curing included a one-day post-curing (specimens TT*-TEN-50 and TT*-TEN-70 in Table 1 and red line in Fig. 1b. As mentioned before, the process of heating prior to testing should be considered as a post-curing and therefore, in specimens TT*-TEN-50 and TT*-TEN-70 two cycles of post-curing were applied. According to the experimental results, no significant effect of an extra cycle of post-curing was observed in the tensile strength and elastic modulus of the epoxy resin (see Fig. 7 and Table 3. This might be a sign of the resin achieving a stable situation after the first post-curing, so that no additional evolution of the mechanical properties was possible. A representative typical failure mode under tension test (rupture near to the mid-section of the specimens) is shown in Fig. 8a.

In addition to tensile properties, behavior under compression was also evaluated under different testing temperatures. Fig. 9a shows the compressive load versus deflection curves for one representative specimen of each testing temperature. Although one strain gauge was installed in every specimen, the peeling of specimen external surface invalidated the registered data. Therefore, deflections presented in Fig. 9a correspond to the movement between grips of testing machine. In general, as observed in tension tests, the increase in the testing temperature was followed by a more flexible response and a decrease of the

Table 3

Tensile strength and elastic modulus for specimens tested at different temperatures (average ± standard deviation).

Specimens ID	Tensile strength, σ_{tu} (MPa)	$\sigma_{tu}/\sigma_{tu\_20}$ [1]	Elastic modulus, E (MPa)	$E / E_{\_20}$ [1]
TT-TEN-20	28.0 ± 0.1	–	8102.4 ± 67.0	–
TT-TEN-40	23.0 ± 0.2	0.82	5520.8 ± 179.0	0.68
TT-TEN-50	19.6 ± 0.7	0.70	4289.6 ± 100.7	0.53
TT*-TEN-50	19.7 ± 0.3	0.70	4128.7 ± 0.1	0.51
TT-TEN-60	6.9 ± 0.2	0.25	673.2 ± 24.5	0.08
TT-TEN-70	2.7 ± 0.1	0.10	271.5 ± 12.9	0.03
TT*-TEN-70	2.8 ± 0.0	0.10	273.9 ± 2.1	0.03
TT-TEN-85	1.9 ± 0.0	0.07	247.5 ± 1.8	0.03

[1] Defined as the ratio between the property value under the specific curing process and the reference property value (i.e. TT-TEN-20 tested at 20 °C)

Fig. 6. Effect of testing temperature on tensile mechanical properties of the epoxy resin. (a) Representative stress–strain curves; (b) Evolution of tensile strength and elastic modulus.

Fig. 7. Effect of additional post-curing on tensile mechanical properties of specimens in Group 2. (a) Representative stress–strain curves; (b) Evolution of tensile strength and elastic modulus.
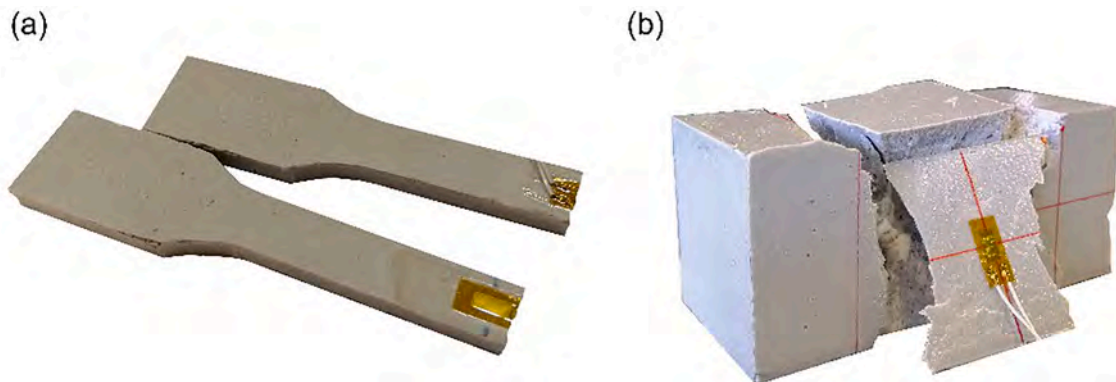
Fig. 8. Typical failure modes (a) Tension test; (b) Compression test.
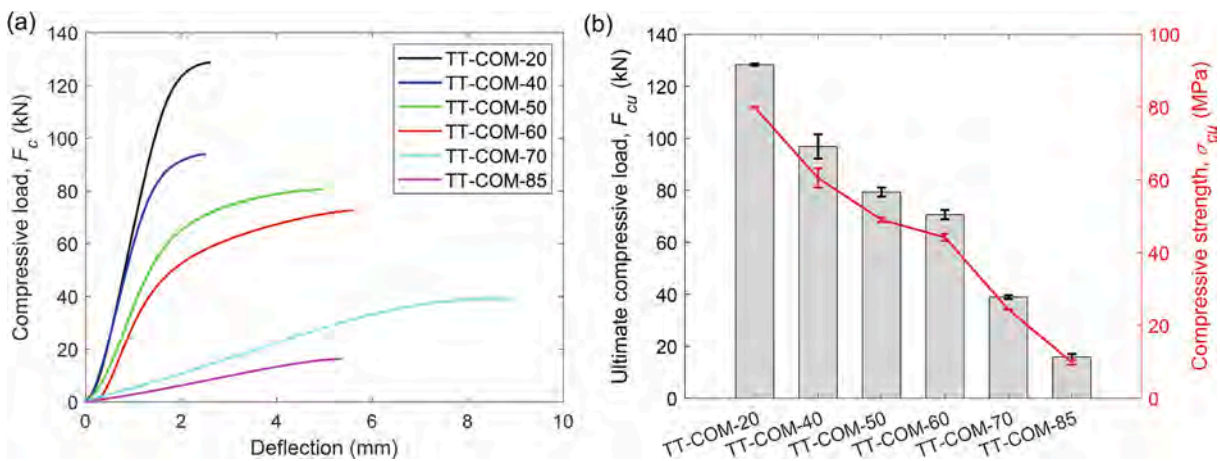
Fig. 9. Effect of testing temperature on compressive mechanical properties of the epoxy resin. (a) Representative load–deflection curves; (b) Compressive strength and ultimate compressive load.

ultimate compressive load.

Averaging the experimental value of ultimate compressive load over the initial area of contact allowed determining the compressive strength of each specimen. Experimental results of compressive properties (ultimate compressive load and compressive strength) are presented in Table 4 and Fig. 9b. According to these results, compressive strength was almost halved for testing temperatures equal to 60 °C, and the reduction

rate highly increased beyond 60 °C.

With the aim at analyzing the possible effect of the inclusion of an extra cycle of post-curing phase in the curing process of the specimens, and similar to what was done for tension tests, two additional configurations were considered (specimens TT*-COM-50 and TT*-COM-70 in Table 1 and red line in Fig. 1b. According to experimental results presented in Table 4 and Fig. 10, the extra cycle of post-curing resulted in a

Table 4

Ultimate compressive load and compressive strength for specimens tested at different temperatures (average ± standard deviation).

Specimens ID	Ultimate compressive load, F_{cu} (kN)	F_{cu} /F_{cu_20} [1]	Ultimate compressive strength, σ_{cu} (MPa)	σ_{cu} /σ_{cu_20} [1]
TT-COM-20	128.4 ± 0.4	–	79.9 ± 0.1	–
TT-COM-40	96.9 ± 4.7	0.75	60.5 ± 2.6	0.76
TT-COM-50	79.3 ± 1.7	0.62	49.0 ± 0.6	0.61
TT*-COM-50	82.2 ± 0.7	0.64	51.8 ± 0.5	0.65
TT-COM-60	70.6 ± 1.8	0.55	44.2 ± 1.0	0.55
TT-COM-70	38.9 ± 0.7	0.30	24.4 ± 0.1	0.31
TT*-COM-70	36.1 ± 1.6	0.28	22.4 ± 0.7	0.28
TT-COM-85	15.9 ± 1.2	0.12	9.9 ± 0.7	0.12

[1]Defined as the ratio between the property value under the specific curing process and the reference property value (i.e. TT-COM-20 tested at 20 °C)
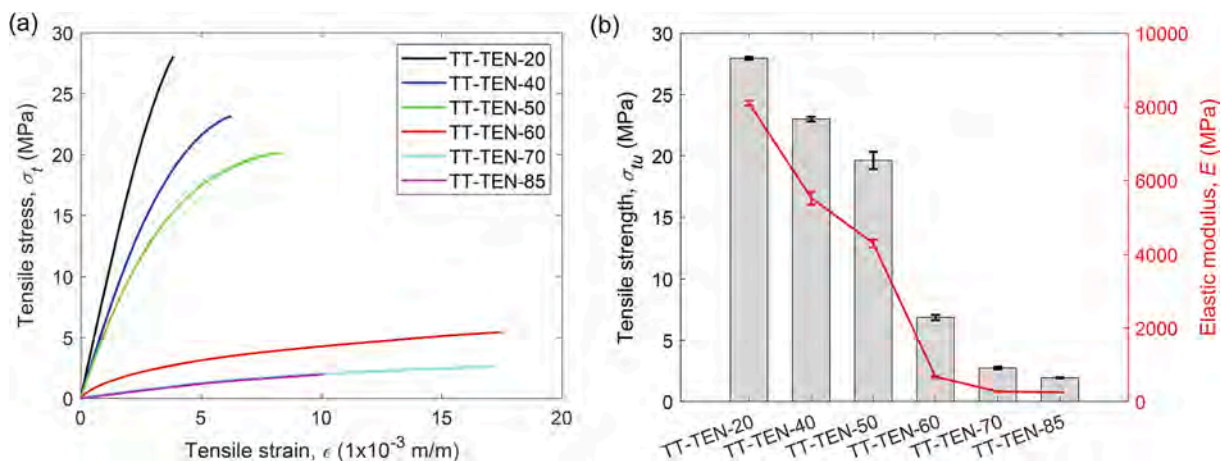

Fig. 10. Effect of additional post-curing on compressive mechanical properties of specimens in Group 2.

small variation in the ultimate compressive load and compressive strength, which can be attributed to typical scatter in experimental results.

A representative typical failure mode of the compressive specimens is shown in Fig. 8b.

3.3. Effect of curing temperature on mechanical properties

With the aim at analyzing the effect of curing temperature on the mechanical properties of the epoxy resin, results on specimens of Group 3 are presented and discussed in this section.

Experimental results in terms of tensile strength and elastic modulus of epoxy cured at different temperatures are presented in Fig. 11 and Table 5, and compared to results on specimens TT-TEN-20, belonging to Group 2, which were cured and tested at 20 °C. From this comparison it can be observed that curing the specimens at −15 °C (CT-TEN-(−15)) had no significant effect on epoxy tensile strength and had some detrimental effects on the elastic modulus. The application of −15 °C during curing, in fact, postponed the initiation of curing, as 7 days after being casted, epoxy resin was still soft. Same observations were reported in [7,38]. These observations suggest that, due to cold temperature postponing the initiation of curing, suitable considerations should be taken into account in the cold weather regions to facilitate the adhesive curing process.

According to experimental results on tensile strength and elastic modulus, the increase of curing temperature below $T_{g\infty}$ promotes the increase of cross-linking, which results in the increase of the performance of the adhesive (specimen CT-TEN-50). On the contrary, curing at temperatures above $T_{g\infty}$ possibly produces thermal degradation on the adhesive, which results in a decrease of its mechanical properties (specimen CT-TEN-70). These results confirm that mechanical properties and the T_g properties have similar behaviors.

In addition to previous specimens, two more configurations were also tested whose curing process was followed by a one-day post-curing (specimens CT*-TEN-50 and CT*-TEN-70). Experimental results on tension tests presented in Table 5 and Fig. 12 revealed that the post-curing process did not highly affect the mechanical properties of the

Table 5

Tensile strength and elastic modulus for specimens cured at different temperatures (average ± standard deviation).

Specimens ID	Tensile strength, σ_{tu} (MPa)	σ_{tu} /σ_{tu_20} [1]	Elastic modulus, E (MPa)	E / $E_{\_20}$ [1]
CT-TEN-(−15)	27.7 ± 0.7	0.99	7601.9 ± 56.3	0.94
TT-TEN-20	28.0 ± 0.1	–	8102.4 ± 67.0	–
CT-TEN-50	31.5 ± 1.0	1.13	7992.0 ± 372.8	0.99
CT*-TEN-50	29.8 ± 0.1	1.06	7124.9 ± 516.1	0.88
CT-TEN-70	30.3 ± 1.1	1.08	6892.5 ± 176.4	0.85
CT*-TEN-70	29.0 ± 2.2	1.04	6808.0 ± 60.2	0.84

[1]Defined as the ratio between the property value under the specific curing process and the reference property value (i.e. TT-TEN-20 tested at 20 °C)

Fig. 11. Effect of curing temperature on tensile mechanical properties of the epoxy resin. (a) Representative stress–strain curves; (b) Evolution of tensile strength and elastic modulus.
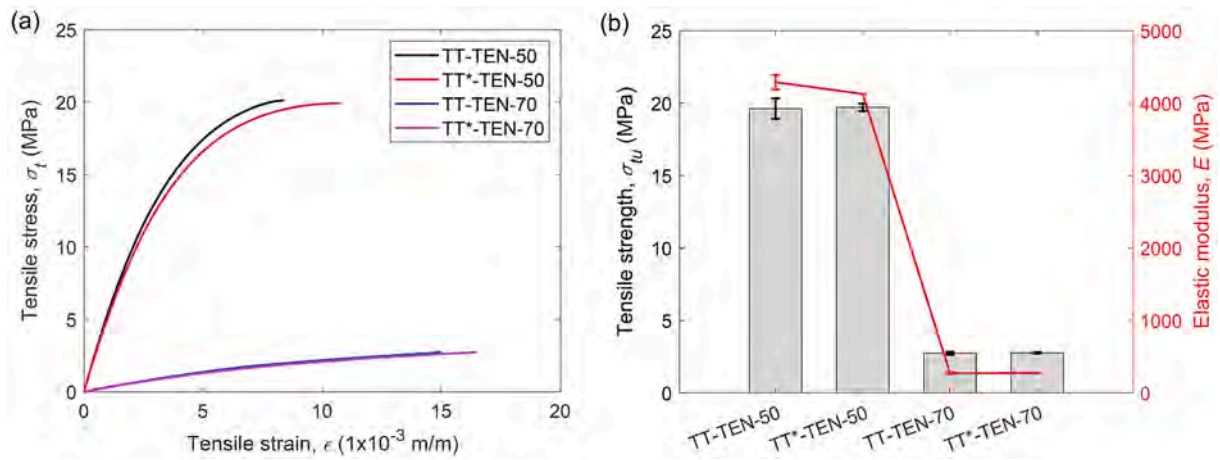
Fig. 12. Effect of additional post-curing on tensile mechanical properties of specimens in Group 3. (a) Representative stress–strain curves; (b) Evolution of tensile strength and elastic modulus.
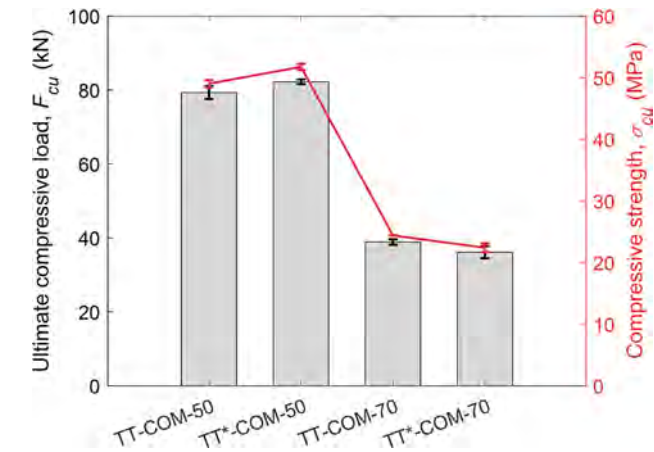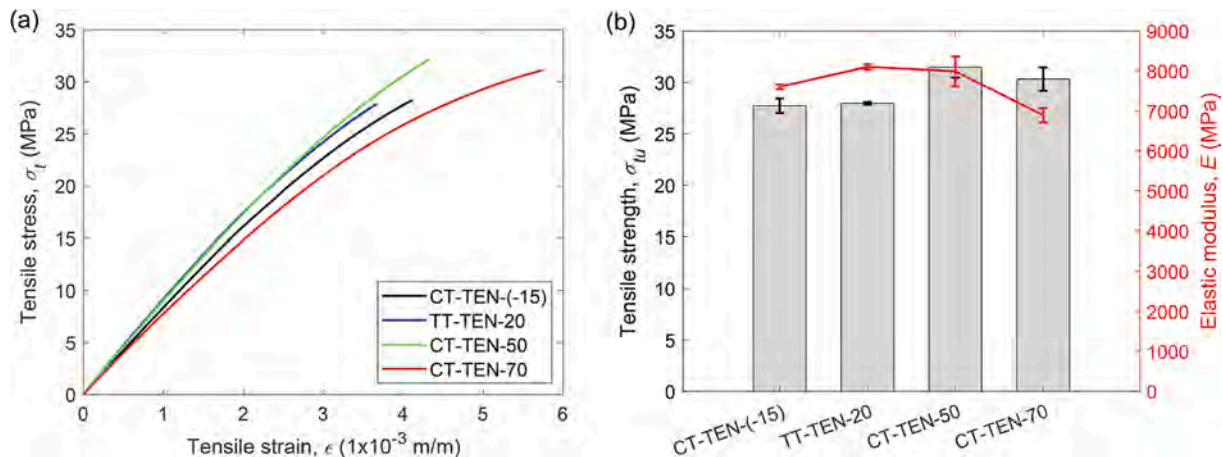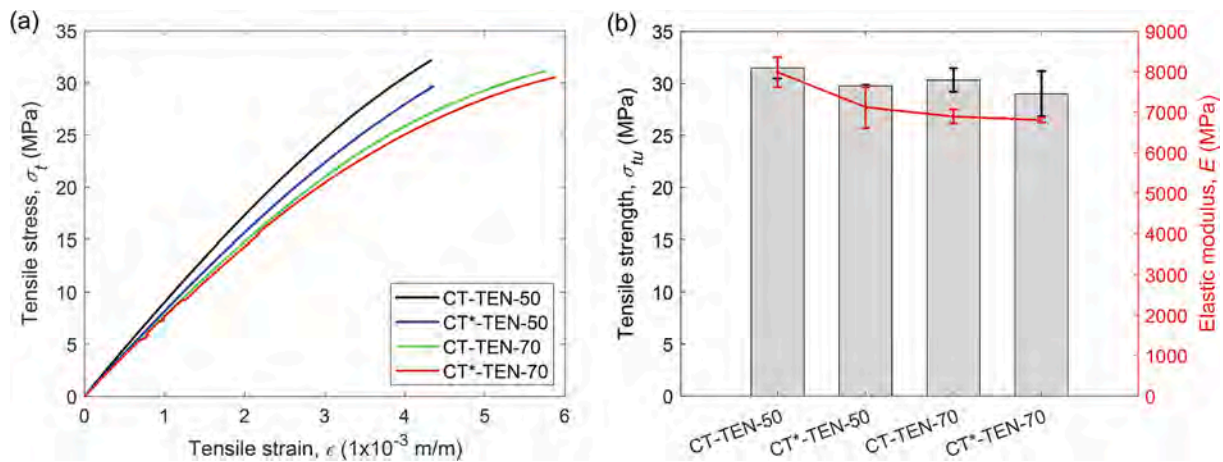
adhesive used in this experimental program. It should be mentioned that a large scatter in experimental results on elastic modulus can be observed for the specimen with an additional post-curing (specimens CT*-TEN-50 and CT*-TEN-70). These results, along with experimental results on specimens of Group 2 having an additional post-curing process (TT*-TEN-50 and TT*-TEN-70), indicate that the application of a post-curing process at a temperature equal to that of the curing process produces no evolution in mechanical properties, because of the stability in the epoxy resin.

Compression tests were also performed to study the possible influence of curing temperature on the compressive mechanical properties of the epoxy resin. Results of these tests are presented in Table 6 and Fig. 13a. The increase in the curing temperature to values below epoxy T_g (i.e. up to 50 °C of the present experimental program) resulted in a monotonic increase of epoxy ultimate compressive load and compressive strength. On the other hand, when curing temperature was beyond epoxy T_g (i.e. 70 °C), a decrease in the compressive mechanical properties was observed. Besides, and according to results on additional specimens with one-day post-curing (specimens CT*-COM-50 and CT*-COM-70), no significant differences were observed between compressive mechanical properties of specimens with and without the post-curing process (see Fig. 13b.

3.4. Effect of post-curing temperature on mechanical properties

In this section, results on mechanical properties of specimens of Group 4 are presented and discussed, with the aim at analyzing the effect of a post-curing process at different temperatures (ranging from 20 °C to 85 °C) on mechanical properties of specimens that were previously

cured at room temperature (i.e. 20 °C). Therefore, specimens TT-TEN-20 and TT-COM-20, from Group 2, are considered as the reference ones.

Experimental results on tensile properties of specimens in Group 4 are presented in Fig. 14 and Table 7, where the mean value and standard deviation are also included. As highlighted in the literature [12,29,30,39], epoxy adhesives cured at ambient temperature may suffer from a not complete cross-linking, that can be reactivated with a post-curing process. This was confirmed by experimental results of Group 4, as tensile strength monotonically increased with the increase in the post-curing temperature, and elastic modulus tended to a constant value. However, for post-curing temperatures larger than 60 °C, an abrupt decay in tensile strength and a more sharped reduction on elastic modulus were observed in specimens post-cured at 70 °C, thus indicating that $T_{g\infty}$ of the adhesive might be in the range of 60 °C to 70 °C. Finally, results on elastic modulus for specimens post-cured at 85 °C continued their downward trend, whilst a groundless increase in tensile strength was observed.

The effect of post-curing on compressive mechanical properties of the epoxy adhesive is shown in Fig. 15 and Table 8. From Fig. 15 it can be observed that the increase in the post-curing temperature from 20 °C to 40 °C resulted in an increase in the ultimate compressive load and compressive strength. On the other hand, for post-curing temperatures beyond 40 °C, a decrease in the compressive mechanical properties took place, with no meaningful changes and results falling within the same range of reference specimen (TT-COM-20).

4. Conclusion

In the present work, a comprehensive experimental program was performed to evaluate the effect of temperature (i.e. testing temperature, curing temperature and post-curing temperature) on the mechanical properties and the T_g of an epoxy adhesive.

From the analysis of the effect of temperature on the measured T_g of the epoxy adhesive (specimens in Group 1), it can be concluded that curing and post-curing temperature affected T_g differently depending whether the applied temperature was below or beyond the epoxy $T_{g\infty}$.

From the analysis of the effect of testing temperature on mechanical properties of the epoxy adhesive (specimens in Group 2), the following conclusions can be drawn:

- The falling trend in tensile mechanical properties experienced the largest decrease when testing temperature exceeded the T_g of the epoxy adhesive. Besides, for testing temperatures beyond 60° C, due to complete rubbery state of the epoxy, the elastic modulus was

Table 6
Ultimate compressive load and compressive strength for specimens cured at different temperatures (average ± standard deviation).

Specimens ID	Ultimate compressive load, F_{cu} (kN)	F_{cu}/F_{cu_20} [1]	Ultimate compressive strength, σ_{cu} (MPa)	$\sigma_{cu}/\sigma_{cu\_20}$ [1]
CT-COM-(−15)	120.2 ± 2.0	0.94	76.2 ± 1.5	0.95
TT-COM-20	128.4 ± 0.4	–	79.9 ± 0.1	–
CT-COM-50	128.7 ± 6.2	1.00	83.7 ± 3.6	1.05
CT*-COM-50	127.2 ± 5.4	0.99	83.2 ± 3.0	1.04
CT-COM-70	111.8 ± 1.8	0.87	70.7 ± 1.7	0.88
CT*-COM-70	107.9 ± 6.0	0.84	69.7 ± 2.5	0.87

[1] Defined as the ratio between the property value under the specific curing process and the reference property value (i.e. TT-COM-20 tested at 20 °C)
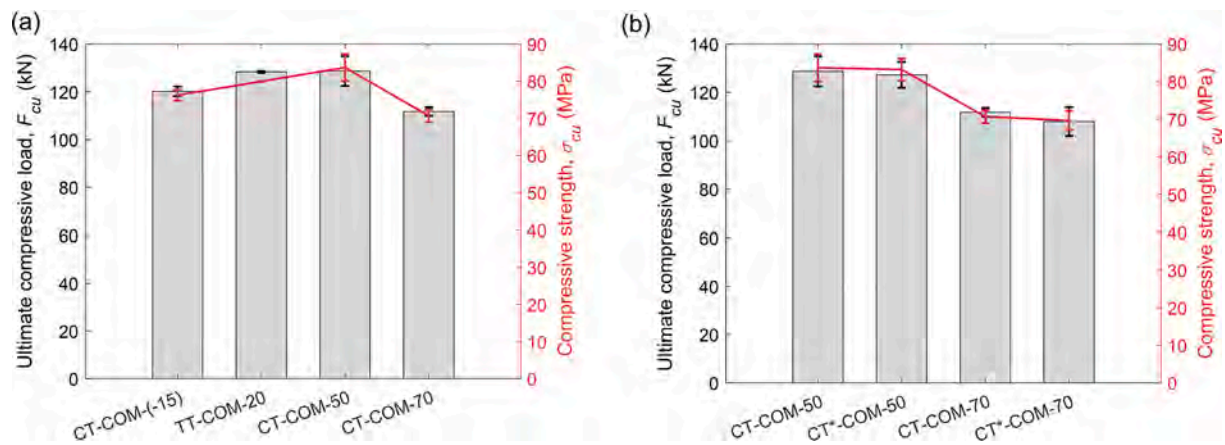
Fig. 13. (a) Effect of curing temperature on compressive mechanical properties of the epoxy resin; (b) Effect of additional post-curing on compressive mechanical properties of specimens in Group 3.
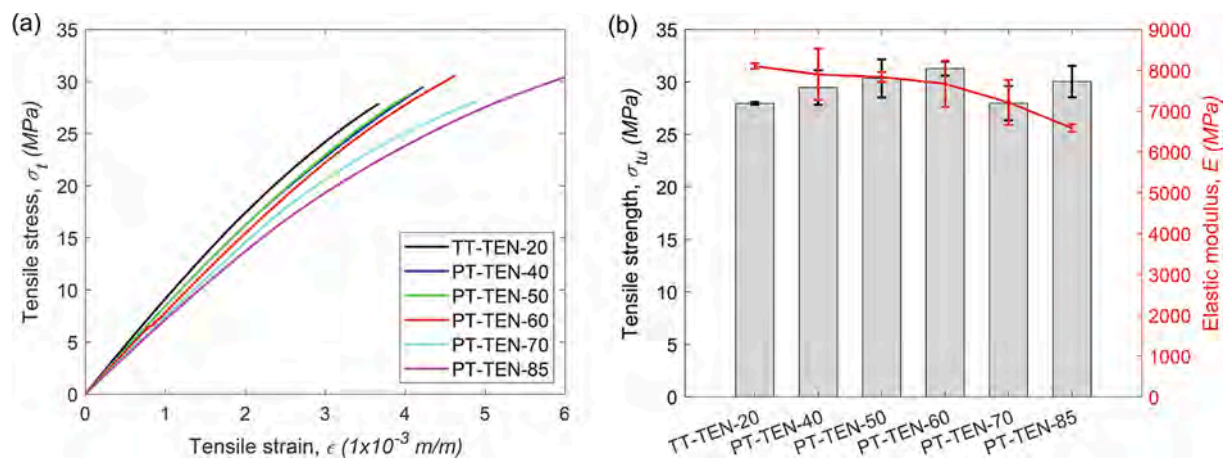

Fig. 14. Effect of post-curing temperature on tensile mechanical properties of the epoxy resin. (a) Representative stress–strain curves; (b) Evolution of tensile strength and elastic modulus.

Table 7
Tensile strength and elastic modulus for specimens post-cured at different temperatures (average ± standard deviation).

Specimens ID	Tensile strength, σ_{tu} (MPa)	$\sigma_{tu}/\sigma_{tu\_20}$ [1]	Elastic modulus, E (MPa)	$E/E_{\_20}$ [1]
TT-TEN-20	28.0 ± 0.1	–	8102.4 ± 67.0	–
PT-TEN-40	29.5 ± 1.6	1.05	7896.9 ± 625.5	0.97
PT-TEN-50	30.3 ± 1.8	1.08	7834.9 ± 119.8	0.97
PT-TEN-60	31.3 ± 0.7	1.12	7668.1 ± 566.6	0.95
PT-TEN-70	28.0 ± 1.6	1.00	7212.0 ± 548.1	0.89
PT-TEN-85	30.0 ± 1.5	1.07	6584.8 ± 95.3	0.81

[1]Defined as the ratio between the property value under the specific curing process and the reference property value (i.e. TT-TEN-20 tested at 20 °C)

almost negligible. For the compression tests, this large reduction took place at the temperature equal 70 °C.

- The inclusion of an extra cycle of post-curing barely affected the mechanical properties of epoxy specimens.

From the analysis of the effect of curing temperature on mechanical properties of the epoxy adhesive (specimens in Group 3), the following conclusions can be drawn:

- Curing temperatures below $T_{g\infty}$ resulted in larger mechanical properties because of the cross-linking promotion. On the other hand, curing temperatures beyond $T_{g\infty}$ produced a possible thermal
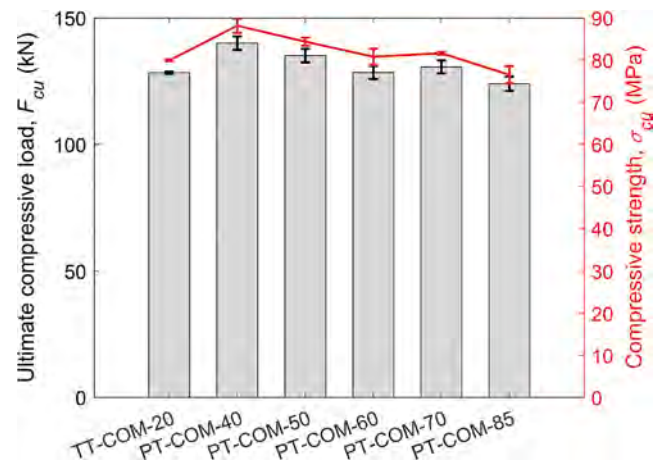

Fig. 15. Effect of post-curing temperature on compressive mechanical properties of the epoxy.

degradation on the adhesive that resulted in a decrease of its mechanical properties.

- No significant effect of an additional post-curing process was observed. This may be due to stabilization of epoxy because of post-curing at the same curing temperature.

Table 8
Ultimate compressive load and compressive strength for specimens post-cured at different temperatures (average $\pm$ standard deviation).

Specimens ID	Ultimate compressive load, F_{cu} (kN)	F_{cu}/F_{cu_20} [1]	Ultimate compressive strength, σ_{cu} (MPa)	$\sigma_{cu}/\sigma_{cu\_20}$ [1]
TT-COM-20	128.4 ± 0.4	–	79.9 ± 0.1	–
PT-COM-40	140.1 ± 2.7	1.09	88.2 ± 1.7	1.10
PT-COM-50	135.1 ± 2.6	1.05	84.2 ± 1.0	1.05
PT-COM-60	128.4 ± 2.6	1.00	80.8 ± 1.9	1.01
PT-COM-70	130.6 ± 2.6	1.02	81.7 ± 0.3	1.02
PT-COM-85	124.0 ± 2.8	0.97	76.5 ± 2.1	0.96

[1]Defined as the ratio between the property value under the specific curing process and the reference property value (i.e. TT-COM-20 tested at 20 °C)

From the analysis of the effect of post-curing temperature on mechanical properties of the epoxy adhesive (specimens in Group 4), the following conclusions can be drawn:

- Post-curing the epoxy at a temperature below the temperature that leads to a fully cured network (near to $T_{g\infty}$) enhanced the mechanical properties because of the reactivation of cross-linking of the non-complete cured epoxy adhesive.
- The largest benefit of post-curing on epoxy compressive strength took place for post-curing temperature equal to 40 °C.

The increase in the mechanical properties of epoxy at curing or post-curing temperatures below or near to the T_g of epoxy can be attributed to the fact that the degrees of cross-linking between the epoxy's molecules has increased, thus having the consequence of an increase in T_g.

CRediT authorship contribution statement

Younes Jahani: Conceptualization, Methodology, Validation, Investigation, Data curation, Writing – original draft. **Marta Baena:** Conceptualization, Validation, Formal analysis, Writing – review & editing, Supervision, Project administration, Funding acquisition. **Cristina Barris:** Formal analysis, Writing – review & editing, Project administration, Funding acquisition. **Ricardo Perera:** Formal analysis, Writing – review & editing, Project administration, Funding acquisition. **Lluís Torres:** Validation, Formal analysis, Writing – review & editing, Supervision.

Declaration of Competing Interest

The authors declare that they have no known competing financial interests or personal relationships that could have appeared to influence the work reported in this paper.

Acknowledgements

References

[1] C. Pellegrino, J.M. Sena-Cruz, Design Procedures for the Use of Composites in Strengthening of Reinforced Concrete Structures: State-of-the-Art Report of the Rilem Technical Committee 234-Duc; Springer: Dordrecht, The Netherlands, 2016, pp. 392. 10.1007/978-94-017-7336-2.

[2] L. De Lorenzis, J.G. Teng, Near-surface mounted FRP reinforcement: An emerging technique for strengthening structures, Compos Part B 38 (2) (2007) 119–143, https://doi.org/10.1016/j.compositesb:2006.08.003.

[3] M. Leone, M.A. Aiello, S. Matthys, Effect of elevated service temperature on bond between FRP EBR systems and concrete, Compos. Part B 40 (2009) 85–93, https://doi.org/10.1016/j.compositesb.2008.06.004.

[4] M. Emara, L. Torres, M. Baena, C. Barris, X. Cahís, Bond response of NSM CFRP strips in concrete under sustained loading and different temperature and humidity conditions, Compos. Struct. 192 (2018) 1–7, https://doi.org/10.1016/j.compstruct.2018.02.048.

[5] L. Gil, J.J. Cruz, M.A. Perez, A pull-shear test for debonding of FRP-laminates for concrete structures, KEM 399 (2009) 141–151, https://doi.org/10.4028/www.scientific.net/KEM.399.141.

[6] S. Wang, T. Stratford, T.P.S. Reynolds, Linear creep of bonded FRP-strengthened metallic structures at warm service temperatures, Constr. Build. Mater. 283 (2021) 122699, https://doi.org/10.1016/j.conbuildmat.2021.122699.

[7] M. Michel, E. Ferrier, Effect of curing temperature conditions on glass transition temperature values of epoxy polymer used for wet lay-up applications, Constr. Build. Mater. 231 (2020) 117206, https://doi.org/10.1016/j.conbuildmat.2019.117206.

[8] E.A.S. Marques, L.F.M. Da Silva, M.D. Banea, R.J.C. Carbas, Adhesive joints for low-and high-temperature use: an overview, J. Adhes. 91 (7) (2015) 556–585, https://doi.org/10.1080/00218464.2014.943395.

[9] J.P. Firmo, M.G. Roquette, J.R. Correia, A.S. Azevedo, Influence of elevated temperatures on epoxy adhesive used in CFRP strengthening systems for civil engineering applications, Int. J. Adhes. Adhes. 93 (2019) 102333, https://doi.org/10.1016/j.ijadhadh.2019.01.027.

[10] M.D. Banea, L.F.M. Da Silva, R.D.S.G. Campilho, Effect of temperature on tensile strength and mode I fracture toughness of a high temperature epoxy adhesive, J. Adhes. Sci. Technol. 26 (7) (2012) 939–953, https://doi.org/10.1163/156856111X593649.

[11] M.D. Banea, F.S.M. De Sousa, L.F.M. Da Silva, R.D.S.G. Campilho, A.M. Bastos de Pereira, Effects of temperature and loading rate on the mechanical properties of a high temperature epoxy adhesive, J. Adhes. Sci. Technol. 25 (18) (2011) 2461–2474, https://doi.org/10.1163/016942411X580144.

[12] C.S. Wu, Influence of post-curing and temperature effects on bulk density, glass transition and stress-strain behaviour of imidazole-cured epoxy network, J. Mater. Sci. 27 (11) (1992) 2952–2959, https://doi.org/10.1007/BF01154105.

[13] J.M.L.D. Reis, Effect of temperature on the mechanical properties of polymer mortars, Mater. Res. 15 (4) (2012) 645–649, https://doi.org/10.1590/S1516-14392012005000091.

[14] M. Emara, L. Torres, M. Baena, C. Barris, M. Moawad, Effect of sustained loading and environmental conditions on the creep behavior of an epoxy adhesive for concrete structures strengthened with CFRP laminates, Compos Part B 129 (2017) 88–96, https://doi.org/10.1016/j.compositesb.2017.07.026.

[15] Y. Jahani, M. Baena, J. Gómez, C. Barris, L. Torres, Experimental Study of the Effect of High Service Temperature on the Flexural Performance of Near-Surface Mounted (NSM) Carbon Fiber-Reinforced Polymer (CFRP)-Strengthened Concrete Beams, Polymers 13 (6) (2021) 920, https://doi.org/10.3390/polym13060920.

[16] E.L. Klamer, A.H. Dick, C.J.H. Michael, The influence of temperature on RC beams strengthened with externally bonded CFRP reinforcement, Heron 53 (2008) 157–185.

[17] R. Krzywoń, Behavior of EBR FRP strengthened beams exposed to elevated temperature, Procedia Eng. 193 (2017) 297–304, https://doi.org/10.1016/j.proeng.2017.06.217.

[18] P.M. Silva, G.G. Escusa, J.M. Sena-Cruz, M. Azenha, Experimental investigation of RC slabs strengthened with NSM CFRP system subjected to elevated temperatures up to 80 °C. In Proceedings of the 8th International Conference on Fibre-Reinforced Polymer (FRP) Composites in Civil Engineering, CICE, Hong Kong, China, 14–16 December 2016.

[19] E. Ferrier, O. Rabinovitch, L. Michel, Mechanical behavior of concrete–resin/adhesive–FRP structural assemblies under low and high temperatures, Constr. Build. Mater. 127 (2016) 1017–1028, https://doi.org/10.1016/j.conbuildmat.2015.12.127.

[20] O. Moussa, A.P. Vassilopoulos, J. de Castro, T. Keller, Time–temperature dependence of thermomechanical recovery of cold-curing structural adhesives, Int. J. Adhes. Adhes. 35 (2012) 94–101, https://doi.org/10.1016/j.ijadhadh.2012.02.005.

[21] J. Michels, J.M. Sena-Cruz, R. Christen, C. Czaderski, M. Motavalli, Mechanical performance of cold-curing epoxy adhesives after different mixing and curing procedures, Compos Part B 98 (2016) 434–443, https://doi.org/10.1016/j.compositesb.2016.05.054.

[22] R. Cruz, L. Correia, S. Cabral-Fonseca, J. Sena-Cruz, Effects of the preparation, curing and hygrothermal conditions on the viscoelastic response of a structural epoxy adhesive, Int. J. Adhes. Adhes. 110 (2021) 102961, https://doi.org/10.1016/j.ijadhadh.2021.102961.

[23] F. Lapique, K. Redford, Curing effects on viscosity and mechanical properties of a commercial epoxy resin adhesive, Int. J. Adhes. Adhes. 22 (4) (2002) 337–346, https://doi.org/10.1016/S0143-7496(02)00013-1.

[24] O. Moussa, A.P. Vassilopoulos, T. Keller, Effects of low-temperature curing on physical behavior of cold-curing epoxy adhesives in bridge construction, Int. J. Adhes. Adhes. 32 (2012) 15–22, https://doi.org/10.1016/j.ijadhadh.2011.09.001.

[25] M.A. Lahouar, J.F. Caron, N. Pinoteau, G. Forêt, K. Benzarti, Mechanical behavior of adhesive anchors under high temperature exposure: Experimental investigation, Int. J. Adhes. Adhes. 78 (2017) 200–211, https://doi.org/10.1016/j.ijadhadh.2017.07.004.

[26] R.J.C. Carbas, E.A.S. Marques, L.F.M. Da Silva, A.M. Lopes, Effect of cure temperature on the glass transition temperature and mechanical properties of

epoxy adhesives, J. Adhes. 90 (1) (2014) 104–119, https://doi.org/10.1080/00218464.2013.779559.

[27] R.J. Varley, J.H. Hodgkin, G.P. Simon, Toughening of trifunctional epoxy system. V. Structure–property relationships of neat resin, J. Appl. Polym. Sci. 77 (2) (2000) 237–248, https://doi.org/10.1002/(SICI)1097-4628(20000711)77:2<237::AID-APP1>3.0.CO;2-5.

[28] J.B. Enns, J.K. Gillham, Effect of the extent of cure on the modulus, glass transition, water absorptio, and density of an amine-cured epoxy, J. Appl. Polym. Sci. 28 (9) (1983) 2831–2846, https://doi.org/10.1002/app.1983.070280914.

[29] S. Ziaee, G.R. Palmese, Effects of temperature on cure kinetics and mechanical properties of vinyl–ester resins, J. Polym. Sci., Part B: Polym. Phys. 37 (7) (1999) 725–744, https://doi.org/10.1002/(SICI)1099-0488(19990401)37:7<725::AID-POLB23>3.0.CO;2-E.

[30] R.J.C. Carbas, L.F.M. Da Silva, E.A.S. Marques, A.M. Lopes, Effect of post-cure on the glass transition temperature and mechanical properties of epoxy adhesives, J. Adhes. Sci. Technol. 27 (23) (2013) 2542–2557, https://doi.org/10.1080/01694243.2013.790294.

[31] P. Silva, P. Fernandes, J.M. Sena-Cruz, J. Xavier, F. Castro, D. Soares, V. Carneiro, Effects of different environmental conditions on the mechanical characteristics of a structural epoxy, Compos Part B 88 (2016) 55–63, https://doi.org/10.1016/j.compositesb.2015.10.036.

[32] A. Benedetti, P. Fernandes, J.L. Granja, J.M. Sena-Cruz, M. Azenha, Influence of temperature on the curing of an epoxy adhesive and its influence on bond behaviour of NSM-CFRP systems, Compos Part B 89 (2016) 219–229, https://doi.org/10.1016/j.compositesb.2015.11.034.

[33] S&P. S&P Resin 220 HP Epoxy Adhesive, Technical Data Sheet; S&P: Seewen, Switzerland, 2019.

[34] ASTM E1356-08. Standard Test Method for Assignment of the Glass Transition Temperatures by Differential Scanning Calorimetry; ASTM International: West Conshohocken, PA, USA, 2008.

[35] ISO 527-1. Plastics-Determination of Tensile Properties—Part 1: General Principles; ISO: Geneva, Switzerland, 2012.

[36] EN 196-1. Methods of Testing Cement – Part 1: Determination of Strength.

[37] M. Savvilotidou, A.P. Vassilopoulos, M. Frigione, T. Keller, Effects of aging in dry environment on physical and mechanical properties of a cold-curing structural epoxy adhesive for bridge construction, Constr. Build. Mater. 140 (2017) 552–561, https://doi.org/10.1016/j.conbuildmat.2017.02.063.

[38] O. Moussa, A.P. Vassilopoulos, J. De Castro, T. Keller, Early-age tensile properties of structural epoxy adhesives subjected to low-temperature curing, Int. J. Adhes. Adhes. 35 (2012) 9–16, https://doi.org/10.1016/j.ijadhadh.2012.01.023.

[39] I. Stewart, A. Chambers, T. Gordon, The cohesive mechanical properties of a toughened epoxy adhesive as a function of cure level, Int. J. Adhes. Adhes. 27 (4) (2007) 277–287, https://doi.org/10.1016/j.ijadhadh.2006.05.003.

A.3 Paper C

Time-dependent behavior of NSM CFRP-strengthened RC beams under different service temperatures

Younes Jahani[1], Marta Baena[1*], Alba Codina, Cristina Barris[1] and Lluís Torres[1]

[1]AMADE, Polytechnic School, University of Girona, 17003, Girona, Spain
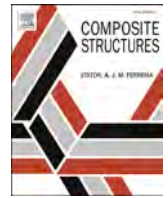
[*]Corresponding author

Time-dependent behavior of NSM CFRP-strengthened RC beams under different service temperatures

Younes Jahani, Marta Baena [*], Alba Codina, Cristina Barris, Lluís Torres

AMADE, Polytechnic School, University of Girona, 17003 Girona, Spain

ABSTRACT

The use of fiber reinforced polymer (FRP) for flexural strengthening of reinforced concrete (RC) beams has become a popular strengthening technique. Significant amount of work is available on the short-term flexural behavior of RC beams strengthened with near-surface mounted (NSM) technique. However, their time-dependent flexural behavior, specifically under high service temperature, has not yet been addressed. This paper presents an experimental work to evaluate the time-dependent behavior of NSM carbon FRP (CFRP)-strengthened RC beams. The experimental program included 23 beams, where the effect of different parameters such as strengthening (CFRP) area, steel reinforcement ratio and applied temperature (20 and 50 °C) have been considered. Experimental results show that the effect of strengthening area is significant on the flexural short-term response of the beams, while minor effects are found on the time-dependent deflections. On the other hand, increasing the service temperature has no significant effect on the short-term tests, but it produces a large increase in the time-dependent deflection of the specimens. Finally, an analytical procedure for the prediction of time-dependent deflections, which is based on the age-adjusted effective modulus method (AEMM), is presented. Good agreement between the experimental results and analytical predictions on time-dependent deflections is shown.

1. Introduction

Strengthening of reinforced concrete (RC) structures may become necessary due to different reasons such as increase in the service loads, design code changes, earthquake activities, deficiencies resulting from environmental effects (e.g. corrosion), changes in the occupancy of buildings, etc. [1,2]. In the last decades, fiber reinforced polymer (FRP) materials have been accepted to be used in two of the principal strengthening techniques for RC elements, namely externally bonding reinforcement (EBR) and near-surface mounted (NSM) systems. In the EBR reinforcing technique, the FRP sheets or laminates are bonded to the tensile concrete surface of the damaged member. In the NSM technique, grooves are cut in the tensile face of the RC element where the FRP strips/bars are inserted and bonded. Therefore, due to the confinement provided by surrounding concrete and epoxy, NSM FRP-strengthening technique is less exposed to aggressive environment (and other detrimental effects) and less prone to premature debonding [3–6].

RC elements are usually subjected to long-term loads that can affect their structural performance in terms of time-dependent deflections,

loading capacity and failure mode [7–10]. Time-dependent deflections are a function of the loading history (and its effect on concrete mechanical properties), age of concrete at the time of loading, the magnitude and duration of the long-term load and material properties. Within material properties, creep and shrinkage of concrete, which are dependent on environmental conditions, are of main importance [11].

Significant amount of work has been done to study the time-dependent behavior of EBR FRP-strengthened RC elements [9,12–17], where different amounts of carbon FRP (CFRP) area and long-term load levels were considered. The results showed that larger time-dependent deflections were obtained when higher levels of long-term load were applied. Besides, the contribution of CFRP strengthening systems to RC elements under flexural long-term loading was not significant when compared to elements under flexural instantaneous loading [9,13].

Unlike the EBR FRP-strengthened system, few works exist in the literature regarding the time-dependent behavior of NSM FRP-strengthened RC beams [18–21]. Sena-Cruz et al. [18], experimentally studied the time-dependent behavior of slab specimens strengthened with NSM CFRP strips. The load was applied in two steps, first 40 % of long-term load was applied for a duration of 78 days, later the load

increased to 100 % for a duration of 55 days. The results showed that the majority of time-dependent deflection occurred at the first step of the loading. Moawad et al. [19] experimentally studied the time –dependent behavior of different series of NSM CFRP-strengthened RC beams with different loading histories and sectional properties. Results showed the influence of the loading sequences and levels of loading in combination with the other parameters. The specimens with higher concrete strength resulted in a larger ratio of time-dependent deflections to instantaneous deflection. Moreover, for the strengthened specimens with compression steel reinforcement, the effectiveness of NSM strengthening was more pronounced in reducing the deflections. Finally, the effect of the long-term load on the residual flexural capacity of NSM CFRP-strengthened RC beams was experimentally studied [20] and an analytical work to predict the time-dependent response of the specimens was presented [21]. With increase in the long-term load, the residual capacity of beams decreased. Furthermore, all specimens failed by end-debonding, but for higher long-term load, the end-debonding occurred in longer bonded length with larger bond deterioration. In addition, the same trend in time-dependent strain evolution in FRP was observed from both experimental data and analytical procedures.

The structures under long-term loading are usually exposed to temperature variation during the different seasons of the year. Being epoxy adhesives the most common ones used in NSM strengthening, and due to their nature, special attention should be given to high service temperature (near or beyond the glass transition temperature, T_g, of the epoxy adhesive) [22–25]. In this sense, the instantaneous behavior of NSM FRP-strengthened RC beams under room temperature [26–34] and elevated temperature (fire conditions) [35–39] has received considerable attention, but less work has been done on the effect of high service temperature [40–43].

According to the literature, few works have been performed to study the time-dependent behavior of NSM FRP-strengthened RC members, and, to the best of authors knowledge, none of them account for the effect of high service temperature on the time-dependent deflections and structural performance. Therefore, the purpose of the present study is to investigate the time-dependent behavior of NSM CFRP-strengthened RC beams subjected to room temperature (20 °C) and high service temperature (50 °C). To this end, a total of 23 beams were cast, where the effect of different parameters was considered (i.e. level of strengthening (CFRP area), steel reinforcement ratio and applied temperature (20 and 50 °C)). Experimental results are presented and discussed in terms of instantaneous load–deflection curves, time-dependent and total deflections, time-dependent strain in concrete, failure modes, residual flexural strength of tested specimens and aging effect. Furthermore, an analytical procedure to predict the time-dependent deflection in NSM CFRP-strengthened RC beams is presented. The analytical procedure is based on the age-adjusted effective modulus method (AEMM) [11,44].

2. Experimental program

2.1. Test matrix and test setup

The experimental program included 23 RC beams distributed in three series as follows (see Table 1): 10 beams were tested under short-term load and were considered as reference specimens (Series 1), 10 beams were tested under long-term load to examine their time-dependent behavior (Series 2) and, finally, 3 beams were cast and rested in the lab (without any loading) to be tested at the end of the long-term experimental program. Series 1 and Series 2 were divided into two groups to evaluate the effect of steel reinforcement ratio (ρ = 0.79 % and 1.14 % for Group 1 and 2, respectively). Group 1 included two control beams and four NSM CFRP-strengthened RC beams, with two different amounts of CFRP strengthening, subjected to 20 and 50 °C. In Group 2, two control beams and two NSM CFRP-strengthened RC beams, strengthened with three CFRP strips, were subjected to 20 and 50 °C.

Specimens' designation reads X-Y-Z-T, where X indicates the type of loading (ST standing for short-term load, LT standing for long-term load and AG meaning aging effect). Moreover, Y denotes the type of beam (CB meaning control beam, and SB1S and SB3S referring to strengthened beams with one and three CFRP strips, respectively). Furthermore, Z indicates the Group that specimen belongs to (i.e. thus indicating the steel reinforcement ratio). Finally, T stands for the testing temperature. For instance, ST-CB-1–20, refers to the control beam in Group 1 (ρ = 0.79 %) tested under short-term loading at 20 °C. Furthermore, LT-SB3S-2–50 refers to a beam strengthened with three CFRP strips from Group 2 (ρ = 1.14 %) and tested under long-term loading at 50 °C.

The beams were tested under a four-point bending configuration (see Fig. 1). The sectional dimensions of the beams were 180 × 140 mm and the total and clear length of specimens were 2400 mm and 2200 mm, respectively. Specimens in Group 1 were reinforced with two steel rebars with a diameter of 10 mm and two steel rebars with a diameter of 6 mm in the tension and compression side of the beam, respectively (ρ = 0.79 %). In Group 2, rebars with a diameter of 12 mm and 8 mm were used in tension and compression side of the beam, respectively (ρ = 1.14

Table 1
Text matrix.

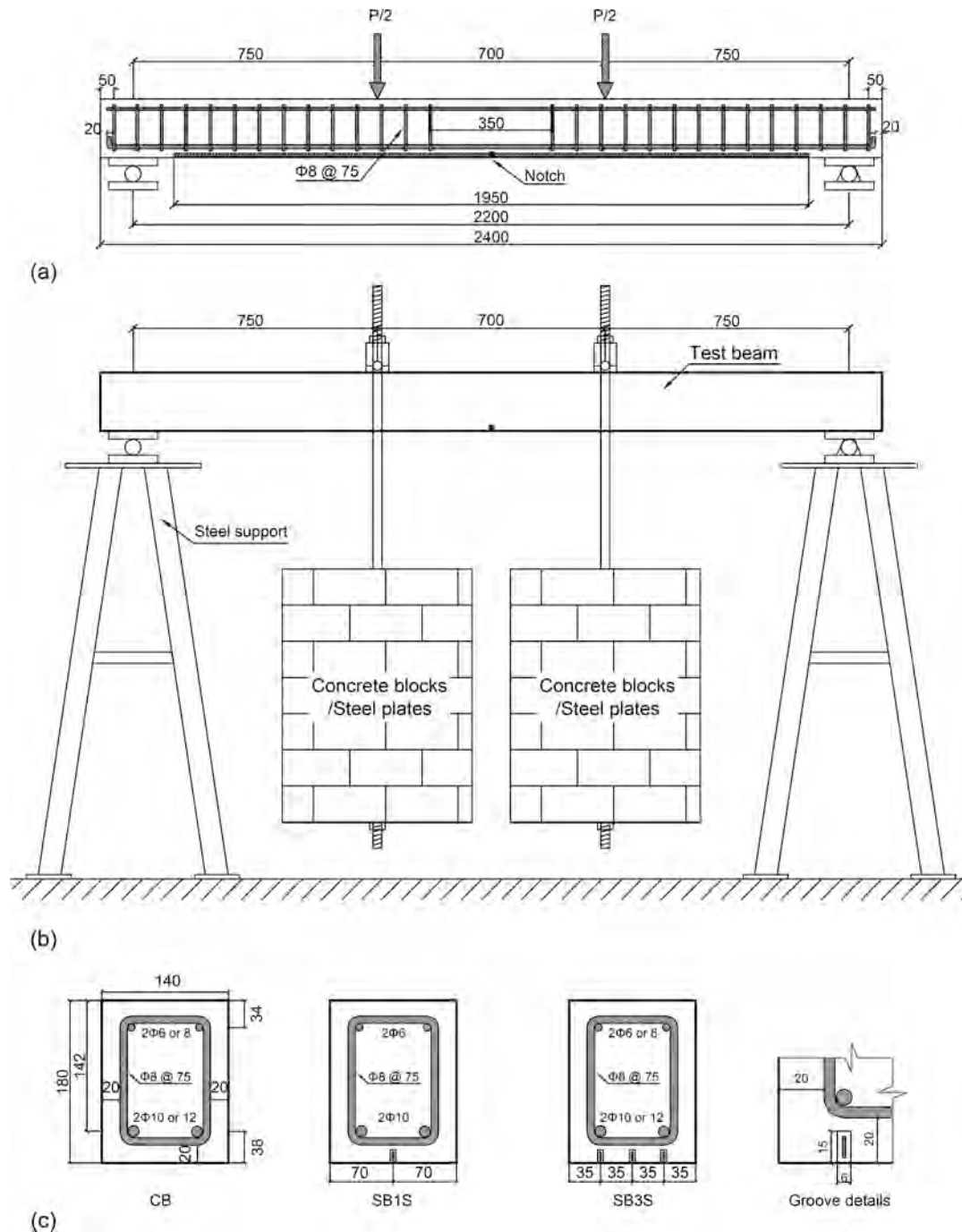| Series	Loading type	Group	Steel reinforcement ratio, ρ (%)	Beam ID	Testing Temperature (°C)	No. of CFRP strips	Total CFRP area (mm²)
Series 1	Short-term	Group 1	0.79	ST-CB-1–20	20	–	–
				ST-CB-1–50	50	–	–
				ST-SB1S-1–20	20	1	14
				ST-SB1S-1–50	50	1	14
				ST-SB3S-1–20	20	3	42
				ST-SB3S-1–50	50	3	42
		Group 2	1.14	ST-CB-2–20	20	–	–
				ST-CB-2–50	50	–	–
				ST-SB3S-2–20	20	3	42
				ST-SB3S-2–50	50	3	42
Series 2	Long-term	Group 1	0.79	LT-CB-1–20	20	–	–
				LT-CB-1–50	50	–	–
				LT-SB1S-1–20	20	1	14
				LT-SB1S-1–50	50	1	14
				LT-SB3S-1–20	20	3	42
				LT-SB3S-1–50	50	3	42
		Group 2	1.14	LT-CB-2–20	20	–	–
				LT-CB-2–50	50	–	–
				LT-SB3S-2–20	20	3	42
				LT-SB3S-2–50	50	3	42
Series 3	Aging	Group 1	0.79	AG-CB-1–20	20	–	–
				AG-SB1S −1–20	20	1	14
				AG-SB3S-1–20	20	3	42

Fig. 1. Details of the tested beams: (a) Short-term setup; (b) Long-term setup and (c) Beam sections (dimensions in mm).

%). To avoid shear failure, stirrups with a diameter of 8 mm were placed every 75 mm in all beams. Furthermore, to strengthen the beams in flexure, and following *fib* Bulletin 90 [45] recommendations, grooves with dimensions of 6 × 15 mm were cut in the soffit of the beams, and strips with dimensions of 1.4 × 10 mm were introduced using an epoxy adhesive. Moreover, a 5 × 15 mm notch was created in the midspan of all beams to act as a crack initiator. For Series 1 and 3 (short-term load before and after aging), the flexural test was performed under displacement control at a rate of 0.6 mm/min, whereas for Series 2 (long-term load), concrete blocks and steel plates were used as dead-weight (see Fig. 1b).

2.2. Instrumentation

Beam instrumentation is shown in Fig. 2. A set of linear vertical displacement transducers (LVDTs) were placed in the beam to register the movement of the beam. One LVDT was used in the midspan of the beam to measure the central deflection (LVDT1). In Series 1 and 3 (subjected to short-term loading), two LVDTs (LVDT 2 and 3) were placed at supports sections to measure the supports settlement. In addition to LVDTs, one strain gauge was installed in the midspan of the specimens to register the strain at the top fiber of concrete (SG$_C$).

In those specimens subjected to the temperature, heating blankets (installed to the soffit of the beam) were used to heat up the beams up to the target temperature (i.e. 50 °C). The heating process was controlled by proportional integral derivative (PID) controller, and Type-T
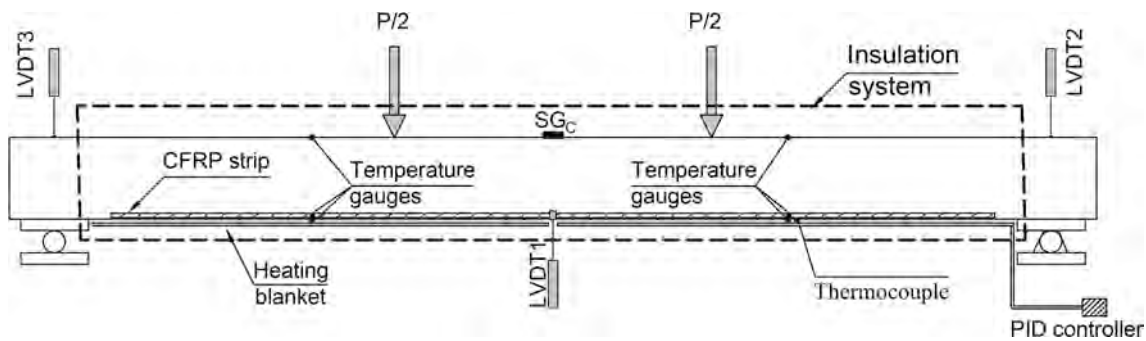
Fig. 2. Beams instrumentation: Position of the linear vertical displacement transducers (LVDTs), concrete strain gauges, temperature gauges, heating system and insulation system.

thermocouples, installed between the heating blanket and the soffit of the beam, were used as temperature controller sensor. In order to ensure a better heat distribution along the beam, an isolation system was used. To monitor and record the temperature during the heating process and flexural testing, different temperature gauges were installed on concrete surface at the top and bottom of the beam, on the surface of the CFRP (it was installed before introducing FRP into the grooves) and on the surface of epoxy adhesive (see Fig. 2). The beams were left to be heated-up for 24 h prior to testing (in both short-term and long-term load) until the average temperature in the soffit of the beam was stabilized to the target value. A general view of short-term and long-term load setup is shown in Fig. 3.

2.3. Temperature and humidity

Registration of lab conditions (temperature and humidity) started the day of concrete casting and continued till the end of the experimental program. An average temperature and humidity of 19.6 °C and 64 % were registered, respectively (see Fig. 4a). In addition, the evolution of temperature and humidity of beams under 50 °C was registered during the heating (24 h prior to testing) until the end of the long-term loading. Average values for temperature and humidity read 50.4 °C and 16 %, respectively (see Fig. 4b).

2.4. Materials

2.4.1. Concrete

The specimens were cast in the structural lab with ready-mix concrete. The cement type was I-42.5R, with a content of 390 kg/m³. The maximum aggregate size was 12 mm, and the water/cement ratio was 0.41. A viscosity modifier and underwater admixture were used to improve workability. In order to determine the mechanical properties of concrete, cylinder specimens with 300 mm nominal height and 150 mm nominal diameter were used. The compressive strength (f_c), tensile strength (f_t) and modulus of elasticity (E_c) of the concrete were determined according to UNE-EN 12390–3 [46], UNE-EN 12390–6 [47], and ASTM C469 [48] standards, respectively. The mechanical properties of concrete at different ages is summarized in Table 2.

The time-dependent behavior of the concrete was determined according to ASTM C512-02 [49]. To this end, four cylindrical specimens (150 mm diameter and 450 mm height) with an embedded strain gauge were manufactured. Two of the four cylinders were kept at 20 °C and the other two were heated up to 50 °C. Each pair of concrete cylinders was stacked on a loading frame and loaded with a long-term load level of $0.35 f_c$ (the same long-term load level in all specimens). The long-term load was applied at the same time as the beams.

To measure free shrinkage strain in concrete (ε_{sh}), two concrete prisms, having the same concrete beam section (180 × 140 mm) and 1 m length, were instrumented with an embedded strain gauge and left unloaded at the same temperature and humidity as beam specimens. The strain evolution with time for both shrinkage specimens (at 20 °C and 50 °C) is shown in Fig. 5a. For the specimen submitted to 50 °C, heating started at the same time as heating of the long-term specimens (Series 2). The effect of heating on concrete shrinkage is clearly visible. In the shrinkage specimen subjected to 50 °C, the thermal strain was also considered in the strain registration. Registers of maximum shrinkage at the end of long-term loading are summarized in Table 3, with shrinkage corresponding to the heated specimen being 35 % higher than that of the specimen at lab conditions.

The concrete creep coefficient was obtained according to Eq. (1):
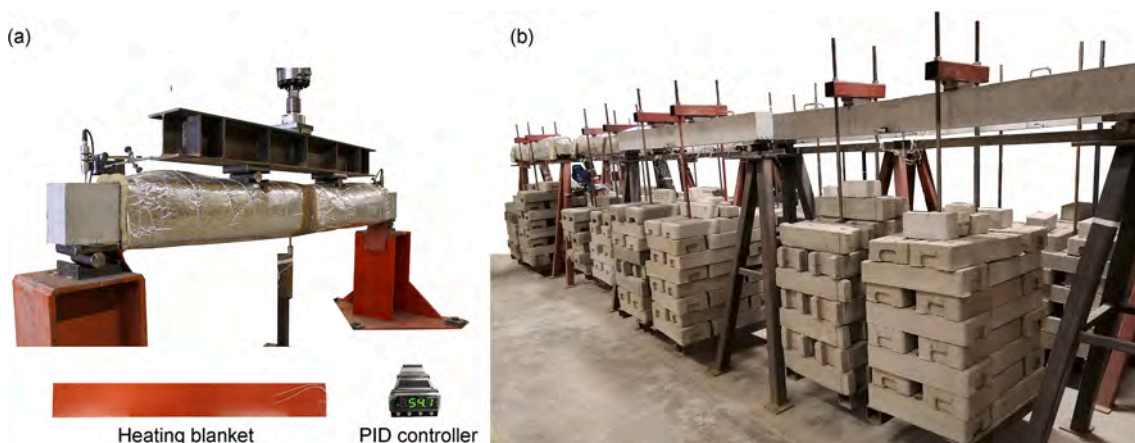

Fig. 3. General view of experimental setup and heating system: (a) Short-term load setup and (b) Long-term load setup.
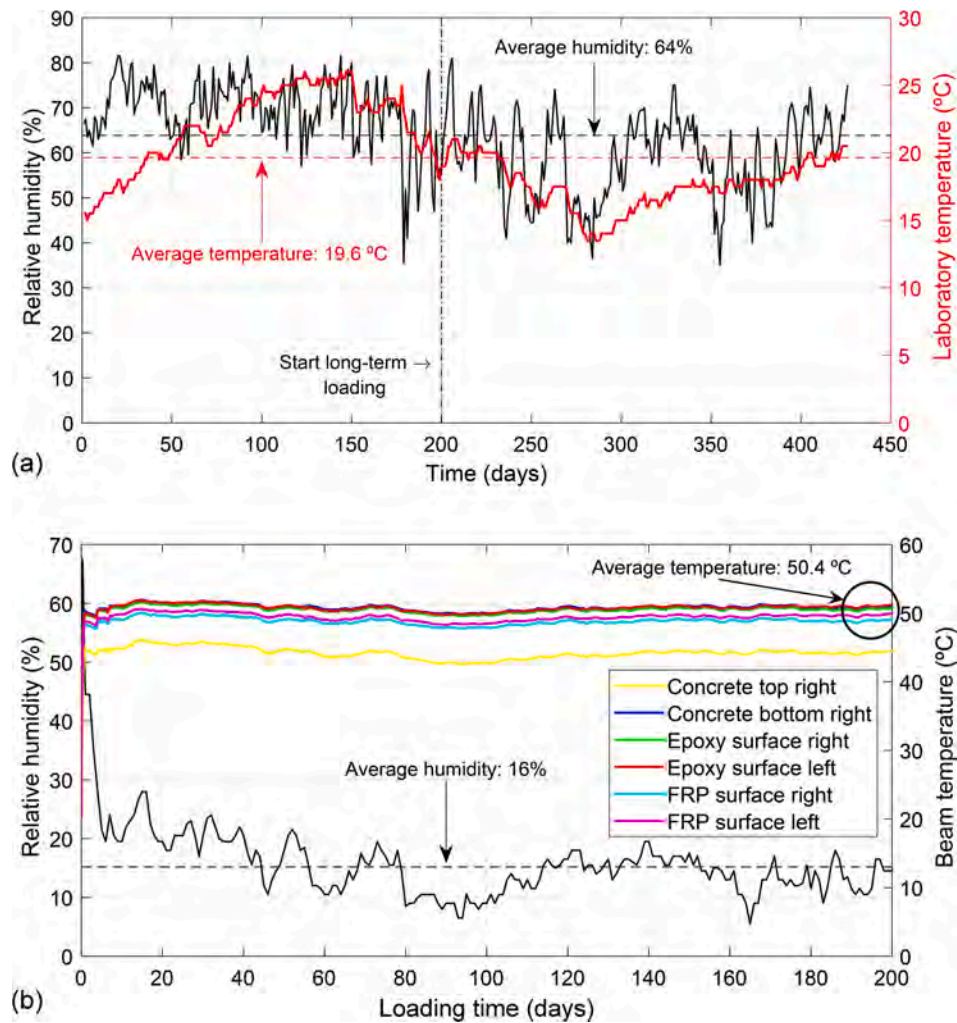
Fig. 4. Registers on temperature and humidity: (a) Lab condition and (b) Inside the beam at 50 °C.

Table 2
Concrete mechanical properties.

Concrete age (days)	Compressive strength, f_c (MPa)	Tensile strength, f_t (MPa)	Modulus of elasticity, E_c (GPa)
90[a]	48.1 (2.3 %)[d]	3.7 (6.0 %)[d]	41.2 (5.3 %)[d]
200[b]	48.3 (2.2 %)[d]	3.7 (9.0 %)[d]	41.9 (4.5 %)[d]
430[c]	53.7 (0.8 %)[d]	3.6 (9.4 %)[d]	47.6 (1.9 %)[d]

[a] Age at short-term test of Series 1.
[b] Age at long-term test of Series 2.
[c] Age at residual flexural test of Series 2 and short-term test of Series 3.
[d] Coefficient of variation (CoV) indicated in brackets.

$$\varphi_c(t, t_0) = \frac{\varepsilon_c(t, t_0) - \varepsilon_{cs}(t, t_0) - \varepsilon_{ci}(t_0)}{\varepsilon_{ci}(t_0)} \tag{1}$$

where t is the loading time, t_0 is the concrete age at the start of loading, $\varphi_c(t,t_0)$ is the concrete creep coefficient, $\varepsilon_c(t,t_0)$ is the total concrete strain, $\varepsilon_{cs}(t,t_0)$ is the concrete shrinkage strain and $\varepsilon_{ci}(t_0)$ is the instantaneous concrete strain caused by the long-term load.

Due to technical issues in the setup of the concrete creep specimen subjected to 50 °C, the concrete creep coefficient was experimentally determined only for specimens at 20 °C (see Fig. 5b). Existing formulation from Model Code 2010 [11] was used to estimate the concrete creep coefficient for the concrete at 50 °C. Experimental values and analytical prediction of concrete creep coefficient are presented in Table 3. For comparison purposes, analytical prediction on concrete creep coefficient of specimen subjected to 20 °C is also included.

2.4.2. Steel reinforcement

Mechanical properties of steel bars were obtained from tension tests based on UNE-EN ISO 15630–1 [50]. The yielding strength (f_y), the ultimate strength (f_u) and the modulus of elasticity (E_s) were 586.4 MPa (CoV = 2.3 %), 707.7 MPa (CoV = 1.7 %) and 205.1 GPa (CoV = 1.0 %) respectively.

2.4.3. CFRP strips

CFRP strips, consisting of unidirectional carbon fibers (with a volume content fiber higher than 68 %) held together by an epoxy vinyl ester resin matrix, were used for strengthening the specimens [51]. The mechanical properties of the CFRP strips were obtained according to ISO 527–5 [52] recommendations. An ultimate tensile strength ($f_{u,FRP}$) of 2251.4 MPa (CoV = 3.2 %), an ultimate tensile strain ($\varepsilon_{u,FRP}$) of 0.0133 (CoV = 7.2 %), and a modulus of elasticity (E_{FRP}) of 169.5 GPa (CoV = 6.3 %) were obtained [40].

2.4.4. Epoxy adhesive

The adhesive used in this study is a high performance, solvent-free, thixotropic, and grey two-component epoxy adhesive specially developed for bonding CFRP to concrete under the commercial name of S&P220HP. According to the manufacturer's product data sheet [53], the components A (resin) and B (hardener) should be mixed at a ratio of 2:1 by weight, and the suggested curing duration is 7 days. Tensile
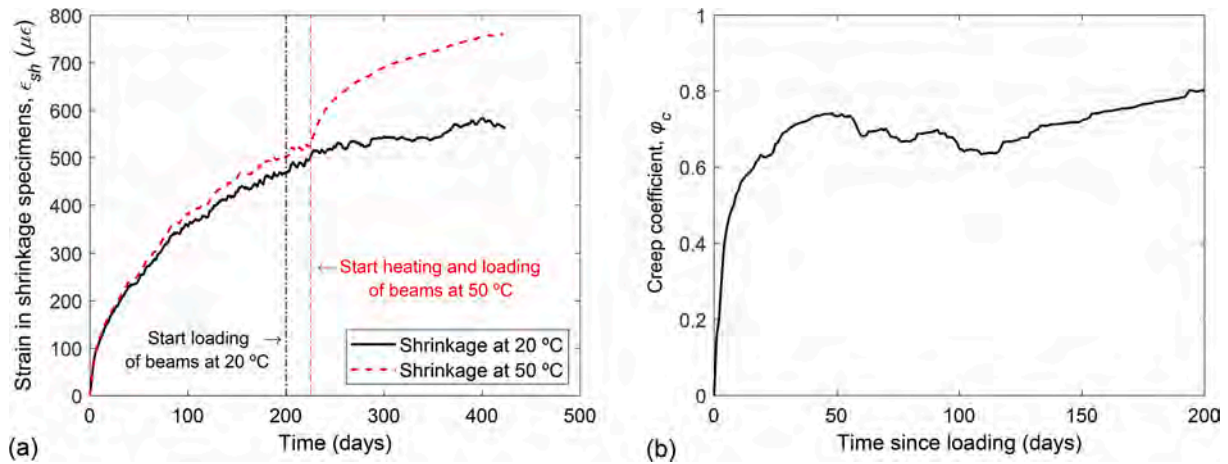
Fig. 5. Experimental time-dependent behavior of concrete: (a) Strain in shrinkage specimens at 20 and 50 °C and (b) Creep coefficient at 20 °C.

Table 3
Concrete creep coefficient and shrinkage strain.

Temperature (°C)	Concrete creep coefficient, φ_c		Experimental shrinkage strain, ε_{sh} ($\mu\varepsilon$)
	Experimental	Model Code 2010 [11]	
20	0.80	0.60	563
50	-[1]	2.64	759

[1] Not available due to failure in setup.

properties of the epoxy adhesive were determined by iSO-527–1 [54] specifications (see Table 4) [24]. To evaluate the effect of temperature on mechanical properties of the epoxy, the specimens were tested under 20 °C and 50 °C. The tensile strength ($f_{u,epoxy}$) and modulus of elasticity (E_{epoxy}) at 50 °C decreased by 30 % and 47 %, respectively, when testing temperature changed from 20 °C to 50 °C. Moreover, the glass transition temperature (T_g) of epoxy was also determined with differential scanning calorimetry (DSC) [55] and dynamic mechanical analysis (DMA) [56]. According to test results, the T_g of epoxy was in the range of 53.9–65.3 °C [40].

The creep coefficient of epoxy adhesive (φ_{epoxy}) was also evaluated at 20 and 50 °C (see Fig. 6). Three levels of long-term load (causing 20 %, 40 % and 60 % of epoxy ultimate strain, 0.0035, obtained from tensile test) were applied to the specimens for a duration of 40 days (1000 h), which is similar to the duration used in the literature [22,57–59]. The long-term loading was applied through a gravity loading system with a lever arm with a magnification factor of 4 [22,60]. The temperature and humidity conditions applied during the epoxy tensile creep tests were the same as those of the beams. For each temperature, two specimens were tested, and all specimens included two strain gauges (one at each side). The creep coefficient of epoxy adhesive was obtained according to Eq. (2):

$$\varphi_{epoxy}(t, t_0) = \frac{\varepsilon_e(t, t_0) - \varepsilon_e(t_0)}{\varepsilon_e(t_0)} \qquad (2)$$

where ε_e (t,t₀) is the epoxy adhesive strain with time and ε_e (t₀) is the epoxy adhesive strain at the loading moment.

According to experimental results, epoxy creep coefficient at 20 °C

was affected by the sudden drop in humidity and temperature in the lab taking place around 200 h after loading (see Fig. 6a). Besides, specimens tested at 50 °C failed after a few hours of loading (see Fig. 6b).

2.5. Test procedure

In this experimental program, 4 loading stages were considered. In stage 1, the beams of Series 1 were tested under four-point bending configuration (see Fig. 1a) to obtain their short-term flexural response. Tests were performed under displacement control mode at a rate of 0.6 mm/min.

In stage 2, prior to long-term test, beams were subjected to pre-loading in order to ensure a level of cracking corresponding to the service load. To this end, beams in Series 2 were subjected to two loading/ unloading cycles up to service load level, P_{ser}. The service load was calculated by limiting the stress in compressed concrete ($\sigma_c < 0.6f_c$) and steel reinforcement ($\sigma_s < 0.8f_y$) [61]. For this pre-loading stage, the same test setup and loading rate as in stage 1 was used.

In stage 3, after the pre-loading, specimens in Series 2 were moved to the long term loading frames (Fig. 1b) and the long-term load was applied for a duration of 200 days. The long-term load was chosen to obtain a concrete compressive stress of 0.35 f_c, so that linear creep behavior of concrete was ensured by being under the Model Code 2010 limitation [11].

Finally, in stage 4, and after the long-term test, specimens in Series 2 were tested up to failure to evaluate their residual flexural strength. Additionally, specimens of Series 3, that were resting in the lab for aging, were tested to obtain their short-term flexural response. In this stage, the same test setup and loading rate as in stages 1 and 2 was used.

3. Experimental results and discussions

3.1. Short-term tests results

Results of short-term flexural tests (Series 1) are presented in Fig. 7 in terms of load versus midspan deflection curves. In each curve, three phases can be distinguished: i) an initial linear behavior representing the elastic behavior of the uncracked element; ii) a second phase, starting at

Table 4
Mechanical properties of epoxy adhesive [24].

Testing temperature (°C)	Tensile strength, $f_{u,epoxy}$ (MPa)	$f_{u,epoxy-50}$ / $f_{u,epoxy-20}$	Modulus of elasticity, E_{epoxy} (MPa)	$E_{epoxy-50}$ / $E_{epoxy-20}$
20	28.0 (0.4 %)[a]	–	8102.4 (0.8 %)[a]	–
50	19.6 (3.6 %)[a]	0.7	4289.6 (2.3 %)[a]	0.53

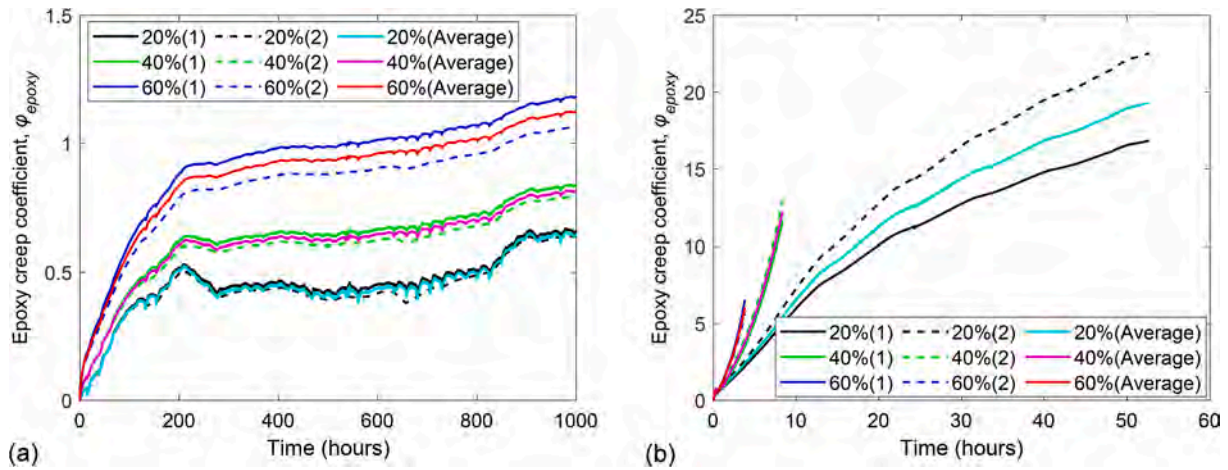[a] Coefficient of variation (CoV) indicated in brackets.

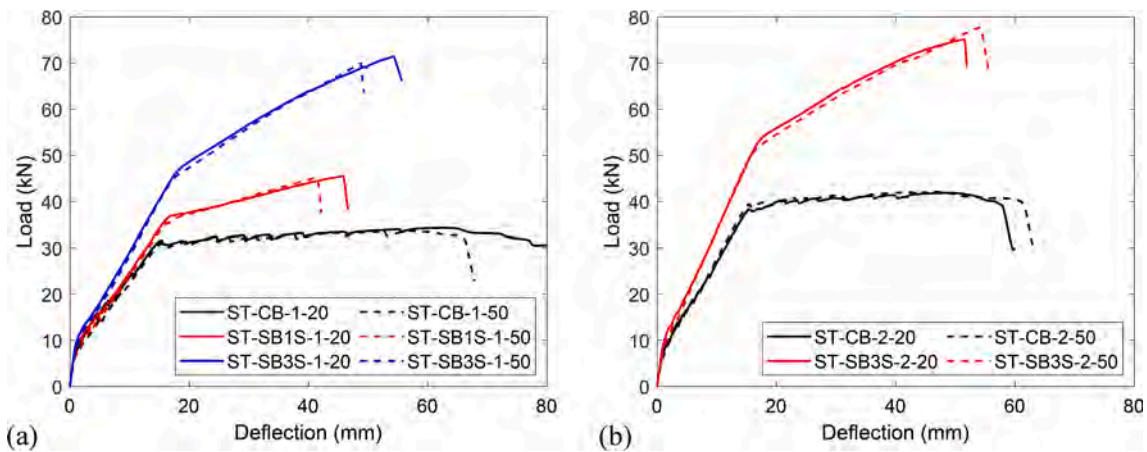**Fig. 6.** Creep coefficient of epoxy adhesive (a) at 20 °C and (b) at 50 °C.

Fig. 7. Load-deflection curves of specimens in Series 1: (a) Group 1 (ρ = 0.79 %) and (b) Group 2 (ρ = 1.14 %).

the cracking load (P_{cr}), where stiffness decreases and load can be increased up to yielding of steel reinforcement; and iii) a post-yielding phase up to failure. For the case of unstrengthened beams (CB), no significant differences between yielding load (P_y) and ultimate load (P_u) exist. For the case of strengthened beams, load can be further increased after steel yielding until the ultimate load. Experimental results of short-term tests (Series 1) are presented in Table 5. As a general result, the increase in the CFRP strengthening area produces an increase in stiffness in the post-cracking and post-yielding stages, which results in larger yielding loads, P_y, and ultimate loads, P_u. According to results presented in Table 5, larger benefits of the CFRP strengthening system were obtained in beams with lower steel reinforcement ratio, as expected and depicted by the comparison between the strength increase ratios of specimens in Groups 1 and 2. Finally, no significant effect of temperature is visible in the load–deflection curves. The similarity in short-term responses between specimens tested at 20 °C and 50 °C can be attributed to the fact that 50 °C was below the T_g of the epoxy (53.9 °C < T_g < 65.3 °C) and epoxy adhesive was post-cured and therefore its mechanical properties improved [24,25,40].

Representative images of failure modes are shown in Fig. 8. Unstrengthened control beams, with and without temperature, failed by concrete crushing (CC) after steel reinforcement yielding. Besides, all strengthened beams failed by FRP rupture, irrespective of the applied temperature and the CFRP strengthening area, and no premature bond failure took place. It should be mentioned that results may change if different test configurations and/or larger temperatures were applied [40].

Table 5
Experimental results of specimens in Series 1 under short-term load.

Specimen ID	P_{cr} (kN)	P_y (kN)	P_u (kN)	Strength increase ratio [a]	Failure mode [b]
ST-CB-1–20	7.43	30.75	34.28	–	CC
ST-CB-1–50	7.00	30.00	33.57	–	CC
ST-SB1S-1–20	7.82	36.88	45.50	1.33	FR
ST-SB1S-1–50	6.00	35.36	45.15	1.34	FR
ST-SB3S-1–20	8.85	46.50	71.40	2.08	FR
ST-SB3S-1–50	6.75	45.25	70.00	2.09	FR
ST-CB-2–20	6.70	37.89	41.84	–	CC
ST-CB-2–50	5.95	38.71	42.10	–	CC
ST-SB3S-2–20	9.60	53.36	75.10	1.79	FR
ST-SB3S-2–50	8.20	51.00	77.68	1.85	FR

[a] Ratio of ultimate load of strengthened beam to ultimate load of the control unstrengthened beam of the same group.
[b] CC = concrete crushing after steel yielding; FR = FRP rupture.

3.2. Pre-loading

Before the application of the long-term load, specimens of Series 2 were subjected to a pre-loading stage, consisting in two cycles of

Fig. 8. Representative views of failure modes of specimens in Series 1.

Table 6
Experimental results for pre-loading stage in Series 2.

Specimen ID	P_{ser} (kN)	P_{LT} (kN)	$\delta_{p,0}$ (mm)
LT-CB-1–20	20.4	13.8	2.14
LT-CB-1–50			2.14
LT-SB1S-1–20	24.8		2.21
LT-SB1S-1–50			2.32
LT-SB3S-1–20	27.1		1.93
LT-SB3S-1–50			1.93
LT-CB-2–20	26.5	15.8	2.22
LT-CB-2–50			2.05
LT-SB3S-2–20	30.0		1.86
LT-SB3S-2–50			1.67

loading/unloading. First, the specimens were loaded up to the service load level (P_{ser}); then, two cycles were applied between the minimum load (2 kN) and maximum load (service load). Table 6 shows the experimental data from the pre-loading stage for all of the specimens in Series 2. Finally, the specimens were rested to relax at lab conditions for 1 day prior to the application of the long-term load. Deflections were continuously registered, even during the relaxation period, so that the permanent deflection after a one-day relaxation ($\delta_{p,0}$) could be computed. Fig. 9 presents representative load–deflection curves for the pre-loading process of LT-SB3S-1–20 and LT-SB3S-2–50. In this Figure, P_{LT} stands for level of long-term load to be applied in long-term tests.

3.3. Time-dependent tests results

Following the pre-loading stage, beams in Series 2 were placed according to the setup shown in Fig. 1b to be tested under long-term loading. The vertical transducer at midspan section allowed registering the evolution of deflection due to long-term load. Similarly, the evolution of concrete strains was also recorded.

3.3.1. Deflections

The evolution of the total deflection (δ_{tot}) with time is presented in Fig. 10. The total deflection results from the addition of the permanent deflection after pre-loading stage ($\delta_{p,0}$), the instantaneous deflection after the application of the long-term load (δ_{ins}) and the time-dependent deflection due to long-term load (δ_{td}). The markers in the vertical axis in Fig. 10 represent the permanent deflection after pre-loading stage ($\delta_{p,0}$). Additionally, time-dependent deflections (δ_{td}) are presented in Fig. 11. According to experimental results, summarized in Table 7, the increase of the CFRP strengthening area in specimens tested at 20 °C resulted in a decrease in the three components of the total deflection (i.e. $\delta_{p,0}$, δ_{ins} and δ_{td}), irrespective of the steel reinforcement ratio. This is due to the increase in the tensile reinforcement stiffness and due to the same long-term load being applied in all specimens of the same group (i.e. long-term load to be applied was the same for control specimens and specimens with CFRP strengthening).

Experimental results on specimens tested at 50 °C revealed that the application of a high service temperature (50 °C) did not have remarkable effects on the instantaneous deflection after the application of the long-term load (δ_{ins}), when compared to that of specimens at 20 °C. However, the application of high service temperature had a clear effect on time-dependent deflections (δ_{td}), irrespective of the steel reinforcement ratio. In this sense, in Group 1, the time-dependent deflection in unstrengthened control beam (LT-CB-1–50) increased by 60 % because of the application of 50 °C, and this percentage increase up to 85 % for strengthened beams with either one or three strips (i.e. LT-SB1S-1–50 and LT-SB3S-1–50). Likewise, in Group 2, the time-dependent deflection increased by 86 % and 100 % in unstrengthened control beam (LT-CB-2–50) and strengthened beam (LT-SB3S-2–50), respectively. It should be mentioned that similar time-dependent deflections were obtained within the same Group of specimens tested at 50 °C, so that the time-dependent response of the strengthened beams approached to the unstrengthened beam.

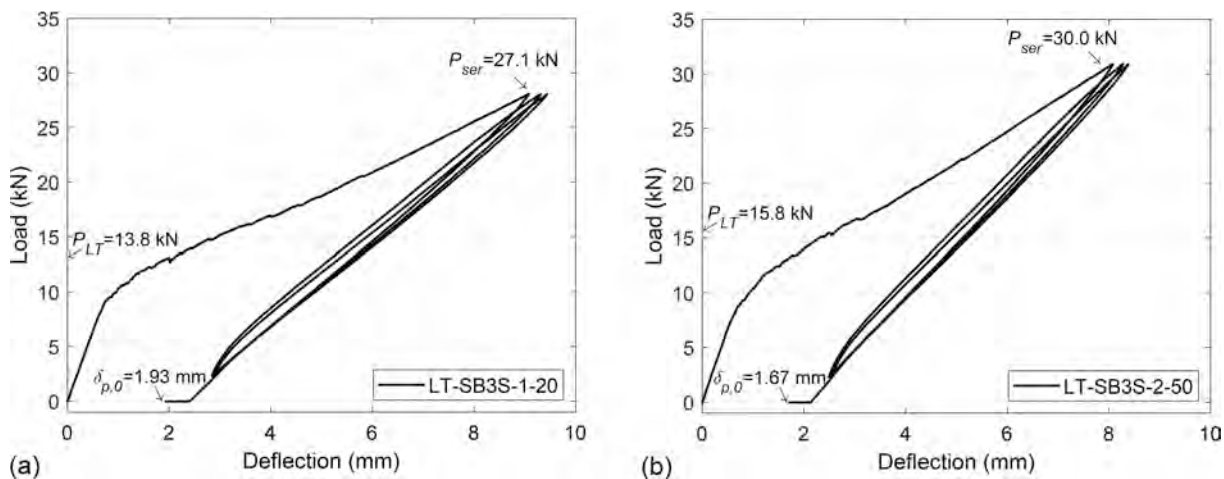An initial explanation lies in the larger concrete time-dependent

Fig. 9. Representative load–deflection curves for pre-loading process for specimens: (a) LT-SB3S-1–20 and (b) LT-SB3S-2–50.
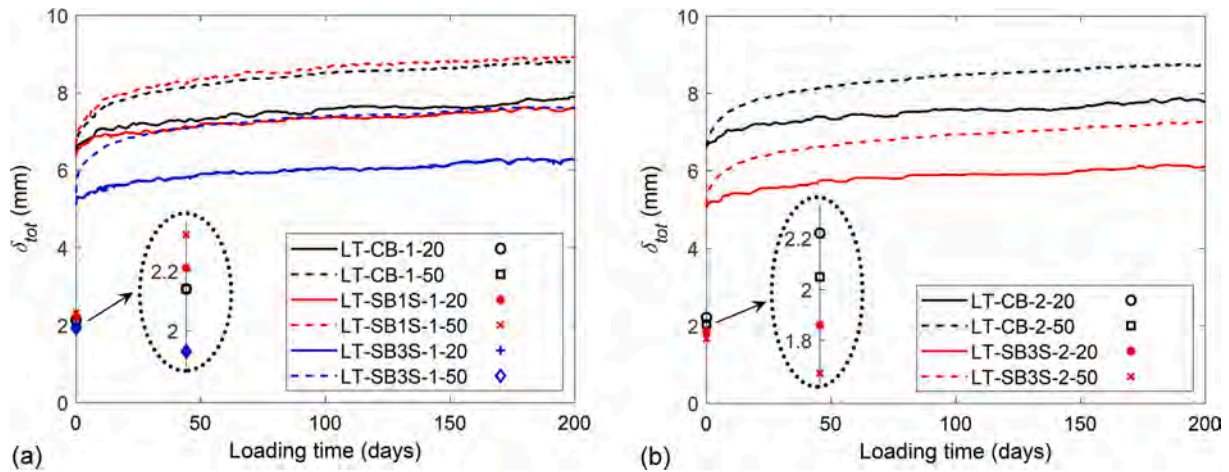
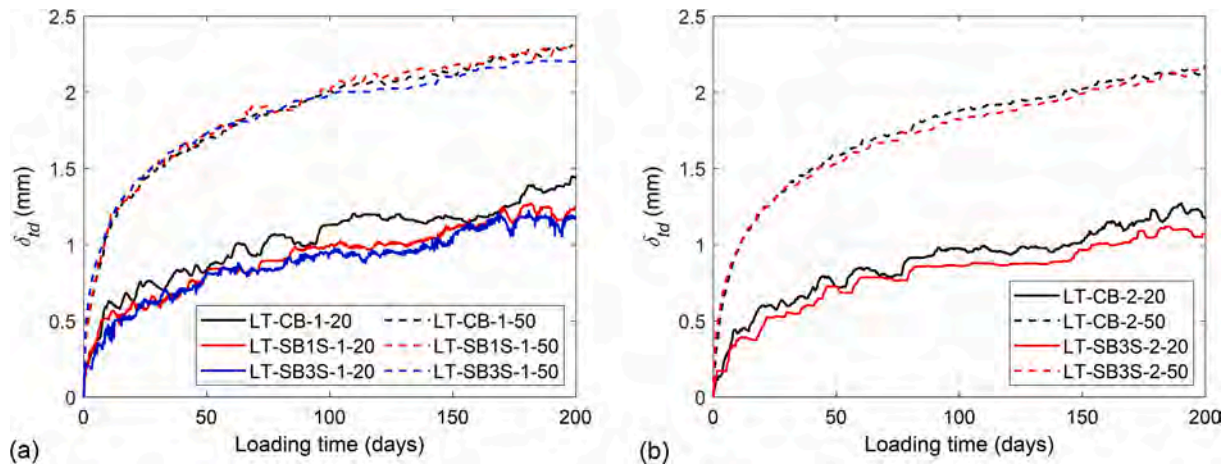**Fig. 10.** Total deflection of beams in Series 2: (a) Group 1 (ρ = 0.79 %) and (b) Group 2 (ρ = 1.14 %).

Fig. 11. Time-dependent deflection of beams in Series 2: (a) Group 1 (ρ = 0.79 %) and (b) Group 2 (ρ = 1.14 %).

Table 7
Deflections from long-term load.

Specimen ID	Deflections (mm)				$\delta_{tot}/\delta_{ins,tot}$
	δ_{ins}	$\delta_{ins,tot} = \delta_{ins} + \delta_{p,0}$	$\delta_{td,max}$[a]	$\delta_{tot} = \delta_{ins,tot} + \delta_{td,max}$	
LT-CB-1–20	4.31	6.45	1.44	7.89	1.22
LT-CB-1–50	4.36	6.50	2.31	8.81	1.36
LT-SB1S-1–20	4.15	6.36	1.24	7.6	1.19
LT-SB1S-1–50	4.31	6.63	2.30	8.93	1.35
LT-SB3S-1–20	3.16	5.09	1.18	6.27	1.23
LT-SB3S-1–50	3.48	5.41	2.20	7.61	1.41
LT-CB-2–20	4.39	6.61	1.17	7.78	1.18
LT-CB-2–50	4.55	6.60	2.18	8.78	1.33
LT-SB3S-2–20	3.17	5.03	1.07	6.1	1.21
LT-SB3S-2–50	3.44	5.11	2.14	7.25	1.42

[a] Maximum time-dependent deflection from Fig. 11.

properties (i.e. shrinkage and creep coefficient) at 50 °C. Based on experimental values for concrete shrinkage in prism specimens (see Fig. 5a), the total shrinkage of the specimens from the day of loading increased from 100 με at 20 °C to 240 με at 50 °C. Furthermore,

according to analytical predictions presented in Table 3, concrete creep coefficient increased from 0.60 to 2.64, showing a 340 % difference. A secondary cause can be the detrimental effect of temperature on both instantaneous and time-dependent mechanical properties of the epoxy adhesive. In this sense, short-term values of epoxy tensile strength ($f_{u,epoxy}$) and tensile modulus of elasticity (E_{epoxy}) decreased by 30 % and 47 %, respectively, when epoxy was submitted to 50 °C (see Table 4). Additionally, higher creep coefficients were found for epoxy at 50 °C (see Fig. 6). Nevertheless, it should be mentioned that the effect of higher temperature on the time-dependent behavior of concrete seems to be dominant, as the time-dependent deflections of the unstrengthened control beams in Groups 1 and 2 subjected to temperature (i.e. LT-CB-1–50 and LT-CB-2–50) were increased by 60 % and 86 %, respectively.

It should be mentioned that the fluctuations observed in the evolution of deflection at 20 °C (Figs. 10 and 11) were probably due to large humidity variations taking place at the structural lab (see Fig. 4a). For the case of heated specimens (submitted to 50 °C), minimum fluctuations in humidity were observed, because of the good performance of the heating and isolation systems (see Fig. 4b).

The normalized deflections of the specimens ($\delta_{tot} / \delta_{ins,tot}$), where $\delta_{ins,tot} = \delta_{ins} + \delta_{p,0}$, are shown in Fig. 12. According to experimental results, larger normalized deflections were obtained in specimens strengthened with three strips, and similar normalized deflections were obtained for beams strengthened with one strip and their counterpart unstrengthened beam. This is due to lower instantaneous deflections ($\delta_{ins,tot}$) for beams with three strips and similar time-dependent deflections (δ_{td}) for
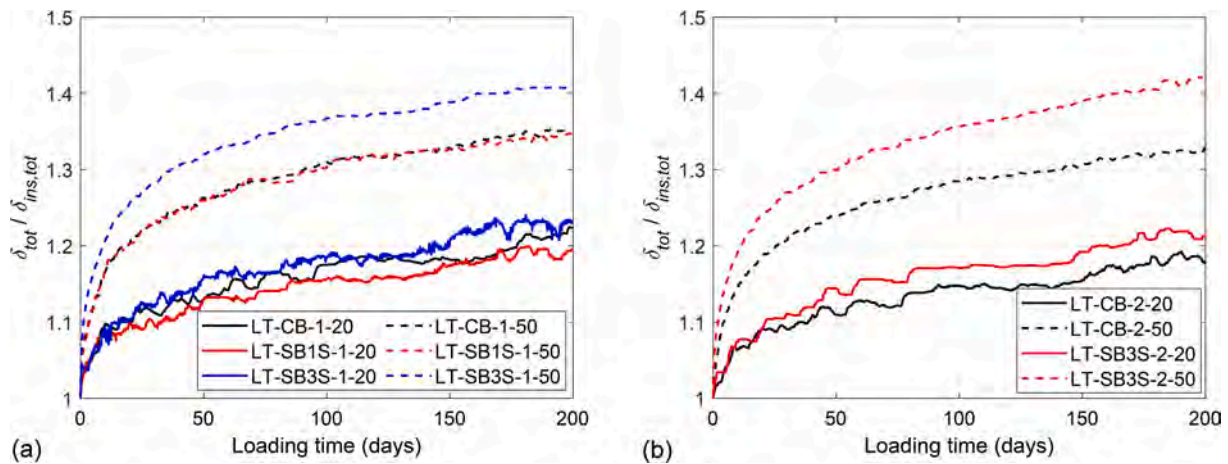
Fig. 12. Ratio of total to instantaneous deflection of beams in Series 2: (a) Group 1 (ρ = 0.79 %) and (b) Group 2 (ρ = 1.14 %).

beams within the same Group. This effect is more clear when deflections of specimens under 50 °C are analyzed.

3.3.2. Concrete strain

The total and time-dependent strain at the top fiber of concrete at the midspan section (see the position of SG_C in Fig. 2) is shown in Figs. 13 and 14 respectively. Similar to evolution of total and time-dependent deflections, strengthening with larger amounts of CFRP area resulted in a reduction in total and time-dependent concrete strain. In addition, the application of high service temperature produced a sharp increase in the time-dependent concrete strain. For instance, for unstrengthened control beams in Group 1 (LT-CB-1–50) and Group 2 (LT-CB-2–50), the time-dependent concrete strain was increased by 65 % and 77 %, respectively. For strengthened beams in Group 1 (LT-SB1S-1–50 and LT-SB3S-1–50) the percentage increased up to 79 % and 88 %, respectively. Furthermore, in strengthened specimens belonging to Group 2 (LT-SB3S-2–50), the time-dependent concrete strain was increased by 136 %. According to the results from unstrengthened beams, and similar to the evolution of time-dependent deflections, time-dependent strains in concrete were mostly affected by concrete time-dependent properties and how they depend on service temperature.

3.4. Residual flexural strength and aging effect

Following long-term tests, specimens in Series 2 were tested up to failure to evaluate their residual flexural strength. The initial deflection prior to the post long-term tests was obtained by registering the ultimate

permanent deflection ($δ_{p,u}$) after removing the long-term load. In addition, specimens in Series 3 were also tested up to failure to evaluate the aging effect on their instantaneous load–deflection response. Fig. 15 shows representative load–deflection curves, and detailed results are listed in Table 8.

The ultimate permanent deflection ($δ_{p,u}$) was used to plot the load–deflection curves of specimens in Series 2 during their testing up to failure after long-term loading (see Fig. 15). According to the results presented in Table 8, it is worthy to mention that the ultimate permanent deflection of specimens subjected to 50 °C was larger than that of specimens at 20 °C, which was in agreement with the trend in time-dependent deflections.

The comparison between results in Series 1 and Series 2 (black and red lines in Fig. 15, respectively) allows accounting for the residual strength of the beams after long-term load. For the case of unstrengthened control beams, similar yielding loads and post-yielding behavior were obtained. The differences in their ultimate deflection can be attributed to the failure mode (concrete crushing) and the values for concrete compressive strain at failure. For the case of strengthened beams, in general slightly higher values for yielding load and post-yielding stiffness were found for the case of beams submitted to previous long-term load, irrespective of the temperature applied during the long-term tests. It should be mentioned that failure mode for strengthened beams remained to be FRP rupture, except for the case of beams strengthened with three strips in Group 2 (LT-SB3S-2–20 and LT-SB3S-2–50). In these latter cases, premature cracking initiated in the compression zone of the specimens and, due to the increase in deflection
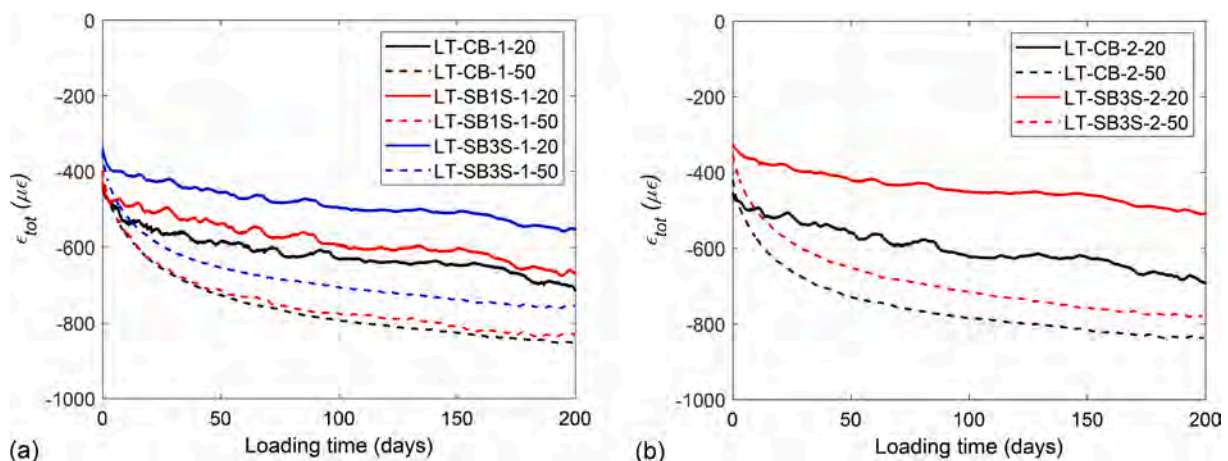

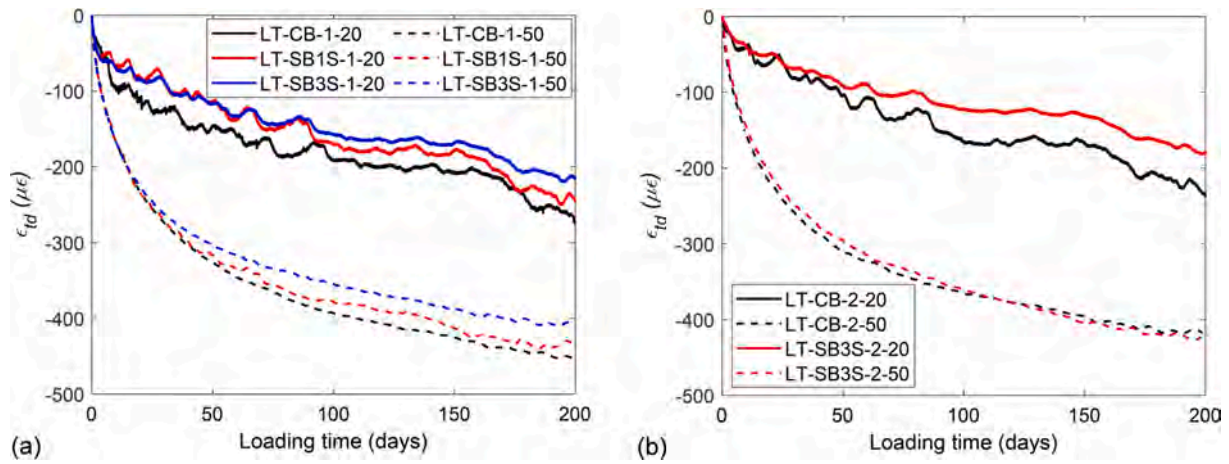Fig. 13. Top fiber concrete total strain evolution: (a) Group 1 (ρ = 0.79 %) and (b) Group 2 (ρ = 1.14 %).

Fig. 14. Top fiber concrete time-dependent strain evolution: (a) Group 1 (ρ = 0.79 %) and (b) Group 2 (ρ = 1.14 %).
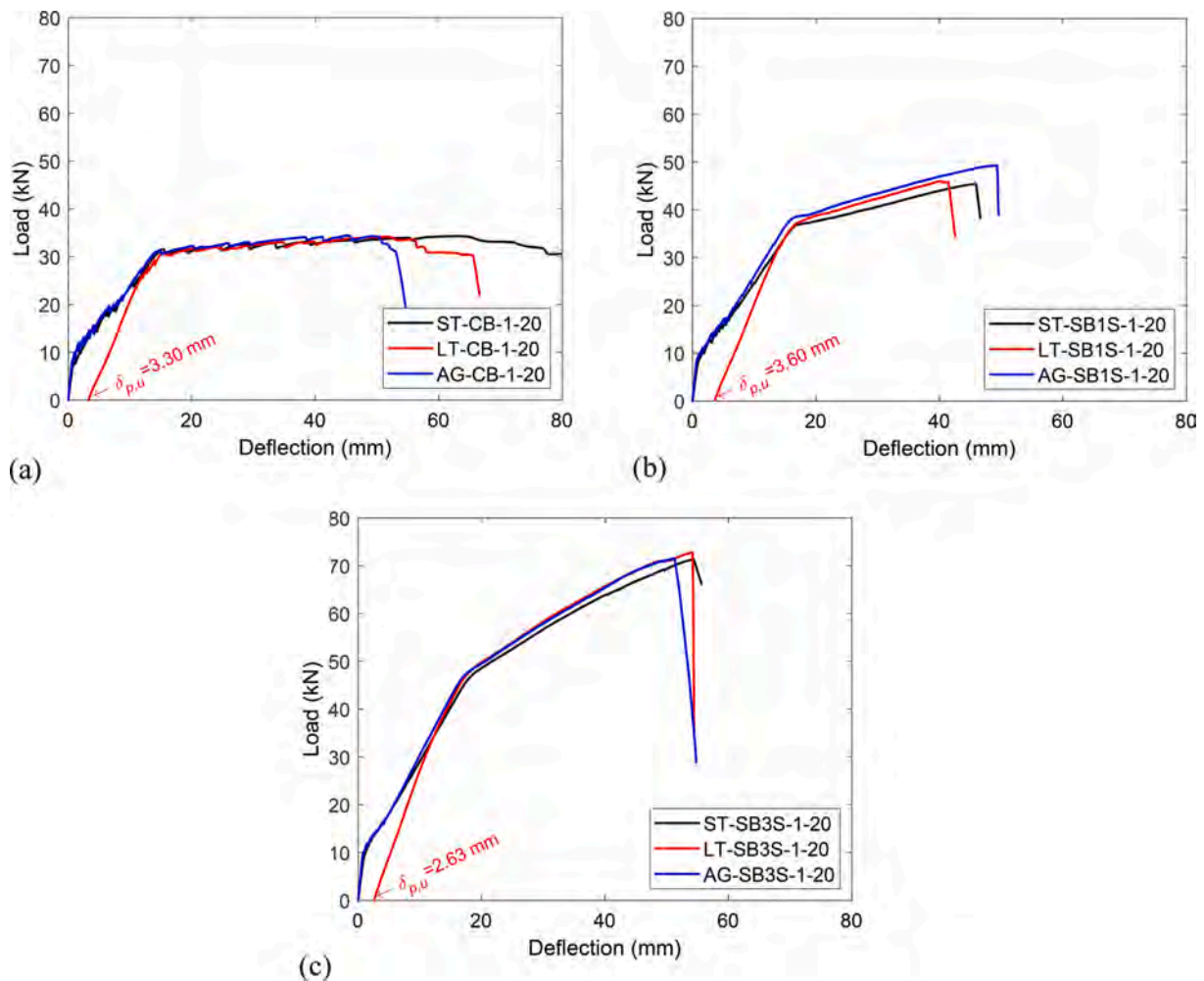

Fig. 15. Representative load–deflection curves for the analysis of residual flexural strength and aging effect: (a) Unstrengthened control beams in Group 1; (b) Strengthened beams with one strip in Group 1; (c) Strengthened beams with three strips in Group 1.

(and curvature), FRP rupture took place (see Fig. 16). This change in failure mode from FRP rupture (FR) to concrete crushing followed by FRP rupture (CC-FR) may be the cause of lower ultimate loads.

The effect of long-term loading is also visible in the initial stiffness of the load–deflection curves. Beams in Series 2 being partially cracked derived in the elastic slope lying between the un-cracked and cracked

stages. The stiffness presented in Table 8 was computed as the ratio between load and deflection corresponding to the long-term load level and the service load level. Initial stiffness of specimens subjected to long-term loading (Series 2) were, by far, the largest ones (see Fig. 15 and Table 8). This behavior is similar to what happened during the pre-loading stage, where two cycles of loading/unloading were applied.

Table 8
Results for the analysis of residual flexural strength and aging effect.

Specimen ID	P_y (kN)	P_u (kN)	Stiffness [a] (kN/mm)	$\delta_{p,u}$ (mm)	Failure mode [b]
LT-CB-1–20	30.43	34.17	3.30	3.30	CC
AG-CB-1–20	30.91	34.42	1.41	–	CC
LT-CB-1–50	29.50	34.05	3.06	5.30	CC
LT-SB1S-1–20	37.25	46.03	3.23	3.60	FR
AG-SB1S-1–20	38.68	49.28	1.75	–	FR
LT-SB1S-1–50	35.72	44.90	2.90	4.48	FR
LT-SB3S-1–20	47.00	72.85	3.64	2.63	FR
AG-SB3S-1–20	47.26	71.56	2.12	–	FR
LT-SB3S-1–50	46.48	69.80	3.46	4.01	FR
LT-CB-2–20	38.00	41.07	3.58	2.48	CC
LT-CB-2–50	38.48	42.73	3.47	4.29	CC
LT-SB3S-2–20	53.57	74.41	4.41	2.80	CC-FR
LT-SB3S-2–50	52.46	73.00	4.20	3.38	CC-FR

[a] Computed as the slope of load–deflection curve between long-term load level and service load level.
[b] CC = concrete crushing after steel yielding; FR = FRP rupture; CC-FR = Concrete crushing followed by FRP rupture.

Finally, the effect of high service temperature is reflected in the reduction of initial stiffness, when compared to specimens tested at 20 °C. This is again a consequence of larger concrete time-dependent properties causing larger ultimate permanent deflections after the removal of the long-term load ($\delta_{p,u}$).

For the analysis of the aging effect, results in Series 1 and Series 3 (black and blue lines in Fig. 15, respectively) should be compared. Similar to what was found in the analysis of the residual strength after long-term load, identical load–deflection curves were obtained for unstrengthened control beams and slightly larger yielding loads and post-yielding stiffness were found for strengthened beams. Failure modes of aged beams did not change when compared to that of Series 1.

4. Analytical predictions on time-dependent deflections

In this section, an analytical procedure based on Gilbert [44] is used to predict time-dependent deflections of CFRP NSM strengthened RC elements. Within the procedure, the age-adjusted effective modulus method (AEMM) is used in the cross-sectional analysis to determine how stresses, strains and curvatures vary with time due to creep and shrinkage of concrete. A schematic view of beam cross-section is shown in Fig. 17a. Furthermore, in both types of loading (i.e. short-term and long-term), a linear distribution of strains was assumed (see Fig. 17b).

Assuming a linear strain distribution (as shown in Fig. 17b), the instantaneous response of a cracked section, in terms of instantaneous maximum concrete compressive strain (ε_{0i}) and initial section curvature (κ_i), can be calculated as follows:

$$\varepsilon_{0i} = \frac{BM_{LT} + IN_{LT}}{E_c(AI - B^2)} \tag{3}$$

$$\kappa_i = \frac{AM_{LT} + BN_{LT}}{E_c(AI - B^2)} \tag{4}$$

where M_{LT} and N_{LT} are the moment and axial force applied at the beginning of the long-term loading, respectively ($N_{LT} = 0$ for RC sections under flexural moment only). Moreover, A is the area of the transformed section, and B and I are the first and second moments of inertia of the area of the transformed section, respectively. Furthermore, E_c is the modulus of elasticity of concrete.

Based on Gilbert [44], the variation with time (i.e. time-dependent) of the maximum concrete compressive strain $\Delta\varepsilon_0(t,t_0)$ and section curvature $\Delta\kappa(t,t_0)$ can be calculated as follows:

$$\Delta\varepsilon_0(t,t_0) = \frac{B_e(t,t_0)\Delta M(t,t_0) + I_e(t,t_0)\Delta N(t,t_0)}{E_e(t,t_0)(A_e(t,t_0)I_e(t,t_0) - B_e^2(t,t_0))} \tag{5}$$
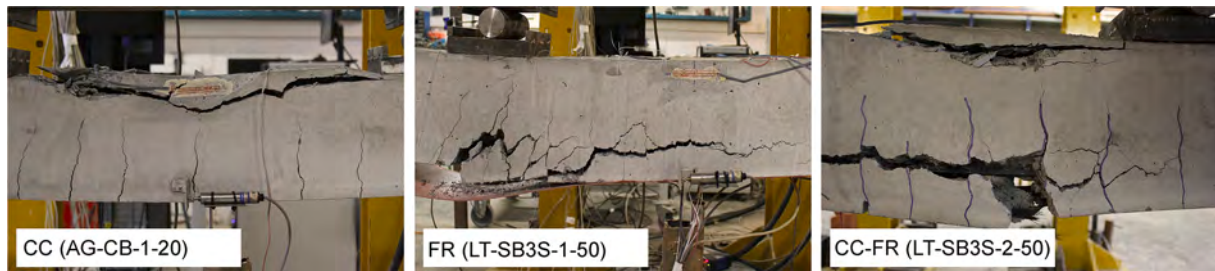

Fig. 16. Representative view of failure modes of the specimens in Series 2 and 3.
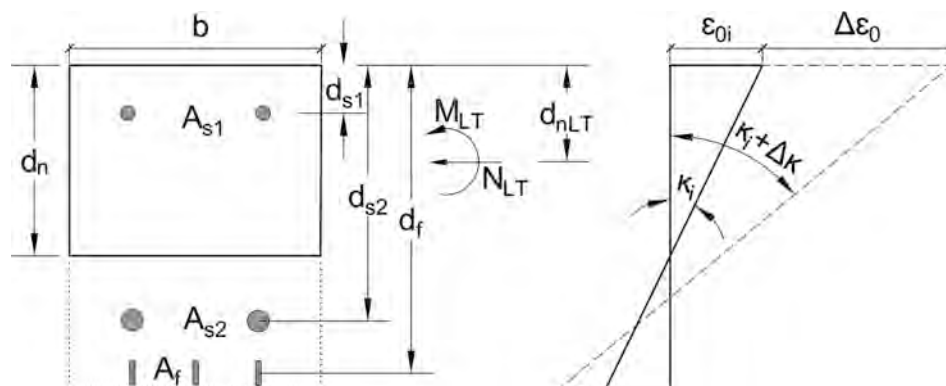

Fig. 17. Time-dependent analysis. (a) Schematic view of beam cross-section and (b) Instantaneous and long-term strains and curvatures in a cracked section.

$$\Delta\kappa(t,t_0) = \frac{A_e(t,t_0)\Delta M(t,t_0) + B_e(t,t_0)\Delta N(t,t_0)}{E_e(t,t_0)(A_e(t,t_0)I_e(t,t_0) - B_e^2(t,t_0))} \quad (6)$$

where t is the age of specimen at the moment considered in days and t_0 is the age of specimen at the beginning of long-term loading in days. In Eqs. (5) and (6), $A_e(t,t_0)$ is the area of the transformed section, and $B_e(t,t_0)$ and $I_e(t,t_0)$ are the first and second moments of inertia of the area of the transformed section, respectively. Finally, $\Delta M(t,t_0)$ and $\Delta N(t,t_0)$ are the restraining force and moment to prevent free development of creep and shrinkage in concrete, and can be calculated as:

$$\Delta N(t,t_0) = E_e(t,t_0)[\varphi_c(t,t_0)(A_c\varepsilon_{oi} - B_c\kappa_i) + \varepsilon_{sh}(t,t_0)A_c] \quad (7)$$

$$\Delta M(t,t_0) = E_e(t,t_0)[\varphi_c(t,t_0)(-B_c\varepsilon_{oi} + I_c\kappa_i) - \varepsilon_{sh}(t,t_0)B_c] \quad (8)$$

where A_c is the area of the concrete section, and B_c and I_c are the first and second moments of inertia of the area of the concrete section (without considering the steel reinforcement), respectively. The instantaneous maximum concrete compressive strain (ε_{0i}) and initial section curvature (κ_i) can be computed from Eqs. (3) and (4), respectively. In addition, $\varphi_c(t,t_0)$ and $\varepsilon_{sh}(t,t_0)$ are the concrete creep coefficient and shrinkage, and $E_e(t,t_0)$ is the effective modulus of elasticity of concrete. In this work, Model Code 2010 [11] predictions for concrete creep coefficient and shrinkage were assumed. Besides, in applying the AEMM, the effective modulus of elasticity of concrete can be obtained as bellow:

$$E_e(t,t_0) = \frac{E_c}{1 + \chi(t,t_0)\varphi_c(t,t_0)} \quad (9)$$

where $\chi(t,t_0)$ is the reduction factor for concrete creep coefficient, which can be taken as 0.8 for normal strength concrete [9,12,16,44].

It should be mentioned that, in addition to the explicit mention of $E_e(t,t_0)$ in Eqs. 5–8, the effective modulus of concrete should also be taken into account for the calculation of geometrical properties of the transformed section, by updating the time-dependent steel modular ratio, $n_s(t,t_0)$, and time-dependent FRP modular ratio, $n_{FRP}(t,t_0)$, as follows:

$$n_s(t,t_0) = E_s/E_e(t,t_0) \quad (10)$$

$$n_{FRP}(t,t_0) = E_{FRP}(t,t_0)/E_e(t,t_0) \quad (11)$$

where E_s is the modulus of elasticity of steel reinforcement and $E_{FRP}(t,t_0)$ is the modulus of elasticity of FRP.

4.1. Comparison with experimental results

In this section, analytical predictions following the previously presented methodology are compared to experimental results on time-dependent deflections (shown in Fig. 11). For the analytical predictions, average values for registers on temperature and humidity during the long-term load (see Fig. 4) were used for determining the concrete creep coefficient and shrinkage following Model Code 2010 [11]. In addition, the effect of temperature on mechanical properties of concrete was considered according to Mode Code 2010 [11]. It should be mentioned that temperature gradient in the height of the section causes an additional curvature/deflection that should be taken into account [44]. In this study, due to uniform heating, the difference in temperature between the bottom and top fibers was about 5 °C, thus causing a negligible extra curvature/deflection.

Comparisons of predicted and experimental time-dependent deflections are shown in Figs. 18-20. According to the results, the analytical predictions at 20 °C underestimate the time-dependent deflection, especially for the unstrengthened control beam with lower steel reinforcement ratio (LT-CB-1–20 with ρ = 0.79 %). Focusing on the prediction of the time-dependent deflections in specimens under a high service temperature, in general, analytical predictions overestimate the time-dependent deflection especially for those of the unstrengthened control beams (LT-CB-1–70 and LT-CB-2–70). It is worthy to mention that the presented analytical methodology could be also applied to members subjected to cyclic temperatures, as for instance day-night or summer-winter. In that case, the temperature and humidity histories should be considered as an input in the analytical model.

5. Conclusions

The present experimental work aims to study the long-term performance of NSM CFRP-strengthened RC beams under different service temperatures. An experimental campaign consisting of 23 NSM CFRP-strengthened RC beams was performed, where beams with different steel reinforcement ratios and different amounts of CFRP strengthening area were loaded for 200 days. After that, post long-term tests were carried out to analyze the residual flexural strength as well as the ageing effect. Besides, an analytical procedure for the prediction of time-dependent deflections is presented and compared to experimental results.

As a general conclusion, temperature did not affect the instantaneous flexural performance of NSM CFRP-strengthened RC beams, but had a significant effect on their time-dependent behavior and ultimate permanent deflections. More detailed conclusions are presented next.

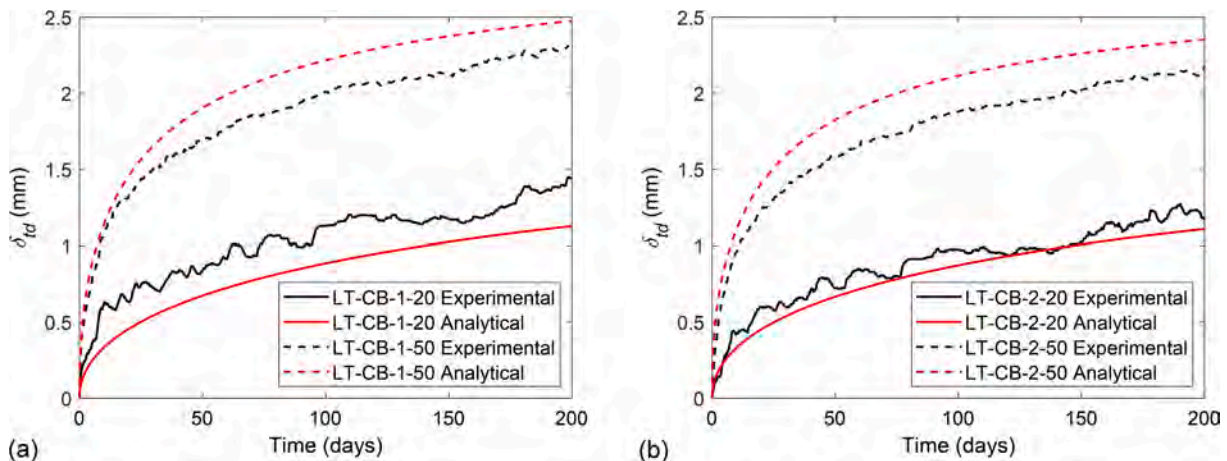From the short-term tests, the following conclusions can be drawn:

Fig. 18. Analytical predictions and experimental time-dependent deflections for unstrengthened control beams. (a) Group 1 (LT-CB-1–20 and LT-CB-1–50) and (b) Group 2 (LT-CB-2–20 and LT-CB-2–50).
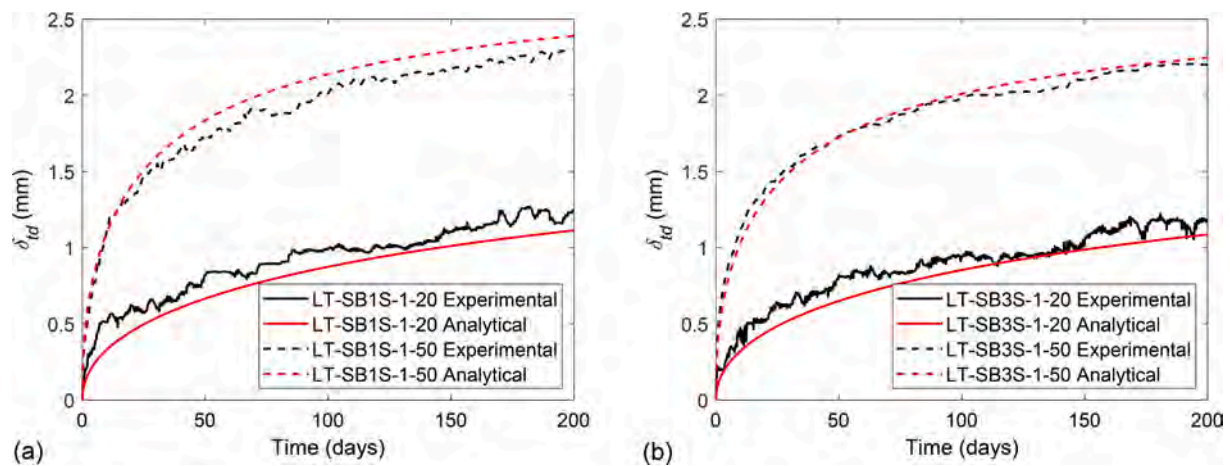
Fig. 19. Analytical predictions and experimental time-dependent deflections for strengthened beams in Group 1 having: (a) one CFRP strip (LT-SB1S–1–20 and LT-SB1S–1–50) and (b) three CFRP strips (LT-SB3S–1–20 and LT-SB3S–1–50).
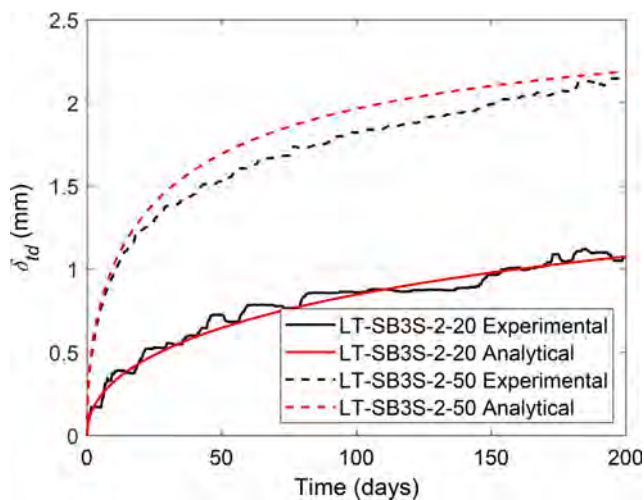

Fig. 20. Analytical predictions and experimental time-dependent deflections for strengthened beams in Group 2 (LT-SB3S-2–20 and LT-SB3S-2–50).

- The increase in the service temperature up to 50 °C had no significant effect on the load–deflection response of the specimens. This can be attributed to this temperature being below the T_g of epoxy adhesive and to an additional possible post-curing of the epoxy adhesive.
- The application of a high service temperature did not affect failure modes, and unstrengthened beams failed by concrete crushing after yielding of the steel reinforcement whilst strengthened beams failed by FRP rupture.

From the long-term tests and analytical predictions, the following conclusions can be drawn:

- The increase in the temperature from 20 °C to 50 °C had an effect on the time-dependent behavior of concrete (larger shrinkage and creep coefficient) and epoxy resin (larger creep coefficient).
- Under 20 °C and the same value of long-term load, lower time-dependent deflections were obtained for beams with larger amounts of FRP strengthening area, as expected. However, for testing temperature equal to 50 °C, the increase in the strengthening area did not have a significant effect on the time-dependent deflections and the time-dependent response of the strengthened beams approached that of the unstrengthened beams.

- The effect of temperature on the time-dependent behavior of concrete appeared to be the dominant factor in time-dependent response of RC beams.
- Analytical predictions based on AEMM and Model Code 2010 were in a good agreement with experimental data.

From the residual flexural strength tests and aging specimens, following conclusions can be drawn:

- Similar to time-dependent deflections, the ultimate permanent deflection of specimens subjected to 50 °C was larger than that of specimens at 20 °C.
- When compared to short-term and aging specimens, no significant change was observed in the residual strength of unstrengthened control beams. On the other hand, for the strengthened beams, a slight increase in yielding load and post-yielding stiffness were found.
- Failure mode of the strengthened specimens with higher reinforcement was changed from FRP rupture to concrete crushing followed by FRP rupture. The rest of the specimens had the same failure mode as in short-term testing.
- The largest initial stiffness was observed for the specimens subjected to long-term load. Furthermore, the specimens subjected to temperature had lower initial stiffness due to larger permanent accumulated deflections.

CRediT authorship contribution statement

Younes Jahani: Conceptualization, Methodology, Validation, Investigation, Data curation, Software, Visualization, Writing – original draft. **Marta Baena:** Conceptualization, Validation, Formal analysis, Writing – review & editing, Supervision, Project administration, Funding acquisition. **Alba Codina:** Validation, Investigation, Writing – review & editing. **Cristina Barris:** Formal analysis, Writing – review & editing, Project administration, Funding acquisition. **Lluís Torres:** Validation, Formal analysis, Writing – review & editing, Supervision.

Declaration of Competing Interest

The authors declare that they have no known competing financial interests or personal relationships that could have appeared to influence the work reported in this paper.

Data availability

Data will be made available on request.

Data availability

The raw/processed data required to reproduce these findings cannot be shared at this time as the data also forms part of an ongoing study.

References

[1] GangaRao HVS, Taly N, Vijay PV. Reinforced Concrete Design with FRP Composites. CRC Press; 2006.

[2] Nanni A. Fiber-Reinforced-Plastic (FRP) Reinforcement for Concrete Structures: Properties and Application. Amsterdam: Elsevier Science; 1993.

[3] Al-Saadi NTK, Mohammed A, Al-Mahaidi R, Sanjayan J. A state-of-the-art review: Near-surface mounted FRP composites for reinforced concrete structures. Constr Build Mater 2019;209:748–69. https://doi.org/10.1016/j.conbuildmat.2019.03.121.

[4] De Lorenzis L, Teng JG. Near-surface mounted FRP reinforcement: An emerging technique for strengthening structures. Compos Part B 2007;38(2):119–43. https://doi.org/10.1016/j.compositesb.2006.08.003.

[5] Parretti R, Nanni A. Strengthening of RC members using near-surface mounted FRP composites: design overview. Adv Struct Eng 2004;7(6):469–83. https://doi.org/10.1260/1369433042863198.

[6] Pellegrino C, Sena-Cruz J. Design Procedures for the Use of Composites in Strengthening of Reinforced Concrete Structures. State-of-the-Art Report of the Rilem Technical Committee. Springer, The Netherlands, 2016. 10.1007/978-94-017-7336-2.

[7] Daud SA, Forth JP, Nikitas N. Time-dependent behaviour of cracked, partially bonded reinforced concrete beams under repeated and sustained loads. Eng Struct 2018;163:267–80. https://doi.org/10.1016/j.engstruct.2018.02.054.

[8] Mias C, Torres L, Turon A, Sharaky IA. Effect of material properties on long-term deflections of GFRP reinforced concrete beams. Constr Build Mater 2013;41: 99–108. https://doi.org/10.1016/j.conbuildmat.2012.11.055.

[9] Kim SH, Han KB, Kim KS, Park SK. Stress–strain and deflection relationships of RC beam bonded with FRPs under sustained load. Compos Part B 2009;40(4):292–304. https://doi.org/10.1016/j.compositesb.2008.12.003.

[10] Malumbela G, Moyo P, Alexander M. Behaviour of RC beams corroded under sustained service loads. Constr Build Mater 2009;23(11):3346–51. https://doi.org/10.1016/j.conbuildmat.2009.06.005.

[11] International Federation for Structural Concrete (fib). Fib Model Code for Concrete Structures 2010. John Wiley & Sons, New York, USA, 2013.

[12] Hong S, Park SK. Long-term behavior of fiber-reinforced-polymer-plated concrete beams under sustained loading: Analytical and experimental study. Compos Struct 2016;152:140–57. https://doi.org/10.1016/j.compstruct.2016.05.031.

[13] Al Chami G, Theriault M, Neale KW. Creep behaviour of CFRP-strengthened reinforced concrete beams. Constr Build Mater 2009;23(4):1640–52. https://doi.org/10.1016/j.conbuildmat.2007.09.006.

[14] Sobuz HR, Ahmed E, Sutan NM, Hasan NMS, Uddin MA, Uddin MJ. Bending and time-dependent responses of RC beams strengthened with bonded carbon fiber composite laminates. Constr Build Mater 2012;29:597–611. https://doi.org/10.1016/j.conbuildmat.2011.11.006.

[15] Li X, Gu X, Ouyang Y, Song X. Long-term behavior of existing low-strength reinforced concrete beams strengthened with carbon fiber composite sheets. Compos Part B 2012;43(3):1637–44. https://doi.org/10.1016/j.compositesb.2012.01.016.

[16] El-Sayed AK, Al-Zaid RA, Al-Negheimish AI, Shuraim AB, Alhozaimy AM. Long-term behavior of wide shallow RC beams strengthened with externally bonded CFRP plates. Constr Build Mater 2014;51:473–83. https://doi.org/10.1016/j.conbuildmat.2013.10.055.

[17] Jiang S, Yao W, Chen J, Tao S. Time dependent behavior of FRP-strengthened RC beams subjected to preload: experimental study and finite element modeling. Compos Struct 2018;200:599–613. https://doi.org/10.1016/j.compstruct.2018.05.110.

[18] Sena-Cruz J, Silva P, Fernandes P, Azenha M, Barros J, Sousa CF, Castro F, Teixeira TAN. Creep behavior of concrete elements strengthened with NSM CFRP laminate strips under different environmental conditions. In: FRPRCS-11: 11th International Symposium on Fiber Reinforced Polymer for Reinforced Concrete Structures. Universidade do Minho, 2013.

[19] Moawad M, Baena M, Barris C, Torres L, Sallam HEM. Time-dependent behavior of NSM strengthened RC beams under sustained loading. Eng Struct 2021;247: 113210. https://doi.org/10.1016/j.engstruct.2021.113210.

[20] Kim YJ, Khan F. Creep-induced distress on flexural behavior of reinforced concrete beams retrofitted with near-surface-mounted carbon fiber-reinforced polymer. ACI Struct J 2015;112(4):493–504. https://doi.org/10.14359/51687705.

[21] Kim YJ. Modeling of near-surface-mounted carbon fiber-reinforced polymer for strengthening reinforced concrete beams in sustained load. ACI Struct J 2015;112 (6):805–13. https://doi.org/10.14359/51687659.

[22] Emara M, Torres L, Baena M, Barris C, Moawad M. Effect of sustained loading and environmental conditions on the creep behavior of an epoxy adhesive for concrete structures strengthened with CFRP laminates. Compos Part B 2017;129:88–96. https://doi.org/10.1016/j.compositesb.2017.07.026.

[23] Firmo JP, Roquette MG, Correia JR, Azevedo AS. Influence of elevated temperatures on epoxy adhesive used in CFRP strengthening systems for civil engineering applications. Int J Adhes Adhes 2019;93:102333. https://doi.org/10.1016/j.ijadhadh.2019.01.027.

[24] Jahani Y, Baena M, Barris C, Perera R, Torres L. Influence of curing, post-curing and testing temperatures on mechanical properties of a structural adhesive. Constr Build Mater 2022;324:126698. https://doi.org/10.1016/j.conbuildmat.2022.126698.

[25] Silva P, Fernandes P, Sena-Cruz J, Xavier J, Castro F, Soares D, et al. Effects of different environmental conditions on the mechanical characteristics of a structural epoxy. Compos Part B 2016;88:55–63. https://doi.org/10.1016/j.compositesb.2015.10.036.

[26] Barris B, Sala P, Gómez J, Torres L. Flexural behaviour of FRP reinforced concrete beams strengthened with NSM CFRP strips. Compos Struct 2020;241:112059. https://doi.org/10.1016/j.compstruct.2020.112059.

[27] Al-Mahmoud F, Castel A, François R, Tourneur C. RC beams strengthened with NSM CFRP rods and modeling of peeling-off failure. Compos Struct 2010;92(8): 1920–30. https://doi.org/10.1016/j.compstruct.2010.01.002.

[28] Al-Mahmoud F, Castel A, François R, Tourneur C. Strengthening of RC members with near-surface mounted CFRP rods. Compos struct 2006;91(2):138–47. https://doi.org/10.1016/j.compstruct.2009.04.040.

[29] Capozucca R. Static and dynamic response of damaged RC beams strengthened with NSM CFRP rods. Compos Struct 2009;91(3):237–48. https://doi.org/10.1016/j.compstruct.2009.05.003.

[30] Reda RM, Sharaky IA, Ghanem M, Seleem MH, Sallam HEM. Flexural behavior of RC beams strengthened by NSM GFRP Bars having different end conditions. Compos Struct 2016;14:131–42. https://doi.org/10.1016/j.compstruct.2016.03.018.

[31] Sena Cruz J, Barros J. Bond between near surface mounted carbon-fiber-reinforced polymer laminate strips and concrete. J Compos Constr 2004;8(6):519–27. https://doi.org/10.1061/(ASCE)1090-0268(2004)8:6(519).

[32] Sena-Cruz J, Barros J, Coelho MR, Silva LF. Efficiency of different techniques in flexural strengthening of RC beams under monotonic and fatigue loading. Constr Build Mater 2012;29:175–82. https://doi.org/10.1016/j.conbuildmat.2011.10.044.

[33] Bilotta A, Ceroni F, Di Ludovico M, Nigro E, Pecce M, Manfredi G. Bond efficiency of EBR and NSM FRP systems for strengthening concrete members. J Compos Constr 2011;15(5):757–72. https://doi.org/10.1061/(ASCE)CC.1943-5614.0000204.

[34] Triantafyllou G, Rousakis T, Karabinis A. Corroded RC beams at service load before and after patch repair and strengthening with NSM CFRP strips. Build 2019;9(3): 67. https://doi.org/10.3390/buildings9030067.

[35] Palmieri A, Matthys S, Taerwe L. Fire endurance and residual strength of insulated concrete beams strengthened with near-surface mounted reinforcement. J Compos Constr 2012;17:454–62. http://hdl.handle.net/1854/LU-3238162.

[36] Palmieri A, Matthys S, Taerwe L. Experimental investigation on fire endurance of insulated concrete beams strengthened with near surface mounted FRP bar reinforcement. Compos B Eng 2012;43:885–95. https://doi.org/10.1016/j.compositesb.2011.11.061.

[37] Firmo JP, Correia JR. Fire behaviour of thermally insulated RC beams strengthened with NSM-CFRP strips: experimental study. Compos B Eng 2015;76:112–21. https://doi.org/10.1016/j.compositesb.2015.02.018.

[38] Carlos TB, Rodrigues JPC, de Lima RC, Dhima D. Experimental analysis on flexural behaviour of RC beams strengthened with CFRP laminates and under fire conditions. Compos Struct 2018;189:516–28. https://doi.org/10.1016/j.compstruct.2018.01.094.

[39] Burke PJ, Luke AB, Mark FG. Effects of elevated temperature on near surface mounted and externally bonded FRP strengthening systems for concrete. Cem Concr Compos 2013;35:190–9. https://doi.org/10.1016/j.cemconcomp.2012.10.003.

[40] Jahani Y, Baena M, Gómez J, Barris C, Torres L. Experimental study of the effect of high service temperature on the flexural performance of Near-Surface Mounted (NSM) Carbon Fiber-Reinforced Polymer (CFRP)-Strengthened Concrete Beams. Polymers 2021;13(6):920. https://doi.org/10.3390/polym13060920.

[41] Silva P, Escusa GG, Sena-Cruz J, Azenha M. Experimental investigation of RC slabs strengthened with NSM CFRP system subjected to elevated temperatures up to 80 °C. In: Proc. 8th Int. Conf. on Fibre-Reinforced Polymer (FRP) Composites in Civil Engineering, CICE, Hong Kong, China, 2016. http://hdl.handle.net/1822/43902.

[42] Azevedo AS, Firmo JP, Correia JR, Tiago C. Influence of elevated temperatures on the bond behaviour between concrete and NSM-CFRP strips. Cem Concr Compos 2020;111:103603. https://doi.org/10.1016/j.cemconcomp.2020.103603.

[43] Leone M, Matthys S, Aiello MA. Effect of elevated service temperature on bond between FRP EBR systems and concrete. Compos B Eng 2009;40(1):85–93. https://doi.org/10.1016/j.compositesb.2008.06.004.

[44] Gilbert RI. Time effects in concrete structures. Amsterdam: Elsevier; 1988.

[45] Fib Bulletin 90. Externally Applied FRP Reinforcement for Concrete Structures; International Federation for Structural Concrete: Lausanne, Switzerland, 2019.

[46] UNE-EN 12390-3. Testing Hardened Concrete—Part 3: Compressive Strength of Test Specimens; AENOR: Madrid, Spain, 2003.

[47] UNE-EN 12390-6. Testing Hardened Concrete—Part 6: Tensile Splitting Strength of Test Specimens; AENOR: Madrid, Spain, 2010.

[48] ASTM C469/C469M-14. Standard Test Method for Static Modulus of Elasticity and Poisson's Ratio of Concrete in Compression; ASTM International: West Conshohocken, PA, USA, 2014.

[49] ASTM, ASTM C512 - Standard Test Method for Creep of Concrete in Compression, ASTM International, West Conshohocken, 2010.

[50] UNE-EN ISO 15630-1. Steel for the Reinforcement and Prestressing of Concrete-Test Methods—Part 1: Reinforcing Bars, Wire Rod and Wire; AENOR: Madrid, Spain, 2011.

[51] S&P. S&P Cfrp Laminate, Technical Datasheet; S&P: Seewen, Switzerland, 2017.

[52] ISO 527-5. Plastics-Determination of Tensile Properties—Part 5: Test Conditions FOR Unidirectional Fibre-Reinforced Plastic Composites; ISO: Geneva, Switzerland, 2009.

[53] S&P. S&P Resin 220 HP Epoxy Adhesive, Technical Data Sheet; S&P: Seewen, Switzerland, 2019.

[54] ISO 527-1. Plastics-Determination of Tensile Properties—Part 1: General Principles; ISO: Geneva, Switzerland, 2012.

[55] ASTM E1356-08. Standard Test Method for Assignment of the Glass Transition Temperatures by Differential Scanning Calorimetry; ASTM International: West Conshohocken, PA, USA, 2008.

[56] ASTM D5023-15. Standard Test Method for Plastics: Dynamic Mechanical Properties: In Flexure (Three-Point Bending); ASTM International: West Conshohocken, PA, USA, 2015.

[57] Costa I, Barros J. Tensile creep of a structural epoxy adhesive: experimental and analytical characterization. Int J Adhes Adhes 2015;59:115–24. https://doi.org/10.1016/j.ijadhadh.2015.02.006.

[58] Silva P, Valente T, Azenha M, Sena-Cruz J, Barros J. Viscoelastic response of an epoxy adhesive for construction since its early ages: experiments and modelling. Compos Part B 2016;116:266–77. https://doi.org/10.1016/j.compositesb.2016.10.047.

[59] Majda P, Skrodzewicz JA. Modified creep model of epoxy adhesive at ambient temperature. Int J Adhes Adhes 2009;29(4):396–404. https://doi.org/10.1016/j.ijadhadh.2008.07.010.

[60] Gómez J, Barris C, Jahani Y, Baena M, Torres L. Experimental study and numerical prediction of the bond response of NSM CFRP laminates in RC elements under sustained loading. Constr Build Mater 2021;288:123082. https://doi.org/10.1016/j.conbuildmat.2021.123082.

[61] EN 1992-1-1. Eurocode 2. Design of Concrete Structures—Part 1-1: General Rules and Rules for Buildings; British Standard Institution: London, UK, 2004.